Yukihiro Ozaki · Satoshi Kawata *Editors*

Far- and Deep-Ultraviolet Spectroscopy

Springer

Far- and Deep-Ultraviolet Spectroscopy

Yukihiro Ozaki • Satoshi Kawata
Editors

Far- and Deep-Ultraviolet Spectroscopy

Springer

Editors
Yukihiro Ozaki
School of Science and Technology
Kwansei Gakuin University
Sanda, Hyogo, Japan

Satoshi Kawata
Graduate School of Engineering
Osaka University
Suita, Osaka, Japan

ISBN 978-4-431-55548-3 ISBN 978-4-431-55549-0 (eBook)
DOI 10.1007/978-4-431-55549-0

Library of Congress Control Number: 2015943615

Springer Tokyo Heidelberg New York Dordrecht London

Printed on acid-free paper

Springer Japan KK is part of Springer Science+Business Media (www.springer.com)

Preface

This book provides the fundamentals of science and technology of far and deep ultraviolet (UV) spectroscopy. It has been known that many atoms and molecules exhibit effective optical response in far and deep UV regimes, hence a variety of applications of far and deep UV (FUV and DUV) spectroscopy have been expected in materials analysis, biosensing, catalysis, sterilization, and semiconductor fabrication. In recent decades, significant progress has been made in the development of detectors and light sources as well as optical materials to manipulate far and deep UV light. Compared to visible and near-UV spectroscopy, studies with DUV–FUV spectroscopy as analytical methods are still in progress. Due to the strong absorptive characteristic of materials, this spectroscopy has been considered to be applicable only to limited cases. DUV–FUV spectroscopy can be used for fundamental chemistry, biology, material science, and industrial applications, and the reader will find here a diversity of knowledge about this wavelength range.

The UV region is generally recognized as that of 10–380 nm, although the region has no international official definition. The 10–380 nm region corresponds to the 1,000,000–26,316 cm^{-1} region. Thus, one can easily recognize that from the high-energy edge to the low-energy edge of the UV region, the energy changes by approximately 40 times. The characteristics of the UV region vary largely from the high-energy edge to the low-energy edge, and the whole UV region is concerned with electronic transitions. The UV region is so wide that it is divided into several regions. The higher-energy region, the region of 10–200 nm, has often been called the vacuum UV region because an spectrometer must have been evacuated to eliminate the effects of strong absorption of oxygen molecules. However, nowadays the 140–200 nm region does not always require evacuation of an instrument because a nitrogen gas purge is usually good enough to overcome the problem. Thus, the 10–140 nm region may be designated the vacuum UV region.

The purpose of the present book is to outline recent progress in spectroscopy in the 140–300 nm region. In this book the 140–200 nm region is tentatively defined as the FUV region and the 200–380 nm region as the DUV region. FUV and DUV regions can be differentiated in several ways, but most simply they are separated by the fact that the former (particularly below 180 nm) needs vacuum

evaporation or nitrogen gas purge while the latter does not. Spectroscopy in both regions has recently received keen interest because of a number of breakthroughs in both regions. For example, in the FUV region an attenuated total reflection (ATR)–FUV spectrometer has recently been developed. This development has opened spectroscopy in this region for condensed matter. In the DUV region, DUV enhanced surface-enhanced Raman scattering (SERS) spectroscopy has emerged. Thanks to the development of plasmonics in the DUV range, the localization and intensification of DUV photons in the vicinity of metal nanostructures has been possible, leading to the high-sensitivity spectroscopic measurements for Raman/Rayleigh scattering or fluorescence. DUV-plasmonics was extended to high spatial resolution imaging such as tip-enhanced Raman spectroscopy (TERS) and improvement of LED and opto-electronic devices. Besides these breakthroughs, both DUV and FUV spectroscopy have benefitted from the recent developments in optics, light sources, and optical detectors.

This book consists of nine chapters. Chapter 1 is concerned with a general introduction to FUV and DUV spectroscopy by Ozaki, Saito, and Kawata. Chapter 2 is a detailed description of FUV instrumentation by Ikehata, Morisawa, and Higashi. In Chap. 3, fundamental optical phenomena in FUV are overviewed by Morisawa and Ehara. Chapters 4, 5 and 6 are devoted to various applications of FUV spectroscopy, e.g., water by Ikehata and Goto, industrial applications by Higashi, and titanium dioxide by Tanabe. In the last three chapters the recent progress in DUV spectroscopy is discussed. In Chap. 7 DUV imaging is reviewed by Kumamoto, the DUV–SERS/TERS is introduced in Chap. 8 by Taguchi, and the final chapter is devoted to photon–electron conversions in DUV by Saito.

We hope readers of this book will learn a great deal about the potential of FUV and DUV spectroscopy in basic and applied science. In closing, we would like to thank Dr. Shinichi Koizumi and Ms. Taeko Sato of Springer Japan for their continuous efforts in publishing this book.

Sanda, Japan — Yukihiro Ozaki
Suita, Japan — Yuika Saito
Suita, Japan — Satoshi Kawata
February 2015

Contents

Chapter 1
Introduction to FUV and DUV Spectroscopy

Yukihiro Ozaki, Yuika Saito, and Satoshi Kawata

Abstract Recently, both far ultraviolet (FUV) and deep UV (DUV) spectroscopies have received keen interest as new spectroscopies because they offer novel possibilities for studying electronic structure and transition, selective molecular imaging, high resolution microscopy, as well as applications for photoelectric devices. In this chapter after brief history of UV light, UV, FUV, and DUV regions are defined. Then, principles and brief history of FUV spectroscopy are described, followed by the discussion of its characteristics and advantages. Recent progress in FUV spectroscopy is also introduced. In the second part of this chapter, principles, methods, and recent progress of DUV spectroscopy are mentioned. Finally, the characteristics of FUV and DUV spectroscopies are compared.

Keywords UV • Ultraviolet spectroscopy • FUV spectroscopy • DUV spectroscopy • Plasmonically enhance spectroscopy • Surface-enhance Raman scattering • Electronic transition • Rydberg transition • Molecular imaging • Near-field microscopy • Photocatalysis

1.1 Introduction

The discovery of ultraviolet (UV) light was largely due to spectroscopists and chemists in the eighteenth century, before the spectrometer was invented. It was known from the seventeenth century that sunlight has the power to induce photochemical reactions such as the blackening of silver nitride or silver chloride crystals. Moreover, the violet component of sunlight, extracted using a prism, was particularly effective. It was in 1801 that Johann Ritter, a German scientist,

Y. Ozaki (✉)
School of Science and Technology, Kwansei Gakuin University, Sanda, Hyogo, Japan
e-mail: ozaki@kwansei.ac.jp

Y. Saito
Department of Applied Physics, Osaka University, Suita, Japan
e-mail: yuika@ap.eng.osaka-u.ac.jp

S. Kawata
Graduate School of Engineering, Osaka University, Suita, Osaka, Japan

Y. Ozaki, S. Kawata (eds.), *Far- and Deep-Ultraviolet Spectroscopy*,
DOI 10.1007/978-4-431-55549-0_1

finally discovered that the effect is even stronger when a paper soaked with silver chloride was placed in the region of the solar spectrum beyond violet light [1]. This invisible component of sunlight was then called "chemical rays," but is now called "ultraviolet" light because it was found beyond the violet end of the solar spectrum. Following Maxwell's electromagnetic theory, Planck theorized in the beginning of the twentieth century that radiation is composed of tiny packets of energy called "quanta." Einstein clarified that Planck's quanta were massless particles of energy called photons. The development of quantum theory highlighted the importance of UV light, as a single UV photon can accomplish something that a number of infrared photons cannot. The wavelength dependence of the photoelectric effect was experimentally verified by Millikan, who measured the photocurrent of an anode under illumination [2].

Light with a wavelength shorter than that of visible rays (>380 nm) and longer than that of X-rays (<10 nm) is considered to be UV [3]. As observed during its original discovery, UV light can induce strong chemical interactions, which can be either useful or harmful to life. Biologists developed a different terminology to emphasize the effects of solar UV light on living creatures. The term "UVA" is used for the 320–400 nm region that can penetrate window glass and has physiological effects on organisms. The term "UVC" refers to the solar region shorter than 290 nm, which is absorbed by the ozone layer in the Earth's upper atmosphere. Finally, the term "UVB" is applied to the region between UVC and UVA (290–320 nm). Since sunlight reaching the earth has a non-negligible amount of this component, it has been believed to be responsible for the deleterious effects of sunlight on living organisms [1].

This book is concerned with the ultraviolet (UV) spectroscopy in the region of 120–300 nm. We refer to the wavelength range 120–200 nm and 200–300 nm as the far UV (FUV) and deep UV (DUV). The word "vacuum UV region" is not appropriate anymore at least for the 120–200 nm region because most of recent spectrometers used in this region do not have the vacuum evaporation system but have the nitrogen gas-purged system. Both FUV and DUV spectroscopies are concerned with electronic transitions of a molecule, and the differences between them may be summarized as follows [4–11]: (1) the DUV region is free from absorption of oxygen, so that this region does not request a vacuum evaporation system or a nitrogen gas-purged system. On the other hand, the FUV region needs a vacuum evaporation system or a nitrogen gas-purged system. (2) In the DUV region, absorption bands due to various kinds of electronic transitions such as π-π^* and n-π^* transitions appear, but σ-σ^* transitions do not appear. In the FUV region, not only σ-σ^* transitions but also Rydberg transitions may be observed (Chap. 3). It is noted that water, alkanes, and alcohols do not show any peak in the DUV region but they yield very strong bands in the FUV region. DUV absorption spectroscopy has long been well developed. DUV-excited resonance Raman spectroscopy has also a rather long history [9–11]. Recently, DUV-excited surface-enhanced Raman scattering (SERS) spectroscopy has received keen interest. Compared with DUV spectroscopy, the advance in FUV spectroscopy has been rather slow because of three major reasons [7, 8]. One is the trouble in instrumentation mentioned above

(vacuum evacuation or nitrogen gas purge). Another is the very high absorptivity of a molecule in the FUV region. Yet another is that it was difficult to find application of FUV spectroscopy. For the last decade or so, there has been marked progress in both FUV and DUV regions. In this chapter basic principles and recent progress of FUV and DUV regions will be described.

1.2 FUV Spectroscopy

1.2.1 Basic Principle and Brief History of FUV Spectroscopy

Spectra in the FUV region have been studied for molecules in the gas phase for more than 50 years. Many gas molecules with sufficient vapor pressure were subjected to FUV measurement, and it was found from these studies that various kinds of molecule shave strong absorptions due to electronic transitions to low-lying Rydberg states in the FUV region until their vertical ionized energy. Rydberg transitions of organic molecules have primarily been studied in gaseous states owing to the limitations of experimental techniques. Indeed, investigations of Rydberg states in the gas phase date back almost 50 years [6]. In 1974, Robin [12] assigned a few bands produced by gaseous propane to transitions including Rydberg states based on term value analysis.

Raymonda and Simpson [13] measured FUV spectra in the 11.5–7.1 eV region of *n*-alkanes ($n = 2$–9) in the gas state by using a transmission method. Au et al. [14] also observed FUV spectra in the 40–7 eV of *n*-alkanes ($n = 1$–8) in the gas state. The latter group assigned a peak in the 10.6–8.5 eV and a shoulder in the 9.8–8.0 eV to Rydberg transitions.

Cheng et al. measured FUV spectra in the 107–220 nm region of CH_3OH, CH_3OD, CD_3OH, and CD_3OD in the gas phase by using a high-resolution spectrometer with synchrotron radiation. Based on the experimental results including those for the deuterated species together with time-dependent density functional theory (TD-DFT) calculations, they assigned three absorptions at around 183 nm (6.8 eV), 160 nm (7.7 eV), and 149 nm (8.3 eV) to the transitions between the ground state X^1A' and three excited states 1 $^1A''$ ($2a''$-$3s$), 2 $^1A''$ ($2a''$-$3p$), and 3 $^1A''$ ($2a''$-$3p''$) or 3 $^1A'$ ($2a''$-$3p''$), respectively [15].

Electronic transitions of acetone in the gas phase have been investigated by using standard absorption [12, 16–18], energy loss [19, 20], and resonance-enhanced multiphoton (REMPI) spectroscopy [21, 22]. Several theoretical investigations have also been carried out on the vertical transition energy of acetone in the FUV region [22–24]. These studies suggested the assignments for a few absorptions in the 7.45–4.38 eV region of acetone in the gas phase. Although the first electronic transition, the valence n-π^* transition, is a dipole-forbidden transition, it is observed in the UV region (5.4–3.8 eV) as an electro-vibronic transition [25]. In the FUV region, n-3s Rydberg and n-3p Rydberg transitions of acetone in the gas phase are observed at 6.35 and 7.4 eV, respectively, as strong and weak absorptions.

Kaya et al. measured FUV spectra of six kinds of amides in the gas phase. They assigned the major absorption band to the π-π^* transition and found a peak shift to lower energy upon CH_3 substitution on the N atom. The peak shifts to low energy region were attributed to hyperconjugation with the substitution of methyl groups [26].

Band assignments in the FUV region are not straightforward and have not been well established. In general, liquid and solid samples have very strong absorption in the FUV region. Many materials that do not show a significant absorption in the region longer than about 200 nm yield intense absorptions in this region. Water is a good example [27–29].

FUV spectra of liquid and solid samples have also been investigated for more than 40 years, although their examples are limited (Chaps. 3, 4, 5, and 6). In 1971, Rubloff et al. [30] tried to measure FUV spectra of solids in the region of 36–6 eV (34–207 nm) using synchrotron radiation from an electron storage ring. Jung and Gress [31, 32] also used synchrotron radiation to observe transmission FUV spectra in the 115–207 nm (10.8–6.0 eV) region of CH_3OH and C_2H_5OH in liquid phases. Kuo et al. [33] measured FUV absorption spectra of CH_3OH in neat solid and rare gas mixtures.

Only a few studies have suggested the existence of Rydberg transitions in the liquid [34] and solid states [35]. For example, Weiss et al. [35] suggested the existence of the Rydberg state in the Langmuir–Blodgett film of Ca–arachidate for the solid state using X-ray spectroscopy. Costner et al. [34] also indicated the existence of Rydberg transitions in liquid alkanes based on the intensities of the tails near 175 nm of strong bands in the 170–200 nm region measured by a transmission method by which the peak positions could not be observed owing to the strong bands.

Several research groups reported transmission spectra of water down to 155 nm (8.0 eV) or below by preparing an extremely thin water film (2,850 Å thick) [35, 36]. This technique was not convenient and suffered from poor repeatability. Therefore, reflection spectra of water were measured instead in the wavelength region shorter than 170 nm. Painter et al. [37–40] calculated the absorption spectra of water from reflectance measurements, but poor sensitivity of the reflection measurements prevented the study of important questions such as how minute levels of dissolved substances affect absorption bands of water. Many FUV spectroscopy studies have been carried out for water, aqueous solutions, and liquids using the region of the long-wavelength wing near 190 nm where commercially available spectrometers can be used because intensity, position, and bandwidth are very sensitive to changes in hydrogen bondings and hydration of water [7, 8, 41–46].

Sério and coworkers [47] measured the FUV–DUV absorption spectra of TiO_2 using the synchrotron radiation facility; however, reliable data were limited to the DUV region (>200 nm) because of the strong influence of water absorption in the FUV region.

1.2.2 Characteristics and Advantages of FUV Spectroscopy

Let us first illustrate the characteristics and usefulness of FUV spectroscopy by discussing the absorption spectrum of water [7, 8] (Chap. 4). Figure 1.1 shows the spectrum of water from the infrared (IR) to the FUV region [48]. In this figure the intensity is shown in absorbance units assuming a path length of 100 nm based on literature data of molar absorptivities. In the IR region we observe two major bands at about 2,900 nm (3,400 cm^{-1}) and 6,200 nm (1,650 cm^{-1}) assigned to H–O–H stretching and bending modes, respectively. Bands due to their overtones and combinations are observed in the near-infrared (NIR) region. The ultraviolet–visible (UV–vis) region does not show significant absorption of water, but it is noted that the FUV region contains an absorption due to water at about 150 nm that is stronger by several orders of magnitude than the H–O–H stretching band. This intense band is called simply the first electronic transition ($\tilde{A} \leftarrow \tilde{X}$) of water because it arises from the electronic transition of the lowest energy site [25]. The fact that the $\tilde{A} \leftarrow \tilde{X}$ absorption of water is considerably stronger than the IR absorptions makes it difficult to measure the band maxima of the $\tilde{A} \leftarrow \tilde{X}$ absorption of liquid water and aqueous solutions.

FUV spectroscopy has the following advantages for liquid and solid studies [7, 8, 46, 49–66]. The FUV region contains rich information about the electronic

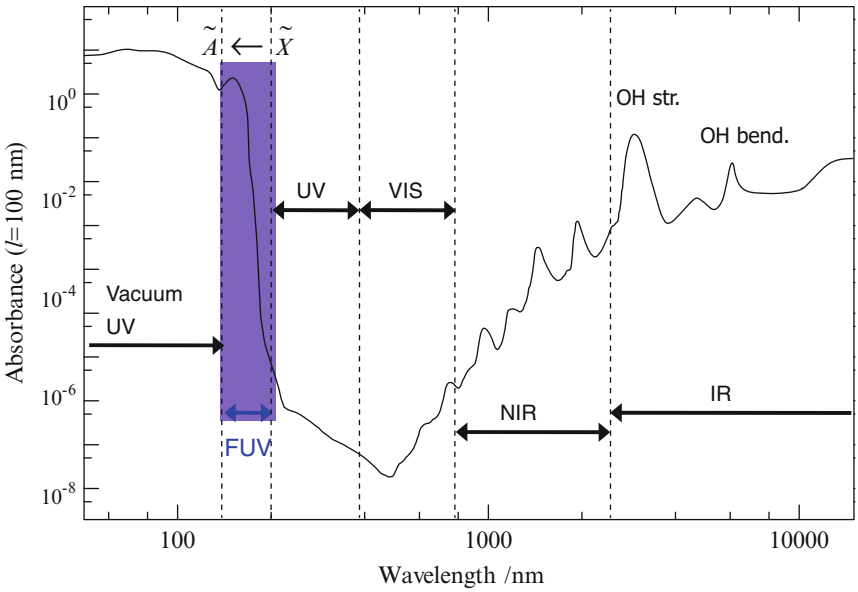

Fig. 1.1 An absorption spectrum of water from IR to FUV region. The intensity is an absorbance unit assuming a path length of 100 nm

transitions and structure of a molecule. It is possible to extract unique information about them, which one cannot get from ordinary UV spectroscopy (Chaps. 3, 4, and 6). For example, one can explore Rydberg transitions of liquids [54–58, 65, 66]. It is also possible to investigate transitions concerning σ electrons of various molecules and the π-π* transitions of small molecules such as simple amides by using FUV spectroscopy (Chap. 3). FUV spectroscopy is powerful to explore hydrogen bondings and hydration of water, aqueous solutions, and inorganic and organic molecules (Chaps. 3, 4, and 6). One can apply FUV spectroscopy for qualitative analysis and discrimination analysis of various liquid and solid samples because each molecule shows a unique FUV spectrum, and FUV spectra are very sensitive to variations such as those in chemical bonding, molecular conformations, and molecular environments (Chaps. 3 and 4). FUV spectroscopy is useful for highly sensitive quantitative analysis because almost all molecules give rise to strong absorption in the FUV region, and the intensity and wavelength of an FUV band are very sensitive to changes in concentration, temperature, pH, and so on (Chaps. 4 and 5). It is also possible to employ FUV spectroscopy for a wide range of applications such as online analysis, process monitoring, water analysis, photocatalysis, and polymer film characterization as is mentioned later (Chaps. 5 and 6). Time-resolved (TR) FUV spectroscopy has also a considerable potential for basic science and application (Chap. 2).

1.2.3 Recent Progress in FUV Spectroscopy

To develop liquid- and solid-state FUV spectroscopy, two kinds of FUV spectrometers with quite different designs have been designed [7, 8, 14, 49] (Chap. 2). One is a compact FUV spectrometer designed for online monitoring of aqueous solutions. By using this instrument, one can measure spectra of liquid samples down to 180 nm with nitrogen gas purge [49]. Its size is only 30 cm × 16 cm × 16 cm, including a UV light source, a grating, a photoabsorption cell, and an optical sensor. The other is an ATR–FUV spectrometer that covers the wavelength range from 140 to 300 nm [67]. In this spectrometer, the design of a very small internal reflection element (IRE) probe has led to successful measurement of a whole $\tilde{A} \leftarrow \tilde{X}$ transition absorption band of water and aqueous solutions.

FUV transient absorption spectrometer based on TRATR has also recently been developed and tested for aqueous solutions of phenol and tryptophan in the region of 170–185 nm [61]. In this region, a stable tunable laser was not available, and thus, white light from a laser-driven Xe lamp source was employed. The time resolution, which was determined by the time response of a continuous light detector, was 40 ns.

Thus far, the ATR–FUV spectra have been studied for water [53, 59, 66], aqueous solutions, alcohols [54], *n*- and branched alkanes [56, 57], ketones [55], and amides [58] observed in the liquid phase. The FUV spectra of *n*-alkanes show a band near 150 nm, while the branched alkanes yield an additional shoulder at around 180 nm. The 150 nm band shows a lower energy shift with a significant intensity

increase as the alkyl chain length increases. The assignments of absorption bands were investigated for the *n*-alkanes and branched alkanes in the liquid states and the cause of lower energy shift of the 150 nm feature by comparing the experimental results with quantum chemical calculations [57]. The 150 nm band of *n*-alkanes has been assigned to the σ-Rydberg $3p_y$ transition, and its longer-wavelength shift has been considered to be caused by the destabilizing effect of the next highest occupied molecular orbital (HOMO) level and the stabilization of Rydberg 3p level, which is expanded as the carbon chain increase. These studies of FUV spectra of alkanes have provided new insight into Rydberg states and transitions of liquid alkanes [57].

The $\tilde{A} \leftarrow \tilde{X}$ transition of liquid water entails the lone pair electrons of an oxygen atom of the water molecule, and thus, the $\tilde{A} \leftarrow \tilde{X}$ transition band of liquid water sensitively reflects the hydrogen-bonding state of a water molecule [53, 66]. With the addition of salts to liquid water, the electric field of an ion forces the rearrangement of the hydrogen-bonding state of water molecules from the bulk state. ATR–FUV spectroscopy provides new insights into the hydration states of cations from the perspective of the electronic transition of water molecules [9, 53]. Ikehata et al. [53] explored the effect of cations (Li^+, Na^+, K^+, Rb^+, and Cs^+) on the first electronic transition ($\tilde{A} \leftarrow \tilde{X}$) of liquid water by ATR–FUV spectroscopy. They found that the peak energy of the $\tilde{A} \leftarrow \tilde{X}$ band of water, which shows a marked red shift with decreasing hydrogen-bond strength, decreases with increasing cation size. The peak energies of the $\tilde{A} \leftarrow \tilde{X}$ band can be approximated by a linear function of the inverse of the ionic radii of the alkali metal cations, which indicates that the first electronic transition of water is characterized by the salvation energy of the cations.

The FUV region of amides in the liquid phase is very important because a valence–Rydberg coupling is expected for a π-π* transition, and a direct interaction occurs via a hydrogen bond [58]. Thus, the electronic transitions of five kinds of amides in the liquid phase, namely, formamide, *N*-methylformamide, *N*-methylacetamide, *N*,*N*-dimethylformamide, and *N*,*N*-dimethylacetamide, were studied using ATR–FUV spectroscopy [58]. It was revealed by combining the experimental results and the results of quantum chemical calculations that the major band of the amides at around 190 nm can be attributed mainly to the π-π* transition but several types of Rydberg transitions also exist in its vicinity and mixing of orbitals with the same symmetry occurs and that the valence–Rydberg coupling of the π-π* transition is more significant than the n-π* transition, which also holds in the pure liquid phase.

The corresponding electronic transitions were investigated also for five kinds of nylons (nylon 6, nylon 11, nylon 12, nylon 6/6, and nylon 6/12) in cast films using ATR and transmittance (Tr) FUV spectroscopy [65]. The assignments in the 145–250 nm region of these nylons have been proposed by the quantum chemical calculations and also comparing with the spectra of *n*-alkanes and amides. By analyzing the difference in the FUV spectra of these five kinds of nylons, the effects of the nylon structures and intermolecular hydrogen bonding based on the transition dipole coupling in the possible nylon sheet were clarified [65].

As mentioned above, FUV spectroscopy holds considerable promise for a variety of applications from qualitative and quantitative analysis to online analysis

and process monitoring. For example, Higashi et al. [51] applied ATR–FUV spectroscopy to monitor the quality of semiconductor wafer cleaning solutions. They employed it for direct measurement of the concentrations of semiconductor wafer cleaning fluids such as SC-1 (aqueous solution of NH_3 and H_2O_2) and SC-2 (aqueous solution of HCl and H_2O_2) [51].

Sato et al. [52] demonstrated the potential of FUV–DUV spectroscopy in the 120–300 nm region in the nondestructive classification of commercial food wrap films (polyethylene (PE) films from three sources, two polyvinylidene chloride (PVDC) films with different additives, and one polyvinyl chloride (PVC) film; each film was about 10 lm in thickness). More recently, Tanabe et al. [63, 64] measured absorption spectra (150–300 nm) of TiO_2 and TiO_2 modified with metal (Pt, Pd, and Au) nanoparticles using the ATR–FUV spectrometer. The deposition of metal nanoparticles altered the spectral shape and intensity, indicating changes in the electronic states and photocatalytic activities of TiO_2.

1.3 DUV Spectroscopy

1.3.1 An Overview of DUV Light

The range 200–300 nm is called the deep UV (DUV) and extends between the vacuum UV that can only exist in an oxygen-free environment and the near UV that is barely accessible to visible optics. It is difficult to present a comprehensive list of the applications of DUV light, because its short wavelength and stability in the air provide a variety of applications, ranging from fundamental science (such as spectroscopy) to industrial uses. Artificial DUV light sources are available, such as metal-vapor lamps and lasers. Mercury lamps are dominated by several emission lines at 185 and 254 nm, whereas xenon excimer lamps have a strong emission at 172 nm and are widely used. UV lamps have been used for cleaning, for hydrophilization of glass or metal surfaces, and to coagulate photoresists in many industrial lithographic processes. Note that the mercury lamp is a suitable disinfection tool, since DNA has an absorption peak at 254 nm [68]. High-power pulsed DUV lasers are typically based on excimers, e.g., XeCl (308 nm), KrF (248 nm), and ArF (193 nm), and have been mainly used for laser processing of LSI circuits and highly dense optical memories and for laser-induced chemical vapor deposition and etching processes [69].

1.3.2 Optics for DUV Spectroscopy

DUV spectroscopy is a developing technology that has only recently become widely accessible because of recent developments in stable and powerful UV light sources and highly sensitive photodetectors. A conventional visible spectroscopy system

can be converted to DUV, but some of the components must be changed due to the transmission and reflection properties of the materials. For reflection optics, an aluminum mirror is applicable, as it has 90 % reflectance at wavelengths longer than 200 nm. The transmission optics should be replaced, since the usable range of conventional crown glass is limited to longer than 350 nm. The candidates for use at DUV wavelengths are fused silica (transmission > 250 nm), synthetic silica (> 190 nm), sapphire (> 230 nm), and CaF_2 and MgF_2 (extended to FUV) [70]. For spectroscopic use, both the transmission efficiency and the dispersion relation (specifically, Abbe's number of the material) should be taken into account. Aberration is a serious problem when choosing an imaging apparatus, such as an objective lens, microscope, or imaging spectrometer. In practice, objective lenses for DUV wavelengths are limited in bandwidth, throughput, and resolving power, compared to those used for visible wavelengths with the same magnification and numerical aperture (NA). High NA (>1) objective lenses for the DUV range are difficult to obtain. A reflection-type Cassegrain objective lens is another option for broadband spectroscopy. Interference filters are available for the DUV range, but their transmittance efficiency and edge response are inferior to those of visible light filters because of absorption losses in the material.

Photodetectors for weak spectroscopic signals such as photomultiplier tubes (PMT) and photodiodes are also available in the DUV range. Photoelectric surface materials for PMTs have been designed for DUV use, such as bi-alkali metals [71]. Silicon is active as a UV photodiode, but wide-bandgap semiconductors are considered to be more useful as DUV optical sensors because of their superior signal to noise (SN) ratios and their stability. Recently, a highly oriented diamond film with a bandgap of 5.5 eV was demonstrated as a DUV–FUV sensitive detector [72]. For multiplex spectroscopy, a highly sensitive 2D detector has been employed. A charge-coupled device (CCD), which achieves nearly 95 % quantum efficiency (QE) in the visible range, has considerably reduced efficiency in the DUV range [73]. The QE of a silicon photodiode used in a sensor array can be improved to 50 % by fabricating a thinner diffusion layer to extend the carrier lifetimes and by optimizing the antireflective coating on the back-illuminated CCD.

A flat diffraction grating similar to the one used in visible spectroscopy can also be found in DUV. However, the spectroscopic performance is reduced due to the energy dispersion relation at DUV wavelengths. Moreover, the reflection losses from each of the optics are higher than for visible wavelengths. Therefore, considering the total throughput, the efficiency of DUV spectroscopy should empirically be 3–5 times lower than that of visible spectroscopy.

Both lamps and lasers are available for spectroscopic applications of DUV light sources. Detailed explanations of these light sources will be provided in the upcoming discussion of spectroscopic methods. As there has been considerable recent progress in blue light-emitting diodes (LEDs), DUV-LEDs are expected to be commercialized within a few years. Moreover, as semiconductor lasers have been extended to shorter wavelengths, we also expect that a fully solid-state wavelength-tunable DUV laser for molecular selective spectroscopy will be possible in the near future.

1.3.3 Basic Principles and Methods of DUV Spectroscopy

DUV spectroscopy includes several techniques, such as absorption and scattering spectroscopy, vibrational spectroscopy, photoluminescence, and plasmonically enhanced spectroscopy. This spectroscopic technique has been applied to materials that specifically interact with photons with DUV energies. The methods are not confined to component analysis, but have also been extended to microscopy (Chap. 7) and nanoscopy (near-field microscopy, Chap. 8), although the field is still in its infancy.

Absorption spectroscopy is the most widely applicable technique, because many molecules have intrinsic absorption of a few electron volts, which corresponds to the FUV–DUV range. For example, nucleotide bases (250–270 nm), peptides (200–215 nm), and aromatic amino acids (280 nm) have been investigated [74, 75]. The absorption spectra reflect the electronic structure of each molecular species, and the absorption efficiency at the target wavelength can be used to determine the concentration of the species. However, typical absorption spectra are as broad as several tenths of a nanometer in a condensed phase and quite often overlap with each other. Therefore, careful spectral analysis and data treatment are required for mixed samples. Absorption spectroscopy including DUV is a popular analytical technique, as it can be performed using a commercially available UV–vis spectrometer. Deuterium (185–400 nm) and xenon (300 nm visible) lamps have been used as broadband light sources covering wavelengths from UV to visible. One experimental concern is that the short-wavelength detection edge is limited by absorption and scattering from the solvent and sample cell.

Rayleigh scattering spectroscopy provides comparable information to absorption spectroscopy, because both methods have maximum sensitivity at the electronic resonance of the molecule. As scattering is an isotropic phenomenon, the signal can be obtained from an off-axis direction. This provides a higher SN ratio than is available in absorption mode. Dark-field illumination and detection in scattering spectroscopy are good for microscopic observation, as it can easily highlight small objects. The efficiency of Rayleigh scattering spectroscopy depends on the shape, volume, and inhomogeneity of the sample, and the sample boundaries greatly complicate the interpretation of the experimental data [76].

There have been few reports of DUV absorption or scattering microscopy or 2D mapping, because DUV imaging techniques are still immature [77]. Recently, however, a laser-driven light source (LDLS) was developed through the creation of a xenon plasma by focused strong laser irradiation. LDLS enables extreme brightness over a broad spectral range, from 170 nm to IR, and the lifetime is an order of magnitude longer than that of a traditional lamp [78]. The development of the broadband light sources will surely accelerate the advancement of DUV absorption and Rayleigh scattering microscopy.

Vibrational spectroscopy, or Raman spectroscopy, is widely used among scientists and engineers of various fields. Each molecular species exhibits a specific Raman spectrum, and the sharp spectral features enable the identification of the

exact energy level of each molecular vibration. Thus, the Raman spectrum has been called a molecular fingerprint [79]. An excitation laser of any wavelength can be used; however, if this wavelength is close to one of the electronic excitations for a molecule, the process is called resonance Raman scattering. When the excitation laser energy is within the electronic absorption band of a molecule, it is called "rigorous resonance Raman scattering," whereas if it is at the longer edge of the absorption band, it is called "pre-resonance Raman scattering." It is likely that DUV Raman spectroscopy will be a resonant process for many samples.

The dominant feature of resonance Raman spectroscopy is that the extraordinarily intense Raman signal will make it possible to observe a small concentration of molecules (-6 M or less) in a composite sample. According to the Kramers–Heisenberg–Dirac dispersion formula, the signal intensity should theoretically be infinite under exactly rigorous resonance Raman conditions, which do not occur in practice because of vibrational dampening. It should be noted that not all Raman modes are equally enhanced, because the resonance Raman effect appears selectively for each vibrational mode, depending on the symmetry. According to Albrecht's theory, the enhancement mechanism of resonance Raman scattering can be considered the summation of two contributions, which are called the A-term and the B-term [80]. For the resonance effect originating from the A-term, a single excited electronic state resonant with the excitation laser is involved; at the same time, the overlap of the vibrational wave functions (Franck–Condon factor) has to be nonzero. On the other hand, for the resonance effect originating from the B-term, two excited electronic states (both states are allowed transitions) are coupled through a specific vibrational mode. A strong Raman enhancement is observed for the mode governing the coupling. Roughly speaking, a totally symmetric vibrational mode is more likely to be influenced by the A-term resonance, although there are some exceptional cases. A non-totally symmetric mode, on the other hand, should be influenced only by the B-term resonance. Theoretically, studying resonance Raman scattering should help develop an understanding of the electronic structure of molecules, in addition to the vibrational structure.

The resonance Raman intensity strongly depends on the excitation wavelength, and this dependence is called the excitation profile [81]. Besides signal enhancement, a major advantage of resonance Raman spectroscopy is the molecular selectivity that is made possible based on the excitation profile. Recently, molecularly selective resonance Raman microscopic imaging of biological cells using DUV has been reported [82]. The nucleotide distribution in a HeLa cell has been determined, with resonant bands attributable to guanine and adenine, which are excited at 257 nm. The results clarified DNA localization at the nucleoli in the nucleus and the RNA distribution in the cytoplasm.

The choice of excitation laser is essential for DUV resonance Raman spectroscopy. With a wavelength-changeable UV laser, molecularly selective resonance Raman microscopy could be realized. The second harmonics of an argon ion laser offers several emission lines in the DUV range (257, 244, 238, 229 nm) that are suitable for wavelength-selective resonance Raman spectroscopy. Solid-state DUV lasers are also available based on harmonic generation with infrared lasers, typically

YAG (266 nm) or YLF (263 nm) lasers. Even CW emission has been realized with high-quality BBO crystals [83].

Photoluminescence, including fluorescence and phosphorescence, originates from the S_1 and T_1 states of a molecule as a result of absorption [84]. The fluorescence spectra usually appear as a mirror image of the absorption spectra, occurring at longer wavelengths. Therefore, our current interest is mainly focused on excitation by DUV light. When exciting with a strong DUV light source, one can observe auto-fluorescence originating from intrinsic chromophores in the sample, which is normally weak. Photoluminescence is often used for microscopic imaging of a specific molecule, especially in biological research. For a complex sample such as a cell, a target molecule is chemically labeled with a variety of fluorophores. Labeling is an advantage, but also a disadvantage, of fluorescence microscopy. The labeling is free from complex spectral assignment because the origin of the signal is clear, but artificial fluorophores, which usually have a non-negligible size compared to the target molecule, may affect the intrinsic function of the molecule. DUV laser excitation of auto-fluorescence (e.g., tryptophan, tyrosine) can realize label-free molecular imaging with a reasonable sensitivity [85].

Absorption is not necessarily a linear process; sometimes, it occurs as a nonlinear process. Multiphoton absorption photoluminescence has advantages for microscopic applications because nonlinearity usually occurs where the photon density is high, leading to a better spatial resolution. Moreover, the longer excitation wavelength results in deeper penetration into the sample than with direct short-wavelength excitation. Molecular mapping by photoluminescence has been investigated in both 2D and 3D, including the depth direction [86].

1.3.4 Recent Progress in DUV Spectroscopy

Plasmonically enhanced spectroscopy has accompanied other spectroscopic methods since the discovery of surface-enhanced Raman spectroscopy (SERS) in 1970. The discovery that the intensity of the Raman scattering signal was drastically enhanced in the vicinity of a rough metal electrode attracted considerable attention. The enhancement was due to coupling between photons and free electrons in a metal nanostructure. Plasma resonance of electrons in free-electron metals exhibits unique optical phenomena that occur on surfaces with nanostructures and are referred to as “surface plasmons.” The use of surface plasmons has been proposed in various fields, such as nanometer resolution near-field optical microscopy, nanoscale optical circuits, single-molecule detection, molecular sensors, cancer treatment, solar cells, lasers, and holography. The study of plasma resonance is called “plasmonics” and is expected to provide an entirely new field of spectroscopy [87]. However, the effective optical range for plasmonics has been limited to the visible and near-infrared for conventional plasmonic metals such as silver and gold. In the energy range exceeding the plasma resonance frequency, silver and gold become dielectrics and completely lose their conductivity and plasmonic effect. It is highly

expected that plasmonics will be extended to the UV and DUV range. UV-DUV plasmonics will be an important future theme of photonics, as exemplified by DUV microscopes, lithography, sterilization, photocatalysis, and bio-sensing and analysis [88] (Chap. 8). Among the metals, aluminum and indium show ideal properties as plasmonic materials in the UV to DUV range due to their high plasma frequency and low absorption loss owing to the small imaginary part of the dielectric constant at these wavelengths. Moreover, aluminum is a nontoxic and noncombustible material with a very thin oxidized surface layer that can be used as a protective layer. It has been reported that localized surface plasmon resonance (LSPR) wavelengths from near UV to DUV were realized by fabricating aluminum and indium nanostructures of different sizes [89, 90]. Due to the successful formation of plasmonic nanostructures for LSPR, SERS at DUV wavelengths was realized for several biological molecules with high detection sensitivity [90].

Near-field microscopy is another useful application of DUV plasmonics. In this method, scanning probe microscopy was combined with optical microscopy. A nano-sized probe was coated with plasmonic materials to localize the incident light at its apex. The spectroscopic signal was obtained primarily at the probe apex, realizing a nanoscale imaging resolution. Recently, near-field DUV Raman scattering with an aluminum tip has been reported with an enhancement factor of 1,300 [91]. Both crystal violet and adenine molecules showed electronic resonance at the 266 nm excitation used in the experiments. The details of near-field microscopy will be discussed in the following chapters.

The applications of DUV plasmonics have not been confined to spectroscopic use. Recently, photocatalysis on the popular wide-bandgap photocatalyst TiO_2 was enhanced by an order of magnitude with the assistance of aluminum plasmonics [92]. The photon localization and enhancement effects of plasmonics can also be applied to amplify photochemical reactions, luminescence from LEDs [93], and the efficiency of solar cells [94]. DUV plasmonics is now a hot topic, since it is deeply related to environmental and energy generation issues (Chap. 9).

DUV covers an interesting spectral range, in which short wavelengths and high photon energies can provide new information via spectroscopy and improved applications of photocatalytic effects, solar cells, and lithography. These short wavelengths can intrinsically lead to better spatial resolution in microscopy, so the extension of DUV spectroscopy to imaging techniques will be of great benefit, as will the component analysis capability. The inclusion of DUV plasmonic effects will result in much higher sensitivity in microscopy and nanoscopy (e.g., near-field microscopy and SERS) than is available in the visible range. Even though the advantages of the DUV spectral range have long been recognized, there have been limited efforts to explore DUV applications in spectroscopy (especially at the micro- to nanoscale), high-resolution imaging, or plasmonics. Now is therefore the time to review the various aspects of DUV applications, discuss the future scope and possibilities, and inspire additional researchers to contribute to this field.

References

1. P.E. Hockberger, Photochem. Photobio. **76**, 561A (2002)
2. R.A. Millikan, Phys. Rev. **7**, 0355 (1916)
3. W.C. Röntgen, Radiology **45**, 428 (1945)
4. G. Herzberg, *Molecular Spectra and Molecular Structure III: Electronic Spectra and Electronic Structure of Polyatomic Molecules* (Van Nostrand, New York, 1966), p. 489
5. N. Damany, J. Romand, B. Vodar (eds.), *Some Aspects of Vacuum Ultraviolet Radiation Physics* (Pergamon Press, Oxford, 1974)
6. C. Sándorfy (ed.), *The Role of Rydberg States in Spectroscopy and Photochemistry-Low and High Rydberg States* (Kluwer Academic Publishers, Dordrecht, 1999)
7. Y. Ozaki, Y. Morisawa, A. Ikehata, N. Higashi, Appl. Spectrosc. **66**, 1 (2012)
8. Y. Morisawa, T. Goto, A. Ikehata, N. Higashi, Y. Ozaki, *Encyclopedia of Analytical Chemistry* (Jhon Wiley & Sons, Chichester, UK, 2013)
9. K.I. Lednev, A.S. Karnoup, M.C. Sparrow, S.A. Asher, J. Am. Chem. Soc. **121**, 8074 (1999)
10. R. Schweitzer-Stenner, J. Raman Spectrosc. **32**, 711 (2001)
11. V. Mikhonin, N.S. Myshakina, S.V. Bykov, S.A. Asher, J. Am. Chem. Soc. **127**, 7712 (2005)
12. M.B. Robin, *Higher Excited States of Polyatomic Molecules*, vol. II (Academic, New York, 1974)
13. J.W. Raymonda, W.T. Simpson, J. Chem. Phys. **47**, 430 (1967)
14. J.W. Au, G. Cooper, G.R. Burton, T.N. Olney, C.E. Brion, Chem. Phys. **173**, 209 (1993)
15. B.-M. Cheng, M. Bahou, W.-C. Chen, C.-H. Yui, Y.-P. Lee, L.C. Lee, J. Chem. Phys. **117**, 1633 (2002)
16. E.E. Barnes, W.T. Simpson, J. Chem. Phys. **39**, 670 (1963)
17. M.B. Robin, N.A. Kuebler, J. Mol. Spectrosc. **33**, 274 (1970)
18. R. McDiarmid, J. Chem. Phys. **95**, 1530 (1991)
19. M. Nobre, A. Fernandes, A. Ferreiru da Silva, R. Antunes, D. Almeida, V. Kokhan, S.V. Hoffmann, N.J. Mason, S. Eden, P. Limao-Vieira, Phys. Chem. Chem. Phys. **10**, 550 (2008)
20. K.N. Walzl, C.F. Koerting, A. Kuppermann, J. Chem. Phys. **87**, 3796 (1987)
21. J.G. Philis, L. Goodman, J. Chem. Phys. **98**, 3795 (1993)
22. M. Merchan, B.O. Roos, R. McDiarmid, X. Xing, J. Chem. Phys. **104**, 1791 (1996)
23. S.R. Gwaltney, R.J. Bartlett, Chem. Phys. Lett. **241**, 26 (1995)
24. K.B. Wiberg, A.E. de Oliveira, G. Trucks, J. Phys. Chem. A **106**, 4192 (2002)
25. M.B. Robin, *Higher Excited States of Polyatomic Molecules*, vol. III (Academic, Orlando, 1985), p. 176
26. K. Kaya, S. Nagakura, Theor. Chim. Acta **7**, 117 (1967)
27. M. Rubio, L. Serrano-Andres, M.J. Merchan, Chem. Phys. **128**, 104305 (2008)
28. M. Chergui, N. Schwentner, Chem. Phys. Lett. **219**, 237 (1994)
29. P. Gurtler, V. Saile, E.E. Koch, Chem. Phys. Lett. **51**, 386 (1977)
30. G.W. Rubloff, H. Fritzsche, U. Gerhardt, J. Freeouf, Rev. Sci. Instrum. **42**, 1507 (1971)
31. J.M. Jung, H. Gress, Chem. Phys. Lett. **359**, 153 (2002)
32. J.M. Jung, H. Gress, Chem. Phys. Lett. **377**, 495 (2003)
33. Y.-P. Kuo, H.-C. Lu, Y.-J. Wu, B.-M. Cheng, J.F. Ogilvie, Chem. Phys. Lett. **447**, 168 (2007)
34. E.A. Costner, B.K. Long, C. Navar, S. Jockusch, X. Lei, P. Zimmerman, A. Campion, N.J. Turro, C.G. Willson, J. Phys. Chem. A **113**, 9337 (2009)
35. K. Weiss, P.S. Baguo, C. Wöll, J. Chem. Phys. **III**, 6834 (1999)
36. R.E. Verrall, W.A. Senior, J. Chem. Phys. **50**, 2746 (1969)
37. L.R. Painter, R.D. Birkhoff, E.T. Arakawa, J. Chem. Phys. **51**, 243 (1969)
38. G.D. Kerr, J.T. Cox, L.R. Painter, R.D. Birkhoff, Rev. Sci. Instrum. **42**, 1418 (1971)
39. L.R. Painter, R.N. Hamm, E.T. Arakawa, R.D. Birkhoff, Phys. Rev. Lett. **21**, 282 (1968)
40. J.M. Heller, R.N. Hamm, R.D. Birkhoff, L.R. Painter, J. Chem. Phys. **60**, 3483 (1974)
41. M. Halmann, I. Platzner, J. Phys. Chem. **70**, 580 (1966)
42. T.H. Keil, Phys. Rev. **144**, 582 (1966)

43. T.I. Quickenden, J.A. Irvin, J. Chem. Phys. **72**, 4416 (1980)
44. F. Williams, S.P. Varma, S. Hillenius, J. Chem. Phys. **64**, 1549 (1976)
45. T.W. Marin, K. Takahashi, D.M. Bartels, J. Chem. Phys. **125**, 104314 (2006)
46. N. Higashi, Y. Ozaki, Appl. Spectrosc. **58**, 910 (2004)
47. S. Sério, M.E. Melo Jorge, M.L. Coutinho, S.V. Hoffman, P. Limão-Vieria, Y. Nunes, Chem. Phys. Lett. **508**, 71 (2011)
48. D.J. Segelstein (http://www.philiplaven.com/p20.html) (1981)
49. N. Higashi, H. Yokota, S. Hiraki, Y. Ozaki, Anal. Chem. **77**, 2272 (2005)
50. M. Mitsuoka, H. Shinzawa, Y. Morisawa, N. Kariyama, N. Higashi, M. Tsuboi, Y. Ozaki, Anal. Sci. **27**, 177 (2011)
51. N. Higashi, A. Ikehata, N. Kariyama, Y. Ozaki, Appl. Spectrosc. **62**, 1022 (2008)
52. H. Sato, N. Higashi, A. Ikehata, Y. Ozaki, Appl. Spectrosc. **61**, 780 (2007)
53. A. Ikehata, M. Mitsuoka, Y. Morisawa, N. Kariyama, N. Higashi, Y. Ozaki, J. Phys. Chem. **114**, 8319 (2010)
54. Y. Morisawa, A. Ikehata, N. Higashi, Y. Ozaki, Chem. Phys. Lett. **476**, 205 (2009)
55. Y. Morisawa, A. Ikehata, N. Higashi, Y. Ozaki, J. Phys. Chem. **115**, 562 (2011)
56. S. Tachibana, Y. Morisawa, A. Ikehata, H. Sato, N. Higashi, Y. Ozaki, Appl. Spectrosc. **65**, 221 (2011)
57. Y. Morisawa, S. Tachibana, M. Ehara, Y. Ozaki, J. Phys. Chem. **116**, 11957 (2012)
58. Y. Morisawa, M. Yasunaga, R. Fukuda, M. Ehara, Y. Ozaki, J. Chem. Phys. **139**, 154301 (2013)
59. T. Goto, A. Ikehata, Y. Morisawa, N. Higashi, Y. Ozaki, Phys. Chem. Chem. Phys. **14**, 8097 (2014)
60. T. Goto, A. Ikehata, Y. Morisawa, N. Higashi, Y. Ozaki, Inorg. Chem. **51**, 10650 (2012)
61. Y. Morisawa, N. Higashi, K. Takaba, N. Kariyama, T. Goto, A. Ikehata, Y. Ozaki, Rev. Sci. Instrum. **83**, 073103 (2012)
62. T. Goto, Y. Morisawa, N. Higashi, A. Ikehata, Y. Ozaki, Anal. Chem. **85**, 4500 (2013)
63. I. Tanabe, Y. Ozaki, Chem. Commun. **50**, 2117 (2014)
64. I. Tanabe, T. Ryoki, Y. Ozaki, Phys. Chem. Chem. Phys **16**, 7749 (2014)
65. Y. Morisawa, M. Yasunaga, H. Sato, R. Fukuda, M. Ehara, Y. Ozaki, J. Phys. Chem. B **118**, 11855 (2014)
66. A. Ikehata, Y. Ozaki, N. Higashi, J. Chem. Phys. **129**, 234510 (2008)
67. N. Higashi, A. Ikehata, Y. Ozaki, Rev. Sci. Instrum. **78**, 103107 (2007)
68. M.A. Tycon, A. Chakraborty, C.J. Fecko, J. Photochem. Photobio. B **102**, 161 (2011)
69. M.H.R. Hutchinson, Excimers and excimer lasers. Appl. Phys. **21**, 95 (1980)
70. M. Maeda (ed.), *Excimer Lasers* (Gakkai Publishing Center, Tokyo, 1993), p. 193
71. Hamamatsu Photonics K.K. Alkali photocathode. http://www.hamamatsu.com/jp/ja/technology/innovation/index.html (2013). Accessed 18 Sept 2014.
72. K. Hayashi, Y. Yokota, T. Tachibana, K. Kobashi, J. Achard, A. Gicquel, C. Olivero, M. Castex, A. Treshchalov, Diam. Relat. Mater. **10**, 1794 (2001)
73. K. Yonemoto, *CCD/CMOS Imaging Sensor* (CQ Publishing, Tokyo, 2003), p. 116
74. A. Ito, T. Ito, Photochem. Photobio. **44**, 355–358 (1986)
75. J.B. Birks (ed.), *Photophysics of Aromatic Molecules* (Oxford, London, 1970), p. 44
76. R.S. Gurjar, V. Backman, L.T. Perelman, I. Georgakoudi, K. Badizadegan, I. Itzkan, R.R. Dasari, M.S. Feld, Nat. Med. **7**, 1245 (2001)
77. B.J. Zeskind, C.D. Jordan, W. Timp, L. Trapani, G. Waller, V. Horodincu, D.J. Ehrlich, P. Matsudaira, Nat. Methods **4**, 567 (2007)
78. M. Islam, L. Ciaffoni, G. Hancock, G.A.D. Ritchie, Analyst **138**, 4741 (2013)
79. E. Smith, G. Dent (eds.), *Modern Raman Spectroscopy* (Wiley, Chichester, 2005), p. 135
80. A.C. Albrecht, J. Chem. Phys. **34**, 1476 (1961)
81. F. Inagaki, M. Tasumi, T. Miyazawa, J. Mol. Spectrosc. **50**, 286 (1974)
82. Y. Kumamoto, A. Taguchi, N. Smith, S. Kawata, J. Biomed. Opt. **17**, 076001 (2012)
83. M. Oka, H. Imai, N. Eguchi, S. Kubota, Laser Rev. **27**, 463 (1999)
84. J.R. Lakowicz (ed.), *Principles of fluorescence spectroscopy*, 3rd edn. (Springer, New York, 2006), p. 5

85. Q. Li, S. Seeger, Anal. Chem. **78**, 2732 (2006)
86. M. Diaspro, J. Robello, J Photochem. Photobiol. B Biol **55**, 7940 (2000)
87. S. Kawata (ed.), *Near Field Optics and Surface Plasmon Polariton* (Springer, Tokyo, 2001), p. 15
88. S. Kawata, Plasmonics: Future outlook. Jpn. J. Appl. Phys. **52**, 010001 (2013)
89. A. Taguchi, Y. Saito, K. Watanabe, Y. Song, S. Kawata, Appl. Phys. Lett. **101**, 081110 (2012)
90. Y. Kumamoto, A. Tauguchi, M. Honda, Y. Saito, S. Kawata, ACS Photo **1**, 598–603 (2014)
91. N. Taguchi, K. Hayazawa, H. Furusawa, S. Ishitobi, J. Kawata, Raman Spectrosc. **40**, 1324 (2009)
92. M. Honda, Y. Kumamoto, A. Taguchi, Y. Saito, S. Kawata, Appl. Phys. Lett. **104**, 061108 (2014)
93. K. Huang, N. Gao, C. Wang, X. Chen, J. Li, S. Li, X. Yang, J. Kang, Sci. Rep. **4**, 4380 (2014)
94. N.P. Hylton, X.F. Li, V. Giannini, K.H. Lee, N.J. Ekins-Daukes, J. Loo, D. Vercruysse, P. Van Dorpe, H. Sodabanlu, M. Sugiyama, S. A. Maier, Scientific Reports **3**, 2873 (2013)

Chapter 2
Instrumentation for FUV Spectroscopy

Akifumi Ikehata, Yusuke Morisawa, and Noboru Higashi

Abstract This chapter describes recent breakthroughs in the instrumentation for far-ultraviolet (FUV) spectroscopy. The key technique is attenuated total reflection (ATR) that is frequently used in the infrared region. ATR technique decreases the absorbance of samples with strong absorptivity because of the penetration depth of the evanescent wave less than 100 nm. Therefore, ATR–FUV spectroscopy realizes the measurement of FUV spectra of samples in liquid and solid states. Some applications (in-line monitoring, characterization of polymers and time-resolved spectroscopy in sub-microsecond) are introduced in terms of instrumentation. This chapter explains not only the detail of the instruments but also the mathematical correction for ATR spectra to separate the absorption and refraction indices.

Keywords Attenuated total reflection (ATR) • Internal reflection element • Kramers–Kronig transformation • Time-resolved ATR–FUV spectroscopy

2.1 Introduction

FUV spectra give considerable information, but the absorption intensities are so strong particularly for liquids and solids that the light cannot penetrate even in a thin film. Therefore, FUV spectroscopy had been exclusively used for the measurement of gas. The use of FUV spectroscopy for liquids and solids was very limited for the regular reflection from the surface of the sample with troublesome operations. As an effective technique to obtain spectra of materials with strong absorption, attenuated

A. Ikehata (✉)
National Food Research Institute, National Agriculture and Food Research Organization, (NARO), 2-1-12 Kannondai, Tsukuba, Ibaraki 305-8642, Japan
e-mail: ikehata@affrc.go.jp

Y. Morisawa
Department of Chemistry, School of Science and Engineering, Kinki University, 3-4-1 Kowakae, Higashi-Osaka, Osaka 577-8502, Japan

N. Higashi
Kurabo Industries Ltd., 14-5 Shimokida-cho, Neyagawa, Osaka 572-0823, Japan
e-mail: Noboru_Higashi@ad.kurabo.co.jp

Y. Ozaki, S. Kawata (eds.), *Far- and Deep-Ultraviolet Spectroscopy*,
DOI 10.1007/978-4-431-55549-0_2

total reflection infrared (ATR-IR) spectroscopy with an internal reflection element (IRE) has been widely used [1–3]. Since the penetration depth of the evanescent wave, defined as the distance required for the electric field amplitude to fall e^{-1} of its value from the surface of the IRE [4], is less than the wavelength, the ATR method allows the spectral measurement similar to that of transmittance spectra with a very short optical path length. Thus, the ATR method provides benefits both in terms of quantitative measurements and easy handling of liquid or solid samples with strong absorption, compared to transmittance spectroscopy. Despite the fact that ATR techniques have been modified in a multitude of ways to obtain IR [3, 5, 6], near IR [7, 8], and UV-visible spectra [9–12], there were no ATR methods for the FUV region before 2007. ATR–FUV spectroscopy opened the way for the measurement of the dense materials with strong absorptivities [13].

Recently the time-resolved ATR–FUV spectrometer was developed for the study of radical species in chain reaction to measure the transient absorption spectra of stable and radical species based on ATR [14]. In order to investigate a chemical reaction, in particular a chain reaction, both the product and the reactant should be observed. Typical reactants, that is to say generally stable species, do not show absorption spectra in the UV–VIS region but do so in the FUV region. Moreover, by setting the observation region to be at a higher energy than that of the excitation laser light that induces photochemical reactions, we have been able to avoid the effects of fluorescence on our spectroscopic observations.

The former part of this chapter describes the technical problems of ATR measurement in the FUV region, and the latter part explains an expanded application of ATR–FUV spectroscopy to the detection of transient phenomena in aqueous solutions.

2.2 Attenuated Total Reflection Spectroscopy in FUV Region

Higashi and coworkers designed and constructed an ATR-based FUV spectrometer [15]. In this spectrometer the design of a small internal reflection element (IRE) probe has led to successful measurement of the entire $\tilde{A} \leftarrow \tilde{X}$ transition absorption band of water and aqueous solutions.

Figure 2.1 shows a schematic diagram of this instrument [15]. Figure 2.1a depicts a portionof the custom design of a commercial FUV spectrometer (KV-200, Bunko-Keiki, Tokyo, Japan). Figure 2.1b illustrates a flow cell unit formed between the sapphire IRE probe (7) and a fluorinated resin holder (8) enlarged from the area marked with a dashed line (part b) in Fig. 2.1a. The probe is fixed in place by the holder made by PTFE (8), with the flow sample cell formed by a space between the PTFE guide (9) and the aperture (1) of the probe. A liquid sample for measurement is drawn into the 2-mm-diameter aperture in the IRE probe. Air in the sealed instrument is purged with pure nitrogen gas. To control the sample temperature over the range of 5–80 °C, a Peltier element (10) is in contact with the probe holder (8) by a heat pipe (11).

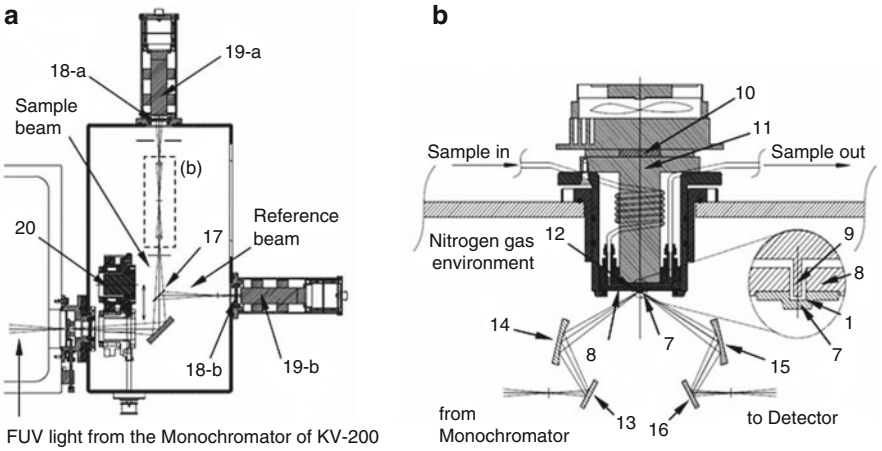

Fig. 2.1 Schematic diagram of the ATR–FUV spectrometer. (**a**) Originally designed semi-double beam part for the commercial KV-200 spectrometer. (**b**) The ATR probe with temperature control system

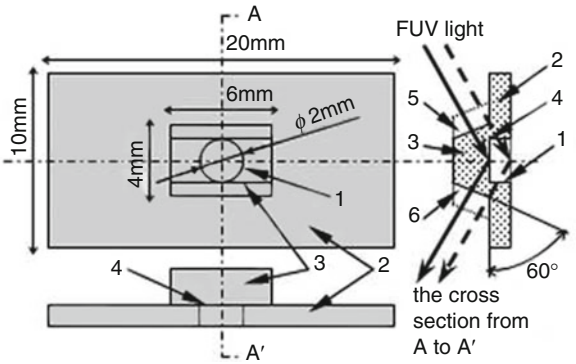

Fig. 2.2 Description of the ATR probe. It consists of a trapezoidal internal reflection element (IRE) and a rectangular base plate with a cylindrical aperture

A 30-W deuterium lamp was used as the light source for the KV-200 spectrometer, which incorporated a diffraction grating with 2,400 grooves/mm and a blazed wavelength of 150 nm. As depicted in Fig. 2.1a, the FUV light from the monochromator is split into a reference beam and a sample beam by an MgF_2 beam splitter. The reflected light and the reference beam finally pass through a synthetic quartz plate coated with sodium salicylic acid, which fluoresces. Fluorescence of each beam is then detected by a photomultiplier.

Figure 2.2 depicts the developed IRE probe [15]. The IRE used with the ATR technique must satisfy following two important conditions. One is that the refractive index of the IRE must be greater than that of the sample material, and another is that the IRE material must have sufficient transmission in the measured wavelength range. For the full FUV region (120–200 nm), there seemed no ideal IRE material that fulfills both conditions. Materials such as sapphire with a higher refractive index

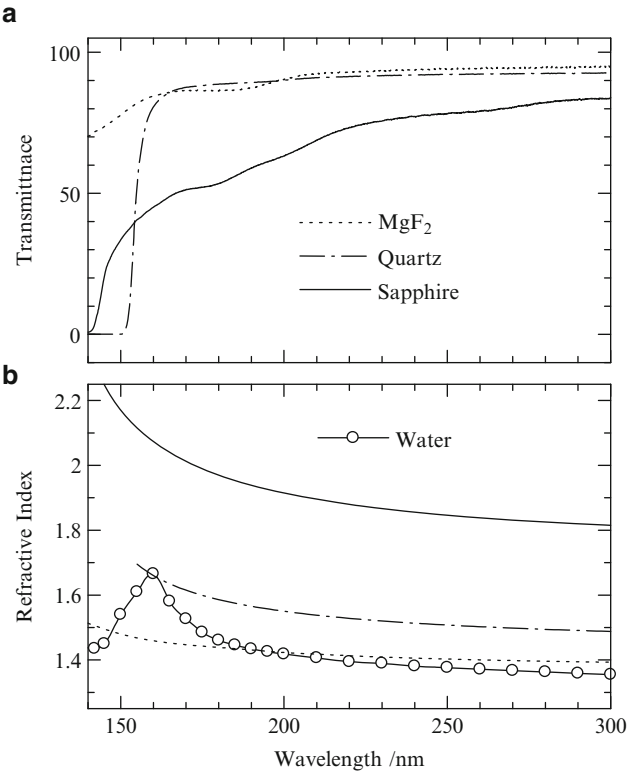

Fig. 2.3 Transmittance (**a**) and refractive indices (**b**) of materials in the FUV–UV region

than water have insufficient transmission, while those with sufficient transmission (e.g., MgF_2, CaF_2, and synthetic quartz) have lower refractive indices than water in the FUV region (see Fig. 2.3). Although sapphire lacks sufficient transmission in the wavelength region shorter than 145 nm, the property of the high refractive indices is suitable for the IRE for FUV spectroscopy. Higashi et al. therefore used sapphire for the IRE with a single reflection and an angle of incidence of 60°.

The ATR probe consists of two parts: a trapezoidal IRE and a rectangular base plate with a cylindrical aperture (1) as shown in Fig. 2.2. These two parts are integrated by an optical contact technique. Adhesives are not used to prevent sample contamination and residue from remaining in the device. The base plate sits on the same side of the IRE at which it comes into contact with the sample through the aperture at the interface surface (4). The IRE itself has both an incident surface (5) and an outgoing surface (6), which are not in contact with the sample. FUV light entering the incident surface perpendicularly strikes the incident interface surface and then perpendicularly exits the outgoing surface. For the ATR instrument, any

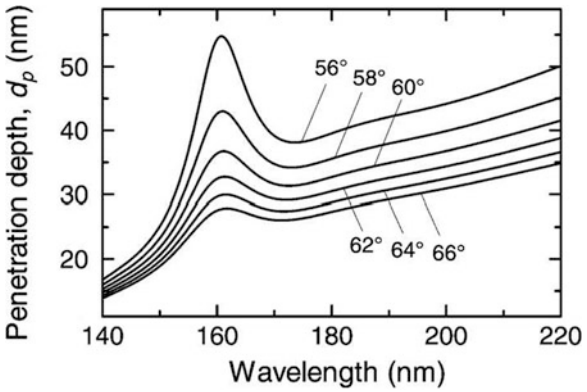

Fig. 2.4 Simulated penetration depth of the evanescent wave in water for incident angles over the range of 56°–66° by Eq. (2.1)

kind of liquids can be used as the sample. Solid samples can also be investigated but good contact between the IRE and a solid sample is required.

The penetration depth of the evanescent wave d_p is dependent on the ratio of the refractive indices of the IRE, n_1, and sample, n_2, as follows: [16]

$$d_p = \frac{\lambda}{2\pi n_1 \sqrt{\sin^2\theta - (n_2/n_1)^2}} \tag{2.1}$$

Figure 2.4 shows simulated results of penetration depth of the evanescent wave in water from sapphire IRE in different incident angles over the range of 56°–66°. For the calculation, reported refractive indices of water [17] and sapphire [18] were substituted into Eq. (2.1). A marked increase of the penetration depth happens at around 161 nm as shown in Fig. 2.4, as the refractive index of water has a maximum value over 1.65 between normal and anomalous dispersions at 159 nm (see Fig. 2.5a) [15]. The dash-dot line in Fig. 2.5a represents refractive index and the solid line depicts the absorption index of water. The refractive index n and the absorption index k have distinct maxima at 159 and 151 nm, respectively. Figure 2.5b shows the calculated (broken lines) and measured (solid lines) ATR–FUV spectra at a variety of incident angles. It is noted that the peak wavelength of both the measured and calculated ATR spectra for different incident angles of $\theta = 56°$–$64°$ is closely matched at around 157 nm. The deviation of experimental and calculated results may be caused by the range of incident angles in the measuring beam focused on the IRE surface.

However ATR spectra are not identical to the transmittance spectra. It is known that ATR spectra include not only absorption but also refractive index. The intensity shift can be readily corrected by Eq. (2.1), but the shift in the wavelength due to the refractive index cannot be corrected. In order to separate the contributions of the absorption and refractive indices, Kramers–Kronig transformation (KKT) and Fresnel formulas should be used [19]. The experimentally observed reflectivity R

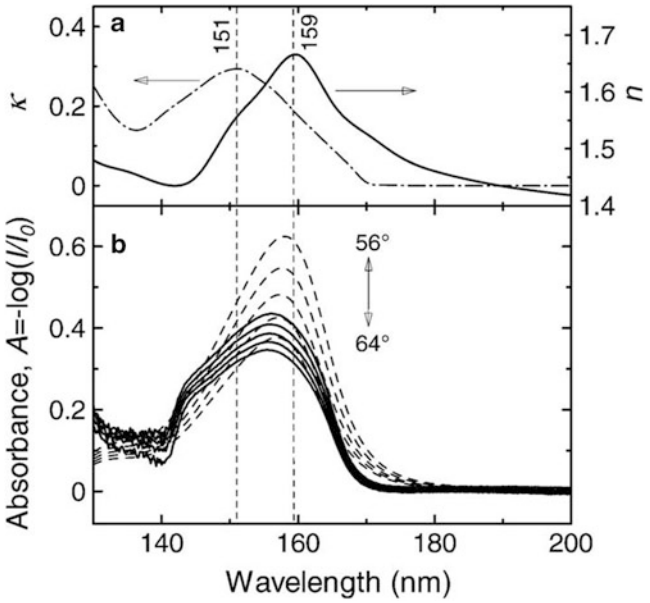

Fig. 2.5 (**a**) The refractive indices and absorption indices of water obtained by Painter et al. [17]. (**b**) *Broken* and *solid lines* show the simulated and measured ATR–FUV spectra, respectively, at a variety of incident angles

can be converted into the phase shift spectra by using KKT that can be written as a function of frequency, i.e.,

$$\Phi(v) = I - \frac{2v}{\pi}\int_0^{\infty} \frac{\ln n\sqrt{R\,(v')}}{v'^2 - v^2}dv' \tag{2.2}$$

where I is a correction term for the phase shift at a reflection surface [20]. In order to apply Eq. (2.1) to the discrete reflection data, Maclaurin's formula is adopted as an approximation [21]. The phase spectra for this case are eventually given by

$$\Phi_i = \mathrm{Arc\,tan}\left(\frac{\sqrt{n_\mathrm{p}^2\sin^2\theta - n_\infty^2}}{n_\mathrm{p}\sin\theta}\right) + \frac{2v_i}{\pi}2\,(v_{i+1} - v_i)\sum_j \frac{\ln\sqrt{R_j}}{v_j{}^2 - v_i{}^2} \tag{2.3}$$

where n_p and θ represent the refractive index of an IRE and the angle of incidence, respectively. For the sapphire IRE, we set np as 2.0. The summation is performed by taking every other data point. That is, l is odd, $m = 2, 4, 6, \ldots, l-1, l+1, \ldots,$ and when l is even, $m = 1, 3, 5, \ldots, l-1, l+1, \ldots$. According to the Fresnel reflection, amplitude reflectance is given by $r = \sqrt{R}\exp(i\,\Phi)$. The refractive index n and absorption index κ are thus calculated using the formulas

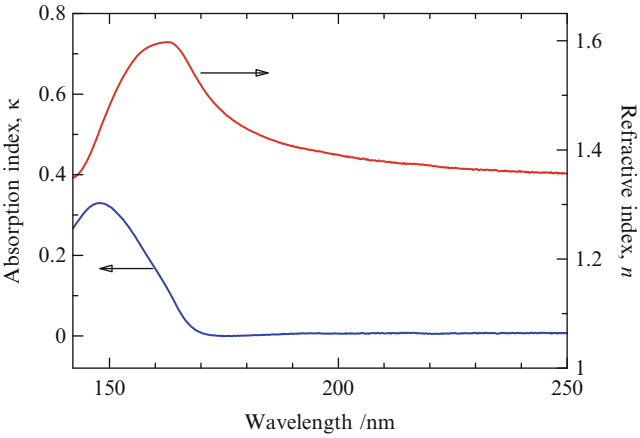

Fig. 2.6 The separated κ and n spectra of water by KKT from an ATR–FUV spectrum measured at 25 °C

$$n = n_\infty \mathrm{Re}\left[\sqrt{\sin^2\theta + \left(\frac{1-\tilde{r}}{1+\tilde{r}}\right)^2 \cos^2\theta}\right] \tag{2.4}$$

and

$$\kappa = -n_\infty \mathrm{Im}\left[\sqrt{\sin^2\theta + \left(\frac{1-\tilde{r}}{1+\tilde{r}}\right)^2 \cos^2\theta}\right], \tag{2.5}$$

where n_∞ is a refractive index of sample in the high-frequency limit. The KKT algorithm can be validated using an artificial absorption band on the basis of Lorentzian distribution. We employ the values of n_D at 589 nm instead of n_∞ for the actual case, for example, $n_\mathrm{D} = 1.333$ for water. In order to obtain the desired result, the experimental data should be probably extrapolated. In case of water absorption, the spectrum was extrapolated from 145 nm to 120 nm by nonlinear least squares fit with an ATR spectrum modeled with Gaussian line shapes based on Heller's optical constants of water [22]. Figure 2.6 shows the separated κ and n spectra of water measured at 25 °C. The absorption spectrum shows the first electronic transition peaked at 148 nm that is shorter than that found in the raw ATR spectrum. In the n spectrum, a strong dispersion is found in the FUV region of $\lambda < 163$ nm. A peak appears at around 163 nm and an anomalous dispersion is estimated below 163 nm. The property of the ATR–FUV spectra of water in different states will be detailed in Chap. 4.

The ATR–FUV spectrometer has been used for both basic research on hydrogen bonding and hydration of water and electronic transitions and structure of organic molecules such as alcohols and ketones and has been applied to qualitative and

quantitative analysis and on-line monitoring. The current trends in the development of optical devices toward the FUV region have brought us the use of high-groove density gratings, small light sources, and small detectors. Higashi et al. developed a miniaturized practical spectrometer for semiconductor manufacturing processes with a nitrogen purging system and realized the in-line monitoring of liquid chemicals in very low concentration level [23]. Of course ATR–FUV spectroscopy is useful for the measurement of solid samples. The practicability has been gradually confirmed for some polymer film sample. As will be shown in Chap. 3, Sect. 3.3.5, the cast films of nylons were measured by using an ATR–FUV spectrometer mentioned in this section. This study demonstrated that one can investigate the electronic structure and transitions of polymers on the extreme surface.

2.3 Time-Resolved ATR–FUV Spectroscopy

An FUV transient absorption spectrometer based on time-resolved (TR) ATR has developed and tested for aqueous solutions of phenol and tryptophan in the region 170–185 nm [13]. Figure 2.7 shows a schematicdiagram of the TR-ATR–FUV spectrometer. The conception of the TR-ATR–FUV is based on a nanosecond transient absorption spectrometer with an ATR–FUV sample compartment. In this region, a stable tunable laser was not available, and therefore, white light from a laser-driven Xe lamp source was used as a probe light. The probe light is incident to the IRE at an incident angle of 70°. The IRE was placed in the ATR probe. A new ATR probe where a sample liquid is exchanged continuously by a flow system was designed to reduce efficiently the stray light from the excitation light. Figure 2.8a

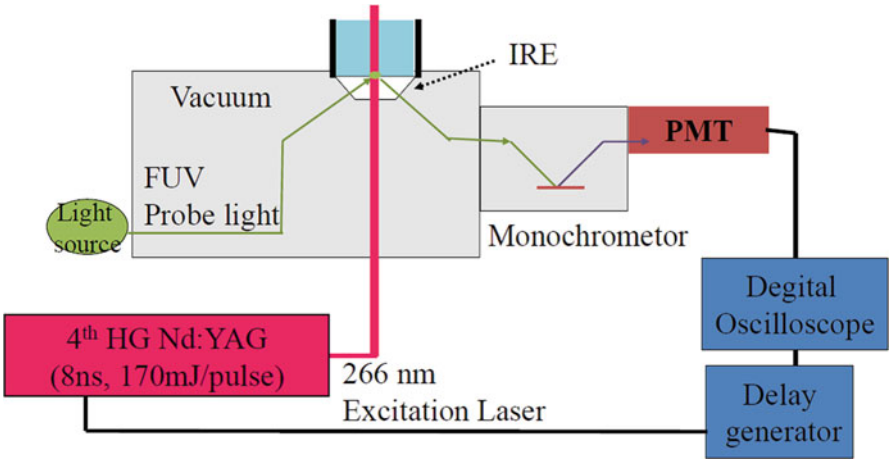

Fig. 2.7 A schematic diagram of the time-resolved attenuated total reflectance far-ultraviolet spectrometer that we developed

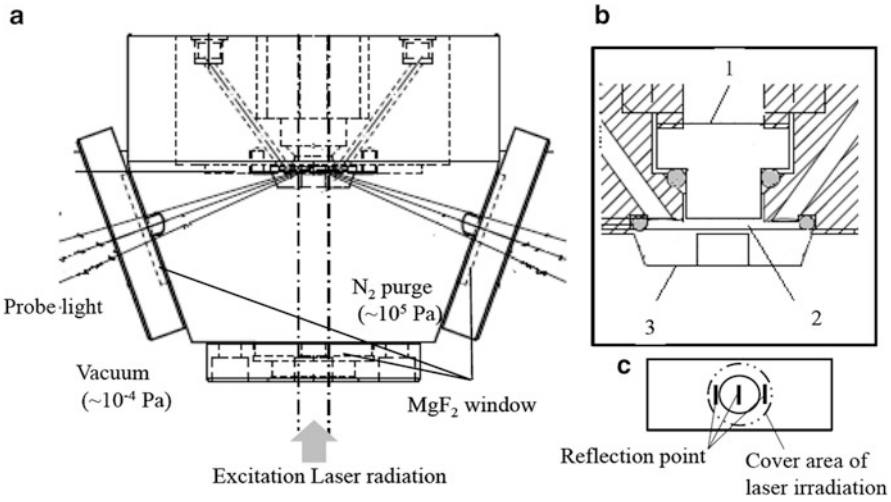

Fig. 2.8 The attenuated total reflectance probe used as part of the time-resolved attenuated total reflectance far-ultraviolet spectrometer (**a**). An enlarged figure of the internal reflection element in side view (**b**) and bottom view (**c**)

illustrates the ATR probe. The sample solution flows through the cell (Fig. 2.8b-2) at 80 ml/min. A three-time internal reflection (Fig. 2.8c) element (IRE) made of quartz is employed (Fig. 2.8b-3). Subsequent to the IRE, a monochromator is placed. A solar blind response photomultiplier (PMT; R6835, Hamamatsu Photonics) with a homemade preamplifier is used to detect the probe light. The time resolution, which was determined by the time response of a continuous light detector, was 40 ns.

We have examined the performance of the instrument by using 5×10^{-3} mol dm^{-3} phenol aqueous solution irradiated by a 266-nm laser pulse in the range of 170–185 nm. Figure 2.9 shows a temporal signalfor 172- and 181-nm probe light that was delayed by the laser irradiation. As for the signal at 172 nm, a difference signal in a unit of absorbance suddenly increases in a limit of response time, and then the signal gradually decreased. Compared to signal at 172 nm, the signal at 181 nm suddenly decreased after laser irradiation and then gradually increased. Figure 2.10 shows the transientabsorption spectra of the aqueous solution of phenol in the region 170–185 nm for various time delays. In the very short time delay, the transient absorption increased for the wavelength region that was greater than 175 nm, while the absorption signal decreased for the region that was shorter than 176 nm. The absorption at 172 nm that increased immediately after laser irradiation may have been due to the transient species created by photodissociation. On the other hand, the intensity that decreased in the longer wavelength region at 176 nm that was induced by the laser irradiation may be ascribed to the decrease in the phenol π-π^* band due to the photodissociation of phenol. Many studies on the photodissociation of phenol in aqueous solutions over various time ranges have been carried out [24, 25]. For the time range of 250 μs on which our system focuses,

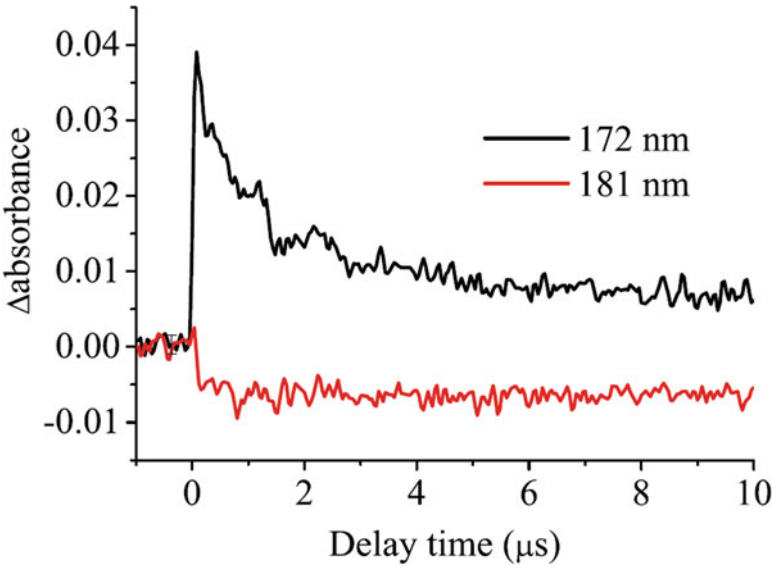

Fig. 2.9 A temporal signal for 172- and 181-nm probe light delayed from the laser irradiation

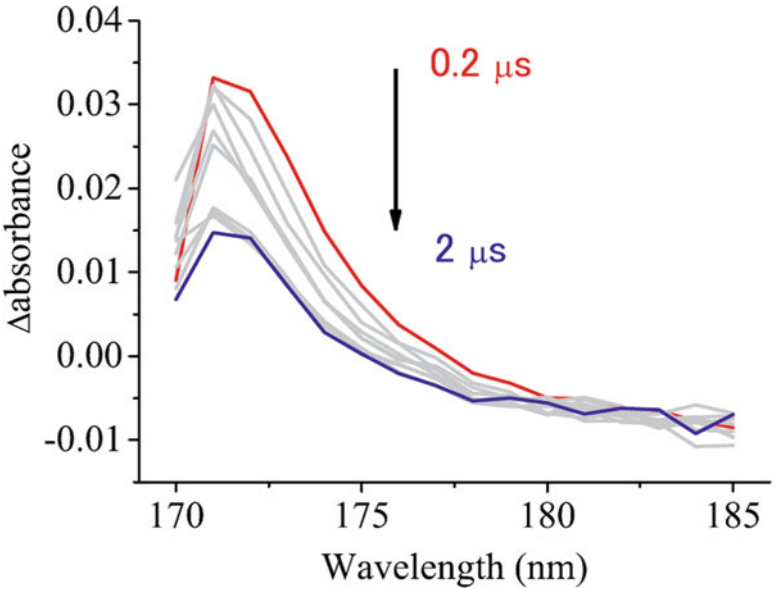

Fig. 2.10 Transient absorption spectra in the 170–185-nm region of the phenol solution (3.0×10^{-3} mol dm^{-3})

previous studies examined the time-resolved EPR, and time-resolved transient absorption spectra were measured for phenol aqueous solutions [24, 25]. With reference to these studies, we inspected the signal in Fig. 2.9 and concluded that the decrease in intensity of the phenol signal within 10 ns after laser irradiation was in good agreement with the decrease in intensity of the longer wavelength region at 177 nm.

2.4 Conclusion

FUV spectroscopy had not been widespread in the past several tens of years because of interference by the strong absorption of oxygen in air. The solution has been thought to be evacuation of the instrument; therefore the wavelength region was called vacuum ultraviolet. The nitrogen purge is the alternative approach to the FUV region and it realizes the spectral measurements under atmospheric pressure. This approach simplifies the instruments and provides possibility of transmittance measurements with a fragile cell as well as the ATR measurements. Unfortunately, there have been no innovations in the light source and detector in the FUV spectrometer explained in this chapter. For example, the photomultiplier still needs wavelength conversion with a sodium salicylic acid film. To provide a highly sensitive measurement, more stable elements should be developed. We hope that the findings by the ATR–FUV spectrometer motivate and accelerate the developments of optical elements in the FUV region.

References

1. J.-J. Max, M. Trudel, C. Chapados, Appl. Spectrosc. **52**, 234 (1998)
2. J.-J. Max, C. Chapados, Appl. Spectrosc. **52**, 963 (1998)
3. K. Masuda, T. Haramaki, S. Nakashima, B. Habert, I. Martinez, S. Kashiwabara, Appl. Spectrosc. **57**, 274 (2003)
4. N. J. Harrick, *Internal Reflection Spectroscopy Harrick* (New York, 1987)
5. A. Hartstein, J.R. Kirtley, J.C. Tsang, Phys. Rev. Lett. **45**, 201 (1980)
6. S. Morita, M. Tanaka, Y. Ozaki, Langmuir **23**, 3750 (2007)
7. L. Xu, J.R. Schlup, Appl. Spectrosc. **50**, 109 (1996)
8. A. Ikehata, X. Li, T. Itoh, Y. Ozaki, J.-H. Jiang, Appl. Phys. Lett. **83**, 2232 (2003)
9. K. Matsubara, S. Kawata, S. Minami, Appl. Spectrosc. **42**, 1375 (1988)
10. A. Pirnia, C.S.P. Sung, Macromolecules **24**, 6104 (1991)
11. W.M. Doyle, L. Tran, Spectroscopy **14**, 46 (1999). Amsterdam
12. D.R. Thompson, E. Kougoulos, A.G. Jones, M.W. Wood-Kaczmar, J. Cryst. Growth **276**, 230 (2005)
13. Y. Ozaki, Y. Morisawa, A. Ikehata, N. Higashi, Appl. Spectrosc. **66**, 1 (2012)
14. Y. Morisawa, N. Higashi, K. Takaba, N. Kariyama, T. Goto, A. Ikehata, Y. Ozaki, Rev. Sci. Instrum. **83**, 073103 (2012)
15. N. Higashi, A. Ikehata, Y. Ozaki, Rev. Sci. Instrum. **78**, 103107 (2007)
16. N.J. Harrick, Phys. Rev. Lett. **4**, 224 (1960)

17. L.R. Painter, R.D. Birkhoff, E.T. Arakawa, J. Chem. Phys. **51**, 243 (1969)
18. D.B. Leviton, T.J. Madison, P. Petrone, Proc. SPIE-Soc. Opt. Eng. **3425**, 219 (1998)
19. A. Ikehata, Y. Ozaki, N. Higashi, J. Chem. Phys. **129**, 234510 (2008)
20. J.A. Bardwell, M.J. Dignam, J. Chem. Phys. **83**, 5468 (1985)
21. K. Ohta, H. Ishida, Appl. Spectrosc. **42**, 952 (1988)
22. J.M. Heller Jr., R.N. Hamm, R.D. Birkhoff, L.R. Painter, J. Chem. Phys. **60**, 3483 (1974)
23. N. Higashi, H. Yokota, S. Hiraki, Y. Ozaki, Anal. Chem. **77**, 2272 (2005)
24. A. Bussandri, H. van Willigen, J. Phys. Chem. A **106**, 1524 (2002)
25. T.A. Gadosy, D. Shukla, L.J. Johnston, J. Phys. Chem. A **103**, 8834 (1999)

Chapter 3
Electronic Structure and Transition in the Far-Ultraviolet Region

Yusuke Morisawa and Masahiro Ehara

Abstract This chapter overviews the investigations by using the attenuated total reflection far-ultraviolet (ATR-FUV) spectroscopy. These studies elucidate the electronic structure and electronic transition of molecules in the FUV region. The target molecules or systems include *n*- and branched alkanes, alcohols, ketones, amides, and nylons in the liquid or solid phase. The reliable and consistent assignments were performed with the help of quantum chemical calculation protocols, namely, time-dependent density functional theory (TD-DFT) and symmetry-adapted cluster–configuration interaction (SAC-CI) calculations. The typical features in the FUV region of *n*- and branched alkanes, ketones, amides, and nylons were interpreted in detail. The confined Rydberg transitions were clearly probed in the studies of alkanes and ketones. The intermolecular interaction via hydrogen bonding and the polarization of the surroundings in the liquid or solid phase was analyzed for amides and nylons using the present spectroscopy.

Keywords ATR-FUV • Liquid state • Rydberg state • Quantum chemical calculations

3.1 Introduction

Far-ultraviolet (FUV) spectroscopy holds great potential in revealing electronic transitions and structure of a wide range of molecules in condensed phases [1–4]. FUV spectroscopy in the 145–200 nm region has recently been a matter of intense

Y. Morisawa (✉)
Department of Chemistry, School of Science and Engineering, Kinki University, 3-4-1 Kowakae, Higashi-Osaka, Osaka 577-8502, Japan
e-mail: morisawa@chem.kindai.ac.jp

M. Ehara (✉)
Research Center for Computational Science, Institute of Molecular Science, 38 Nishigo-Naka, Myodaiji, Okazaki, Aichi 444-8585, Japan

Elements Strategy Initiative for Catalysts and Batteries (ESICB), Kyoto University Katsura, Kyoto 615-8520, Japan
e-mail: ehara@ims.ac.jp

Y. Ozaki, S. Kawata (eds.), *Far- and Deep-Ultraviolet Spectroscopy*,
DOI 10.1007/978-4-431-55549-0_3

interest because many kinds of organic [5–10] and inorganic [11–16] materials in the condensed phase show bands coming from electronic transitions in the FUV region. The spectroscopy is available not only for basic studies but also for various applications such as monitoring of the quality of semiconductor wafer clearwing [3, 17, 18]. For example, the photo catalytic activities of metal-modified TiO_2 were studied by using an attenuated total reflection (ATR)-FUV spectroscopy [15, 16]. Such rapid progress in FUV spectroscopy has been introduced by the development of ATR-FUV spectrometer, which has enabled us to measure the spectra in the complete FUV region for liquid and solid samples without facing problems such as peak saturation [3, 4]. Moreover, significant progress of quantum chemical calculations for electronic excitation states of molecules improves our interpretations of the FUV spectra.

In the series of studies, we investigated the FUV region of various molecules by ATR-FUV spectroscopy, namely, water and aqueous solutions [11–13], alcohols [5], *n*- and branched alkanes [6, 7], ketones [8], amides [9], and nylons [10] in the liquid or solid phase. The ATR-FUV spectroscopy enables us to examine the existence of confined Rydberg transitions in the liquid phase.

The FUV spectra of *n*-alkanes gave a broad feature near 150 nm, while the branched alkanes show an additional shoulder at ∼180 nm. The 150 nm band shows a lower-energy shift with a significant intensity increase as the alkyl chain length increases. It was found that the 150 nm band of *n*-alkanes arises from the σ-Rydberg $3p_y$ transition and its red shift is caused by the destabilization of σ orbital and the stabilization of Rydberg 3*p* level, which is enhanced as the carbon chain increases. These FUV spectra of alkanes have provided new insight into Rydberg states and transitions of liquid alkanes [7].

The FUV spectra were also measured for aliphatic and branched ketones using the ATR-FUV technique [8]. The n-3*s*, n-3*p*, and n-3*d* Rydberg transitions were investigated for these compounds in the liquid phase. Three regions of absorption bands were found in these spectra. A comparison of the spectra of the liquid phase with those of the gas phase revealed that bands observed in 175–200 and 160–175 nm are strongly correlated with the molecular structure of the investigated ketones and are assigned to the n-3*s* and n-3*p* Rydberg transitions, respectively. Band broadening and the higher-energy shift from the gas phase to the liquid phase were also considered.

The FUV region of amides in the liquid phase is also of interest because valence–Rydberg coupling is anticipated in the π–π* transition and the direct interaction via hydrogen bonding affects the excited states. Thus, we studied the electronic transitions of five amides in the liquid phase by using ATR-FUV spectroscopy [9]. It was shown that the major band of the amides at ∼190 nm can be attributed mainly to the π–π* transition but several types of Rydberg transitions also exist in its vicinity and that the valence–Rydberg coupling of the π–π* transition is more significant than the n–π* transition.

Nylons include both alkane chain and amide group, and therefore, their FUV spectra have both features of alkanes and amides. Thus, we are able to examine the characteristic features of these functional groups and the influence of surroundings

in the solid state by the measurement of the FUV region of nylons [10]. The transmittance (Tr) absorption spectra of nylons were originally reported in 1970 [19]. The π–π* amide band was observed at ∼190 nm, and another band below 165 nm was found to become strong as the number of methylene unit; however, the assignment of the latter band has not been clear in the solid state or condensed phase. Unfortunately, most theoretical works on the solid amides and polyamides [20] have not focused on the Rydberg transitions. Recent ATR-FUV works [7–9] for liquids, on the other hand, revealed that the Rydberg transitions do exist even in the liquid or condensed phase.

In this chapter, we overview the recent works of *n*- and branched alkanes, alcohols, ketones, amides, and nylons, using both ATR-FUV and Tr-FUV spectroscopy with the help of quantum chemical calculations. Details of the ATR-FUV spectrometer used have been explained in Chap. 2. The quantum chemical calculations include density functional theory (DFT) and wave function theory. For excited states, time-dependent DFT (TD-DFT) and symmetry-adapted cluster–configuration interaction (SAC-CI) [21–23] approaches were used. We provided the reliable assignments in the 145–250 nm region of these systems and investigated the confined Rydberg transitions in the liquid phase as well as the effects of hydrogen bonding and polarization of the surroundings on the electronic transitions in the liquid or solid phase.

3.2 Theory

ATR-FUV spectra cover wide-energy region up to 140 nm, where both valence and Rydberg transitions appear and sometimes strong valence–Rydberg coupling occurs. To perform reliable assignments or interpretation of the electronic spectra, special care should be taken for the selection of methods and basis sets. In TD-DFT, it is generally recognized that valence excited states are well described by the global hybrid functionals like B3LYP [24, 25] and PBE0 [26], while for the charge transfer states or Rydberg states, the long-range corrected functionals, for instance, LC-PBE [27] and CAM-B3LYP [28], provide better results. It is also known that the TD-DFT method is less basis set dependent compared to ab initio wave function theory. In the wave function theory, sufficient amount of electron correlations should be included for describing valence excited states, and the flexible basis sets are necessary for Rydberg transitions. The computational cost is also practically important. In the works presented here, we adopted DFT/TD-DFT and SAC-CI methods to analyze the electronic excited states observed by ATR-FUV spectroscopy. These methods are applied to the FUV region of *n*- and branched alkanes, ketones, amides, and nylons.

The DFT/TD-DFT calculations were carried out for real molecules or model system. The B3LYP [24, 25] and CAM-B3LYP [28] functionals were used for the ground and excited states, respectively, except for the special cases where the functionals are specified. The ground-state geometries were obtained by the

optimization at B3LYP/cc-pVTZ [29] level of approximation followed by the vibrational analysis to confirm the calculated structures are true local minimum. For calculating the vertical transition energies of these model systems, the TD-CAM-B3LYP calculations were carried out with cc-pVDZ basis sets with diffuse s and p functions on the first-row atoms; the exponents of diffuse functions are taken from aug-cc-pVDZ [29]. In the following sections, we use the simple terms of DFT or TD-DFT which means DFT(B3LYP) and TD-DFT(CAM-B3LYP), respectively.

The transition energy in the liquid phase was calculated using the polarizable continuum model (PCM) [30] in the linear response scheme (LR-PCM) [31–33]. In the case of amides and nylons, the direct intermolecular interaction via hydrogen bonding is assessed using the dimer or higher cluster models (trimer, tetramer, and pentamer). Thus, for analyzing the environmental effects in the liquid phase, the dimer or higher cluster models predominantly describe the direct hydrogen bond interaction, while PCM provides the polarization effect of surroundings. The LR-PCM describes only the linear effect of polarization, while the SS-PCM [34] includes the nonlinear effect, namely, the polarization of the electronic state of surroundings caused by the electronic transition of solute. The higher cluster models beyond dimer describe both multiple hydrogen bonding interaction and many-body polarization.

In the case of nylons, the effects of hydrogen bondings and the coupling of the excitations of sheet structure on the π–π^* transition energy are of interest. Thus, for nylon 6 and nylon 6/6, monomer to trimer units were examined. In particular, for nylon, the trimer models include the unit cell of the hydrogen-bonded sheets that represent the π–π^* transition, namely, double and single unit cells for nylon 6 and nylon 6/6, respectively. These model systems which were designed for the α phase and assumed to be planar, namely, C_s structures, were adopted. In this case, the geometry optimization of these models was carried out at B3LYP/cc-pVDZ followed by the calculations of the vertical transition energy at TD-CAM-B3LYP with cc-pVDZ plus diffuse s and p functions only on N and O atoms.

We also performed direct SAC-CI calculations for the *n*- and branched alkanes and five amides. The basis sets used in the SAC-CI calculations were aug-cc-pVDZ (C, N, and O) and cc-pVDZ (H). To reduce the computational cost of SAC-CI, the excitation operators were selected using the perturbation selection scheme [35]. Because we calculated several excited states, moderate accuracy with the level two threshold for the perturbation selection was used: 5×10^{-6} and 1×10^{-6} a.u. for the ground and excited states, respectively. The direct algorithm was adopted in the SAC-CI calculations [36].

In the case of amides, the environmental effects on a single molecule in the liquid phase were estimated using the PCM SAC-CI method [37]. Geometry relaxation in the PCM environment was not considered, and the gas-phase geometries were used. The nonequilibrium solvation scheme was used for calculating vertical excitation energies, namely, nonequilibrium state-specific (SS) PCM SAC-CI [38]. In the SS-PCM SAC/SAC-CI calculations, we adopted lower-level basis sets, aug-cc-pVDZ (C, N, O) and cc-pVDZ (H), because of the high computational cost of the SS-PCM SAC-CI calculations. The default parameters of the IEF PCM given by Gaussian 09

were used except for NMA. The values, $\varepsilon_0 = 172.8$ and $\varepsilon_\infty = 2.04$, were used for NMA. For evaluating the hydrogen bonding effects, the dimer model of amides was also examined as in TD-DFT calculations where the same geometrical structures were used.

All calculations were performed using the Gaussian 09 suite of program development version [39].

3.3 Applications

3.3.1 n- and Branched Alkanes

Figure 3.1 compares the ATR-FUV spectra and the theoretical spectra by the TD-DFT/aug-cc-pVTZ in the range of 9.5–6.5 eV (130–190 nm) of *n*-alkanes (C_mH_{2m+2}, $m = 5$–9) [6, 7]. The calculated main peak clearly shows a red shift with a significant increase in intensity along the alkyl chain length. This trend is in good agreement with the observed FUV spectra, although the calculations overestimate the peak positions about 0.5 eV.

To analyze the absorption spectrum in detail, the peaks calculated in the 9.5–6.5 eV region of *n*-hexane are shown with the convoluted spectrum in Fig. 3.2. Many transitions contribute to an absorption band at around 9 eV. The dominant peaks are summarized in Table 3.1. The most intense peak is the transition from HOMO-2(σ) to Rydberg $3p_y$ (hereafter denoted as T1). The transition nature of T1 is the same for all *n*-alkanes, although the energy level of HOMO-2(σ) interchanges with HOMO-3(π) at $m = 7$ (*n*-heptane). The second intense transition (T2) is a transition from HOMO-1(π) to Rydberg $3p_y$ for all *n*-alkanes. The other transitions, namely, π-Rydberg $3p_x$ and σ-Rydberg $3p_x$, also contribute to this broadband.

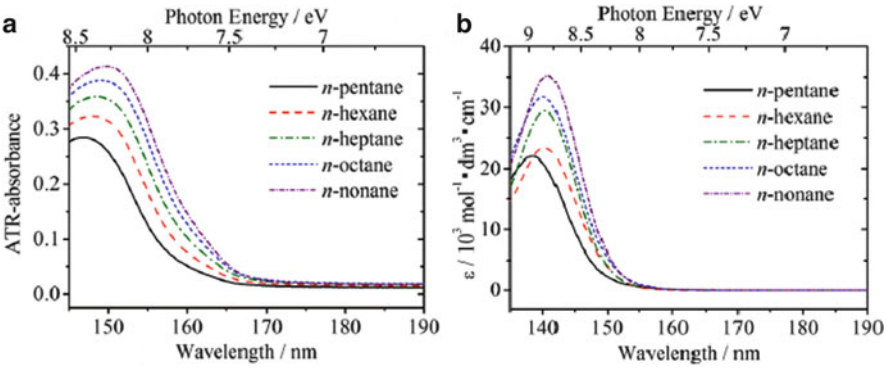

Fig. 3.1 (**a**) ATR-FUV spectra and (**b**) theoretical spectra of *n*-alkanes (C_mH_{2m+2}, $m = 5$–9). Cited from Refs. [6, 7]

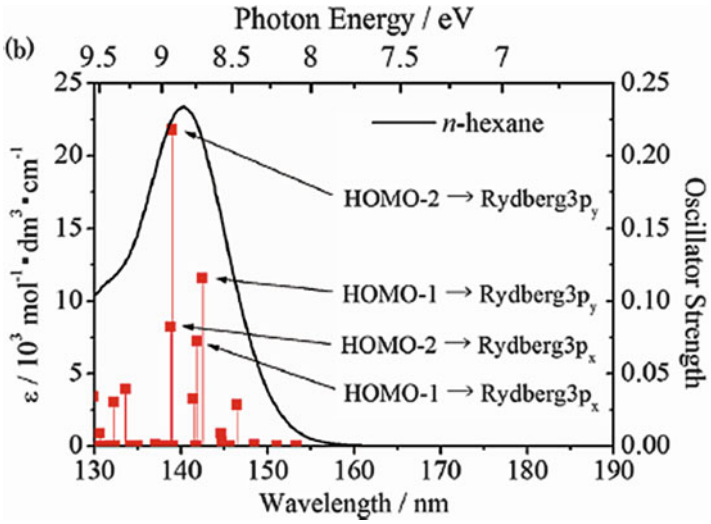

Fig. 3.2 Theoretical spectra of *n*-hexane calculated by TD-DFT [7]

Table 3.1 Transition energy (ΔE, eV) and oscillator strength (f) of *n*-pentane in the gas phase and in the liquid phase by using TD-DFT [7].

State	Transition character	Gas phase		In solvent	
		ΔE	f	ΔE	f
B_1 (T2)	b_1 (H-1) → a_1 (Ryd. $3p_y$)	8.73	0.102	8.71	0.138
A_1	b_1 (H-1) → b_1 (Ryd. $3p_x$)	8.79	0.069	8.77	0.116
A_1 (T1)	a_1 (H-2) → a_1 (Ryd. $3p_y$)	8.96	0.179	8.93	0.192
B_1	a_1 (H-2) → b_1 (Ryd. $3p_x$)	8.98	0.053	8.98	0.057

Figure 3.3 displays the calculated HOMO ~ HOMO-3 and Rydberg $3p_y$ of *n*-hexane. Among these MOs, HOMO-1(π) and HOMO-2(σ) are relevant to the electronic dipole-allowed transitions. Transitions from these MOs to Rydberg $3p_y$ and $3p_x$ have large oscillator strength as noted above, while those from HOMO (a_g) have small intensities and those from HOMO-3 (a_u) are dipole forbidden.

The SAC-CI calculations were also performed for the absorption spectra of *n*-alkane (C_mH_{2m+2}, $m = 5$–8) in the FUV region. The SAC-CI spectra have similar character as TD-DFT ones, for example, (1) T1 makes the largest contribution to the absorption band, and (2) T2 appears on the low-energy side of T1 and contributes significantly to the absorption band. The contribution from T2 to the band was larger in SAC-CI (72 % of T1) than that in TD-DFT (57 % of T1).

The experimental results revealed that the intensity of the absorption band for *n*-alkanes increases smoothly as the number of carbons increases. Both TD-DFT and SAC-CI results show low-energy shifts of T1 similar to the experimental results. The magnitudes of shifts during the transition from *n*-pentane to *n*-octane are 0.3 and

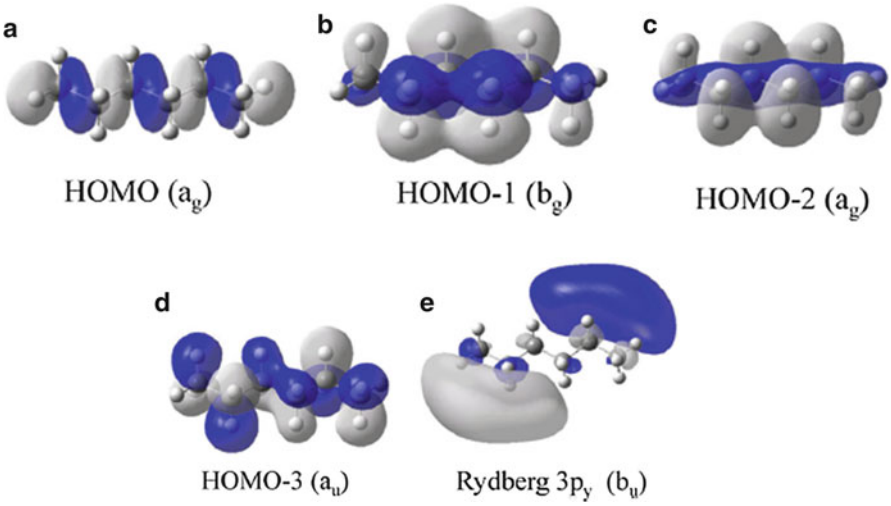

Fig. 3.3 Kohn–Sham orbitals relevant for the excitations of *n*-hexane [7]

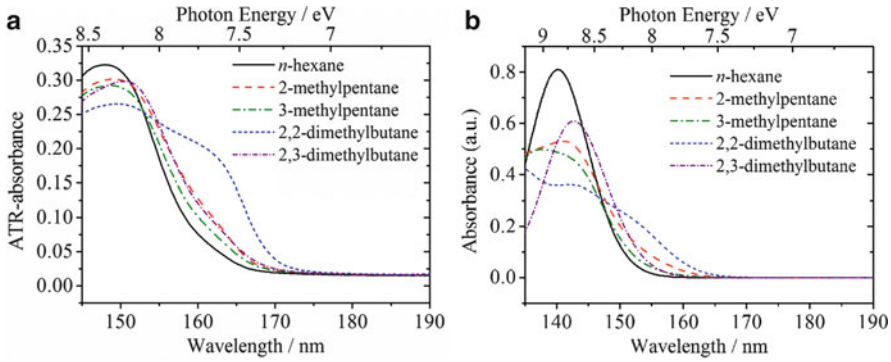

Fig. 3.4 (**a**) ATR-FUV spectra and (**b**) theoretical spectra in the region of 8.55–6.53 eV (145–190 nm) of C_6H_{14} isomer in the liquid phase [7]

0.5 eV for TD-DFT and SAC-CI, respectively, in comparison with the experimental value of 0.2 eV.

The effect of the branching in carbon chain on excitation spectra is of interest. We examined the spectra of *n*-hexane, 2-methylpentane (2MP), 3-methylpentane (3MP), 2,2-dimethylbutane (2,2-DMB), and 2,3-dimethylbutane (2,3-DMB) for this purpose. Figure 3.4a comparesthe ATR-FUV spectra in the 8.5–6.6 eV region of these compounds. In all branched alkanes, the band at ∼8.3 eV (∼150 nm) shows a lower-energy shift. The intensity of the shoulder at ∼7.7 eV (∼160 nm) increases remarkably in the order of alkanes without branches, with tertiary carbon, and with quaternary carbon. The second derivatives of the ATR spectra show a minimum and a maximum peak at around 7.6 and 7.4 eV, respectively, which originates in

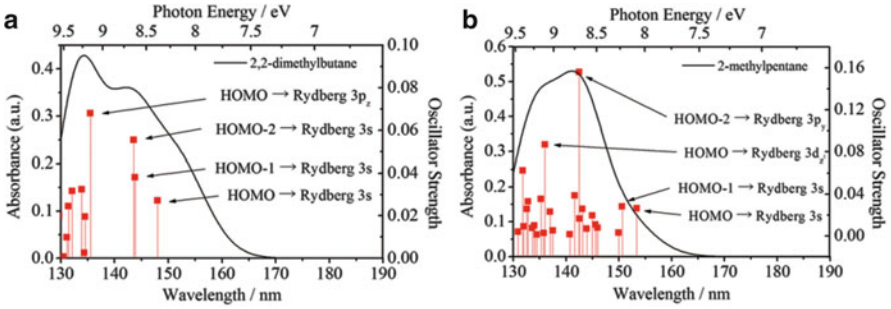

Fig. 3.5 Theoretical spectra of (**a**) 2MP and (**b**) 2,2-DMB by TD-DFT [7]

the shoulder of the ATR absorption spectra. These peaks of 3MP and 2,3-DMB are weak as those of *n*-hexane, while those of 2,2-DMB and 2MP show more significant difference. Minimum peaks at around 8.3 and 7.6 eV in the second derivative spectra correspond to the peak maximum and the shoulder of the ATR absorption spectra, respectively. The differences in those values among the branched alkanes can be seen in Fig. 3.4.

The TD-DFT spectra of *n*-hexane, 2MP, 3MP, 2,2-DMB and 2,3-DMB are compared in Fig. 3.4b. The calculated spectra are in good agreement with the experimental spectra in terms of both the peak shift and the intensity change of the higher-energy band. The increases in intensity of the lower-energy band in the branched alkanes are also reproduced. As for the peak maximum, the lower-energy shift in the branched alkane is well reproduced.

Figure 3.5a shows the theoretical spectrum of 2MP. The shoulder on the lower-energy side is attributed to the $\pi(b_g) \rightarrow 3s$ and $\sigma(a_g) \rightarrow 3s$ transitions, both of which are electronic dipole forbidden in the case of *n*-hexane (Fig. 3.2). The strongest peak is characterized as $\sigma(a_g) \rightarrow$ Rydberg $3p_y$, which is similar to T2/T1 in *n*-hexane. The theoretical spectrum of 2,2-DMB is shown in Fig. 3.5b. Compared to 2MP, the transitions to Rydberg 3*s* in the low-energy region are strong, which provides the remarkable shoulder in the absorption spectra. The $\pi(a_u) \rightarrow$ Rydberg 3*s* transition, which has a transition dipole moment that tilts out of the plane, has strong intensity, especially for 2,2-DMB. Because 2,2-DMB includes quaternary carbon, it causes the electron density to deviate out of the plane. The oscillator strengths of the transitions to Rydberg $3p_x$ or $3p_y$ are distributed to many peaks. These states interact because the branch of the carbon chain is out of the plane.

The branched alkanes with relatively higher symmetry (C_{2v} and C_{2h}) such as 3MP and 2,3-DMB show only a weak shoulder near 7.6 eV, whereas those with relatively lower symmetry (C_s) such as 2MP and 2,2-DMB yield very clear shoulders. Thus, the intensity of the shoulder at ~7.6 eV changes according to the molecular symmetry. It was also inferred that the forbidden transition from $\sigma(a_g)$ to 3*s* becomes allowed in response to the decrease in symmetry that occurs going from *n*-alkanes to branched alkanes with lower symmetry.

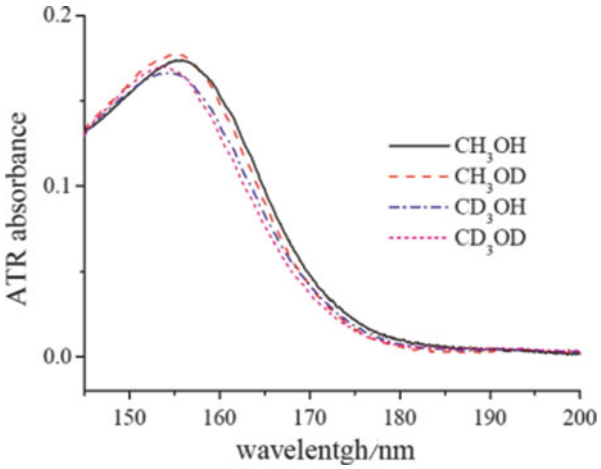

Fig. 3.6 ATR-FUV spectra in the region from 145 to 200 nm of CH_3OH (*solid*), CH_3OD (*break*), CD_3OH (*dot break*), and CD_3OD (*short break*) in the liquid state [5]

3.3.2 Methanol

Figure 3.6 shows ATR-FUV spectra in the region from 145 to 200 nm of CH_3OH, CH_3OD, CD_3OH, and CD_3OD in the liquid phase [5]. As seen in the spectra, the big discrepancy was not observed between OH species and OD species. However, there are significant differences in the peak position and the peak height between the CH_3 species and the CD_3 species.

The peak position shows a blue shift upon the deuterations. The CD_3 substitution yields a greater shift (1.8 and 1.5 nm for CD_3OH and CD_3OD, respectively) than the OD substitution (0.5 and 0.2 nm for CH_3OD and CD_3OD, respectively). Cheng et al. found isotope effects on the $^1A''$ ($2a'' \rightarrow 3s$), $2\ ^1A''$ ($2a'' \rightarrow 3p$), and $3\ ^1A''$ ($2a'' \rightarrow 3p'$) or $3\ ^1A'$ ($2a'' \rightarrow 3p''$) transitions of CH_3OH in the gas phase by comparing an FUV spectrum of CH_3OH with those of CH_3OD, CD_3OH, and CD_3OD in the gas phase [40]. We called these three transitions the A-X, B-X, and C-X transitions, respectively. As for the B-X and C-X transitions in the gas phase, the CD_3 substitution yielded a larger blue shift than the OD substitution. According to our result for the liquid phase, the trends of isotope effects in the peak maximum region (Fig. 3.6) are similar to those for the B-X and C-X transitions of the gas phase. From the comparison with the result for the gas phase, the trend of shifts suggested that the absorption in FUV region arises from the B-X and C-X transitions.

3.3.3 Ketones

We measured ATR-FUV spectra of four aliphatic ketones and two branched ketones whose chemical structures are displayed in Fig. 3.7, namely, acetone, 2-butanone (methyl ethyl ketone, MEK), 2-pentanone (methyl n-propyl ketone,

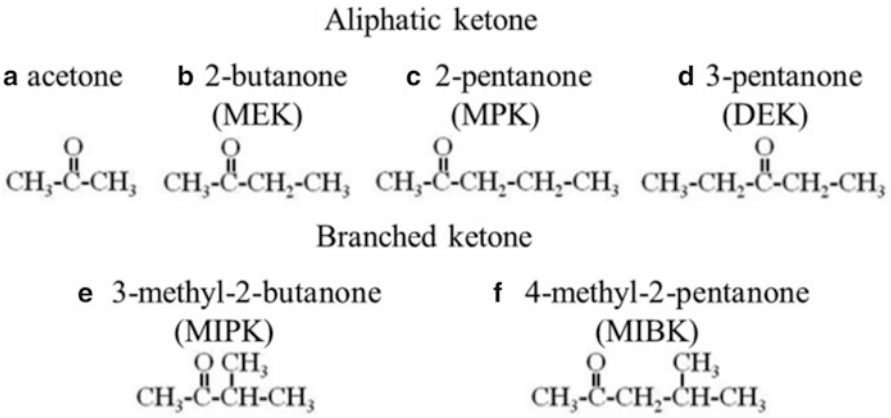

Fig. 3.7 Chemical structures of (**a**) acetone, (**b**) MEK, (**c**) MPK, (**d**) DEK, (**e**) MIPK, and (**f**) MIBK [8]

MPK), 3-pentanone (diethyl ketone, DEK), 3-methyl-2-butanone (methyl i-propyl ketone, MIPK), and 4-methyl-2-pentanone (i-butyl methyl ketone, MIBK) [8].

Figure 3.8a, b shows ATR-FUV spectra of these aliphatic and branched ketones, and the corresponding spectra of the molar absorption coefficient ε derived by KKT are indicated in Fig. 3.8c, d. All the ketones observed have an absorption band at around 6.7 eV. On the other hand, the higher-energy regions are significantly different from one another in the spectral shapes. The branched ketones, MIPK and MIBK, have a clear shoulder near 7.4 eV. Figure 3.8e, f displays the second derivative of these FUV spectra. The second derivative spectra of MPK and DEK show two negative peaks near 8.5 and 6.7 eV, while the MIPK has another negative peak between them (7.4 eV). Similar feature also appears in the second derivative of MIBK. These results strongly suggest that the branched ketones have the third component near 7.4 eV. The absorption peaks at around 6.7 and 8.5 eV are represented as Band A and Band C, respectively. The shoulder seen for the branched ketones is named as Band B.

Figure 3.9 compares the calculated spectral simulations for (a) acetone, (b) MEK, (c) MPK, (d) DEK, and (e) MIPK by EOM-CCSD/aug-cc-pVDZ level with their observed spectra. In order to reproduce the observed spectra in the liquid phase, transition widths of 0.4, 1.1, and 1.8 eV were employed for the transitions around 6.4, 7.5, and 8.0 eV and higher-energy transition. According to the theoretical results, the following assignments can be considered for these ketones:

1. There is an isolated transition from n orbital whose representation is A_1 for C_{2v} species (acetone and DEK) or A' for C_s species (MEK, MPK, MIPK) in the region of 6.4–6.3 eV. This transition is assigned to the n-3*s* transition.
2. There are a group of transitions containing three transitions whose representations are A_1, A_2, and B_2 for C_{2v} species or two A' and A'' for C_s species in the region of 7.60–7.13 eV. These transitions are ascribed to the n-3*p* transition.

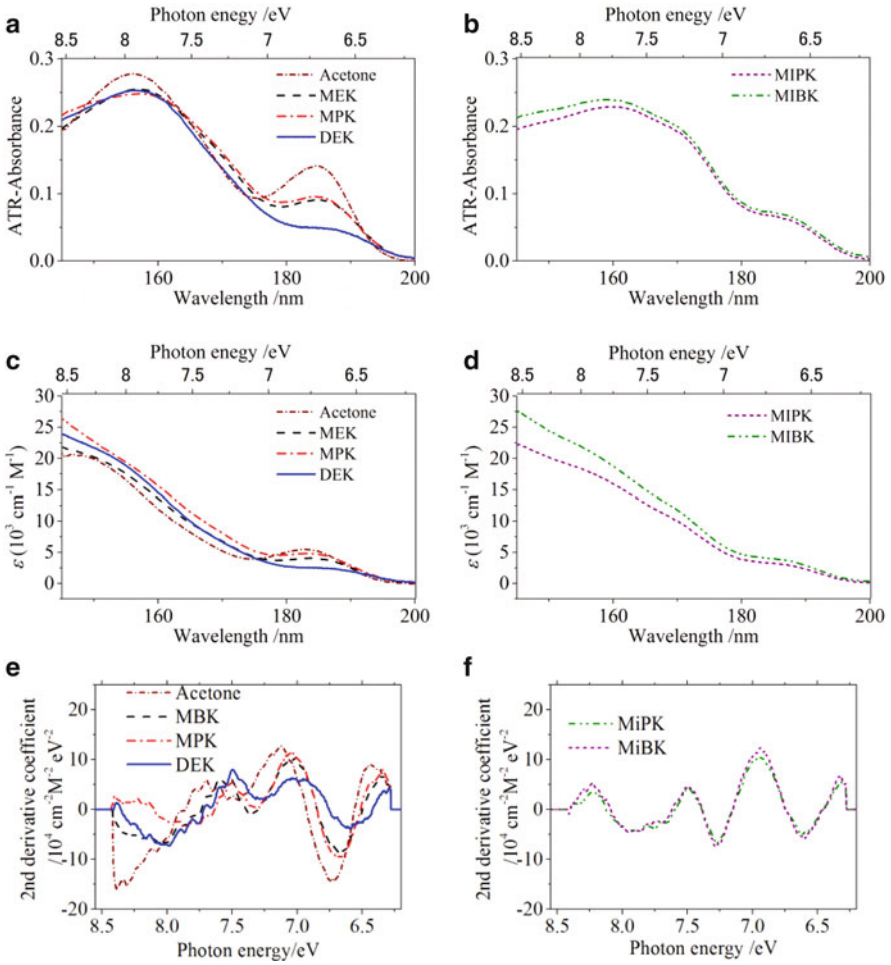

Fig. 3.8 ATR-FUV spectra of (**a**) four aliphatic ketones and (**b**) two branched ketones and molar absorption coefficient ε derived by KKT for (**c**) aliphatic and (**d**) branched ketones in the liquid phase with the second derivatives of their FUV-ε spectra of (**e**) aliphatic and (**f**) branched ketones [8]

3. There are a group of transitions containing 5–7 transitions from n in the region of 8.9–7.8 eV. For acetone, the upper orbital of the transitions is five orbitals of 3*d* Rydberg. As to the other ketones, because of similarity of the strength and transition energy, these include the same kinds of transitions. Additional transition should be a 4*s* or higher components.
4. There is a transition which has the strongest oscillator strength in this region. It is assigned to the π–π^* transition.

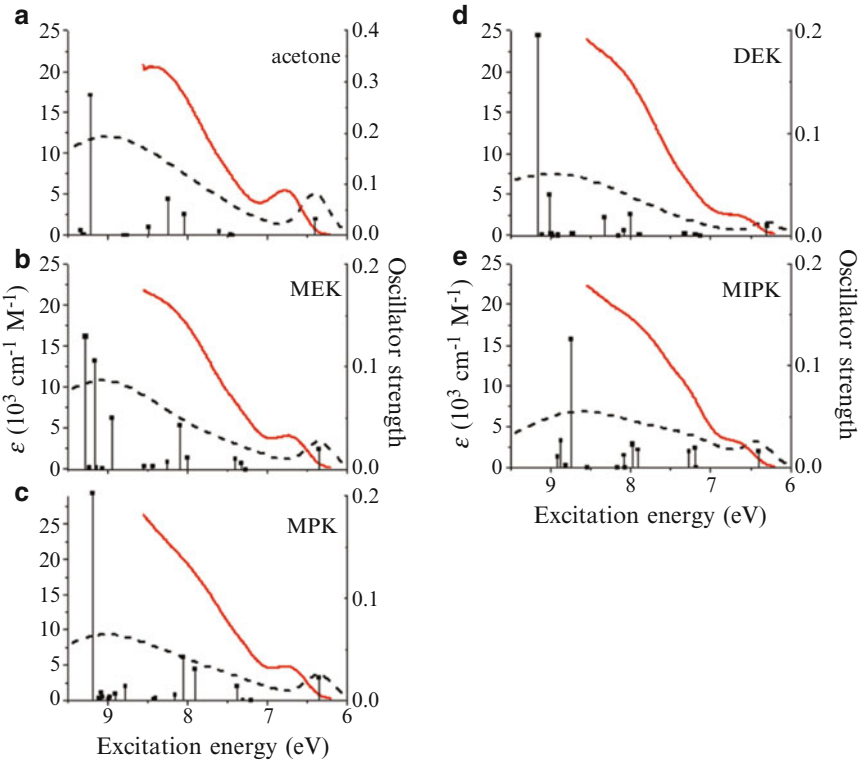

Fig. 3.9 Comparison between calculated (EOM-CCSD) and experimental spectra; (**a**) acetone, (**b**) MEK, (**c**) MPK, (**d**) DEK, and (**e**) MIPK. Stick peaks are calculated peaks with *black dashed lines* simulated spectra and *red solid lines* observed spectra in the liquid phase [8]

The n-3*s* Rydberg transition of acetone was observed at 6.76 eV in the spectrum of the liquid phase. The peak shift occurs to a higher-energy side by 0.39 eV from the corresponding position in the gas phase [41]. This shift is significantly larger than that of the n–π* transition (0.05 eV) [42]. In the case of the n–π* transition, the shift originates from a difference in the dipole–dipole interaction in the liquid phase between the ground and excited states of acetone. Quantum chemical calculations with a PCM are widely used to estimate transition energies in solvents. Since we focused on the n-3*s* Rydberg transition, we applied TD-CAM-B3LYP calculations to reproduce the transition energy of the Rydberg orbitals. Table 3.2 shows the TD-DFT results of acetone in the gas phase and in the neat liquid. The calculated results for the gas phase agree well with the experimental results. The calculated gas-to-liquid energy shift of the n-3*s* Rydberg transition was estimated to be 0.22 eV. It reproduces the larger shift of the n-3*s* transition than n–π* transition. The discrepancy between the shift observed in the FUV absorption spectra and that calculated with PCM should result from the neglect of intermolecular interactions.

Table 3.2 Comparison of an excitation energy (eV) and a gas-to-liquid shift (eV) between experimental and DFT calculation using PCM for the n–π* and the n-3*s* Rydberg transition of acetone [8]

	Experiments			TD-DFT/aug-cc-pVTZ		
	Gas	Neat liq.	Shift	Gas	Neat liq.	Shift
n–π*	4.43	4.51	0.08	4.43	4.60	0.17
n-3*s*	6.36	6.75	0.39	6.39	6.62	0.22

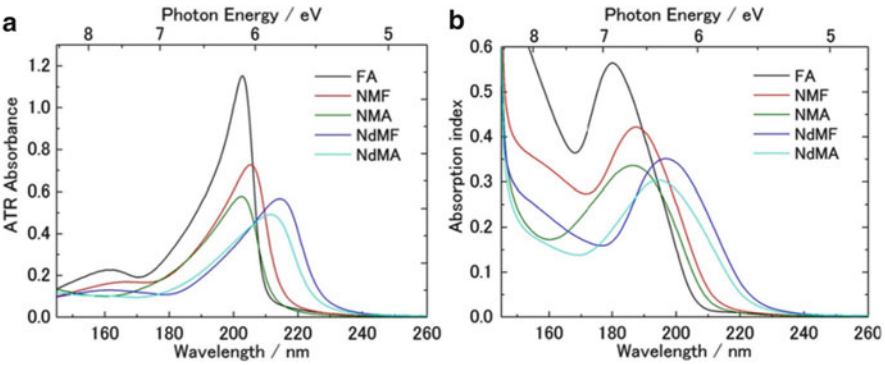

Fig. 3.10 (**a**) ATR-FUV spectra of FA, NMF, NMA, NdMF, and NdMA in the liquid phase and (**b**) their absorption spectra obtained by Kramers–Kronig transformation [9]

Thus, Rydberg transitions were clearly observed for ketones in the liquid phase for the first time. Detailed assignments of the FUV region were performed with the help of quantum chemical calculations. The peak shift was also analyzed by the TD-DFT in PCM.

3.3.4 Amides

Figure 3.10a, b shows ATR-FUV spectra in the 140–260 nm region for formamide (FA), N-methylformamide (NMF), N-methylacetamide (NMA), N,N-dimethylformamide (NdMF), and N,N-dimethylacetamide (NdMA) in the liquid phase and their absorption index spectra obtained by the Kramers–Kronig transformation, respectively [9]. All FUV spectra show a peak due to amide group in the 180–200 nm region. The peak maximum varies in the order of FA (6.88 eV), NMA (6.81 eV), NMF (6.67 eV), NdMA (6.44 eV), and NdMF (6.44 eV) with the intensity being lowered as the number of methyl groups on the N atom increases.

Table 3.3 summarizes the energy of center of balance in the gas and liquid states and the shift between them. The band shift from the gas to the liquid phase depends on the molecule. The red shift was observed for all molecules except for NdMF; it is particularly large for FA (−0.56 eV) and NMF (−0.64 eV). These shifts

Table 3.3 Excitation energy (eV) of the center of balance of the absorption bands in the gas and liquid phase and shift between them [9]

	Gas	Liquid	Gas to liquid
FA	7.44	6.88	−0.56
NMF	7.31	6.67	−0.64
NMA	6.91	6.81	−0.10
NdMF	6.25	6.31	+0.07
NdMA	6.55	6.44	−0.11

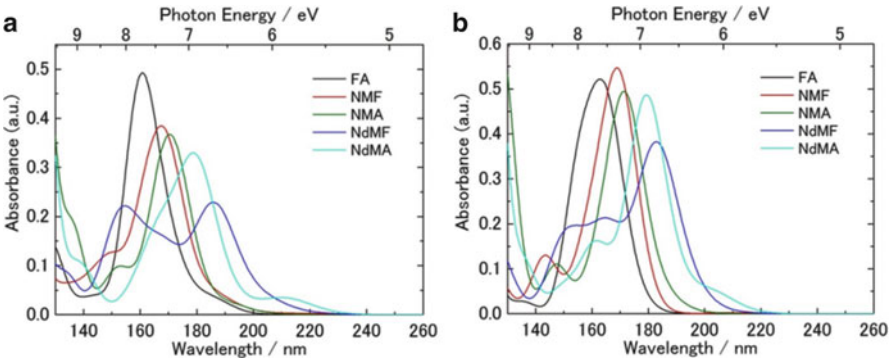

Fig. 3.11 Theoretical spectra of amides (**a**) in vacuum calculated by TD-DFT and (**b**) in the liquid phase by LR-PCM-TD-DFT [9]

reflect various factors such as the effects of hydrogen bonding, the dipole–dipole interactions, and the polarization by electronic transition. The observed amide peaks in the liquid phase can be predominantly attributed to the π–π^* transition. The peaks also contain contributions from the Rydberg transitions via valence–Rydberg mixing.

Theoretical spectra of these five amides are compared in Fig. 3.11 in a vacuum state. The spectra were calculated by TD-DFT/aug-cc-pVTZ with Gaussian convolution where the band width approximately describes the Frank–Condon envelop, namely, vibrational progression or distribution. Theoretical spectra reproduce the observed peak shift to lower energy as the number of methyl groups on the N atom except for the order between NMA and NMF. Assuming the spectra in the liquid phase is described by PCM, the π–π^* absorption band of amides appears in the lower energy in the liquid phase than in the gas phase except for NdMF. Let us consider the effect of the polarization using the LR-PCM-TD-DFT calculations. Figure 3.11b shows the LR-PCM spectra, which account for the effect of the linear response of surrounding molecules. The LR-PCM spectra are similar to those in vacuum regarding the order of the peak positions. This means that the polarization of surrounding does not affect the spectral shape significantly.

The other important effect in the liquid phase is the direct intermolecular interaction via hydrogen bonding, Van der Waals force and other electrostatic interactions. Figure 3.12a, b illustrates the optimized structures of the dimers of five amides and their convoluted theoretical spectra calculated by TD-DFT/aug-cc-pVTZ. In

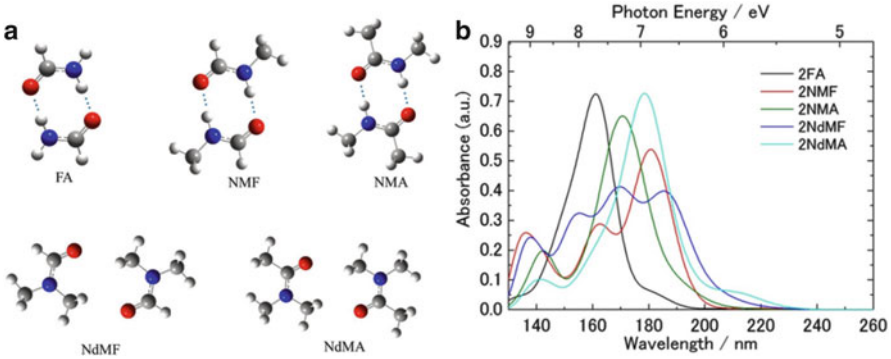

Fig. 3.12 (**a**) The optimized structure of dimers for five amides and (**b**) their spectra in vacuum calculated by TD-DFT [9]

Table 3.4 Excitation energies (eV) of the π−π* transition of FA, NMF, NMA, NdMF, and NdMA calculated by TD-DFT [9]

	Monomer		Dimer	Monomer	Gas
	Gas	PCM	Gas	Gas → PCM	Monomer → dimer
FA	7.80	7.45	7.58	−0.35	−0.22
NMF	7.30	7.28	6.80	−0.02	−0.50
NMA	7.18	7.20	7.06	+0.02	−0.12
NdMF	6.62	6.75	6.60	+0.13	−0.02
NdMA	6.91	6.92	6.90	+0.01	−0.01

the geometry optimization, hydrogen-bonded ring structures are considered for FA, NMF, and NMA, while for NdMF and NdMA, structures with dipole–dipole interactions and coupling between the C=O groups of the dimer are considered. Figures 3.11a and 3.12b reveal that the peak of NMF appears in the lower energy than those of the other amides upon the formation of the dimer.

Table 3.4 presents the TD-DFT results of five amides focusing on the peak maximum. The values were obtained from convoluted spectra. The calculated peak shift from vacuum to LR-PCM represents the solvent effects due to the polarization by electronic transition, while changes from the monomer to the dimer models reflects the effects of the C=O . . . H-N hydrogen bonding of the amide group (FA, NMF, NMA) and the coupling interaction between the C=O groups (NdMF, NdMA).

The observed peak shift of FA was −0.56 eV, while the theoretical values by the LR-PCM-TD-DFT and the dimer model were −0.35 and −0.22 eV, respectively. This means that the effects of hydrogen bonding and polarization of the solute are both important. In the case of NMF and NMA, the calculated peak shifts with dimer model, −0.50 and −0.12 eV, well reproduced the experimental values, −0.64 and −0.10 eV, respectively. These values are better than those by LR-PCM (−0.02 and +0.02 eV). Therefore, in the liquid phase of NMF and NMA, the

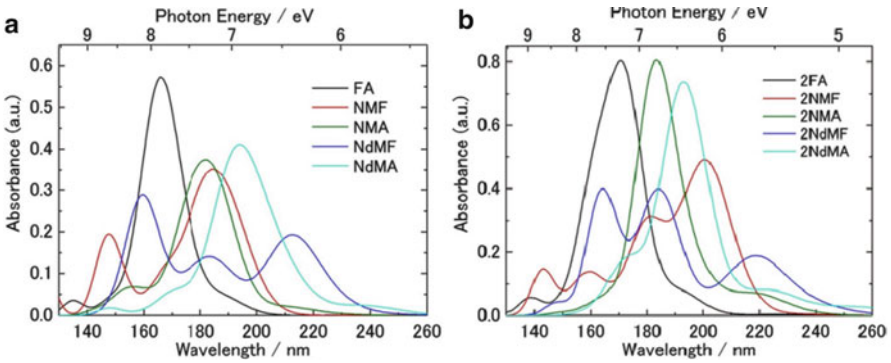

Fig. 3.13 SAC-CI spectra of amides for (**a**) monomer and (**b**) dimer models in vacuum [9]

direct interaction by hydrogen bonding is more important than the polarization of surrounding molecules in the liquid phase. For NdMA and NdMF, neither the dimer model (−0.02 and −0.01 eV) nor the LR-PCM (+0.13 and +0.01 eV) reproduces the experimental results (+0.07 and −0.11 eV). Unlike NMF and NMA, these molecules do not interact strongly, and the effects due to dimerization are trivial. However, the LR-PCM does not take accounts of nonlinear effects such as relaxation of the electronic structure of the solvent, and the electronic spectra of polarized NdMA and NdMF cannot be evaluated.

For these five amides, the SAC-CI calculations were performed for the excited states of these molecules in vacuum and in the liquid phase. Figure 3.13a, b displays the convoluted theoretical spectra calculated by SAC-CI for the amide monomers and dimers, respectively. Although the detailed spectral shape is different, the overall features of the spectra calculated by SAC-CI are similar to those by TD-DFT. The SAC-CI calculated lower excitation energies for all the molecules than TD-DFT. The peak maximum of NMF and NMA was correctly reproduced by SAC-CI. The higher-energy region above 140 nm was not examined by the SAC-CI calculations.

Table 3.5 summarizes the peak positions and peak shifts of five amides calculated by the SAC-CI method in the gas phase and liquid phase. For liquid phase, the nonequilibrium SS-PCM-SAC-CI was performed. This method tends to underestimate the shifts relative to the experimental results. The trends for FA and NMF are similar to those obtained by LR-PCM-TD-DFT. For example, the nonequilibrium effect slightly reduces the red shift of FA as −0.25 eV, and the peak shift evaluated using the dimer model is −0.30 eV. Therefore, both the hydrogen bonding and the polarization are important in the liquid phase of FA. In the case of NMF, the hydrogen bonding interaction dominates, although the calculated value is smaller than the observed red shift. In the case of NMA, the SS-PCM-SAC-CI reproduced the red shift as −0.05 eV in comparison with the experimental value of −0.10 eV. This is different from the TD-DFT results where the hydrogen bonding is suggested to be important. Infrared spectroscopy studies have shown that intermolecular

Table 3.5 Excitation energies (eV) of the π–π* transition of FA, NMF, NMA, NdMF, and NdMA calculated by SAC-CI [9]

	Monomer		Dimer	Monomer	Gas
	Gas	PCM	Gas	Gas → PCM	Monomer → dimer
FA	7.47	7.22	7.17	−0.25	−0.30
NMF	6.47	6.47	6.12	0.00	−0.35
NMA	6.66	6.61	6.77	−0.05	+0.11
NdMF	5.84	5.82	5.63	−0.02	−0.21
NdMA	6.38	6.27	6.44	−0.11	+0.06

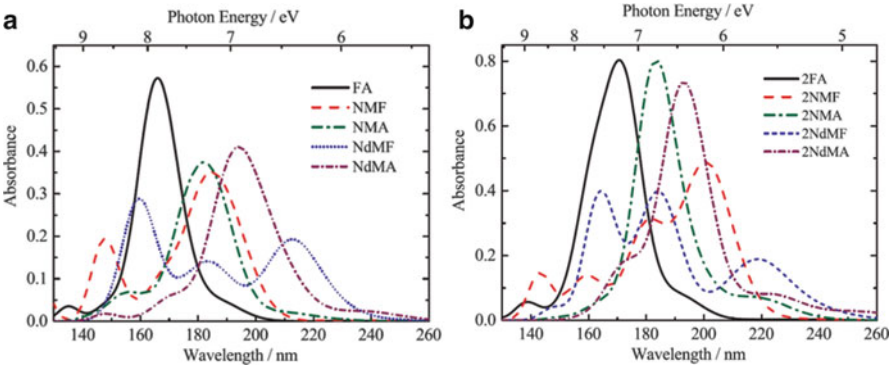

Fig. 3.14 SAC-CI spectra of amides in vacuum for (**a**) monomer and (**b**) dimer models [9]

C=O . . . H-N hydrogen bonds exist in liquid NMA [9]. Using SAC-CI for NdMF and NdMA, it was found that the nonequilibrium SS-PCM model better reproduced the experimental observations than those by the dimer model. The red shifts of NdMF and NdMA were estimated as −0.02 and −0.11 eV, respectively, by the SS-PCM, in better agreement with the experimental values of +0.07 and −0.11 eV compared with those by the dimer model, −0.21 and +0.06 eV. This suggests that the nonlinear effect, the polarization of the solute, included in the SS-PCM model plays an important role.

Based on the analysis of the orbital energy diagram of five amides, the π orbital energy level is less bound with the substitution of CH_3 group on the N atom due to hyper conjugation, while the energy levels of the n and π* orbitals increase with the substitution of CH_3 group on the C atom of the amide C=O group. The energy levels of Rydberg 3*s*, $3p_x$, and $3p_y$ orbitals change only slightly with the CH_3 substitution. In contrast, Rydberg $3p_z$ orbital energy level decreases with CH_3 substitution on the N atom interacting with π* orbital. This enhances the valence–Rydberg mixing.

Figure 3.14 shows theabsorption spectra of five amides calculated by SAC-CI/aug-cc-pVTZ. The results of (a) monomer and (b) dimer model are displayed. The nonequilibrium SS-PCM-SAC-CI calculations only calculate the excitation energy and not oscillator strength because the MOs are different in ground and excited states. For all the molecules, the π–π* transition appears most strongly,

and the Rydberg transitions have transition intensity via valence–Rydberg coupling. For example, in FA, the π–π* transition is located between n-Rydberg $3p_x$ and n-Rydberg $3p_y$ states with distributing the intensity to these two Rydberg transitions and n-Rydberg 3*s* which exists in the lower-energy side. In dimer (2FA), one of the four combinations of π–π* transition has intensity, and two Rydberg transitions represent the shoulder on the higher-energy side. This direct hydrogen bonding interaction is partly responsible for the red shift in the liquid phase in FA. This means that the Rydberg transitions exist in the liquid phase and can be observed in the ATR-FUV spectroscopy as also found in the *n*-alkanes and branched alkanes. More details regarding valence–Rydberg coupling were done with the second moment $<r^2>$ analysis of the SAC-CI results in the original work [9].

The multiple interaction effects beyond dimer model are of interest. These effects in the liquid phase as well as structures are not so clear, although the network structure has been discussed for NMA. We focus on the system which shows relatively large shift in the liquid phase, namely, FA and NMF. The trimer to pentamer structures were examined by TD-DFT. The structures of 3FA-5FA are shown in Fig. 3.15. The interaction energies and the vertical excitation energies including the energy shifts are summarized in Table 3.6. The calculations were performed with cc-pVTZ with s and p diffuse functions on C, N, and O.

The red shifts of the excitation energies for FA gradually increase as the interacting molecules increase, namely, energy shifts range from −0.29 eV to −0.43 eV for dimer to pentamer. The large cluster model includes both hydrogen

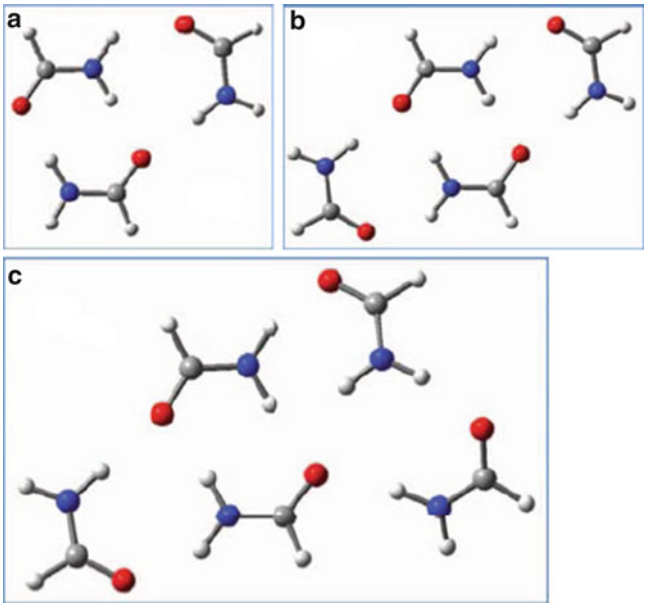

Fig. 3.15 Optimized structures of (**a**) trimer, (**b**) tetramer, and (**c**) pentamer of FA [9]

Table 3.6 Interaction energy, excitation energy, and energy shift of FA and NMF clusters calculated by TD-DFT/aug-cc-pVTZ-diffuse (d, f) at the optimized geometry by DFT/cc-pVTZ [9]

Molecule		E_{int}[a] (kcal/mol)	ΔE (eV)	Shift (eV)
FA	Monomer	–	8.00	–
	Dimer	−14.2	7.71	−0.29
	Trimer	−23.8	7.69	−0.31
	Tetramer	−35.0	7.62	−0.38
	Pentamer	−46.0	7.57	−0.43
NMF	Monomer	–	7.34	–
	Dimer	−11.3	6.94	−0.40
	Trimer	−20.3	7.11	−0.23
	Tetramer	−27.6	7.03	−0.31

[a] $E_{int} = E - n \times E_{monomer}$ (n: number of molecules)

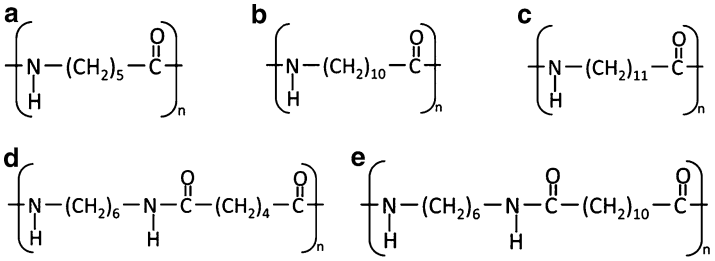

Fig. 3.16 Chemical structures of (**a**) nylon 6, (**b**) nylon 11, (**c**) nylon 12, (**d**) nylon 6/6, and (**e**) nylon 6/12 [10]

bonding interaction and many-body polarization due to excitation, and therefore, it is not straightforward to discuss their effects separately. Note that the calculated interaction energies show that the multiple interactions are favorable; for example, the interaction energy of FA pentamer is larger than the sum of dimer and trimer. For NMF, the effect of hydrogen bonding interaction is not monotonic. The effect in dimer is large, while it is reduced again in trimer and tetramer. The large energy shifts in liquid state of NMF cannot be well explained in the present model system. The trend of the interaction energies is similar to that of FA.

3.3.5 Nylons

Nylon has both alkyl chain and amide group, and therefore, their spectra have character of these groups observed in *n*-alkane and amide. In this section, we focus on nylon 6, nylon 11, nylon 12, nylon 6/6, and nylon 6/12 for which their chemical structures are shown in Fig. 3.16 [10].

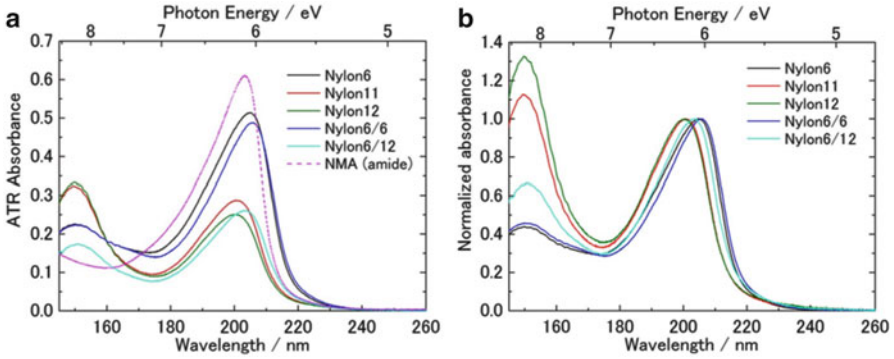

Fig. 3.17 (**a**) ATR-FUV spectra of nylon 6, nylon 11, nylon 12, nylon 6/6, nylon 6/12, and liquid NMA in cast film and (**b**) their normalized spectra with the band near 200 nm [10]

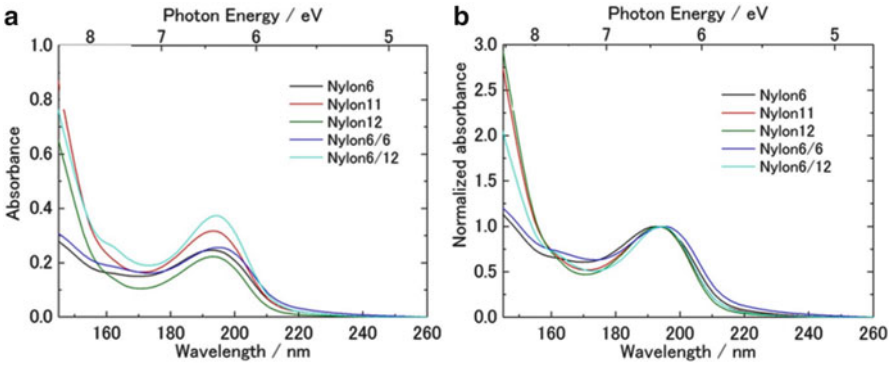

Fig. 3.18 (**a**) Tr-FUV spectra of nylon 6, nylon 11, nylon 12, nylon 6/6, nylon 6/12, and liquid NMA in cast film and (**b**) their normalized spectra with the band near 200 nm [10]

Figure 3.17a compares ATR-FUV spectra in the 150–260 nm region of these nylons and liquid N-methylacetamide (NMA) in cast film. Figure 3.17b shows their normalized spectra with the intensity of the peak near 200 nm. All the nylons have two intense features near 150 and 200 nm. Liquid NMA and other amides give only the band at 190 nm, while liquid *n*-alkanes ($m = 5$–14) show only the 160 nm feature. Thus, the 150 and 200 nm features of nylons are attributed to the alkane and amide parts, respectively. The intensity of the 150 nm band increases as nylon 6 < nylon 6/6 < nylon 6/12 < nylon 11 < nylon 12, which is in agreement to the relative ratio of CH_2 groups. This order is the same as that for *n*-alkanes where the intensity of 150 nm band increases with the number of carbon atoms.

Figure 3.18a displays Tr spectra of nylons in cast film. The intensity in the Tr spectra is influenced by the film thickness. The thickness of nylon films was about 800–400 nm estimated from the absorbance of the Tr spectra and the absorption

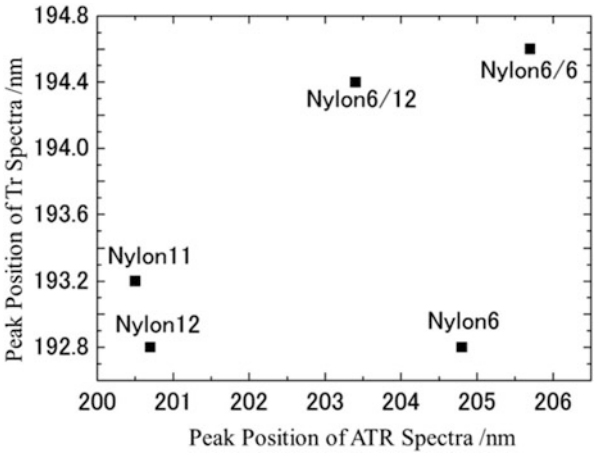

Fig. 3.19 The peak position of the band near 195 nm of the Tr spectra versus that of the band near 205 nm of the ATR-FUV spectra for the five kinds of nylons [10]

coefficients of nylon 6/6 in the literature, but it was difficult to measure it accurately. Thus, we used the spectra normalized by the intensity of 190 nm band shown in Fig. 3.18b. The band near 190 nm is observed at a shorter wavelength by ca. 10 nm in the Tr spectra compared with the corresponding band in the ATR-FUV spectra. The 150 nm band, which is clearly observed in the ATR-FUV spectra, can be seen only as a tail in the longer-wavelength side in the Tr spectra. This is because an absorption peak appears at a longer-wavelength side in an ATR-FUV spectrum than in a Tr spectrum due to the effect of real part of reflective index.

Figure 3.19 plots the absorption wavelength of the 195 nm peak of the Tr spectra versus that of the 205 nm peak of the ATR spectra. Nylon m/n (nylon 6/6, nylon 6/12) yields the band at a longer-wavelength side for both Tr and ATR spectra. In contrast, nylon m (nylon 6, nylon 11, and nylon 12) gives the peak at a shorter-wavelength side in the Tr and ATR spectra except for the ATR spectrum of nylon 6. In general, nylon m/n has stronger hydrogen bondings than nylon m. Thus, the longer-wavelength shift of the bands in both Tr and ATR spectra is in good agreement with this fact. There may be two possibilities to explain the longer-wavelength shift of the bands in nylon 6. One is that nylon 6 has a larger reflective index, yielding a larger effect of its real part. Another possibility is that there may be a stronger hydrogen bonding in the surface of nylon 6.

To perform assignments and interpretation of ATR-FUV spectra of nylons, we carried out TD-DFT calculations for monomer units of nylon 6, nylon 11, and nylon 12. Figure 3.20 shows the computed spectra with bars and their convolution. The calculated spectra yield bands near 170 and 140 nm. Taking accounts of TD-DFT providing higher transition energy and also not considering the effects of the surroundings, these bands should correspond to the observed bands near 200 and 150 nm, respectively.

The hydrogen bonding would be responsible for the longer-wavelength shift of the $\pi-\pi^*$ absorption peak of nylon 6, nylon 6/6, etc. Therefore, we assessed the effects of hydrogen bonding using the monomer, dimer, and trimer models.

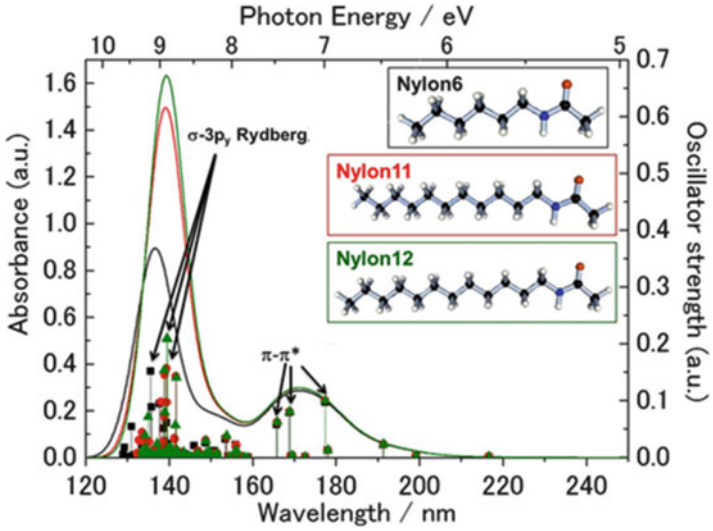

Fig. 3.20 Calculated spectra of model compounds of nylon 6, nylon 11, and nylon 12 in vacuum [10]

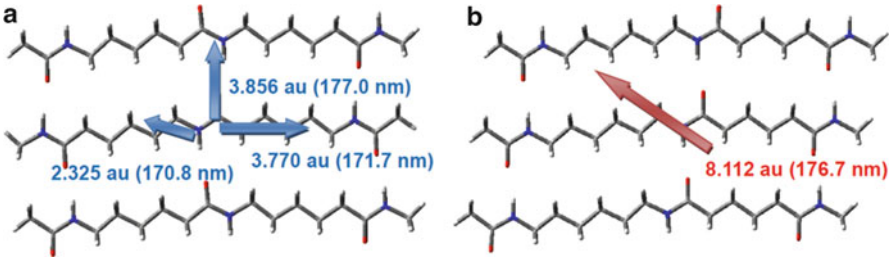

Fig. 3.21 Computational trimer models of hydrogen-bonded systems for (**a**) nylon 6 and (**b**) nylon 6/6 with the transition dipole strengths [10]

The structures of nylon 6 and nylon 6/6 trimer models are shown in Fig. 3.21 with calculated transition dipole strengths. In nylon 6 model, hydrogen bonds are perfectly constituted by inverting alternate chains in the α-form, and the progressive shear structure is adopted in the α-form of nylon 6/6. These trimer models represent the hydrogen-bonded system of unit cell regarding the π–π* transitions. The crystalline structure and its IR spectrum of nylon 6 polymorphs were studied using DFT calculations. The TD-DFT results of the π–π* and few σ-Rydberg transitions are summarized in the original paper [10].

The peak positions of the π–π* bands which are calculated by summing over the convoluted bands show a red shift as 171, 172, and 173 nm (171, 175, and 176 nm) for the monomer, dimer, and trimer models of nylon 6 (nylon 6/6), respectively. The oscillator strength is considerably distributed to many transitions in the wide range

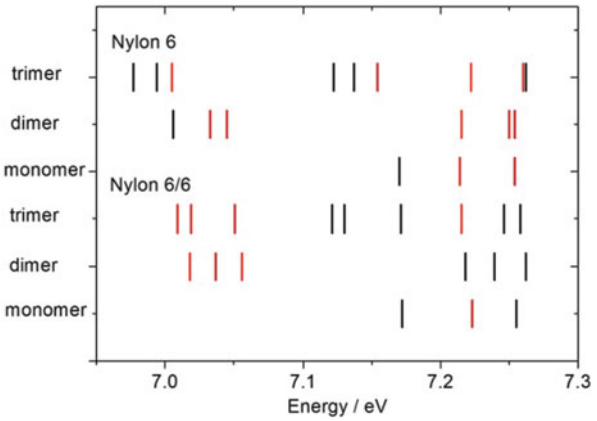

Fig. 3.22 Distribution of π–π* transitions with relatively strong ($f \geq 0.1$, *red bar*) and weak ($f < 0.1$, *black bar*) intensity calculated with three models of nylon 6 and nylon 6/6 [10]

of spectra in the dimer or trimer models via hydrogen bonding effects. The red shift (∼5 nm) almost converges at the trimer model of nylon 6/6. The difference in the calculated red shift between nylon 6 and nylon 6/6 is about 3 nm (0.12 eV) which qualitatively matches with the experimental value of 0.06 eV. In nylon 6/6 trimer model, an intense transition at 176.7 nm is enhanced as seen in Fig. 3.21, while in nylon 6 trimer model, three dominant transitions at 170.8, 171.7, and 177.0 nm of the transition dipole moments with similar dipole strength exist because of its crystal structure, namely, the inversion of alternate chain. This different transition dipole coupling scheme can be ascribed to the difference in the red shift of nylon 6 and nylon 6/6.

To interpret the difference of amide π–π* transition, the distribution of π–π* transitions is compared for nylon 6 and nylon 6/6 trimer models in Fig. 3.22. Typical MOs relevant for π–π* transition of these models are also shown in Fig. 3.23. In nylon 6/6 model, the first three transitions with relatively large oscillator strength are characterized as the transitions from/to the relatively delocalized MOs; namely, as seen in Fig. 3.23b, π and π* amplitudes are located in two or more amide groups. The intensities of the low-lying transitions are enhanced by the linear combination of the delocalized π–π* configurations, while those of higher-energy transitions are canceled out. The most intense transition at 176.7 nm with $f = 1.395$ is weighted by many configurations. Orbital energies of both occupied and unoccupied MOs are affected by about 0.08 eV via hydrogen bondings, and the delocalization over hydrogen bond is observed. On the other hand, valence π orbitals of nylon 6 are well localized in each amide group. In the dimer and trimer, these states individually generate a series of π–π* states; however, the coupling between these two series is weak. The MOs are localized even in the dimer and trimer models as shown in Fig. 3.23a. Consequently, two or three intense π–π* states exist in the dimer and trimer of nylon 6.

The calculated hydrogen bonding energies were 22.2 and 48.5 (22.7 and 49.4) kcal/mol for the dimer and trimer models of nylon 6 (nylon 6/6), respectively. These energies are not additive and some nonlinear effects exist. Though the present results

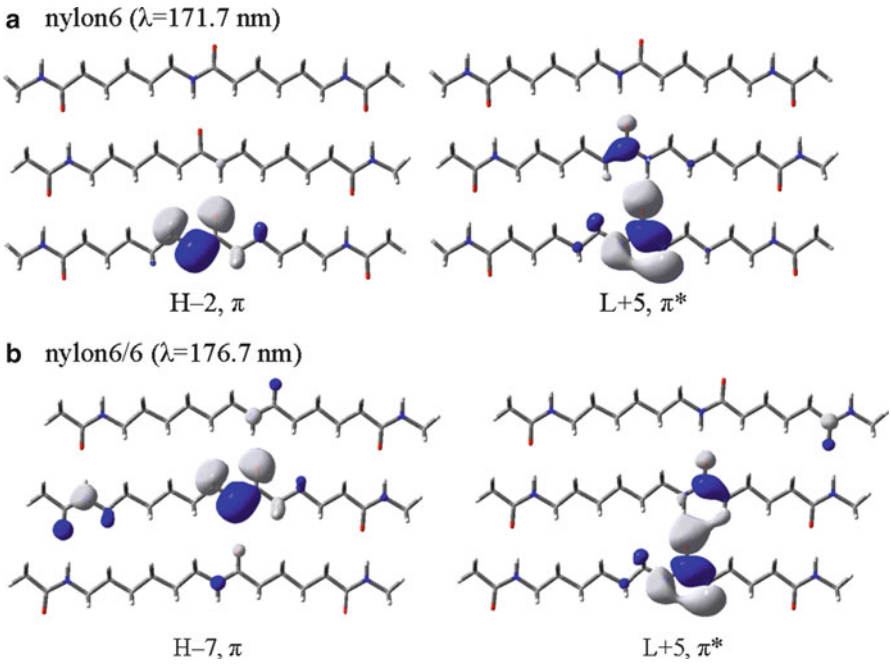

Fig. 3.23 Typical MOs relevant for the π–π* transition in the trimer model of nylon 6 and nylon 6/6 [10]. (**a**) Nylon 6 (λ = 171.7 nm). (**b**) Nylon 6/6 (λ = 176.7 nm)

agree with the experimental trend, these are not enough to explain the difference of hydrogen bonding interactions of nylon 6 and nylon 6/6; the present models only consider the local structure, and the global structure of these two polymers must be important. Within this model system, the unit cell distance was calculated as 9.7 Å for nylon 6 (C-C distance) which is in good agreement with the experimental value of 9.56 Å.

3.4 Summary

In this chapter, we overview the recent works using ATR-FUV spectroscopy applied to the molecules which have characteristic electronic transitions in the FUV region. It was demonstrated that this spectroscopy is a powerful tool for investigating the electronic structures and transitions in the FUV energy region that is not easily accessible by other spectroscopies. Using this spectroscopy with the help of quantum chemical calculations, we have extracted interesting physics and chemistry in the condensed phase, for example, the existence of confined Rydberg excited states in liquid phase, the strong valence–Rydberg coupling, and the effects of intermolecular hydrogen bondings on the excited states and polarization of the

surroundings. These interesting issues have been systematically examined by a series of studies on *n*- and branched alkanes, alcohols, ketones, amides, and nylons. These important physical insights together with robust experimental technique itself provide many possibilities for the future works in the wide field of chemistry, in particular for investigating the electronic structure and transitions characteristic to the FUV region.

References

1. M.B. Robin, *Higher Excited States of Polyatomic Molecules* (Academic Press, New York/London, 1974)
2. M. Chergui, N. Schwentner, Chem. Phys. Lett. **219**, 237–242 (1994)
3. N. Higashi, A. Ikehata, Y. Ozaki, Rev. Sci. Instrum. **78**, 103107 (2007)
4. Y. Ozaki, Y. Morisawa, N. Higashi, A. Ikehata, Appl. Spectrosc. **66**, 1–25 (2012)
5. Y. Morisawa, A. Ikehata, N. Higashi, Y. Ozaki, Chem. Phys. Lett. **476**, 205–208 (2009)
6. S. Tachibana, Y. Morisawa, A. Ikehata, N. Higashi, Y. Ozaki, Appl. Spectrosc. **65**, 221–226 (2011)
7. Y. Morisawa, S. Tachibana, M. Ehara, Y. Ozaki, J. Phys. Chem. A **116**, 11957–11964 (2012)
8. Y. Morisawa, A. Ikehata, N. Higashi, Y. Ozaki, J. Phys. Chem. A **115**, 562–568 (2011)
9. Y. Morisawa, M. Yasunaga, R. Fukuda, M. Ehara, Y. Ozaki, J. Chem. Phys. **139**, 154301 (2013)
10. Y. Morisawa, M. Yasunaga, H. Sato, R. Fukuda, M. Ehara, Y. Ozaki, J. Phys. Chem. B **118**, 11855–11861 (2014)
11. A. Ikehata, N. Higashi, Y. Ozaki, J. Chem. Phys. **129**, 234510 (2008)
12. A. Ikehata, M. Mitsuoka, Y. Morisawa, N. Kariyama, N. Higashi, Y. Ozaki, J. Phys. Chem. A **114**, 8319–8322 (2010)
13. T. Goto, A. Ikehata, Y. Morisawa, N. Higashi, Y. Ozaki, Phys. Chem. Chem. Phys. **14**, 8097–8104 (2012)
14. T. Goto, A. Ikehata, Y. Morisawa, N. Higashi, Y. Ozaki, Inorg. Chem. **51**, 10650–10656 (2012)
15. I. Tanabe, Y. Ozaki, Chem. Commun. **50**, 2117–2119 (2014)
16. I. Tanabe, T. Ryoki, Y. Ozaki, Phys. Chem. Chem. Phys. **16**, 7749–7753 (2014)
17. Y. Morisawa, N. Higashi, K. Takaba, N. Kariyama, T. Goto, A. Ikehata, Y. Ozaki, Rev. Sci. Instrum. **83**, 073103 (2012)
18. T. Goto, Y. Morisawa, N. Higashi, A. Ikehata, Y. Ozaki, Anal. Chem. **85**, 4500–4506 (2013)
19. S. Onari, Jpn. J. Appl. Phys. **9**, 227 (1970)
20. L. Serrano-Andres, M.P. Fulscher, J. Am. Chem. Soc. **120**, 10912–10920 (1998)
21. H. Nakatsuji, Chem. Phys. Lett. **59**, 362–364 (1978)
22. H. Nakatsuji, Chem. Phys. Lett. **67**, 329–333 (1979)
23. M. Ehara, J. Hasegawa, H. Nakatsuji, Chapter 39 – SAC-CI method applied to molecular spectroscopy, in *Theory and Applications of Computational Chemistry: The First 40 Years, A Volume of Technical and Historical Perspectives*, ed. by C.E. Dykstra, G. Frenking, K.S. Kim, G.E. Scuseria (Elsevier, Oxford, 2005), pp. 1099─1141
24. C. Lee, W. Yang, R.G. Parr, Phys. Rev. B **37**, 785–789 (1988)
25. A.D. Becke, J. Chem. Phys. **98**, 5648–5652 (1993)
26. C. Adamo, V. Barone, J. Chem. Phys. **108**, 664–675 (1998)
27. H. Iikura, T. Tsuneda, T. Yanai, K. Hirao, J. Chem. Phys. **115**, 3540–3544 (2001)
28. T. Yanai, D.P. Tew, N.C. Handy, Chem. Phys. Lett. **91**, 51–57 (2004)
29. T.H. Dunning Jr., J. Chem. Phys. **90**, 1007–1023 (1989)
30. J. Tomasi, B. Mennucci, R. Cammi, Chem. Rev. **105**, 2999–3094 (2005)
31. R. Cammi, B. Mennucci, J. Tomasi, J. Phys. Chem. A **104**, 5631–5637 (2000)
32. M. Cossi, V.J. Barone, Chem. Phys. **115**, 4708–4717 (2001)

33. R. Improta, V. Barone, G. Scalmani, M.J. Frisch, J. Chem. Phys. **125**, 054103 (2006)
34. M. Caricato, B. Mennucci, J. Tomasi, F. Ingrosso, R. Cammi, S. Corni, G. Scalmani, J. Chem. Phys. **124**, 124520 (2006)
35. H. Nakatsuji, Chem. Phys. **75**, 425–441 (1983)
36. R. Fukuda, H. Nakatsuji, J. Chem. Phys. **128**, 094105 (2008)
37. R. Cammi, R. Fukuda, M. Ehara, H. Nakatsuji, J. Chem. Phys. **133**, 024104 (2010)
38. R. Fukuda, M. Ehara, H. Nakatsuji, R. Cammi, J. Chem. Phys. **134**, 104109 (2011)
39. M.J. Frisch, G.W. Trucks, H.B. Schlegel, G.E. Scuseria, M.A. Robb, J.R. Cheeseman, G. Scalmani, V. Barone, B. Mennucci, G.A. Petersson, H. Nakatsuji, M. Caricato, X. Li, H.P. Hratchian, A.F. Izmaylov, J. Bloino, G. Zheng, J.L. Sonnenberg, M. Hada, M. Ehara, K. Toyota, R. Fukuda, J. Hasegawa, M. Ishida, T. Nakajima, Y. Honda, O. Kitao, H. Nakai, T. Vreven, J.A. Montgomery Jr., J.E. Peralta, F. Ogliaro, M. Bearpark, J.J. Heyd, E. Brothers, K.N. Kudin, V.N. Staroverov, T. Keith, R. Kobayashi, J. Normand, K. Raghavachari, A. Rendell, J.C. Burant, S.S. Iyengar, J. Tomasi, M. Cossi, N. Rega, J.M. Millam, M. Klene, J.E. Knox, J.B. Cross, V. Bakken, C. Adamo, J. Jaramillo, R. Gomperts, R.E. Stratmann, O. Yazyev, A.J. Austin, R. Cammi, C. Pomelli, J.W. Ochterski, R.L. Martin, K. Morokuma, V.G. Zakrzewski, G.A. Voth, P. Salvador, J.J. Dannenberg, S. Dapprich, A.D. Daniels, O. Farkas, J.B. Foresman, J.V. Ortiz, J. Cioslowski, D.J. Fox, *Gaussian09 Rev. B.01* (Gaussian Inc., Wallingford, 2010)
40. B.-M. Cheng, M. Bahou, W.-C. Chen, C.-H. Yui, Y.-P. Lee, L.C. Lee, J. Chem. Phys. **117**, 1633–1640 (2002)
41. M. Nobre, A. Fernandes, A. Ferreiru da Silva, R. Antunes, D. Almeida, V. Kokhan, S.V. Hoffmann, N.J. Mason, S. Eden, P. Limao-Vieira, Phys. Chem. Chem. Phys. **10**, 550–560 (2008)
42. I. Renge, J. Phys. Chem. A **113**, 10678–10686 (2009)

Chapter 4
Water Research by Far-Ultraviolet Spectroscopy

Takeyoshi Goto and Akifumi Ikehata

Abstract Far-ultraviolet (FUV) absorption spectroscopy provides molecular information about valence electronic transitions: σ, n, and π electron excitation and charge transfer (CT). FUV spectral measurements of liquid water and aqueous solutions had been limited, because the absorptivity of liquid water is very intense (absorptivity 10^5 cm^{-1} at 150 nm). We have developed an attenuated total reflection (ATR)-type FUV spectrophotometer in order to measure FUV spectra of liquid water and aqueous solutions. The ATR–FUV spectroscopy reveals the features of the valence electronic transition of liquid water. This chapter introduces a brief overview of the first electronic transition $\left(\tilde{A} \leftarrow \tilde{X}\right)$ of liquid water (Sect. 4.1) and the FUV spectral analyses (140–300 nm) of various aqueous solutions including how the hydrogen bonding interaction of liquid water affects the $\tilde{A} \leftarrow \tilde{X}$ transition of water molecules (Sect. 4.1); how the $\tilde{A} \leftarrow \tilde{X}$ bands of water molecules in Groups I, II, XIII, and lanthanoid (Ln^{3+}) electrolyte solutions are associated with the hydration states of the metal cations (Sects. 4.2 and 4.3) how the protonation states of amino acids in aqueous solutions affect the electronic transition of the amino acids (Sect. 4.4) and the analysis of O_3 pulse-photolytic reaction in aqueous solution using a nanosecond pump-probe transient FUV spectrophotometer (Sect. 4.5).

Keywords Far ultraviolet (FUV) • Attenuated total reflection (ATR) • Liquid water • Hydrogen bond • Hydration • Electrolyte solution • Amino acids • Aqueous ozone photolysis

T. Goto
Department of Chemistry, School of Science and Technology, Kwansei Gakuin University, 2-1 Gakuen, Sanda 669-1337, Japan

A. Ikehata (✉)
National Food Research Institute, National Agriculture and Food Research Organization, (NARO), 2-1-12 Kannondai, Tsukuba, Ibaraki 305-8642, Japan
e-mail: ikehata@affrc.go.jp

Y. Ozaki, S. Kawata (eds.), *Far- and Deep-Ultraviolet Spectroscopy*,
DOI 10.1007/978-4-431-55549-0_4

4.1 First Electronic Transition of Liquid Water

Water is a colorless medium; it does not absorb visible light, while infrared (IR) and far-ultraviolet (FUV) light is strongly absorbed. Figure 4.1 shows the absorption spectrum of liquid water from the IR to the FUV region calculated from literature data of molar absorptivities [1] by assuming a path length of 100 nm. In the IR region, two major peaks appear around 2,900 nm (3,400 cm^{-1}) and 6,200 nm (1,650 cm^{-1}) assigned to H–O–H stretching and bending modes, respectively. In the near-infrared (NIR) region, relatively small absorptions due to the overtones and combination modes of the H–O–H vibrations are observed. As mentioned at the beginning, the ultraviolet–visible (UV-vis) region does not show significant absorption. In the FUV region, a strong absorption band arises where the wavelength is shorter than 190 nm. This is the first electronic transition of water, and the absorptivity of this band is stronger by several orders of magnitude relative to the H–O–H stretching band in the IR region. For decades, it has been known that the absorption edge of this band (around 190 nm) shifts to a shorter wavelength with the increase in the strength of hydrogen bonding [2–5]. This band is simply called the $\tilde{A} \leftarrow \tilde{X}$ because it is due to the lowest electronic transition. Specifically, this band is assigned to the transitions from the $1b_1$ (nonbonding orbital) to the $4a_1$ (antibonding σ* orbital) and partly to the 3s orbitals (Fig. 4.2) [6, 7]. Since the former $1b_1 \rightarrow 4a_1$ is caused by a transition to valence band of the oxygen atom, the $\tilde{A} \leftarrow \tilde{X}$ absorption of water has an aspect of an excitonic transition [8]. In condensed phases, the lone-pair valence band edge approaches the conduction band. Hahn et al. clarified that the average electron-hole distance is longer in the condensed phase than in

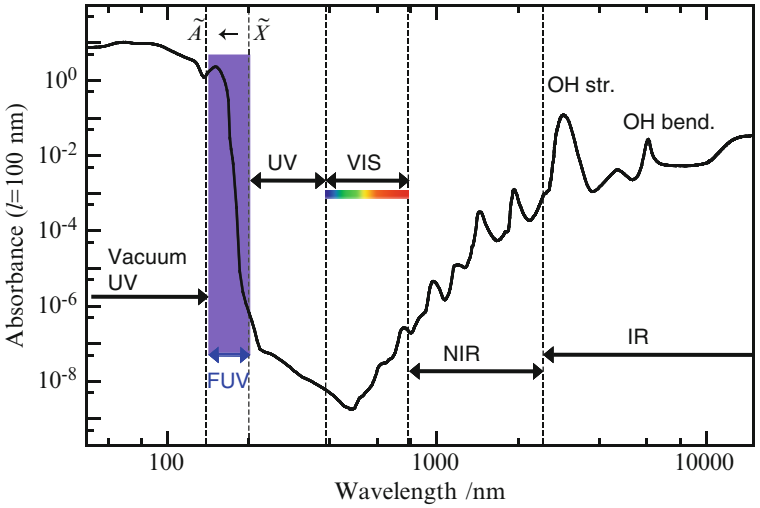

Fig. 4.1 The absorbance spectrum of water from the IR to FUV region, assuming a path length of 100 nm (From Ref. [1])

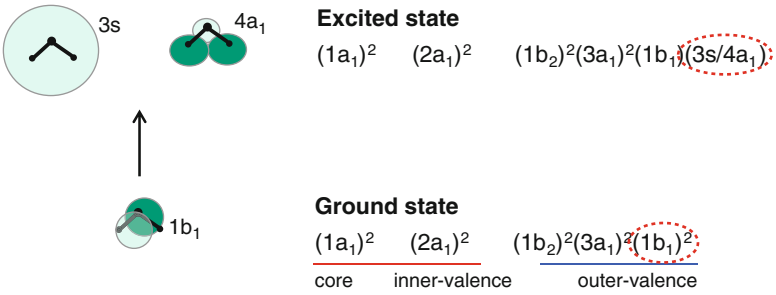

Fig. 4.2 Molecular orbitals of water molecule in the ground state and the first excited states

an isolated water molecule by theoretical calculations [9]. This result supports the experimentally observed blueshifts of $\tilde{A} \leftarrow \tilde{X}$. The latter $1b_1 \rightarrow 3s$ is a transition to the Rydberg series, often called molecular orbital (MO) Rydbergization [6, 10]. The radii of the electron orbitals of Rydberg states are several to several tens of times larger than those of the corresponding ground state, so that the Rydberg states in condensed phases are sensitive to the effects of surrounding molecules. The obvious blueshift that was experimentally observed for matrix-isolated water with a decrease in the size of the matrix constituents represented a proof for Rydbergization [11]. Actually the excited states of valence and Rydberg orbitals are complementary by the O–H distances. When the O–H distance becomes shorter (i.e., in condensed phase), Rydberg nature of the excited molecular orbital becomes dominant [10].

From the peak shifts of the $\tilde{A} \leftarrow \tilde{X}$ band by phase transitions of water, one can easily understand the fact that the first electronic transition of water varies with changes in hydrogen bonding and molecular density. The band maxima of $\tilde{A} \leftarrow \tilde{X}$ of water are observed at 168 nm (7.4 eV) [12, 13], 148–150 (8.4–8.3 eV) [14–18], and 144 nm (8.6 eV) [18–20] for the gas, liquid, and solid states, respectively. However, the $\tilde{A} \leftarrow \tilde{X}$ absorption of water is considerably stronger than the IR absorptions corresponding to the fundamental H–O–H stretching vibrations as shown in Fig. 4.1, and this fact makes it difficult to measure the band maxima of the $\tilde{A} \leftarrow \tilde{X}$ absorption of liquid water and aqueous solutions by transmittance spectroscopy. In fact, the positions of the band maxima of liquid water and ice mentioned in the foregoing researches [11, 15] were determined by regular reflection measurements. As for liquid water and aqueous solutions, many other scientists had to observe the band tail over 190 nm (below 6.5 eV) by using transmittance cells and have discussed the onset of the absorption [2–5, 8]. A redshift occurs at the onset of the $\tilde{A} \leftarrow \tilde{X}$ absorption with an increase of temperature [8, 21, 22]. This phenomenon has been discussed in the context of Urbach rule [23], which is based on the characteristic behavior of phonon-broadened absorption bands. Williams et al. compared the energy gap for the $\tilde{A} \leftarrow \tilde{X}$ band of liquid water with that of the band of isolated water from a viewpoint of an amorphous semiconductor on the basis of temperature dependence measurements of UV spectra [8]. The studies conducted before 1998 were adequately reviewed by

Bernas [22, 24]. Considerable computational efforts were also made recently [25–32]. However, experimental study of the $\tilde{A} \leftarrow \tilde{X}$ absorption of liquid water had not been fully explored due to the difficulty in directly observing the transmittance FUV spectra of water. The situation has dramatically changed by the development of ATR–FUV spectroscopy [33]. One can easily observe the entire shape of the $\tilde{A} \leftarrow \tilde{X}$ absorption band of water because the evanescent wave with the ATR geometry reduces a path length in the sample on the reflection element less than 100 nm. Since the $\tilde{A} \leftarrow \tilde{X}$ band moves to a shorter wavelength with the increase in the strength of hydrogen bonding, it is expected that the $\tilde{A} \leftarrow \tilde{X}$ band of liquid water continuously shifts with temperature and hydration by ions, inorganic molecules, and organic molecules. The use of $\tilde{A} \leftarrow \tilde{X}$ band by ATR–FUV spectroscopy is now becoming a method to explore the hydrogen bonding and hydration of water and also a method in quantitative and qualitative analysis of aqueous solutions [34].

The origin of the low-lying electronic transition band of water had not been conclusively established before the development of the ATR–FUV because the observation of the $\tilde{A} \leftarrow \tilde{X}$ band tail was the only one way to know the electronic property. To make sure whether the shift of the $\tilde{A} \leftarrow \tilde{X}$ band tail by heating is caused by broadening or energy shift, the ATR–FUV was first used for studying temperature dependence on the $\tilde{A} \leftarrow \tilde{X}$ transition by employing a single-reflection ATR accessory with a sapphire crystal [14]. The ATR–FUV spectra of light water (H_2O) and heavy water (D_2O) measured at different temperatures (10–70 °C) are shown in Fig. 4.3. The maximum absorptions for all the spectra of D_2O lie at higher energies than those for the spectra of H_2O at the same temperature. The

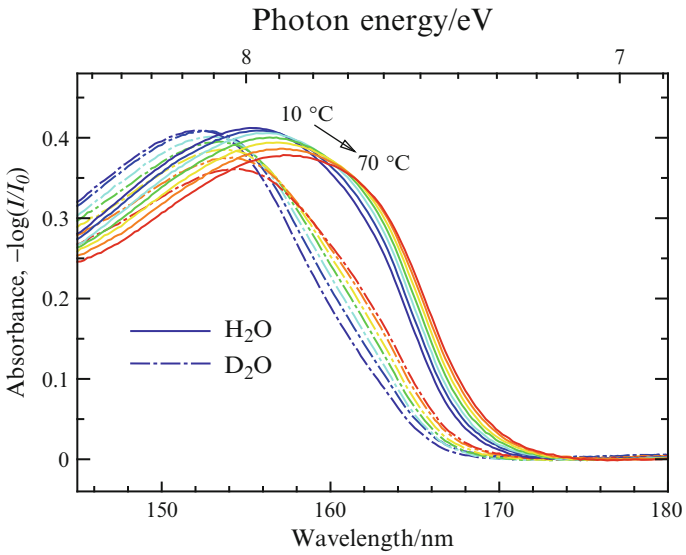

Fig. 4.3 ATR–FUV spectra (ATR absorbance) of H_2O and D_2O at different temperatures (From Ref. [14])

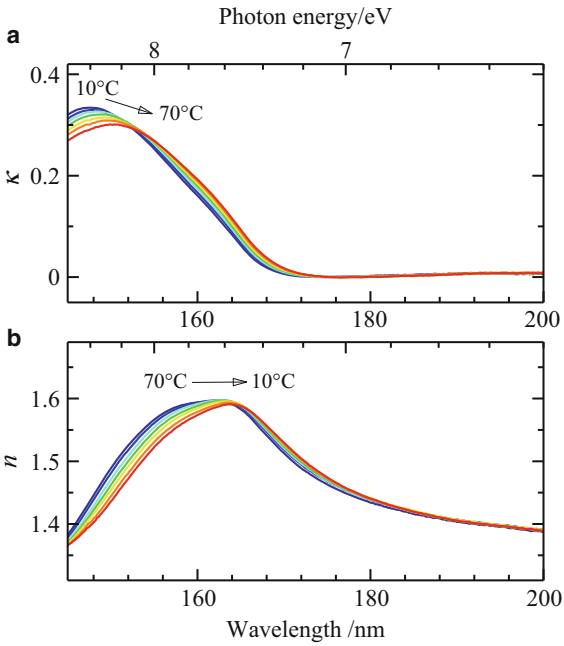

Fig. 4.4 The absorption index κ (**a**) and the refractive indices n (**b**) of H_2O converted from the ATR–FUV spectra shown in Fig. 4.3 by the Kramers–Kronig transformation (From Ref. [14])

deviation arises from the difference in the vibrational zero-point energies between H_2O and D_2O [17]. The $\tilde{A} \leftarrow \tilde{X}$ peaks showmarked redshifts on heating, and the peak intensities decrease. However, the ATR spectra of water are not identical to its transmission spectra. Since the ATR technique is based upon a reflection method, the spectra involve shifts not only in peak intensity but also in the wavelength. Kramers–Kronig transformation (KKT) and Fresnel formulas are available to separate the contributions of the absorption and refractive indices. Figure 4.4a, b displays the calculated results of absorption indices, κ, and refractive indices, n, of H_2O, respectively [14]. The indices correspond to the real and imaginary parts of the complex refractive index as follows: $\tilde{n} = n + i\kappa$. It can be seen that every spectrum of the optical indices shifts to the low-energy side on heating. The peak wavelengths of the absorption indices are plotted against temperature in Fig. 4.5. The best-fit linear functions to the data are indicated by solid lines. The band maximum of H_2O linearly shifts from 8.4 to 8.26 eV on increasing the temperature from 10 to 70 °C, and consequently, the slope is -2.4×10^{-3} eV/K. A prediction by using an extrapolation fit of a Gaussian profile to the experimentally observed UV tails shows a smaller slope of -1.86×10^{-3} [5]. The slope for D_2O, -2.1×10^{-3} eV/K, is thought to be the same as that for H_2O. This result suggests that with regard to the thermal shifts of the band peaks, the ATR–FUV spectra are relatively in good agreement with the transmittance spectra. On the other hand, the bandwidth of the $\tilde{A} \leftarrow \tilde{X}$ band in the absorption indices, κ, becomes very slightly narrow with an increase in the temperature. Therefore, it is revealed that the shift of the tail of $\tilde{A} \leftarrow \tilde{X}$ absorption observed in the UV spectra is dominated by the energy shift

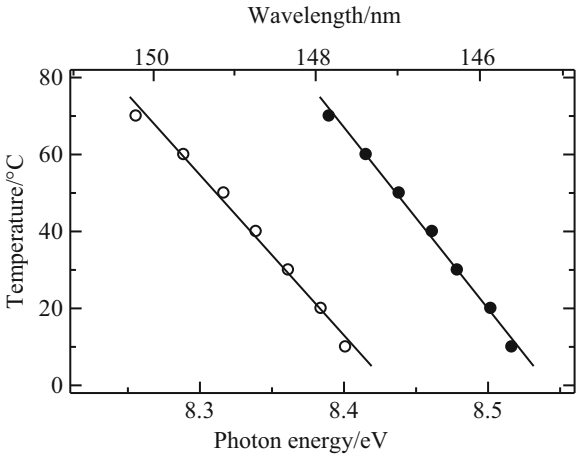

Fig. 4.5 Plots of the peak positions of the $\tilde{A} \leftarrow \tilde{X}$ band for H_2O (*open circles*) and D_2O (*filled circles*) against temperature (From Ref. [14])

of the $\tilde{A} \leftarrow \tilde{X}$ transition. In this way, systematic measurements of the ATR–FUV spectra of water and the analysis of KKT reveal that the $\tilde{A} \leftarrow \tilde{X}$ band of liquid water shifts to lower energy on heating.

4.2 Cationic Effects on the $\tilde{A} \leftarrow \tilde{X}$ Transition of Liquid Water: Group I, II, and XIII Cations

Because the $\tilde{A} \leftarrow \tilde{X}$ transition of liquid water involves nonbonding electrons of an oxygen atom of a water molecule [6], the $\tilde{A} \leftarrow \tilde{X}$ transition of liquid water is sensitively affected by the hydrogen bonding state of water molecules. The addition of salts in liquid water induces the rearrangement of the hydrogen bonding structure, and the strength of water molecule structuring by an ion is characterized with the charge and the size of the ion [35, 36]. The high-charge-density ions electrostatically bind to the surrounding water molecules and form the first and even second coordination spheres [37]. The hydration energy of an ion expresses the change of the electric energy induced by the insertion of an ion into water solvent. Hydration of ions has been extensively studied from the macroscopic properties (viscosity and entropy of ion solvation) [38, 39] and the molecular structure with X-ray [40], nuclear magnetic resonance (NMR) [41], and vibrational [42] spectroscopy. Herein, ATR–FUV spectroscopy provides new insights into the hydration of cations from the perspective of the electronic transition of water molecules [43, 44].

The $\tilde{A} \leftarrow \tilde{X}$ transition energy of liquid water increases with the addition of salts, and the increase in the energy linearly correlates with the thermodynamic solvation energies of the cations [43, 44]. Figure 4.6 shows the ATR–FUV spectra of 1 M Group I metal nitrate solutions and pure water at 25 °C. The same counter-anion, nitrate, was employed for all the electrolyte solutions to negate the effect of counter-

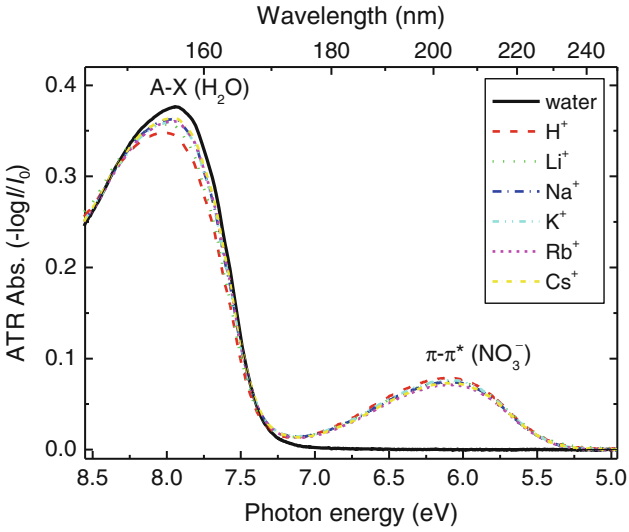

Fig. 4.6 ATR–FUV spectra of aqueous solutions of 1 M alkali metal nitrates measured at 25 °C (From Ref. [43])

anions on the measured spectra. The absorption bands around 6.1 eV (203 nm) and 8.0 eV (155 nm) are assigned to the $\pi - \pi^*$ transition of NO_3^- and the $\tilde{A} \leftarrow \tilde{X}$ transition of water molecules, respectively. The $\tilde{A} \leftarrow \tilde{X}$ bands of the electrolyte solutions are slightly blueshifted, and their absorbances are smaller relative to the pure water band. The $\tilde{A} \leftarrow \tilde{X}$ transition energies of the electrolyte solutions become higher as the cation sizes are smaller in each group. Figure 4.7 shows plots of the barycenter energies of the $\tilde{A} \leftarrow \tilde{X}$ bands of the Group I, II, and XIII metal nitrate electrolyte solutions (1 M) versus the Gibbs hydration energies of the cations (ΔG_{hyd}). The ΔG_{hyd} values were taken from the reference [45]. Because the concentrations of the nitrate anion are different among the Groups I, II, and XIII, the correlation can be examined within each group. The higher-charge-density cations which hold the larger negative values of ΔG_{hyd} show the higher $\tilde{A} \leftarrow \tilde{X}$ transition energies of the water molecules for each group. This linear relation indicates that the hydration of the cations stabilizes the ground-state electronic energies of the water molecules, resulting in the increase in the $\tilde{A} \leftarrow \tilde{X}$ transition energies of the electrolyte solutions. The correlations of the extremely high-charge-density cations, H^+, Li^+, and Be^{2+}, deviate from the linear relations. This deviation is probably attributed to the energy differences in the electronic excited state of the water molecules hydrating different cations, because the thermodynamic hydration energy of a cation is associated with the ground-state electronic energy. The electronic state calculation of the hexagonal ice water shows that the spatial distribution of the excited electrons is extensively distributed and sensitive to the neighboring molecular environment [9]. Therefore, the extremely

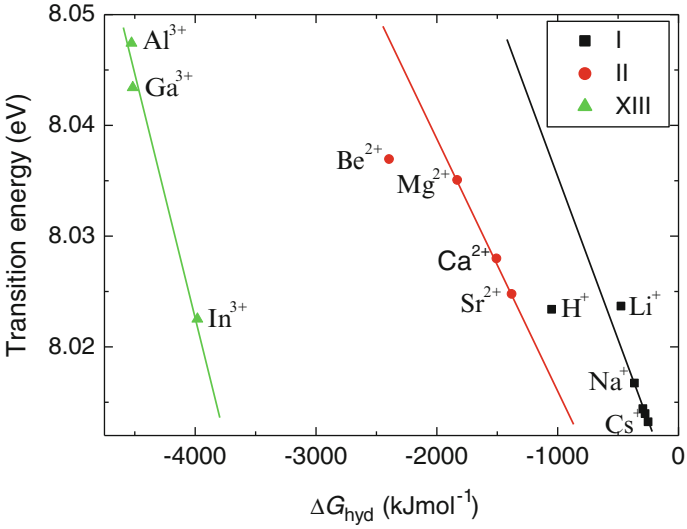

Fig. 4.7 Plot of the $\tilde{A} \leftarrow \tilde{X}$ transition energies of Group I, II, and XIII electrolyte solutions versus the Gibbs energies of hydration (ΔG_{hyd}) corresponding the cations. The ΔG_{hyd} values were taken from the reference [45] (From Ref. [43])

high-charge-density cations more strongly perturb the molecular orbital (MO) transformation of a water molecule accompanied with the electronic transition than the low-charge-density cations.

The electronic state calculations of water and water–cation complexes reveal how the electron donation from water molecules to a metal cation affects the $\tilde{A} \leftarrow \tilde{X}$ transition of the water molecules [43]. The time-dependent density-functional theory (TDDFT) calculations of the $\tilde{A} \leftarrow \tilde{X}$ transitions of the monomer and the dimer of water molecules (*mono*-H_2O and *di*-H_2O) and the water-monovalent cation complexes (H_2O-M^+) using the M06-2X functional with the 6-31++G** basis set show a clear dependence of the $\tilde{A} \leftarrow \tilde{X}$ transition energy on distance between the electron donor (nonbonding electrons of an oxygen atom) and the acceptor (M^+ or a hydrogen atom of a water molecule) ($r_{\mathrm{D-A}}$) as shown in Fig. 4.8. The longest and shortest $r_{\mathrm{D-A}}$ distances of each cation complex correspond with the inner and outer positions of the first hydration shell edges of the cations. As $r_{\mathrm{D-A}}$ is shorter, the $\tilde{A} \leftarrow \tilde{X}$ transition energies of all the cation complexes and *di*-H_2O (b) become larger than that of the water monomer. The *di*-H_2O (a) transition appears below the *mono*-H_2O. But the oscillator strength of the *di*-H_2O (a) transition gets smaller as $r_{\mathrm{D-A}}$ is shorter, whereas that of the *di*-H_2O (b) transition doesn't change. From the results of these TDDFT calculations, the blueshifts of the $\tilde{A} \leftarrow \tilde{X}$ bands of the electrolyte solutions can be elucidated as the following: (1) The electron donor–acceptor interaction between the cations and the water molecules induces deformation of the MO of the water molecules, and (2) a closed-packing hydrogen bonding structure of the water molecules caused by the electric fields of the cations generates the stronger

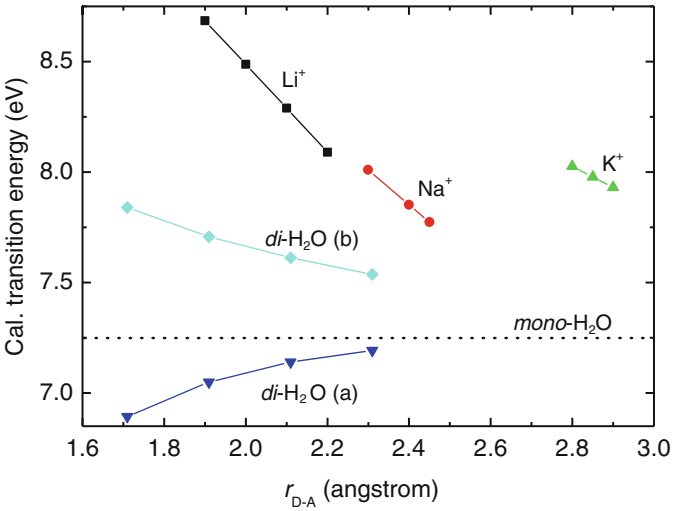

Fig. 4.8 The $\tilde{A} \leftarrow \tilde{X}$ transition energies for the H_2O dimer (*di*-H_2O (*a*) and *di*-H_2O (*b*)), H_2O-Li^+, H_2O-Na^+, and H_2O-K^+ complexes calculated by M06-2X/6-31++G** at various $r_{D\text{-}A}$ distances. The longest and shortest r_{D-A} distances correspond with the lengths between the inner and outer positions of the hydration shell edges of each cation. The *broken line* shows the $\tilde{A} \leftarrow \tilde{X}$ transition energy of the H_2O monomer (From Ref. [43])

hydrogen bond interaction among the water molecules. Consequently, the $\tilde{A} \leftarrow \tilde{X}$ bands of the high-charge-density cation electrolyte solutions are more blueshifted than those of the low-charge-density electrolyte solutions and pure water. Also, the calculated $\tilde{A} \leftarrow \tilde{X}$ transition energy spread between the longest and shortest r_{D-A} distances of the H_2O-M^+ complexes linearly correlates with the full with at half maximums of the $\tilde{A} \leftarrow \tilde{X}$ bands of the electrolyte solutions measured with ATR–FUV spectroscopy as shown in Fig. 4.9. Therefore, the $\tilde{A} \leftarrow \tilde{X}$ bandwidths of the electrolyte solutions directly exhibit how the cation centers are hydrated by the solvent water molecules.

4.3 Cationic Effects on the $\tilde{A} \leftarrow \tilde{X}$ Transition of Liquid Water: Lanthanoid Cations

Physicochemical properties of lanthanoid cation (Ln^{3+}) hydrates depend on the 4f electron occupation state of the Ln^{3+} cations in the electronic [46, 47] and electric aspects [48]. Accordingly, those vary across the 4f period in either monotonous or inmonotonous trend. As the nuclear charge (Z) increases, the coordination number of Ln^{3+} hydrates decreases inmonotonously from 9 to 8; specifically, the amount of change varies around Eu^{3+} and Gd^{3+} [48–50]. The Ln–OH_2 bond distances

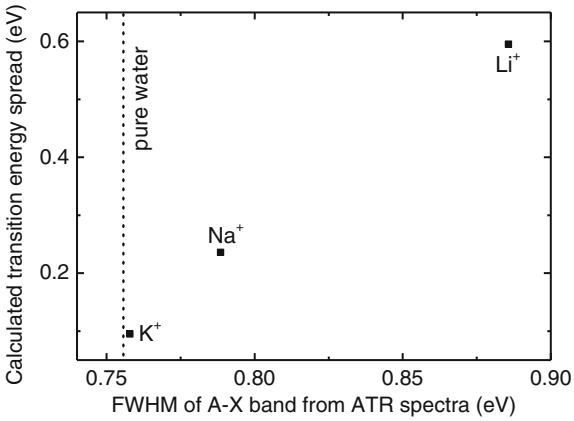

Fig. 4.9 Plot of the calculated $\tilde{A} \leftarrow \tilde{X}$ transition energy spreads for the widths of hydration shells versus the full width at half maximums (FWHM) of the $\tilde{A} \leftarrow \tilde{X}$ bands measured with ATR–FUV spectroscopy. The *broken line* shows the FWHM of the $\tilde{A} \leftarrow \tilde{X}$ band of pure water (From Ref. [43])

monotonously decrease [51–53], and the Gibbs energies of hydration of Ln^{3+} cations monotonously increase [45, 54], as the Z values become large. The variation of the lanthanoid liquid–liquid extraction with Z shows a characteristic tetrad trend [55]. The tetrad trends of Ln^{3+} hydrates are known as the tetrad effects [46, 47]. Herein, ATR–FUV spectroscopy reveals that the $\tilde{A} \leftarrow \tilde{X}$ transition energies of the Ln^{3+} electrolyte solutions show a tetrad trend across the 4f period, which accounts for the ligand field splitting (LFS) of the 4f electronic states of the Ln^{3+} hydrates [56].

The $\tilde{A} \leftarrow \tilde{X}$ transition energies of the Ln^{3+} electrolyte solutions are higher than that of pure water. Figure 4.10 shows the plots of the $\tilde{A} \leftarrow \tilde{X}$ transition energies of the Ln^{3+} and the Group XIII nitrate electrolyte solutions (1 M) versus the Gibbs energies of hydration (ΔG_{hyd}) of each cation. The ΔG_{hyd} values were taken from the reference [45]. Because the same counter-anion (nitrate) for all the salts was employed, the spectral differences are attributed to the cation effects. From the linear correlation, the hydration energies of the Group XIII cations account for the decrease in the electronic energies of the ground state of the water molecules and the increases in the $\tilde{A} \leftarrow \tilde{X}$ transition energies of the Group XIII electrolyte solutions. In contrast, the $\tilde{A} \leftarrow \tilde{X}$ transition energies of all the Ln^{3+} electrolyte solutions including the noble gas-like cation La^{3+} ([Xe]$4f^0$) do not have a linear relation with ΔG_{hyd}. Because the cations in each Group I, II, or XIII (s- and p-block metals) exhibit a linear relation as shown in the previous section, the deviation from the linearity for the Ln^{3+} cations is associated with the 4f electronic states.

The 4f electron occupation state can characterize the $\tilde{A} \leftarrow \tilde{X}$ transition energies of the Ln^{3+} electrolyte solutions in a tetrad manner; that is, there are four local trends in the 4f series. Figure 4.11 shows a plot of the $\tilde{A} \leftarrow \tilde{X}$ transition energies (filled squares, left axis) and ΔG_{hyd} (filled circles, right axis) versus the number of 4f electrons of the Ln^{3+} cations. For the half occupation period of the 4f electrons, the $\tilde{A} \leftarrow \tilde{X}$ transition energies decrease from La^{3+} ($4f^0$, 8.0375 eV) to Nd^{3+} ($4f^3$, 8.0277 eV) and increase from Sm^{3+} ($4f^5$, 8.0279 eV) to Gd^{3+} ($4f^7$, 8.0374 eV). For the complete occupation period, there are two local minima at Dy^{3+} ($4f^9$,

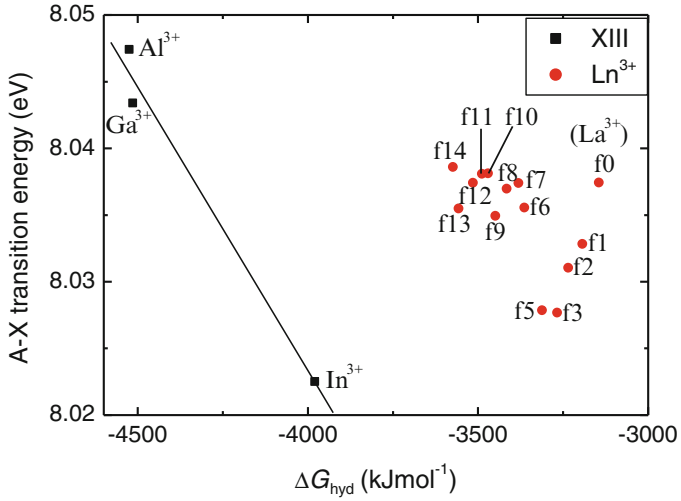

Fig. 4.10 Plots of the $\tilde{A} \leftarrow \tilde{X}$ transition energies of Ln^{3+} and Group XIII electrolyte solutions versus the Gibbs energies of hydration (ΔG_{hyd}) for the corresponding cations. The ΔG_{hyd} values were taken from the reference [45] (From Ref. [56])

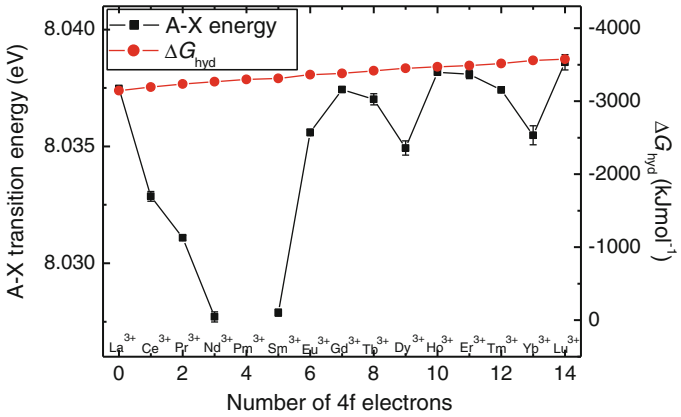

Fig. 4.11 Plot of the $\tilde{A} \leftarrow \tilde{X}$ transition energies (*filled squares*, *left axis*) and ΔG_{hyd} (*filled circles*, *right axis*) versus the number of 4f electrons of the Ln^{3+} cations. The ΔG_{hyd} values were taken from the reference [45] (From Ref. [56])

8.0349 eV) and Yb^{3+} ($4f^{13}$, 8.0355 eV). The $\tilde{A} \leftarrow \tilde{X}$ transition energies at the nodes (La^{3+}, Gd^{3+}, Ho^{3+}, and Lu^{3+}) slightly increase as Z increases from La^{3+} (8.0374 eV) to Gd^{3+} (8.0374 eV) and Ho^{3+} (8.0382 eV) to Lu^{3+} (8.0386 eV). Consequently, the primary trend of the $\tilde{A} \leftarrow \tilde{X}$ transition energies of the Ln^{3+} electrolyte solutions is a linear relation with the hydration energies of the Ln^{3+} cations, and that is the same as the Group I, II, and XIII cations.

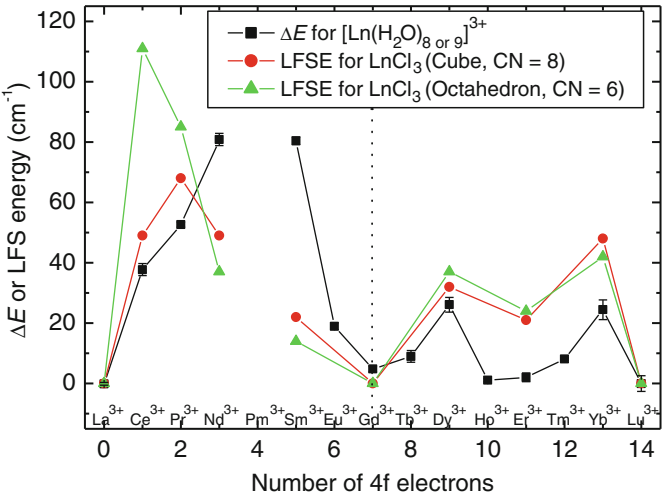

Fig. 4.12 The differences (ΔE, *filled squares*) between the measured $\tilde{A} \leftarrow \tilde{X}$ transition energies and the line between La^{3+} and Lu^{3+} and the LFS energy of the $LnCl_3$ crystals at the vertices of a cube (CN = 8, *filled circles*) and an octahedron (CN = 6, *filled triangles*) from Ref. [58] (From Ref. [56])

The difference of the $\tilde{A} \leftarrow \tilde{X}$ transition energy of each Ln^{3+} from the line, which goes through the nodes, (ΔE), more clearly characterizes the tetrad trend deviation. Figure 4.12 shows the plots of ΔE across the 4f period. For the half occupation period, the ΔE value increases from La^{3+} to Nd^{3+} (9.98×10^{-3} eV, 80.5 cm^{-1}) and decreases from Sm^{3+} (9.97×10^{-3} eV, 80.4 cm^{-1}) to Gd^{3+} (5.99×10^{-4} eV, 4.83 cm^{-1}). For the complete occupation period, the ΔE shows the local maxima at Dy^{3+} (3.24×10^{-3} eV, 26.1 cm^{-1}) and Yb^{3+} (3.03×10^{-3} eV, 24.5 cm^{-1}) and the local minimum between Ho^{3+} and Er^{3+}.

The tetrad trend of ΔE across the 4f period is ascribed to the LFS effect on the inner 4f electrons of the Ln^{3+} cations. The observed ΔE values are the comparable order of magnitude with the splitting ground-state multiplets of Ln^{3+} complexes induced by ligand fields in the range from 0 to 400 cm^{-1} [57–64]. From the electronic state calculation with INDO/S-CI method, the energy split is from 0 to 263 cm^{-1} for $[Pr(H_2O)_9]^{3+}$ complex (D_{3h} symmetry) and from 0 to 196 cm^{-1} for $[Tm(H_2O)_8]^{3+}$ complex (D_{2d} symmetry) [64]. Also, the observed ΔE profile along the 4f period is similar with the LFS profile of the ground-state multiplets of the cube geometry (coordination number (CN) = 8) rather than the octahedron geometry (CN = 6) of the Ln^{3+} halides crystals. Yatsimirskii et al. calculated the ground-state multiplets of the Ln^{3+} halide crystals [14]. The calculated LFS energies for the cube (filled circle) and the octahedron (filled triangle) geometry of a $LnCl_3$ crystal by Yatsimirskii et al. are also plotted in Fig. 4.12. The molecular geometry of Ln^{3+} hydrates in aqueous solution is tricapped trigonal prism (CN = 9) for light elements and square antiprism (CN = 8) for heavy elements [50–52, 65]. The LFS profiles

for those geometries of the Ln^{3+} hydrates are not known at this time. However, the similarity of the ΔE profile with the LFS profile of the cube (CN = 8) geometry rather than octahedron (CN = 6) of the Ln^{3+} halides indicates that the tetrad trend of ΔE results from the LFS of the ground-state multiplets of the Ln^{3+} hydrates.

4.4 Electronic Transitions of Amino Acids in Aqueous Solutions

Amino acids are simple building-block subunits of proteins, and their side chains determine the higher-order structures and the chemical functions of proteins. The FUV spectral measurements of amino acids especially in gas and solution states are very challenging, because the vapor pressures of amino acids are quite low [66], and the photoabsorption of solvents including water is very intense [7, 14]. Just a few FUV absorption spectra of amino acids were reported in the thin solid films [67, 68], the gas states [69, 70], and the solution states [71, 72]. Actually, the FUV spectra of amino acids in aqueous solutions can be easily obtained by using the ATR method. This section will introduce the FUV spectra of 20 naturally occurring amino acids in pure water, acidic, and basic aqueous solutions in the region from 145 to 300 nm [73].

Glycine (Gly) is the simplest molecule in the 20 amino acids, and the FUV spectrum of Gly is the most appropriate to show the electronic transition of the backbone structure of amino acids. The primary chromophore of Gly is the carboxyl group. Figure 4.13 shows the FUV spectra of 2 M Gly in 1.81 M H_2SO_4, pure water, and 3.36 M NaOH aqueous solutions. Because the pK_{a1} and pK_{a2} values of Gly are 2.34 and 9.60, the protonation states are ammonium carboxylic acid, zwitterion, and aminocarboxylate anion in acidic solution, pure water, and basic solution, respectively. The intense bands appear at 157.5 nm (molar absorption coefficient $\varepsilon = 5.15 \times 10^3$ M^{-1} cm^{-1}), 168.9 nm (7.76×10^3 M^{-1} cm^{-1}), and 169.9 nm (7.73×10^3 M^{-1} cm^{-1}) for the acid, the zwitterion, and the anion forms, respectively. Those are assigned to the $(\pi - \pi^*)_1$ transitions of the carboxyl and the carboxylate groups. In accordance with the conversion from the acid form to the zwitterion, the $(\pi - \pi^*)_1$ band is redshifted by 11.4 nm, the maximum ε value increases by 2.61×10^3 M^{-1} cm^{-1}, and the new band appears at 145.8 nm (5.77×10^3 M^{-1} cm^{-1}) which is tentatively denoted as $(\pi - \pi^*)_2$. The $(\pi - \pi^*)_2$ band of the carboxylate anion form was reported from the quantum chemical calculations of electronic transition and circular dichroism (CD) of hydrated alanine (Ala) [74, 75] and the absorption spectra of the amino acid solid films [67, 68]. Osted et al. reported that the electronic transition energies of the $(\pi - \pi^*)_1$ and $(\pi - \pi^*)_2$ bands are around 170 and 149 nm for the micro-hydrated zwitterion form of Ala from the coupled cluster singles and doubles (CCSD) level calculations [75]. In conversion from the zwitterion form to the anion, the $(\pi - \pi^*)_1$ band is slightly redshifted by 1 nm, and the $(\pi - \pi^*)_2$ band becomes indistinguishably smaller.

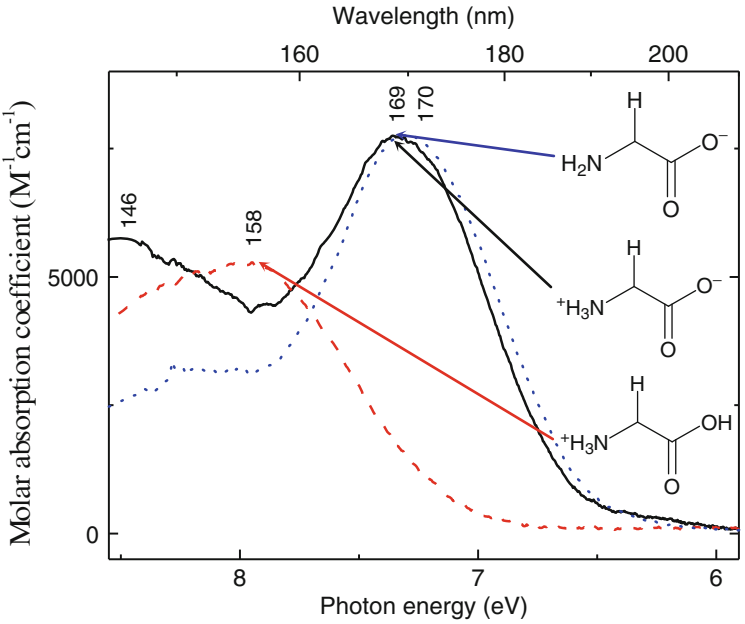

Fig. 4.13 FUV absorption spectra of 2 M Gly in the protonated, zwitterion, and deprotonated forms (From Ref. [73])

Accordingly, the $(\pi - \pi^*)_1$ and $(\pi - \pi^*)_2$ transitions electronically correlate with the intra- and intermolecular interaction between the ammonium and the carboxylate anion groups.

The amino acids whose side chains possess the π-electron conjugated groups, imidazolyl (His), phenyl (phenylalanine (Phe)), indolyl (tryptophan (Trp)), and hydroxyphenyl (tyrosine (Tyr)), yield the characteristic spectral patterns in the FUV region. Figure 4.14 shows the FUV spectra of the acid and the anion forms of these amino acids ((a) His, (b) Phe, (c) Trp, and (d) Tyr). In comparison of the ε spectra determined from the present ATR method with those from transmission methods in the wavelength region from 200 to 300 nm [76, 77], the positions of the band maxima nearly match each other, but the ε values determined by the ATR method are smaller by 0.55 times. This disagreement of the molar absorptivities mainly comes from the different orders of the sample concentrations ($10^{-6} - 10^{-3}$ M for the transmission and 1–2 M for the ATR study).

For Phe and Tyr, the characteristic bands appear from 175 to 300 nm, which are mainly derived from the $\pi - \pi^*$ transitions of the phenyl and hydroxyphenyl groups of the side chains. The $\pi - \pi^*$ bands of the carboxyl groups are completely obscured within the $\pi - \pi^*$ bands of the side chains. From the absorption spectra of benzene and substituted benzenes [78, 79], the intense bands around 190 nm and the weak bands around 250 nm correspond to the symmetry-allowed $\pi - \pi^*$ transition (^{1}B) and the symmetry-forbidden $\pi - \pi^*$ transitions (^1L_a and ^1L_b), respectively. By comparing the ^{1}B bands between the acid and anion forms, (1) the band positions

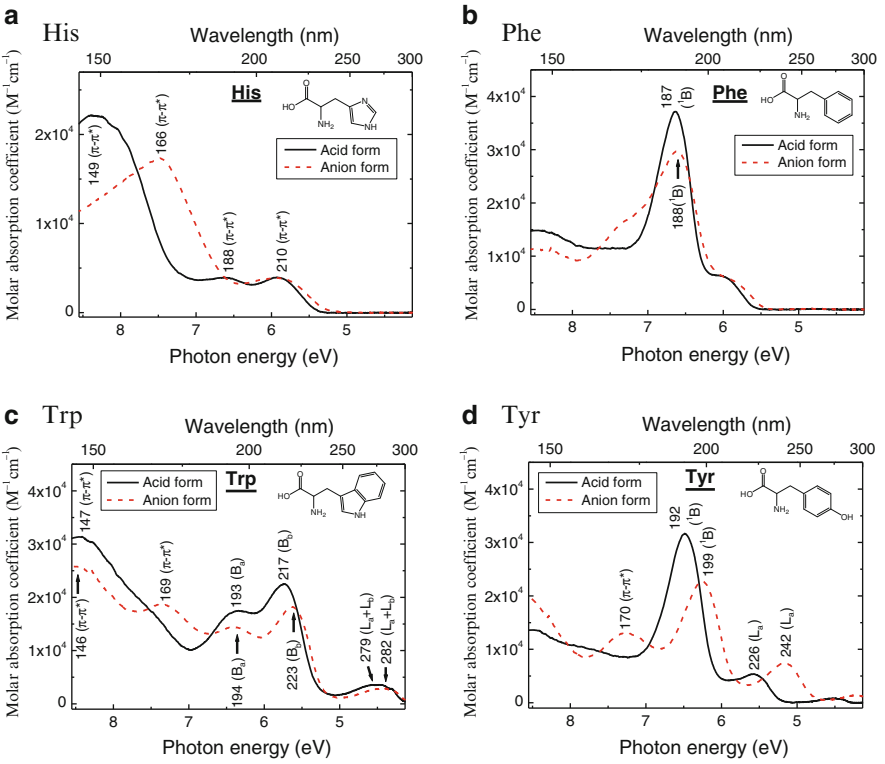

Fig. 4.14 FUV absorption spectra of ammonium carboxylic acid and aminocarboxylate anion forms of amino acids with aromatic side chain (**a**) His, (**b**) Phe, (**c**) Trp, and (**d**) Tyr (From Ref. [73])

of the acid forms stay at shorter wavelength than the anion forms, (2) the molar absorption coefficients of the acid forms are larger, and (3) the bandwidths of the acid forms are narrower. Those differences probably arise from the hydration strength of the amino acid molecules. The anion forms of the amino acids interact more strongly with the solvent water molecules than the acid forms.

The characteristic absorption bands of Trp spread over the entire FUV region, and those are mostly derived from the $\pi - \pi^*$ transitions of the indolyl group in the side chain. The $\pi - \pi^*$ transition of the carboxyl group is moderately obscured within the intense absorption of the indolyl group. The spectral changes upon protonation are relatively small, because the molecular structure of the side chain does not change with the proton concentrations. The bands around 193, 230, and 280 nm are assigned to the $\pi - \pi^*$ transitions to the B_a state, the B_b state, and the overlapping L_a and L_b states, respectively [80]. In comparison of the spectra among Phe, Trp, and Tyr, the electronic transition energies of the B bands decrease, and the molar absorption coefficients of the L bands increase for both the acid and anion forms due to the reduced benzene ring symmetry, as the benzene rings are more substituted from Phe to Trp.

4.5 Pulse Laser Photolysis of Aqueous Ozone in the Microsecond Range Studied by Time-Resolved Far-Ultraviolet Absorption Spectroscopy

Advanced oxidation processes (AOP) using aqueous ozone (O_3) with hydrogen peroxide (H_2O_2) and UV light irradiation have been widely employed to oxidatively destruct organic and inorganic contaminants in aqueous solution [81–84]. Even though O_3 has high reactivity to many chemical compounds, the reactivity to some compounds, such as alcohols and carboxylic acids, is quite small [85–87]. Hydroxyl radical (OH), which is a transient species from O_3 decomposition, possesses high reactivity to any target compounds [85–87]. The experimental conditions in the AOP processes were studied to efficiently generate OH at the target sites. However, the real-time monitoring of OH generation by the O_3 photolytic reaction in aqueous solution is not straightforward, because many transient species are short-lived (ns – ms), and their concentrations are relatively low.

FUV absorption spectroscopy is practical to analyze aqueous solutions quantitatively and qualitatively, because liquid water is optically transparent above 200 nm, and the most of organic and inorganic molecules have relatively strong optical absorptions corresponding to various types of electronic transition. The chemical species involved in the O_3 photolytic reaction also have characteristic FUV bands [88–92]. In order to analyze the chemical dynamics of the O_3 pulse-photolytic reaction in aqueous solution, we have developed a pump-probe nanosecond time-resolved FUV spectrophotometer using a nanosecond pulse laser (wavelength, 266 nm; duration, 10 ns) [93, 94]. From the measured spectra, the molar absorptivities (ε) and the concentration-time profiles of the constituted chemical species in the O_3 photolytic reaction can be estimated with a multivariate curve resolution (MCR) method [93]. The real-time monitoring of the constituted chemical concentrations is a basis for controlling the AOP quality in washing processes.

The transient absorption spectra of the O_3 aqueous solutions show the distinct changes upon the nanosecond pulse light irradiance. Figure 4.15 shows the time profiles of the transient absorbances of O_3 (78–480 μM) in 10 mM phosphoric buffer solutions ((a) pH 2.5, (b) 7.3, (c) 9.0, and (d) 11.3) from 190 to 225 nm. The transient absorbance is defined as *Transient* $\mathrm{Abs}(t) = -\log\left(I(t)/I_0\right)$ where $I(t)$ is the signal of the probe light intensity and I_0 is the time-averaged signal before the pump light irradiation. Because the transient absorbance of O_3 in pure water (pH 4.7) is similar with that in the pH 5.2 buffer solutions, the effects of the phosphate anions on the O_3 pulse-photolytic reaction are negligible. The time at 0 s corresponds to the nanosecond pulse laser irradiation timing. For all the pH conditions, the transient absorbances decrease just after the pulse laser irradiation till 20 μs and become mostly stable between 20 and 50 μs. The decreases in the absorbances become larger and the time decay shorter, as the wavelength is longer. For pH 2.5, the absorbances at 20 μs are 0.014 and 0.095 for 190 and 225 nm, respectively. The time decay constants with single exponential (τ_1) are 3.8 and 1.0 μs for 190 and 225 nm, respectively. As pH increases, the decreases of the absorbances become small especially in the short wavelength region. For

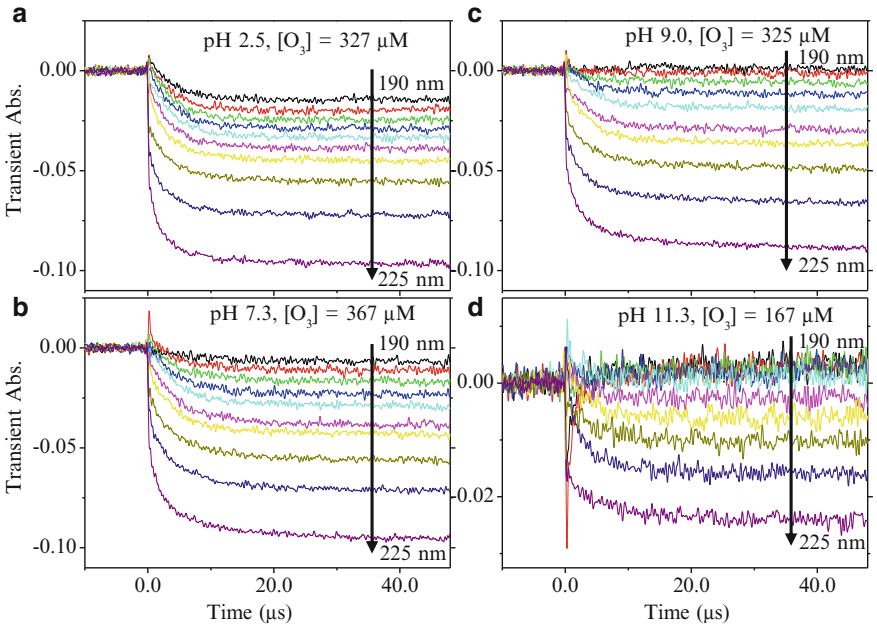

Fig. 4.15 Time profiles of the transient absorbance of O_3 in aqueous solutions at (**a**) pH 2.5, (**b**) 7.3, (**c**) 9.0, and (**d**) 11.3. The nanosecond laser pulses are irradiated at 0 s (From Ref. [93])

pH 11.3, the signal-to-noise ratio (SNR) of the transient absorbance is much lower than the other pH conditions, and the signals around 0 s highly fluctuate. This SNR degradation in the basic solutions indicates that the decomposition reaction of O_3 with OH^- lowers the O_3 concentration at the measurement position and increases the scattered light of the pump laser due to the formed O_2 bubbles. From the studies of stationary O_3 photolysis [95–99], the decreases of the transient absorbances in the longer wavelength region are mainly ascribed to the photodecomposition of O_3 and the increases in the shorter wavelength region to the formation of H_2O_2.

The measured transient spectrum matrix (**A**, time × wavelength channels) can be decomposed into the molar absorption coefficient matrix (**S**, wavelength × number of chemical species (n)) and the concentration-time profile matrix (**C**, time × n channels) based on Beer's law, as shown in the following equation [100]:

$$\mathbf{A} = \mathbf{C}\mathbf{S}^{\mathrm{T}} + \mathbf{R} \tag{4.1}$$

The ε value of each chemical component involved in the O_3 photolytic reaction in aqueous solution (O_3, H_2O_2, OH, O_3^-, HO_2, O_2^-, and HO_2^-) was employed from the references [89–103] as the initial **S** matrices for alternating least-square fitting. The number of the constituted chemical components was determined as three, because the elements of the residual absorbance matrix (**R**) are completely random patterns along the time and the wavelength directions by applying three components: O_3, H_2O_2, and one of the transient chemical components. This analysis result indicates

that the contribution from other than the O_3 decomposition and the H_2O_2 formation can be described as the concentration change of one chemical component from the linear decomposition of the measured transient spectra. In order to distinguish which of the transient species (OH, O_3^-, HO_2, O_2^-, and HO_2^-) is the most probable as the third component, the MCR analyses were carried out in a way O_3 and H_2O_2 were always selected as the first and second components, and one of the transient species was selected as the third component. Then, the **S** and **C** matrices were calculated using each third component. To determine the most probable chemical species as the third component, the following conditions were applied to the calculated **C** matrices: (1) The concentration changes of H_2O_2 and the third component are not negative along the time, and (2) the concentration changes of H_2O_2 and the third component increase as the initial concentration of O_3 is higher. From the calculated **C** matrices, the probable third species that satisfy the above conditions are OH and HO_2.

The ε spectra ($\mathbf{S}_3$) of OH and HO_2 including wavelength region not reported in the references (190–225 nm) were determined from the following Eqs. (4.2) and (4.3) in order to evaluate which OH or HO_2 is more suitable as the third component contributing the changes in the transient absorbance.

$$\mathbf{A}_3 = \mathbf{A}_{\text{exp.}} - \mathbf{S}_1\mathbf{C}_1 - \mathbf{S}_2\mathbf{C}_2 \tag{4.2}$$

$$\mathbf{S}_3 = \left(\mathbf{C}_3^{\mathrm{T}}\mathbf{C}_3\right)^{-1}\mathbf{C}_3^{\mathrm{T}}\mathbf{A}_3 \tag{4.3}$$

$\mathbf{A}_{\text{exp.}}$ is the measured transient absorbance matrix, $\mathbf{C}_n$ is nth row of the calculated **C** matrix, and the columns of $\mathbf{S}_1$ and $\mathbf{S}_2$ are extended to 190 nm with the ε values of O_3 and H_2O_2 from the references. As the transient absorbance matrix **A** (time × wavelength channels) is not a square matrix, the calculated ε matrix $\mathbf{S}_3$ is a compromise solution. Figure 4.16 shows the calculated ε spectrum of each OH

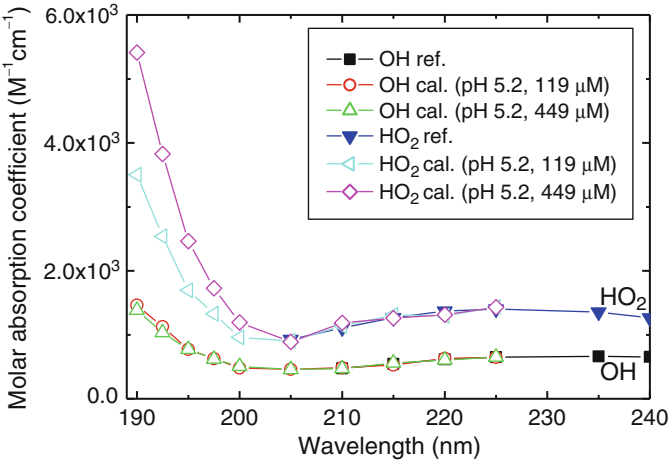

Fig. 4.16 Calculated ε spectra of OH and HO_2 extended to the shorter wavelength to 190 nm using Eqs. (4.2) and (4.3) and the ε values from the references [89, 103] (From Ref. [93])

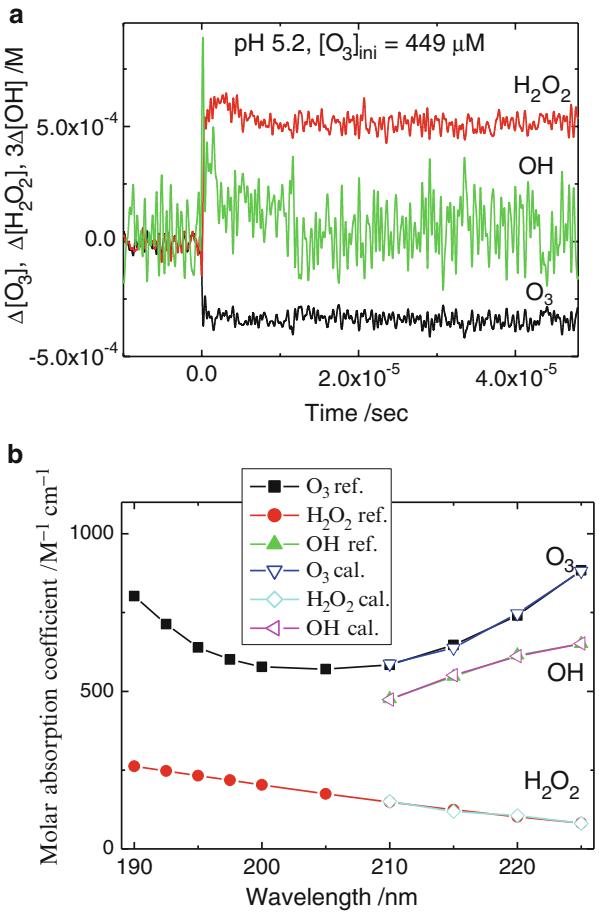

Fig. 4.17 Calculated **C** (**a**) and **S** (**b**) matrices from the transient absorbance ($[O_3]_{ini} = 449$ μM,pH 5.2) in the cases of OH as the third component and the ε values from the reference [89, 92, 103]. The concentration of OH was magnified by 3 times for clarity (From the reference [93])

and HO_2 in the region from 190 to 225 nm (OH cal., HO_2 cal.) with the reference spectra (OH ref., HO_2 ref.) [89, 103]. In the case of HO_2, the ε value below 205 nm increases as the initial concentration of O_3 is higher, while that of OH is mostly identical for all the initial concentrations of O_3. Thus, it can be said that OH is more suitable than HO_2 as the third component.

The decomposed **C** and **S** matrices reveal the chemical dynamics of the O_3 pulse-photolytic reaction in aqueous solution. Figure 4.17 shows the **C** (Fig. 4.17a) and **S** (Fig. 4.17b) matrices calculated from the time profiles of the transient absorbances at the condition ($[O_3]_{ini} = 449$ μM, pH 5.2) in the cases of OH as the third component. The vertical axis of Fig. 4.17a shows the concentration differences of O_3, H_2O_2, and

OH between before and after the pulse irradiation. The concentration change of OH (Δ[OH]) is magnified by 3 times for clarity. Upon the pulse laser irradiation, the O_3 concentration instantaneously decreases by 73 % from 449 to 120 μM for the first 0.3 μs, and then it becomes almost stable. The H_2O_2 concentration instantaneously increases to 550 μM for the first 0.3 μs and slightly increases further to 610 μM around 2 μs, and then it decreases to 460 μM around 20 μs. The OH concentration increases to 120 μM till 1 μs and gradually decreases to 20 μM till 20 μs, and then it remains stable after 20 μs. The examination of the chemical dynamics around 0 s is difficult, because the signal fluctuations due to the scattered light of the pump pulse laser cannot be completely removed. Figure 4.17b also shows the reference spectra of O_3, H_2O_2, and OH [89, 92, 103]. The calculated ε spectra of O_3, H_2O_2, and OH from $\mathbf{S}_3$ match closely the reference spectra.

The present MCR analysis of the O_3 pulse-photolytic reaction becomes an important basis for real-time monitoring of chemical dynamics of AOP in washing processes with compact FUV spectrophotometers using optical filters.

References

1. D.J. Segelstein, http://www.philiplaven.com/p20.html
2. D.P. Stevenson, G.M. Coppinger, J.W. Forbes, J. Am, Chem. Soc. **83**(21), 4350–4352 (1961)
3. M. Halmann, I. Platzner, J. Phys. Chem. **70**, 580 (1966)
4. M.F. Fox, E. Hayon, J. Phys. Chem. **76**, 2703 (1972)
5. T.W. Marin, K. Takahashi, D.M. Bartels, J. Chem. Phys. **125**, 104314 (2006)
6. R.S. Mulliken, J. Chem. Phys. **3**, 506 (1935)
7. G. Herzberg, *Molecular Spectra and Molecular Structure III: Electronic Spectra and Electronic Structure of Polyatomic Molecules* (Van Nostrand, New York, 1966), p. 489
8. F. Williams, S.P. Varma, S. Hillenius, J. Chem. Phys. **64**, 154 (1976)
9. P.H. Hahn, W.G. Schmidt, K. Seino, M. Preuss, F. Bechstedt, J. Bernholc, Phys. Rev. Lett. **94**, 037404 (2005)
10. M. Rubio, L. Serrano-Andres, M.J. Merchan, Chem. Phys. **128**, 104305 (2008)
11. M. Chergui, N. Schwentner, Chem. Phys. Lett. **219**, 237 (1994)
12. K. Watanabe, M. Zelikoff, J. Opt. Soc. Am. **43**, 753 (1953)
13. P. Gurtler, V. Saile, E.E. Koch, Chem. Phys. Lett. **51**, 386 (1977)
14. A. Ikehata, Y. Ozaki, N. Higashi, J. Chem. Phys. **129**, 234510 (2008)
15. L.R. Painter, R.D. Birkhoff, E.T. Arakawa, J. Chem. Phys. **51**, 243 (1969)
16. G.D. Kerr, R.N. Hamm, M.W. Williams, R.D. Birkhoff, L.R. Painter, Phys. Rev. A **5**, 2523 (1972)
17. R.E. Verrall, W.A. Senior, J. Chem. Phys. **50**, 2746 (1969)
18. T. Shibaguchi, H. Onuki, R. Onaka, J. Phys. Soc. Jpn. **42**, 152 (1977)
19. K. Kobayashi, J. Phys. Chem. **87**, 4317 (1983)
20. R. Onaka, T. Takahashi, J. Phys. Soc. Jpn. **24**, 548 (1968)
21. T.I. Quickenden, J.A. Irvin, J. Chem. Phys. **72**, 4416 (1980)
22. A. Bernas, C. Ferradini, J.-P. Jay-Gerin, J. Photochem. Photobiol. A **117**(171) (1998)
23. F. Urbach, Phys. Rev. **92**, 1324 (1953)
24. A. Bernas, C. Ferradini, J.-P. Jay-Gerin, Chem. Phys. **222**, 151 (1997)
25. J.V. Coe, A.D. Earhart, M.H. Cohen, G.J. Hoffman, H.W. Sarkas, K.H. Bowen, J. Chem. Phys. **107**, 6023 (1997)
26. O. Christiansen, T.M. Nymand, K.V. Mikkelsen, J. Chem. Phys. **113**, 8101 (2000)

27. R. van Harrevelt, M.C. van Hemert, J. Chem. Phys. **114**, 9453 (2001)
28. Y. Miller, E. Fredj, J.N. Harvey, R.B. Gerber, J. Phys. Chem. A **108**, 4405 (2004)
29. D.M. Chipman, J. Chem. Phys. **122**, 044111 (2005)
30. P.C. do Couto, B.J.C. Cabral, J. Chem. Phys. **126**, 014509 (2007)
31. P.C. do Couto, D.M. Chipman, J. Chem. Phys. **137**, 184301 (2012)
32. M. Aschi, M. D'Abramo, C. Di Teodoro, A. Di Nola, A. Amadei, ChemPhysChem **6**, 53 (2005)
33. N. Higashi, A. Ikehata, Y. Ozaki, Rev. Sci. Instrum. **78**, 103107 (2007)
34. Y. Ozaki, Y. Morisawa, A. Ikehata, N. Higashi, Appl. Spectrosc. **66**(1), 1–25 (2012)
35. K.D. Collins, Biophys. J. **72**, 65 (1997)
36. B. Hribar, N.T. Southall, V. Vlachy, K.A. Dill, J. Am. Chem. Soc. **124**, 12302 (2002)
37. E. Vinogradov, P. Smirnov, V. Trostin, Russ. Chem. Bull. Int. Ed. **52**, 1253 (2003)
38. R.A. Robinson, R.H. Stokes, *Electrolyte Solutions* (Butterworth Scientific Publications, London, 1959)
39. G.A. Krestov, *Thermodynamics of Solvation* (Ellis Horwood, Chichester, 1991)
40. H. Ohtaki, N. Fukushima, J. Solut. Chem. **21**, 23 (1992)
41. V.I. Chizhik, A.V. Egorov, A.V. Komolkin, A.A. Vorontsova, J. Mol. Liq. **98–99**, 173 (2002)
42. W. Rudolph, M.H. Brooker, C.C. Pye, J. Phys. Chem. **99**, 3793 (1995)
43. T. Goto, A. Ikehata, Y. Morisawa, N. Higashi, Y. Ozaki, Phys. Chem. Chem. Phys. **14**, 8097–8104 (2012)
44. A. Ikehata, M. Mitsuoka, Y. Morisawa, N. Kariyama, N. Higashi, Y.J. Ozaki, Phys. Chem. A **114**, 8319–8322 (2010)
45. Y. Marcus, J. Chem. Soc. Faraday Trans. **87**, 2995 (1991)
46. C.K. Jørgensen, Spectroscopy of transition-group complexes, in *Advances in Chemical Physics*, ed. by I. Prigogine, vol. 5 (Wiley, Hoboken, 2007); ch 2
47. L.J. Nugent, J. Inorg. Nucl. Chem. **32**, 3485 (1970)
48. J. Kuta, A.E. Clark, Inorg. Chem. **49**, 7808 (2010)
49. M. Duvail, R. Spezia, P. Vitorge, ChemPhysChem **9**, 693 (2008)
50. J. Ciupka, X. Cao-Dolg, J. Wiebke, M. Dolg, Phys. Chem. Chem. Phys. **12**, 13215 (2010)
51. I. Persson, P. D'Angelo, S. De Panfilis, M. Sandström, L. Eriksson, Chem. Eur. J. **14**, 3056 (2008)
52. M. Seitz, A.G. Oliver, K.N. Raymond, J. Am. Chem. Soc. **129**, 11153 (2007)
53. P.G. Allen, J.J. Bucher, D.K. Shuh, N.M. Edelstein, I. Craig, Inorg. Chem. **39**, 595 (2000)
54. S. Goldman, L.R. Morss, Can. J. Chem. **53**, 2695 (1975)
55. D.F. Peppard, G.W. Mason, S. Lewey, J. Inorg. Nucl. Chem. **31**, 2271 (1969)
56. T. Goto, A. Ikehata, Y. Morisawa, N. Higashi, Y. Ozaki, Inorg. Chem. **51**, 10650 (2012)
57. T.C. William, The absorption and fluorescence spectra of rare earth ions in solution, in *Handbook on the Physics and Chemistry of Rare Earths*, ed. by K.A. Gschneidner Jr., L. Eyring, vol. 3 (Elsevier, Amsterdam, 1979); ch 24
58. K.B. Yatsimirskii, N.A. Kostromina, Theor. Exp. Chem. **2**, 436 (1966)
59. F.S. Richardson, M.F. Reid, J.J. Dallara, R.D. Smith, J. Chem. Phys. **83**, 3813 (1985)
60. N. Ishikawa, M. Sugita, T. Okubo, N. Tanaka, T. Iino, Y. Kaizu, Inorg. Chem. **42**, 2440 (2003)
61. M. Zbiri, M. Atanasov, C. Daul, J.M. Garcia-Lastra, T.A. Wesolowski, Chem. Phys. Lett. **397**, 441 (2004)
62. J. Hölsä, M. Karppinen, E. Kestilä, J. Alloys Compd. **207–208**, 65 (1994)
63. M. Atanasov, C. Daul, H.U. Güdel, T.A. Wesolowski, M. Zbiri, Inorg. Chem. **44**, 2954 (2005)
64. M. Kotzian, T. Fox, N. Rosch, J. Phys. Chem. **99**, 600 (1995)
65. M. Zbiri, C.A. Daul, T.A. Wesolowski, J. Chem. Theory Comput. **2**, 1106 (2006)
66. H.J. Svec, D.D. Clyde, J. Chem. Eng. Data **10**, 151 (1965)
67. I.P. Vinogradov, N.Y. Dodonova, Opt. Spectrosc. **30**, 14 (1970)
68. M. Tanaka, K. Yagi-Watanabe, F. Kaneko, K. Nakagawa, J. Phys. Chem. A **114**, 11928 (2010)
69. R. Abouaf, Chem. Phys. Lett. **451**, 25 (2008)
70. O. Plekan, V. Feyer, R. Richter, M. Coreno, M.D. Simone, K.C. Prince, V. Carravetta, J. Phys. Chem. A **111**, 10998 (2007)

71. P.A. Snyder, P.M. Vipond, W.C. Johnson, Biopolymers **12**, 975 (1973)
72. K. Matsuo, Y. Matsushima, T. Fukuyama, S. Senba, K. Gekko, Chem. Lett. **31**, 826 (2002)
73. T. Goto, A. Ikehata, Y. Morisawa, Y.J. Ozaki, Phys. Chem. A **117**, 2517–2528 (2013)
74. T. Fukuyama, K. Matsuo, K. Gekko, J. Phys. Chem. A **109**, 6928 (2005)
75. A. Osted, J. Kongsted, K.V. Mikkelsen, O. Christiansen, Chem. Phys. Lett. **429**, 430 (2006)
76. H. Nishino, A. Kosaka, G.A. Hembury, K. Matsushima, Y. Inoue, J. Chem. Soc. Perkin Trans. **2**, 582 (2002)
77. E. Mihalyi, J. Chem. Eng. Data **13**, 179 (1968)
78. J.R. Platt, H.B. Klevens, Chem. Rev. **41**, 301 (1947)
79. A. Bolovinos, P. Tsekeris, J. Philis, E. Pantos, G. Andritsopoulos, J. Mol. Spectrosc. **103**, 240 (1984)
80. J.A. Sweeney, S.A. Asher, J. Phys. Chem. **94**, 4784 (1990)
81. G.R. Peyton, W.H. Glaze, Environ. Sci. Technol. **22**, 761 (1988)
82. B. Meunier, A. Sorokin, Acc. Chem. Res. **30**, 470 (1997)
83. C.P. Huang, C. Dong, Z. Tang, Waste Manag. **13**, 361 (1993)
84. D. Bahnemann, E.J. Hart, J. Phys. Chem. **86**, 252 (1982)
85. J. Hoigné, H. Bader, Water Res. **17**, 173 (1983)
86. J. Hoigné, H. Bader, Water Res. **17**, 185 (1983)
87. J. Hoigné, H. Bader, W. Haag, J. Staehelin, Water Res. **19**, 993 (1985)
88. K. Sehested, J. Holcman, E. Bjergbakke, E.J. Hart, J. Phys. Chem. **86**, 2066 (1982)
89. G. Czapski, B.H.J. Bielski, Radiat. Phys. Chem. **41**, 503 (1993)
90. P. Pagsberg, H. Christensen, J. Rabani, G. Nilsson, J. Fenger, S.O. Nielsen, J. Phys. Chem. **73**, 1029 (1969)
91. S.O. Nielsen, B.D. Michael, E.J. Hart, J. Phys. Chem. **80**, 2482 (1976)
92. R.E. Buehler, J. Staehelin, J. Hoigne, J. Phys. Chem. **88**, 2560 (1984)
93. T. Goto, Y. Morisawa, N. Higashi, A. Ikehata, Y. Ozaki, Anal. Chem. **85**, 4500 (2013)
94. Y. Morisawa, N. Higashi, K. Takaba, N. Kariyama, T. Goto, A. Ikehata, Y. Ozaki, Rev. Sci. Instrum. **83**, 073103 (2012)
95. M.D. Gurol, A. Akata, AICHE J. **42**, 3283 (1996)
96. T. Garoma, M.D. Gurol, Environ. Sci. Technol. **39**, 7964 (2005)
97. W.H. Glaze, J.-W. Kang, D.H. Chapin, Ozone Sci. Eng. **9**, 335 (1987)
98. G. Wittmann, I. Horváth, A. Dombi, Ozone Sci. Eng. **24**, 281 (2002)
99. B. Soo Oh, K. Suk Kim, M. Gu Kang, H. Je Oh, J.-W. Kang, Ozone Sci. Eng. **27**, 421 (2005)
100. J. Jaumot, R. Gargallo, A. de Juan, R. Tauler, Chemom. Intell. Lab. Syst. **76**, 101 (2005)
101. E.J. Hart, K. Sehested, J. Holoman, Anal. Chem. **55**, 46 (1983)
102. G. Czapski, J. Phys. Chem. **68**, 1169 (1964)
103. C.S. Foote, J.S. Valentine, A. Greenberg, J.F. Liebman (eds.), *Active Oxygen in Chemistry*, 1st edn. (Chapman and Hall, London, 1995)

Chapter 5
Far-Ultraviolet Spectroscopy and Deep-Ultraviolet Spectroscopy: Industrial Applications

Noboru Higashi

Abstract FUV or DUV absorption spectrum has very strong absorptivity with a steep absorption edge. Since the spectral changes in the intensity, position, and bandwidth of the band are observed sensitively even at the portion of the tail band, these spectra can be applied for a powerful method in industrial analytical applications. The potential of FUV and DUV spectroscopy is revealed as a highly sensitive analytical method for aqueous solutions such as mineral water, springwater, and variety of industrial cleaning water. In addition, it is proposed that FUV spectroscopy is useful for not only analysis of aqueous solutions and nonaqueous solvents but also for non-solvent substances such as polymer films.

Keywords Industrial applications • Water analysis • Aqueous solutions • Chemical solutions

5.1 Introduction

There is a wide range of spectroscopy techniques, covering wavelength regions including X-ray, far ultraviolet (FUV), deep ultraviolet (DUV), UV visible, near infrared (NIR), infrared (IR), and terahertz (THz). Some of them were already utilized in the nineteenth century, whereas NIR and THz spectroscopy have shown marked progress from the 1990s. In the meanwhile, FUV and DUV spectroscopy have widely been used as a spectroscopic method corresponding to electronic transitions of various molecules from early in the twentieth century. However, from the point of a practical use, applications of FUV spectroscopy have been very much restricted compared with the other spectroscopic methods because this spectral region has not been accessible to routine measuring techniques especially below 190 nm due to strong absorption of oxygen in air. Furthermore, in the FUV region,

N. Higashi (✉)
Kurabo Industries Ltd., 14-5 Shimokida-cho, Neyagawa, Osaka 572-0823, Japan
e-mail: Noboru_Higashi@ad.kurabo.co.jp

Y. Ozaki, S. Kawata (eds.), *Far- and Deep-Ultraviolet Spectroscopy*,
DOI 10.1007/978-4-431-55549-0_5

observed absorptivity is extremely strong, so that only gas phase is suitable to obtain full absorption spectra without saturation.

Since FUV or DUV absorption spectrum has very strong absorptivity with a steep absorption edge, the spectral changes in the intensity, position, and bandwidth of the band are observed sensitively even at the portion of the tail band. In the first part of this chapter, the potential of FUV spectroscopy and DUV spectroscopy as a highly sensitive analytical method for aqueous solutions is proposed.

In the second part of this chapter, it is revealed that FUV spectroscopy with the restricted spectral resolution such as 2 nm is still very effective for the practical online analysis of aqueous solutions. To evaluate and propose the usefulness of spectrometer with nitrogen gas purge, a practical experiment applying the spectrometer to the determination analyses for peracetic acid (PAA), hydrogen peroxide (H_2O_2), and acetic acid (AA) in disinfectant solutions is performed.

In the last part of the chapter, it is proposed that FUV spectroscopy is useful for not only analysis of aqueous solutions and nonaqueous solvents but also for non-solvent substances such as polymer films. FUV spectra are also very sensitive to the differences in the bonding energy of the C–C bonds caused by the substituent in polymer films.

Compared with other spectroscopic methods, these techniques include advantages of nondestructive analysis, easy spectral measurement, high sensitivity, and simple spectral analysis. These studies show that FUV and DUV spectroscopy are the promising analytical method not only for aqueous solutions but also for analyses of organic components such as polymer films.

5.2 Potential of Far-Ultraviolet Absorption Spectroscopy for Highly Sensitive Analysis of Aqueous Solutions

Far-ultraviolet (FUV) spectroscopy in the range of 190–280 nm has long been used as a highly sensitive and simple method for qualitative and quantitative analysis of liquid water and aqueous solutions [1–9]. In this region, several kinds of ions show a strong band. For example, NO_3^- yields an intense band near 200 nm due to the π-π^* transition [10], and halogen ions give rise to a CTTS (charge transfer to solvent) band in the 170–225 nm region [11]. Ferree and Shannon [5] carried out quantitative analysis of nitrogen compounds in wastewater by using the NO_3^- absorption near 200 nm. Ozaki and I applied FUV spectroscopy in the 190–280 nm region to qualitative analysis of various commercial mineral waters [6] (Fig. 5.1). Various types of waters could be classified clearly based on bands due to the π-π^* transition of NO_3^- and the CTTS transition of halides.

FUV spectroscopy has been applied to qualitative and quantitative analysis of springwater samples in three different areas of Hyogo Prefecture, Japan, in order to demonstrate potentials of FUV spectroscopy analysis [12]. FUV spectroscopy can classify various kinds of springwater samples, clearly reflecting the geology of their

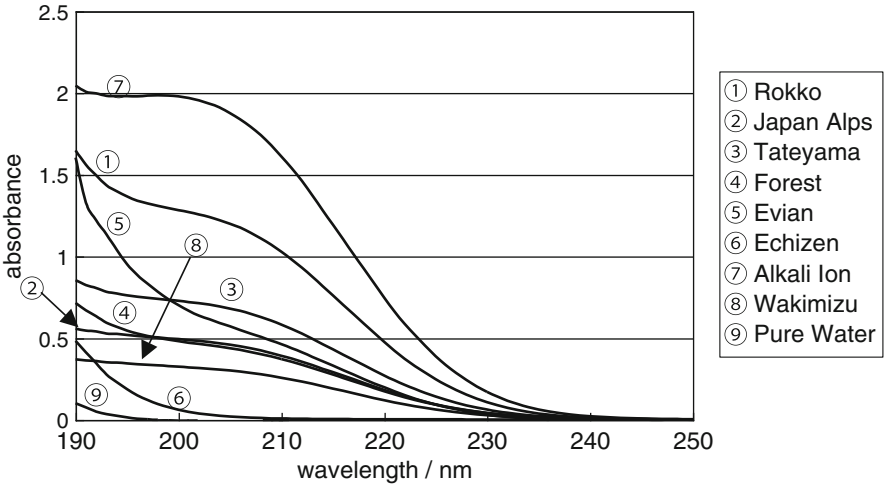

Fig. 5.1 FUV spectra of eight types of natural mineral water and pure water

origin. Good calibration models for ions included in the springwater samples can be developed with the first derivatives of their FUV spectra. FUV spectroscopy may be highly useful for qualitative and quantitative analyses of various kinds of water sources, including river water, seawater, rainwater, lake water, and hot springwater.

Recently, highly sensitive analyses of pure water and its solutions have become increasingly important in a variety of industrial processes. For example, in the semiconductor manufacturing processes, ultrapure water, which contains less than 0.1 μm particles, 2 ppb oxygen gasses, and 1 ppt metal ions, is required for rinse water or solvent for detergent agents for semiconductor wafer surfaces [13]. Pure water is also essential for atomic power generation, as well as medical uses. Therefore, evaluating the quality of pure water is of critical importance.

The RCA cleaning method developed by Kern and Puotinen in 1970 for the Radio Corporation of America is well known for its effectiveness in removing contaminants from silicon wafer surfaces in semiconductor fabrication [14]. This method consists of oxidizing fluids such as NH_3, H_2O_2 and water, and HCl, H_2O_2, and water. A mixture of 29 % NH_3, 31 % H_2O_2, and water with a ratio of 1:1:5 is called SC-1; this effectively removes particulate and organic contamination from wafer surfaces. A 1:1:6 mixture of 36 % HCl, 31 % H_2O_2, and water is called SC-2; this effectively removes metal contamination. "Wet" silicon cleaning systems using these fluids to immerse wafers in a cleaning bath have undergone many improvements and remain in wide use [15]. As cleaning fluid concentration varies within the cleaning process and affects semiconductor fabrication yield, careful monitoring of the concentrations of these components is crucial to ensure timely addition or replacement of cleaning fluid. Near-IR (NIR) spectroscopy is widely used for monitoring; however, this approach necessitates laborious extra sampling lines for analysis. For NIR spectral analysis, a Teflon tube feeding

the fluid in a circulation system as a sample container is often used for more convenient monitoring [16], but to date, there is no direct method of making these measurements in the wet bath. While these NIR methods' effectiveness is compromised for monitoring, concentrations measured at a distance from the wafer surface are no more than estimates of actual concentrations in the wet bath. Further, larger wafers require detailed measurements of concentration distributions within the cleaning bath, necessitating the development of a direct monitoring system either in the bath itself or on the container wall.

Attenuated total reflection (ATR) spectroscopy should be used to measure cleaning fluid concentrations directly with an ATR probe embedded in the wall surface. Quartz is the only material that can be used as a material for a semiconductor cleaning bath in the wafer cleaning process, as other types of glass and crystal may elute impurities in silicon wafers. For this reason, the material used as the internal reflection element (IRE) of an ATR probe embedded in a cleaning bath must be made of quartz as well. Quartz has high transmittance in the NIR region while absorbing light in the IR region; thus, quartz measurement wavelengths are limited to the NIR region or below. However, absorptivity of the NIR region is too small to determine SC-1 and SC-2 concentrations with the ATR method. Meanwhile, FUV spectroscopy is so sensitive that an ATR-based method with FUV wavelengths should be used to monitor SC-1 and SC-2 concentrations from the inner surface of semiconductor wafer cleaning baths.

Figure 5.2 shows ATR-FUV spectra of pure water as well as 5 % NH_3, 5 % HCl, and 10 % H_2O_2 aqueous solutions obtained with a quartz ATR probe. A hidden absorption peak near 180 nm in the absorption spectrum of 5 % NH_3 aqueous solution appears to be a band due to the $n \rightarrow \sigma^*$ transition of NH_3 [17], and a band due to the charge transfer to solvent (CTTS) of Cl^- is also observed near 180 nm [18]. An aqueous solution of H_2O_2 demonstrates a broader featureless absorption

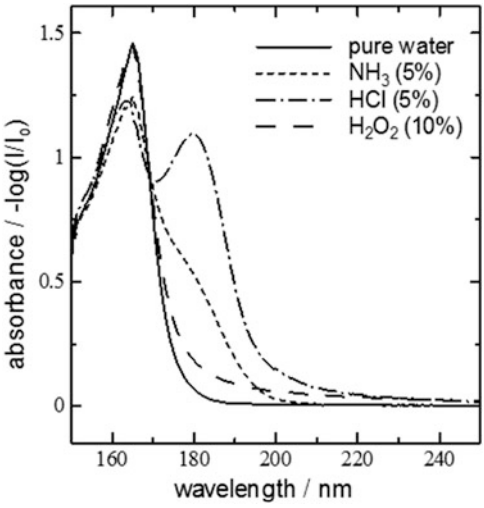

Fig. 5.2 ATR-FUV spectra of pure water, 5 % NH_3, 5 % HCl, and 10 % H_2O_2 using a quartz ATR probe

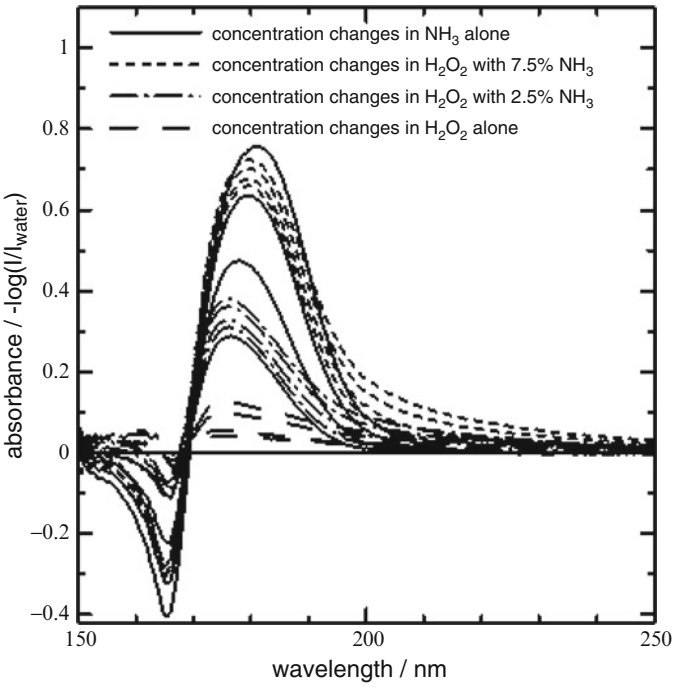

Fig. 5.3 ATR-FUV spectra of NH_3 and H_2O_2 in aqueous solution using a quartz ATR probe. *Solid lines* represent the spectra of NH_3 alone with different concentrations (0, 2.5, 5, 7.5, and 10 %); *long dashed lines*, the spectra of H_2O_2 alone with different concentrations (2.5, 5, 7.5, and 10 %); *dot-dash-dot lines*, the spectra of H_2O_2 (2.5, 5, 7.5, and 10 %) in solutions with 2.5 % NH_3; and *short dashes*, the spectra of H_2O_2 with different concentrations (2.5, 5, 7.5, and 10 %), including 7.5 % NH_3

spectrum below 240 nm. Further, in each spectrum of these aqueous solutions, a band due to the $n \rightarrow \sigma^*$ transition of water should be affected by addition of dissolved components. Therefore, all spectra are distinctly different from each other. Figure 5.3 illustrates ATR-FUV spectra for various mixtures of NH_3 and H_2O_2 obtained by using the reflection intensity of pure water as a background. These spectral changes observed in Fig. 5.3 are generally attributed to changes not only in the bands due to the solutes but also from the $n \rightarrow \sigma^*$ transition band of water itself. The absorption maxima around 180 nm in observed spectra show redshift with increased concentration of NH_3. This is due to shifting of the water band to longer wavelengths by modification of the water molecule's hydrogen bonding [5, 6]. We chose four wavelengths from 175 to 185 with narrow intervals in the multiple linear regression (MLR) analysis in order to detect these modifications precisely. Solute-related spectral features are also observed in the FUV region. Spectral changes due to NH_3 and HCl seem present around 180 nm, and that of H_2O_2 is extended to 220 nm or above.

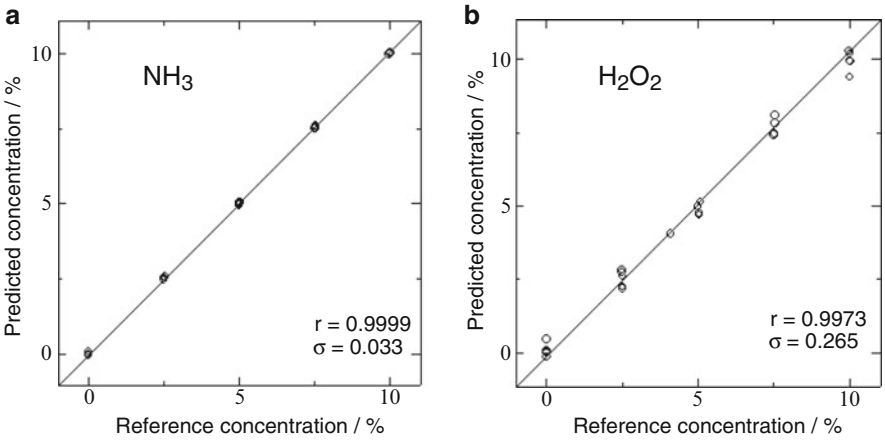

Fig. 5.4 Calibration models for predicting concentrations of (**a**) NH_3 and (**b**) H_2O_2 in aqueous solutions containing NH_3 and H_2O_2

Table 5.1 Prediction results

	SC-1				SC-2			
Mixture ratio	1:1:5		1:1:20		1:1:6		1:1:20	
Components	NH_3	H_2O_2	NH_3	H_2O_2	HCl	H_2O_2	HCl	H_2O_2
Prepared value	4.16	4.44	1.33	1.41	4.50	3.88	1.64	1.41
Measured value	4.16	5.00	1.10	1.94	4.55	3.54	1.62	1.27

Two types of samples were tested to evaluate calibration models developed for SC-1 and SC-2

Figure 5.4a, b show calibration models for predicting concentrations of NH_3 and H_2O_2 in aqueous solutions containing these substances in concentration ranges from 0 to 10 % with MLR analyses. The large spectral changes caused by NH_3 in aqueous solutions enable determination of NH_3 concentration more sensitively than that of H_2O_2. For NH_3 the correlation coefficient (r) is 0.9999, with an SD (σ) of 0.033 %; the corresponding values for H_2O_2 are 0.9973 and 0.265 %, respectively. Table 5.1 summarizes predictions when these calibration models are applied to test samples of SC-1 prepared separately from the standard samples, resulting in acceptable prediction accuracy for monitoring the cleaning process.

Figure 5.5 shows ATR-FUV spectra for aqueous solutions of HCl and H_2O_2 obtained using the reflection intensity of pure water as background. The large absorption band originating from CTTS of Cl^- in the aqueous solutions clearly differentiates contributions from HCl and H_2O_2. Calibration models based on these spectral measurements yielded a correlation coefficient (r) of 1.0 and an SD (σ) of 0.018 % for HCl; corresponding values were 0.9988 and 0.178 % for H_2O_2. Predictions based on these calibration models for test samples of SC-2 are also summarized in Table 5.1, resulting in acceptable prediction accuracy.

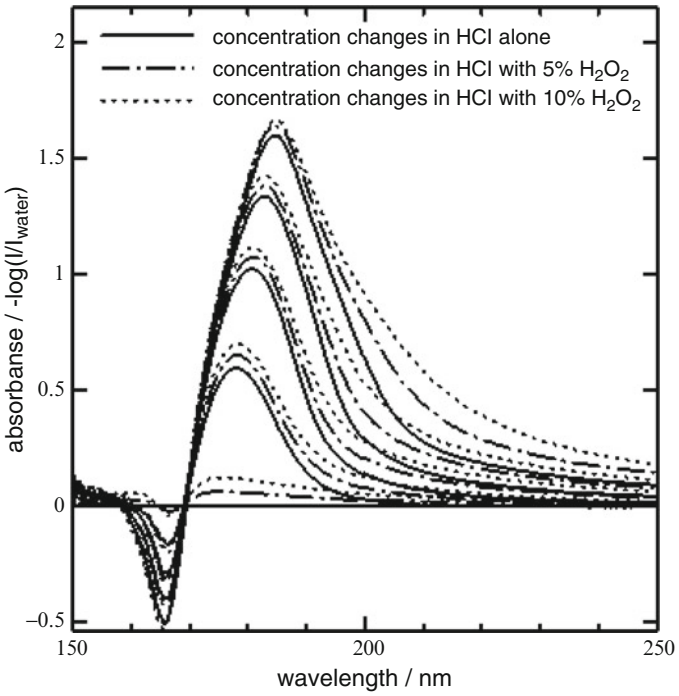

Fig. 5.5 ATR-FUV spectra of HCl and H_2O_2 in aqueous solution using a quartz ATR probe. *Solid lines* show the spectra of HCl only in differing concentrations (0, 2.5, 5, 7.5, and 10 %); *dot-dash-dot lines*, the spectra of HCl in differing concentrations (2.5, 5, 7.5, and 10 %) in solution with 5 % H_2O_2; and *dotted lines*, the spectra of HCl in differing concentrations (2.5, 5, 7.5, and 10 %), including 10 % H_2O_2

Spectral changes observed with ATR measurements are smaller than from transmittance, making ppm-order quantitative analysis problematic. However, further progress in semiconductor manufacturing requires more sensitive analysis of cleaning solutions for silicon wafer surfaces. We attempt FUV transmittance spectroscopy to determine SC-1 concentrations on the order of ppm [6].

Figure 5.6 shows FUV spectra of NH_3 and H_2O_2 solutions with concentrations of 100 ppm. Figure 5.7a–e show FUV spectra of aqueous solutions containing both NH_3 and H_2O_2. NH_3 concentrations in Fig. 5.7a–e are 84, 63, 42, 21, and 0 ppm, respectively, while those of H_2O_2 are varied over a range of 0–96 ppm with an increment of 24 ppm. As shown in Fig. 5.7, we prepared 25 kinds of aqueous solution samples. For two-component system analyses, we used MLR to create calibration models. Figure 5.8a, b show calibration models for predicting concentrations of NH_3 and H_2O_2, respectively. Values of r and σ for NH_3 and H_2O_2 were 0.9988 and 1.44 ppm and 0.9999 and 0.50 ppm, respectively. The detection limit for the determination of NH_3 and H_2O_2 is estimated at 0.2 ppm for the 1 cm cell. Therefore, the present method is very useful for concentration analysis of minute quantities of substances.

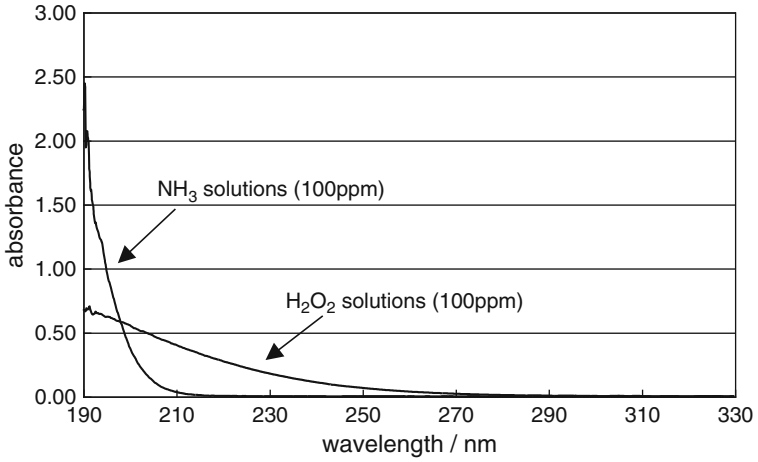

Fig. 5.6 FUV spectra of NH_3 and H_2O_2 solutions (concentration of 100 ppm)

The present study has clearly shown the usefulness of FUV spectroscopy in the quantitative and qualitative analyses of aqueous solutions. The method enables simple and rapid spectral measurements and analyses and requires no reagents. This technique may be utilized for a variety of aqueous solution analyses, including microanalyses, process analyses, and environmental monitoring.

5.3 Direct Measurement of Peracetic Acid, Hydrogen Peroxide, and Acetic Acid in Disinfectant Solutions Using Far-Ultraviolet Absorption Spectroscopy

The use of peracetic acid (PAA) for sterilization has received increasing attention due to deepening concerns about environmental impacts as well as increased needs for cold sterilization. PAA attacks a wide spectrum of microbes [19–22] and maintains sporicidal effects at temperatures even lower than room temperature [23]; further it leaves only nontoxic residues [24]. Therefore, PAA-based disinfectants have been widely used in the food and healthcare industries as an effective means of sterilization [25, 26]. PAA is an ideal disinfectant in sterile clean-in-place (CIP) packing systems for plastic bottle beverages because of its rapid sporicidal effect and low-temperature sterilization [26].

In a typical CIP process, condensed PAA solution is diluted with pure water to a concentration range of 0.15–0.20 wt%, then heated to a temperature range of 40–50 °C. It is then sprayed into each bottle for about 15 s. To ensure disinfectant effects, PAA concentration must be monitored and controlled continuously.

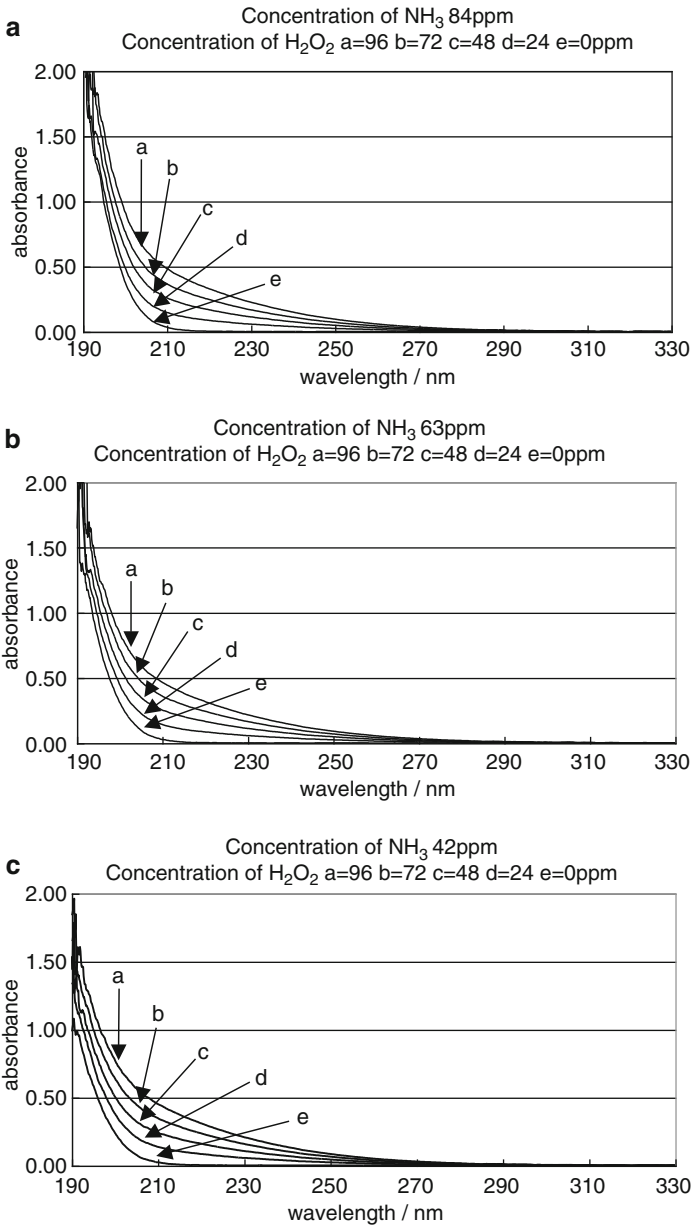

Fig. 5.7 FUV spectra of aqueous solutions containing NH_3 and H_2O_2. Concentration of NH_3: (**a**) 84 ppm, (**b**) 63 ppm, (**c**) 42 ppm, (**d**) 21 ppm, (**e**) 0 ppm. Concentration of H_2O_2: 96, 72, 48, 24, 0 ppm for (**a**), (**b**), (**c**), (**d**), and (**e**), respectively

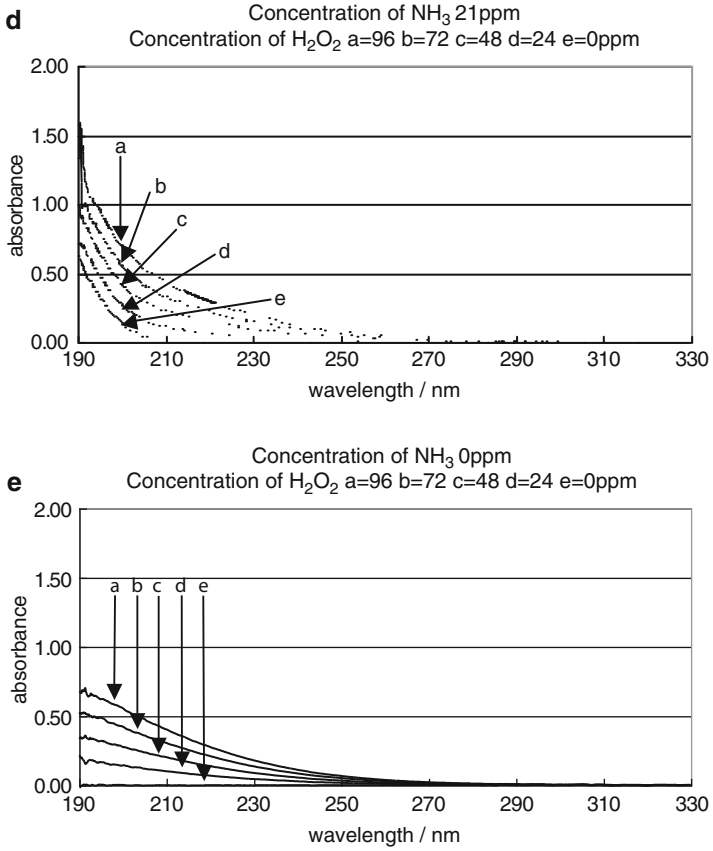

Fig. 5.7 (continued)

A PAA solution is prepared from acetic acid (AA) and hydrogen peroxide (H_2O_2) in the presence of an acidic catalyst, usually H_2SO_4 [27]. The equilibrium state is described by following equation:

$$CH_3COOOH + H_2O \overset{H^+}{\rightleftarrows} CH_3COOH + H_2O_2 \tag{5.1}$$

Thus, industrial PAA solutions always contain significant amounts of H_2O_2. The analysis method for PAA requires high selectivity and less cross-reaction with H_2O_2 and AA in their coexistence.

Here I demonstrate the usefulness of FUV absorption spectroscopy for direct determination of three species: PAA, H_2O_2, and AA in their coexistent solutions. This method enables highly rapid, selective, sensitive, and continuous determination of three species simultaneously without any reagents or complicated procedures.

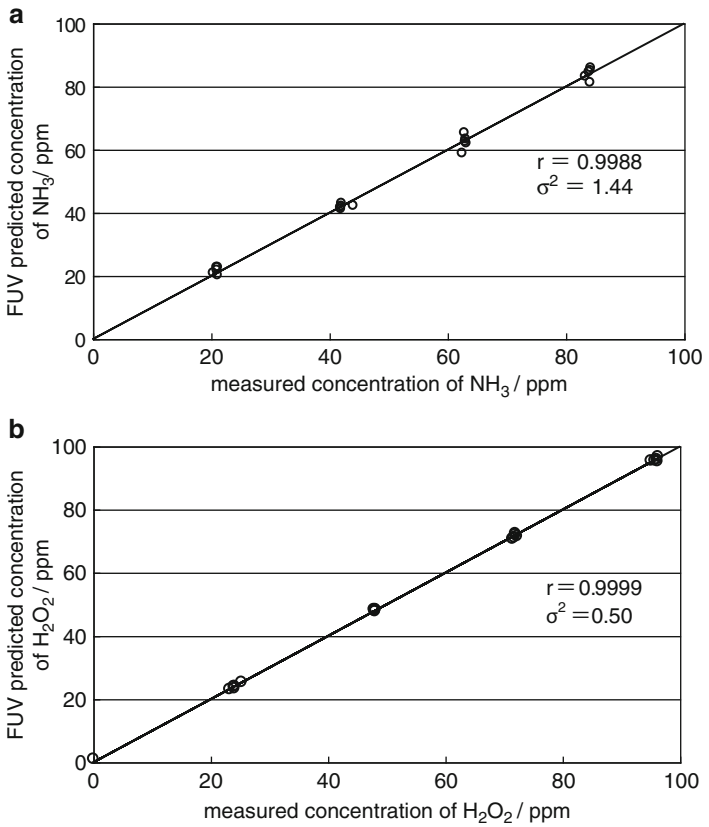

Fig. 5.8 Calibration models for predicting concentrations of NH_3 (**a**) and H_2O_2 (**b**) in aqueous solutions containing NH_3 and H_2O_2

Figure 5.9 depicts FUV absorption spectra of (a) an aqueous solution of AA with concentration of 1.7 wt%, (b) an aqueous solution of H_2O_2 with concentration of 0.2 wt%, and (c) a PAA disinfectant solution with concentrations of 0.86, 0.23, and 0.22 wt% of PAA, H_2O_2, and AA, respectively. The spectra in Fig. 5.9 were obtained using a commercial spectrometer (Shimadzu UV-visible spectrophotometer: UV-2550) and a cuvette cell of path length 10 mm. Figure 5.10 shows their second-derivative spectra. Figures 5.9 and 5.10 demonstrate that these spectra may be used for the measurement of each solute in the coexistence of their species.

To date, little attention has been given to the study that tries to use these absorption spectra for the determination of PAA in a disinfectant solution because a UV absorption band due to PAA in the disinfectant solution, which is measured by using an ordinary UV-visible spectrometer, has very small extinction coefficient in the concentration range lower than 0.2 wt%, and the UV band is usually interfered

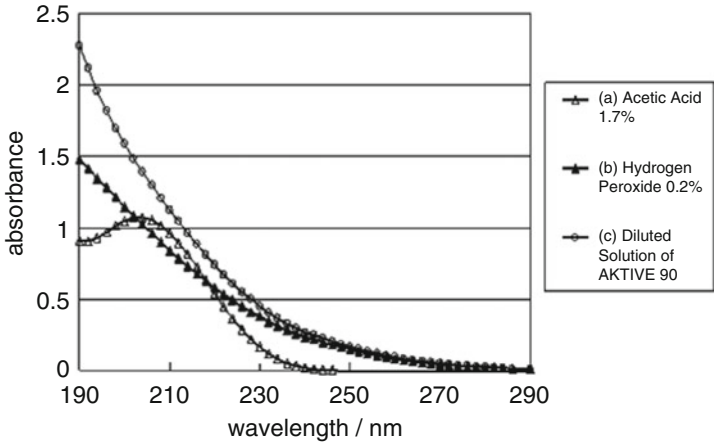

Fig. 5.9 FUV absorption spectra of (*a*) aqueous solution of AA with concentration of 1.7 wt%, (*b*) aqueous solution of H_2O_2 with concentration of 0.2 wt%, and (*c*) diluted PAA disinfectant solution (AKTIVE90) with concentrations of 0.86, 0.23, and 0.22 wt% for PAA, H_2O_2, and AA, respectively

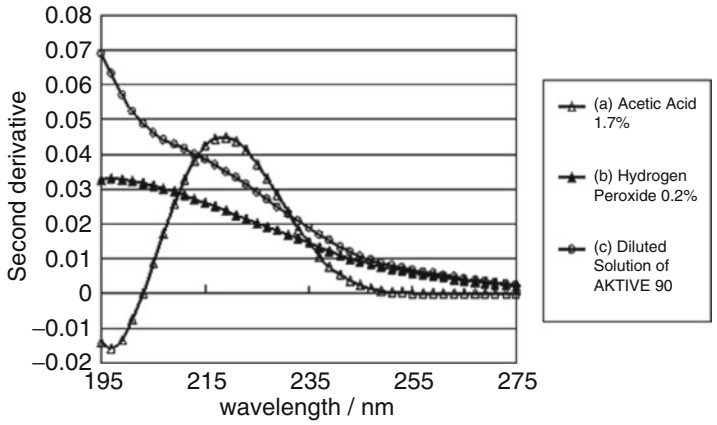

Fig. 5.10 Second-derivative spectra of FUV absorption spectra shown in Fig. 5.9

with the coexistence of a great deal of H_2O_2 in the disinfectant solution. The normal concentration ranges of PAA and H_2O_2 in disinfectant solutions are 0.15–0.2 wt% and 0.5–2.0 wt%, respectively. However, we have found that in diluted disinfectant solutions, a characteristic absorption band from PAA appears below 190 nm (in the vacuum ultraviolet region) because absorption intensity of H_2O_2 decreases with the dilution of disinfectant solutions, while the intensity of the absorption due to PAA remains below 190 nm. Figure 5.11 shows absorption spectra of (a) an aqueous solution of H_2O_2 with concentration of 0.02 wt% and (b) a diluted disinfectant solution containing 0.01 wt% of PAA, 0.02 wt% of H_2O_2, and 0.05 wt% of AA.

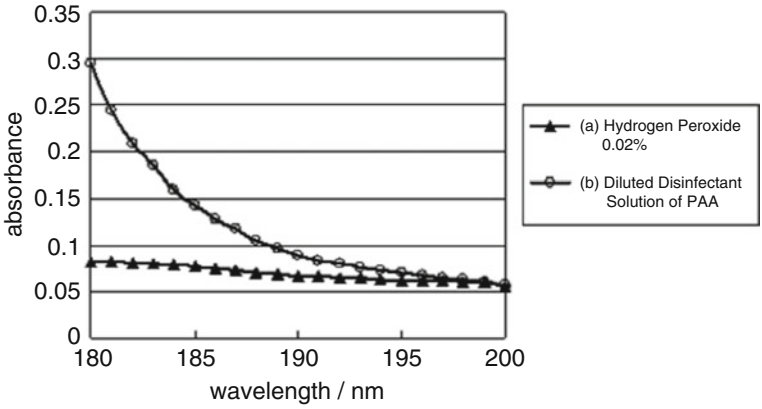

Fig. 5.11 FUV absorption spectra of (*a*) aqueous solution of H_2O_2 with concentration of 0.02 wt% and (*b*) diluted disinfectant solution of PAA with concentrations of 0.01, 0.02, and 0.05 wt% for PAA, H_2O_2, and AA, respectively

We constructed calibration models using 19 types of spectral data shown in Fig. 5.12 and Table 5.2. Figure 5.13a–c illustrate calibration models for predicting the concentrations of PAA, H_2O_2, and AA, respectively. As may be seen from Fig. 5.13, there is good agreement between spectral analysis and titration methods for all measured concentrations of the three species. Correlation coefficients and standard errors for prediction of PAA, H_2O_2, and AA were 0.969 and 0.002 w%, 0.997 and 0.003 w%, and 0.967 and 0.01 w%, respectively. This result demonstrates that inline monitoring of PAA concentration in disinfectant solution is possible with an accuracy of 0.002 wt%.

After we constructed the calibration models, we attempted measurement of a new sample, obtained by heating one of the 19 test samples (no.5) for 1 h at 60 °C to change concentrations due to decomposition. Predicted concentrations were again compared with titration results. Table 5.3 shows a comparison of titration and the FUV measurements. We conclude that the proposed method is quite useful for the measurement of these three species in disinfectant solutions of PAA.

5.4 Potential of Far-Ultraviolet Absorption Spectroscopy for Highly Sensitive Analysis of Polymer Films

Infrared (IR), near-infrared (NIR), and Raman spectroscopy have been successfully used for quantitative and qualitative analysis of polymer films. These methods leverage the fact that vibrational spectra are very sensitive to polymer structure and the strength of chemical bonds of functional groups. NIR spectroscopy has several practical advantages in polymer film analysis, including nondestructive and

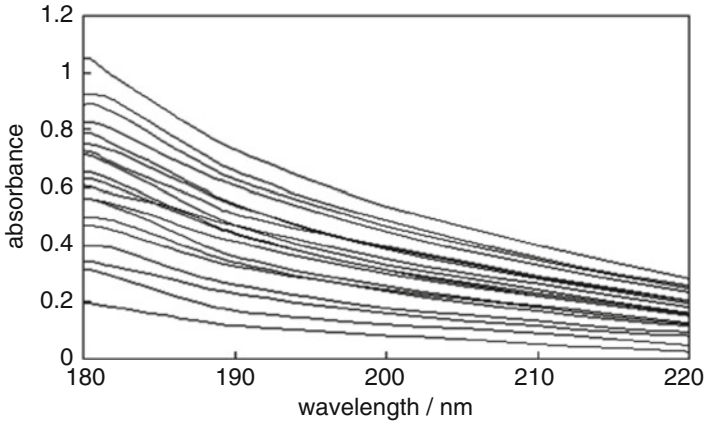

Fig. 5.12 FUV absorption spectra of the 19 types of sample solutions containing PAA, H_2O_2, and AA in differing concentrations. These spectra were used to construct calibration models

Table 5.2 Concentrations of PAA, H_2O_2, and AA in 19 sample solutions used to develop calibration models

	Concentrations [wt%]		
Sample no.	PAA	H_2O_2	AA
1	0.020	0.105	0.095
2	0.022	0.149	0.067
3	0.019	0.128	0.050
4	0.019	0.059	0.052
5	0.019	0.104	0.098
6	0.019	0.082	0.073
7	0.019	0.082	0.067
8	0.017	0.152	0.137
9	0.018	0.128	0.115
10	0.016	0.130	0.119
11	0.011	0.134	0.149
12	0.011	0.107	0.101
13	0.012	0.087	0.034
14	0.013	0.040	0.083
15	0.013	0.039	0.033
16	0.005	0.021	0.131
17	0.003	0.021	0.017
18	0.005	0.111	0.017
19	0.004	0.068	0.063

Concentrations were calculated by multiplying dilution ratios with concentrations measured by titration before dilution

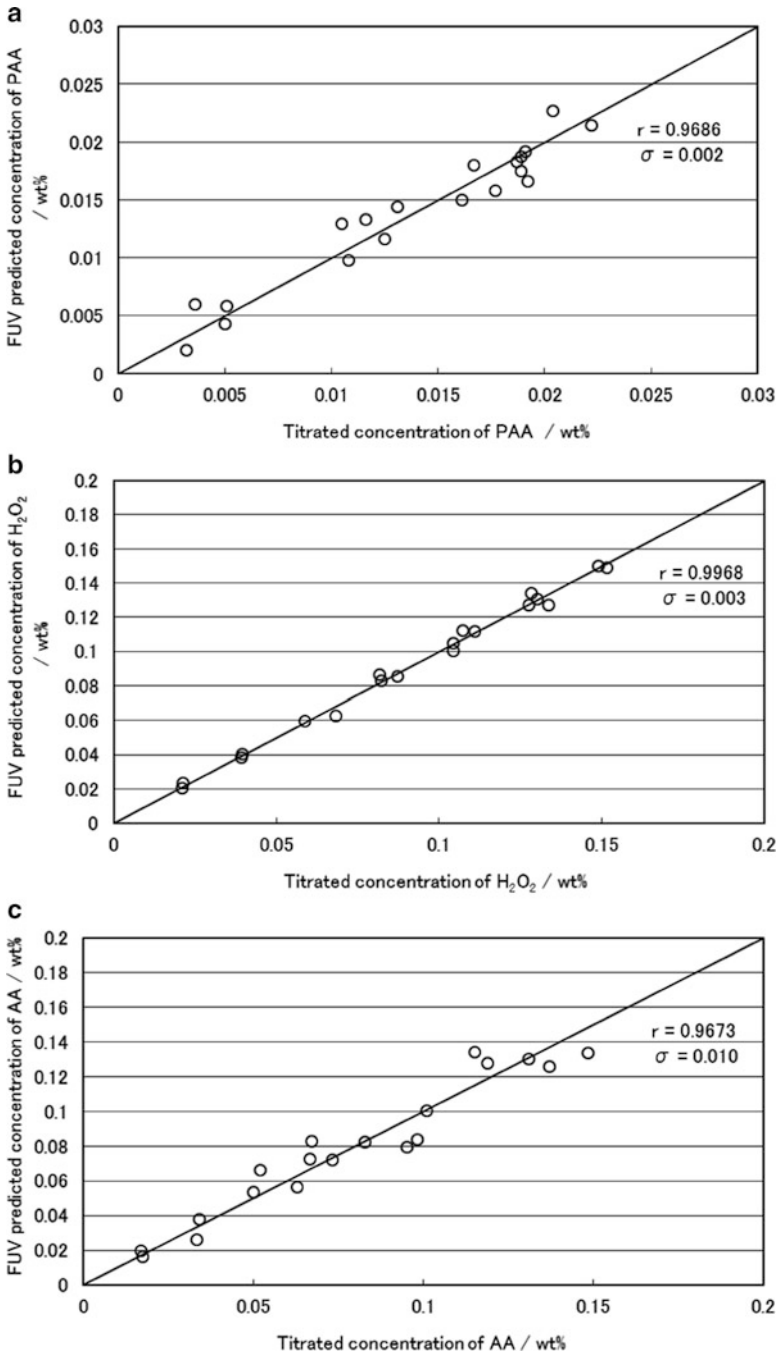

Fig. 5.13 Calibration models for predicting concentrations of (**a**) PAA, (**b**) H_2O_2, and (**c**) AA in concentration ranges of 0–0.02, 0–0.15, and 0–0.15 wt% for PAA, H_2O_2, and AA, respectively

Table 5.3 Comparison of concentrations measured by titration and FUV spectroscopy

	Concentrations [wt%]					
	Before heating			After heating		
Methods	PAA	H_2O_2	AA	PAA	H_2O_2	AA
Titration	0.189	1.044	0.981	0.137	1.048	0.992
FUV measurement	0.187	1.049	0.837	0.146	0.98	0.885

Concentrations were determined for sample no. 5 before and after heating. The FUV measurements were carried out after the ten-time dilution of the sample solutions

in situ measurements as well as the use of light fibers [28–38]. Therefore, NIR spectroscopy has been extensively utilized in polymer film analysis, particularly in inline process monitoring. Raman spectroscopy is also useful for nondestructive and in situ analysis of polymer films [28, 39–45], but this method often suffers from polymer fluorescence. Meanwhile, one of the disadvantages of vibrational spectroscopy is that polymer spectra are often complicated and difficult to interpret. This method necessitates sophisticated spectral analytical methods such as chemometrics [46–48] and two-dimensional correlation [49–51] to unravel the spectra obtained.

This study's goal is to demonstrate the potential of far-ultraviolet (FUV) spectroscopy in the region of 120–300 nm in polymer film analysis. FUV spectroscopy is known as a useful tool in a wide variety of processes, including quality control in crystal generation, thin film and filter analysis, measurement of inorganic ions, and next-generation lithography development [3, 9, 52]. However, FUV spectroscopy (especially involving the spectral region below 200 nm) has not become widely used due to strong absorption from oxygen. FUV instrumentation has seen significant recent progress. Using nitrogen gas purge instead of vacuum evaporation enables easier spectral measurements in the FUV region, as mentioned above. Nevertheless, FUV spectroscopy has not garnered much attention as an analytical method for polymer films.

In this section, I have demonstrated potential of FUV spectroscopy in the 120–300 nm region in the classification of commercial food wrap films (three types of polyethylene (PE), polyvinylidene chloride (PVDC), and polyvinyl chloride (PVC); see Table 5.4). Sato and I have measured FUV spectra in the 120–300 nm region of six types of commercial polymer wrap films [53]. FUV spectroscopy enables classification of polymer thin films in a straightforward manner by using raw spectral data. We also studied identification of three types of polyethylene PE films from different commercial companies. The FUV spectra of these PE films, which have very similar components and additives, are easily separated. The two types of PVDC films can also be identified. The present study has revealed that FUV spectroscopy is a very promising tool for the polymer film analysis.

Table 5.4 Components and additives of six types of commercial food wrap films

	Names	Components	Additives
Sample 1	KUREHA CORPORATION	Polyvinylidene chloride (PVDC)	Fatty acid derivatives
			Epoxidation vegetal oil
Sample 2	Asahi Kasei Co.	Polyvinylidene chloride (PVDC)	Fatty acid derivatives
			Epoxidation vegetal oil
Sample 3	RIKEN TECHNOS Corp.	Polyvinyl chloride (PVC)	Epoxidation vegetal oil
			Calcium compound
Sample 4	Ube Films Co.	Polyethylene (PE)	–
Sample 5	Takamatsuya Co.	Polyethylene (PE)	–
Sample 6	NIPPON PAPER-PAK CO., LTD	Polyethylene (PE)	–

5.4.1 Far-UV Spectra of Six Kinds of Food Wrap Films

Figure 5.14 shows FUV spectra in the 120–300 nm region of the six kinds of commercial food wrap films. All the FUV spectra are rather broad and simple, but it can be seen from Fig. 5.14 that the spectra of three kinds of PE films (Sample 4, Sample 5, and Sample 6), that of the PVC film (Sample 3), and those of the two kinds of PVDC films (Sample 1 and Sample 2) show clearly different spectral features from each other. The PE films show a broad feature below 170 nm and a weak absorption band near 185 nm. The broad feature below 170 nm is due to the σ-σ* transition of C–C bonds of PE, while the weak absorptions near 185 nm seem to come from small alkyl branches of the PEs as will be discussed below. Roughly speaking, a σ-σ* transition arises from the transition from a bonding orbital to an antibonding orbital, and its energy is nearly equal to the double of bonding energy. Ethane shows a band at 135 nm due to the σ-σ* transition of the C–C bond. The absorption maxima of the σ-σ* transition bands of the PE films are not clear in Fig. 5.14 but should be located below 165 nm. The corresponding transitions of PVC and PVDC are shifted to a longer-wavelength region because the σ-σ* transitions of C–C bonds are affected by the existence of C–Cl bond. PVC and PVDC have one and two C–Cl bonds in the polymer units, respectively, and thus PVDC shows much larger longer-wavelength shift.

Figure 5.15a, b show FUV spectra in the 120–300 nm region of pristine polymer films of three kinds of PEs (HDPE, LDPE, and LLDPE) and PVC, respectively. We cannot discuss the differences in the band intensities of these spectra below 170 nm because it was difficult to control the film thickness by casting the samples. However, it is clear from Fig. 5.15a that the intensity of the absorption band near 185 nm is quite different among the three kinds of PE films. LDPE, which has the large side chains compared with HDPE and LLDPE, shows a significantly stronger band near 185 nm. Thus, it is likely that the band near 185 nm is due to the branches of the PEs.

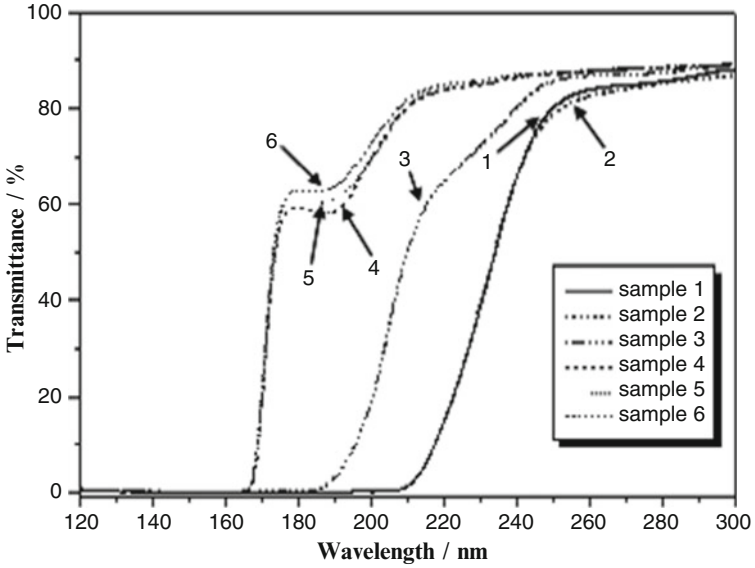

Fig. 5.14 FUV spectra in the 120–300 nm region of two types of PVDC films (Sample 1 and Sample 2), one type of PVC film (Sample 3), and three types of PE films (Sample 4, Sample 5, and Sample 6)

The bonding energy of a C–C bond changes with substituents on the C atoms, and thus the σ-σ* transition is very sensitive to the substituents. Thus, FUV spectra of substituted hydrocarbon compounds also change with the kinds and the number of the substituents. In other words, FUV spectroscopy holds considerable promise as a qualitative analysis method of polymers. It is important to note that the six kinds of polymer films are clearly discriminated by using the raw data in the 120–300 nm region. In this paper, I do not mention thickness dependences of polymer thin films on far-UV spectra, but FUV spectroscopy may be used to determine the film thickness. The spectral region of FUV spectroscopy is so wide (100–300 nm) that polymer films with a wide variety of thickness may be subjected to spectral measurements. The observations in Fig. 5.14 suggest that the FUV spectra in the 120–300 nm region may be used as a highly sensitive and selective tool for polymer film analysis, in general.

5.4.2 Comparison of Far-Ultraviolet Spectra of Three Types of Polyethylene Films and Two Types of Polyvinylidene Chloride Films

It is important to compare the FUV spectra of three types of polyethylene films. Note that the three types of PE films can be clearly differentiated (Fig. 5.14). The

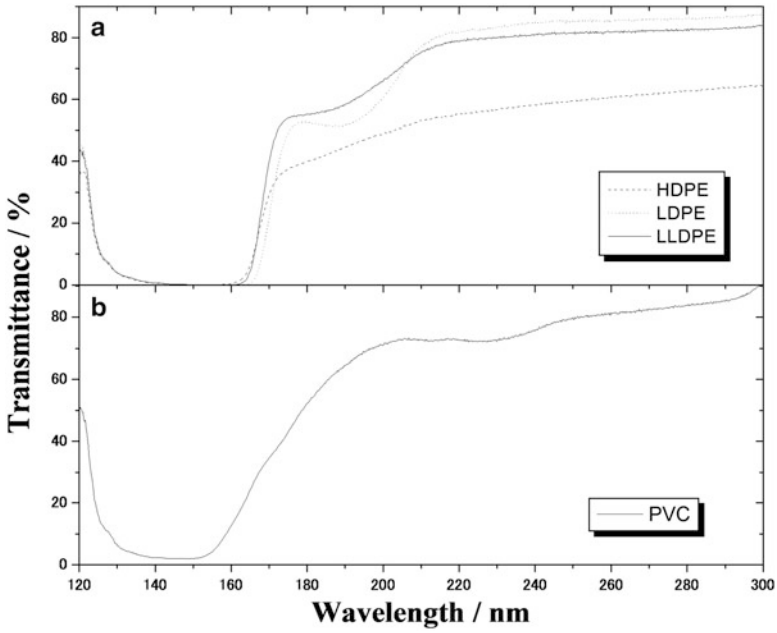

Fig. 5.15 (**a**) Far-UV spectra in the 120–300 nm region of three types of polyethylenes (high-density polyethylene (HDPE), low-density polyethylene (LDPE), and linear low-density polyethylene (LLDPE)). (**b**) Far-UV spectrum of PVC

intensity of the band near 185 nm differs significantly among the three film types. PE wrap films are usually made from LLDPE or LDPE, which have branches on the PE chains to control density; number and types of branches may differ among PE film type. It is thus highly likely that small differences in the types and numbers of branches cause significant variations in FUV spectra. Figure 5.16 shows second-derivative FUV spectra of three types of PE film. Comparing these spectra shows a slight difference in the inflection point of the FUV curves among Sample 4, Sample 5, and Sample 6.

Figure 5.17 shows first-derivative FUV spectra of two types of PVDC films (Sample 1 and Sample 2). These spectra demonstrate sigmoid curves, so second-derivative spectra could not be used for the spectral analysis, which shows that inflection points of the FUV spectra are slightly different between Sample 1 and Sample 2.

This study has revealed the usefulness and unique properties of FUV spectroscopy in polymer film analysis. This methodology is still developing and holds considerable promise for various forms of polymer analysis. In summary, it offers the following advantages: (1) nondestructive and in situ analysis, (2) easy spectral measurement and analysis, and (3) high sensitivity and high selectivity.

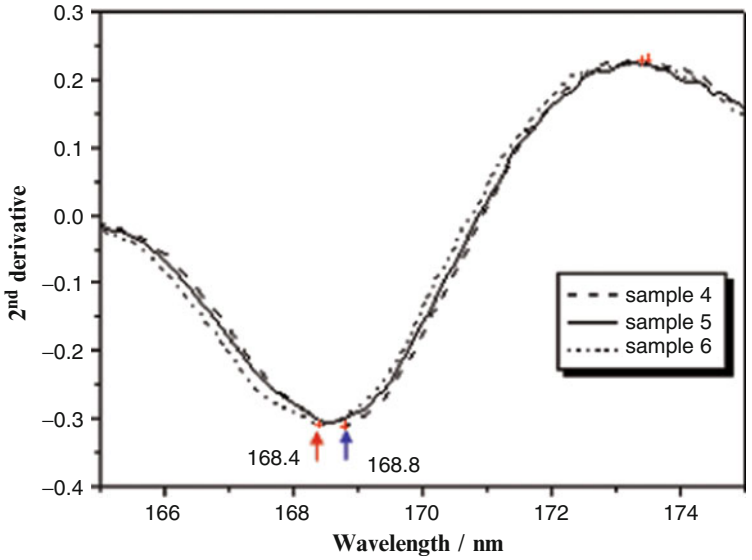

Fig. 5.16 Enlarged second-derivative FUV spectra of three types of PE films shown in Fig. 5.14

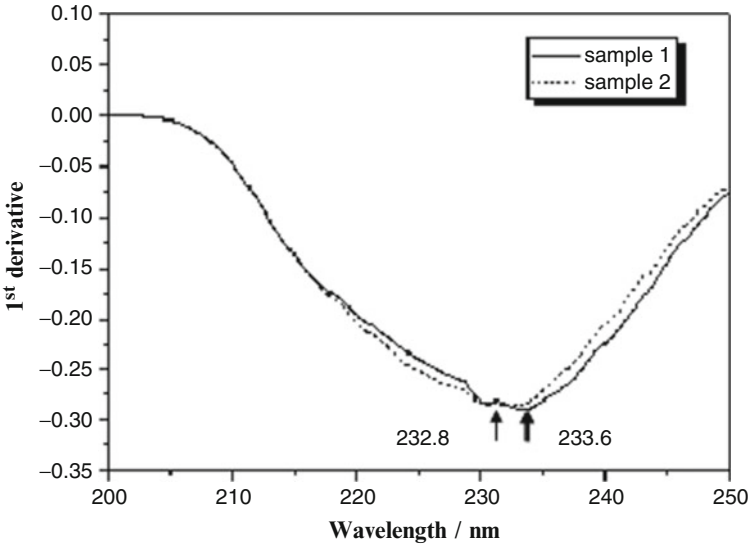

Fig. 5.17 Enlarged first-derivatives FUV spectra of two types of PVDC films shown in Fig. 5.14

References

1. J. Workman, A. Springsteen (eds.), *Applied Spectroscopy* (Academic, New York, 1998)
2. T. Owen, *Fundamentals of Modern UV-Visible Spectroscopy-A Primer* (Hewlett-Packard, Palo Alto, 1996)
3. N. Ogura, T. Hanya, Nature (London) **212**, 758 (1966)
4. P. Foster, Water Res. **19**, 701 (1985)
5. M.A. Ferree, R.D. Shannon, Water Res. **35**, 327 (2001)
6. N. Higashi, Y. Ozaki, Appl. Spectrosc. **58**, 910 (2004)
7. N. Higashi, H. Yokota, S. Hiraki, Y. Ozaki, Anal. Chem. **77**, 2272 (2005)
8. N. Higashi, A. Ikehata, N. Kariyama, Y. Ozaki, Appl. Spectrosc. **62**, 1022 (2008)
9. V.D. Noto, M. Mecozzi, Appl. Spectrosc. **9**, 1294 (1997)
10. H.J. Maria, J.R. Mcdonald, S.P. McGlynn, J. Am. Chem. Soc. **95**, 1050 (1973)
11. D. Majumdar, J. Kim, K.S. Kim, J. Chem. Phys. **112**, 101 (2000)
12. M. Mitsuoka, H. Shinzawa, Y. Morisawa, N. Kariyama, N. Higashi, M. Tsuboi, Y. Ozaki, Anal. Sci. **27**(2), 177 (2011)
13. N. Urai, Clean Techn. **4**, 16 (2001)
14. W. Kern, D.A. Puotinen, RCA Rev. **31**, 187 (1970)
15. M. Itano, F.W. Kern Jr., M. Miyashita, T. Ohmi, IEEE Trans. Semicond. Manuf. **6**, 258 (1993)
16. Y. Lee, S. Nah, H. Namkung, H. Chung, Appl. Spectrosc. **59**, 952 (2005)
17. D.P. Stevenson, G.M. Coppinger, J.W. Forbes, J. Am. Chem. Soc. **83**, 4350 (1961)
18. M.J. Blandamer, M.F. Fox, Chem. Rev. **70**, 59 (1970)
19. J.H. Taylor, S.J. Rogers, J.T.J. Holah, Appl. Microbiol. **87**, 718 (1999)
20. M.G.C. Baldry, J. Appl. Bacteriol. **54**, 417 (1983)
21. S.S. Block, *Peroxygen Compounds: IN: Disinfection, Sterilization and Preservation* (Lea and Febiger, Philadelphia, 1991), pp. 167–181
22. P.A. Lynam, J.R. Babb, A.P. Fraise, J. Hosp. Infect. **30**, 237 (1995)
23. L.A. Jones Jr., R.K. Hoffman, C.R. Phillips, Appl. Microbiol. **15**, 357 (1967)
24. D. Swern, *Organic Peroxides* (Wiley-Interscience, New York, 1970), p. 360
25. M.S. Philip, in *Polymers, Laminations & Coatings Conference*, TAPPI Proceedings, vol. 1 (1990), pp. 293–300
26. R. Nicolas, N. Nishitani, Beverage Jpn. **169**, 62 (1996)
27. G. Boullion, C. Lick, K. Schank, in *The Chemistry of Functional Groups, Peroxides*, ed. by S. Patai (Wiley, London, 1983), pp. 287–298
28. H.W. Siesler, K. Holland-Moritz, *Infrared and Raman Spectroscopy of Polymers, Practical Spectroscopy Series*, vol. 4 (Marcel Dekker, New York, 1980)
29. C.E. Miller, Appl. Spectrosc. Rev. **26**, 277 (1991)
30. J.D. Tate, P. Chauvel, R.D. Guenard, R. Harner, in *Handbook of Vibrational Spectroscopy*, ed. by J.M. Chalmers, P.R. Griffiths, vol. 4 (Wiley, New York, 2002), p. 2737
31. H.W. Siesler, Y. Ozaki, S. Kawata, H.M. Heise (eds.), *Near-Infrared Spectroscopy* (Wiley-VCH, Weinheim, 2002)
32. K.A.B. Lee, Appl. Spectrosc. Rev. **28**, 231 (1993)
33. K. Molt, D. Ihlbrock, Fresenius J. Anal. Chem. **348**, 523 (1994)
34. B. Chabert, G. Lachenal, C. Vinh Tung, Macromol. Chem. Macromol. Symp. **94**, 145 (1995)
35. G. Lachenal, Vib. Spectrosc. **9**, 93 (1995)
36. M.P.B. van Uum, H. Lammers, J.P. de Kleijin, Macromol. Chem. Phys. **196**, 2023 (1995)
37. M.M. Dumoulin, R. Gendron, K.C. Cole, TRIP **4**, 109 (1996)
38. Y. Ozaki, T. Amari, in *Spectroscopy in Process Analysis*, ed. by J.M. Chalmers (Sheffield Academic Press, Sheffield, 2000), p. 53
39. H. Sato, S. Sasao, K. Matsukawa, Y. Kita, T. Ikeda, H. Tashiro, Y. Ozaki, Appl. Spectrosc. **56**, 1038 (2002)
40. H. Sato, M. Shimoyama, T. Kamiya, T. Amari, S. Šašić, T. Ninomiya, H.W. Siesler, Y. Ozaki, J. Appl. Polym. Sci. **86**, 443 (2002)

41. D.N. Batchelder, C. Cheng, G.D. Pitt, Adv. Mater. **3**, 566 (1991)
42. A.H. Fawcett (ed.), *Polymer Spectroscopy* (Wiley, Chichester, 1996), Chapter 7 and 8
43. N. Everall, P. Tayler, J.M. Chalmers, D. MacKerron, R. Ferwerda, J.H. van der Maas, Polymer **35**, 3184 (1994)
44. G. Zerbi, M. Del Zoppo, in *Modern Polymer Spectroscopy*, ed. by G. Zerbi (Wiley-VCH, Weinheim, 1999), p. 87
45. M.J. Pelletier (ed.), *Analytical Applications of Raman Spectroscopy* (Blackwell Science, Oxford, 1999)
46. H. Martens, T. Naes, *Multivariate Calibration* (Wiley, New York, 1989)
47. B.G.M. Vandenginste, D.L. Massart, L.M.C. Buydens, S. de Jong, P.J. Lewi, J. Smeyers-Verbeke, *Handbook of Chemometrics and Qualimetrics* (Elsevier, Amsterdam, 1998)
48. R. Kramer, *Chemometric Techniques for Quantitative Analysis* (Marcel Dekker, New York, 1998)
49. I. Noda, Appl. Spectrosc. **47**, 1329 (1993)
50. I. Noda, A.E. Dowrey, C. Marcott, G.M. Story, Y. Ozaki, Appl. Spectrosc. **54**, 236A (2000)
51. I. Noda, Y. Ozaki, *Two-Dimensional Correlation Spectroscopy* (Wiley, Chichester, 2004)
52. E. Bonera, G. Scarel, M. Fanciulli, J. Non-Cryst. Solids **322**, 105 (2003)
53. H. Sato, N. Higashi, A. Ikeda, N. Koide, Y. Ozaki, Appl. Spectrosc. **61**, 780 (2007)

Chapter 6
Electronic Structure of TiO_2 Studied by Far-Ultraviolet and Deep-Ultraviolet Spectroscopy

Ichiro Tanabe

Abstract The electronic structure and photocatalytic activities of TiO_2 and metal-nanoparticle-modified TiO_2 were investigated by far-ultraviolet and deep-ultraviolet spectroscopy and photodegradation reaction of methylene blue. First, spectra of naked anatase TiO_2 (Sect. 6.2) and metal (Au, Pd, Pt)-nanoparticle-modified TiO_2 (Sect. 6.3) were measured. The naked TiO_2 spectrum corresponded well with the previously reported reflection spectrum and theoretical calculations. Then, the deposition of metal nanoparticles substantially changed the spectral shape, which indicates changes in the electronic states of TiO_2, and the degree of spectral changes strongly depends on the work function of the modified metal. In addition, consistent changes of photocatalytic activities were also observed. Next, two crystalline types of TiO_2 (anatase and rutile) were compared (Sect. 6.4), and a larger enhancement of the photocatalytic activity of rutile TiO_2 upon Pt nanoparticle deposition was revealed. Subsequently, size effects of modified Au nanoparticle on electronic structures and photocatalytic activities of TiO_2 were discussed (Sect. 6.5), and it was made clear that the smaller Au nanoparticle induced the larger electronic-state changes and the higher photocatalytic-activity enhancements. These results demonstrated that the novel far-ultraviolet and deep-ultraviolet spectroscopy is a considerable promising method to investigate the electronic states of materials, leading to the development of high-efficiency optical materials such as photocatalysts and solar cells.

Keywords Titanium dioxide • TiO_2 • Metal nanoparticle • Photocatalyst • Photocatalytic activity

I. Tanabe (✉)
Department of Chemistry, School of Science and Technology, Kwansei Gakuin University, Gakuen 2-1, Sanda, Hyogo, Japan
e-mail: dnv62544@kwansei.ac.jp

Y. Ozaki, S. Kawata (eds.), *Far- and Deep-Ultraviolet Spectroscopy*,
DOI 10.1007/978-4-431-55549-0_6

6.1 Introduction

6.1.1 *TiO_2 and Metal-Nanoparticle-Modified TiO_2 as Photo-Functional Materials*

TiO_2 is considered one of the most attractive materials in a wide range of fields [1–6] and may find application as a photocatalyst [1–3] and next-generation solar-cell material [4–6]. It shows photocatalytic activity under ultraviolet (UV, <400 nm), deep-UV (DUV, <300 nm), and far-UV (FUV, <200 nm) irradiation, as its bandgap is ~3.2–3.0 eV [7]. Under irradiation with these lights, the electrons in the valence band of TiO_2 are promoted into the conduction band, and, at the same time, corresponding holes are generated in the valence band. This photoinduced charge separation is the main cause of its photocatalytic activity; the enhanced electrons and generated holes are then consumed by reduction and oxidation reactions, respectively. Several studies have confirmed that a variety of reactions can be promoted in the presence of TiO_2 and UV light, such as alcohol dehydration [8], oxidation of organic materials [9], and reduction of nitrogen oxide [10]. TiO_2 can even promote water splitting, which produces hydrogen and oxygen [11]. Therefore, it can be applied for the purification of water and air. In addition, TiO_2 is expected to be also suitable for solar cells based on photoinduced charge separation [4–6].

However, the quantum yields of most photocatalytic reactions and incident photon-to-current conversion efficiency of naked TiO_2 are extremely low (<1 %) [12]. To address this issue, a number of studies have been proposed for enhancing the charge-separation efficiency of TiO_2 [13–15]. For example, doping TiO_2 with various transition metal cations (Fe^{3+}, Ru^{3+}, V^{4+}, etc.) [13] and anions such as F^- [14] can increase its photocatalytic activity. The modification of TiO_2 with quantum dots [6] and dye molecules [4, 5] expands its wavelength range to the visible region; quantum-dot and dye-sensitive solar cells are thus considered promising candidates as the next-generation solar cells.

Among other systems, the combination of TiO_2 with metal nanoparticles has been extensively investigated in recent decades by many research groups [1, 16–21]. Loading TiO_2 with Pt nanoparticles increases its activity for hydrogen-production reactions from water and other photocatalytic reactions [16, 17]. The deposition of other metal nanoparticles (e.g., Ag, Au, Pd, and Ir) [18] also improves the photocatalytic activity of TiO_2. These metal nanoparticles function as a photoexcited electron sink, as the electron transfer from TiO_2 to metals shifts the Fermi level of TiO_2 to negative potentials, thus enhancing the photoinduced charge-separation efficiency [20, 21].

6.1.2 *Attenuated Total Reflectance (ATR)–DUV–FUV Spectroscopy*

As mentioned above, naked TiO_2 can be activated by UV, DUV, and FUV irradiations. However, the measurement of the optical properties of TiO_2 in these regions is complicated by its very large absorption (in the 200–300-nm region, the absorbance index α is $\sim 10^6$–10^7 cm^{-1}) [22]. Irradiation in the DUV–FUV region can provide critical information about the electronic states of materials and is typically employed for research activities and a diverse range of applications [23–25]; therefore, the investigation of TiO_2 and modified TiO_2 materials in this region is very important. However, only a few studies provide systematic information about the modification of TiO_2 through spectrum observations in the DUV–FUV region. Most spectroscopic investigations in this region have been carried out only by reflectance or diffuse reflectance spectra measurements, and the measurement ranges were mostly limited to the DUV region (>200 nm) [26]. Moreover, the effects of surface modifications such as metal nanoparticle deposition on TiO_2 electric states cannot be easily estimated; thus, many studies on the enhancement of the charge-separation efficiency of TiO_2 are performed using polycrystalline TiO_2 powders and films [18–21]. Therefore, a versatile DUV–FUV measurement method that can be applied not only to single crystals but also to polycrystalline forms is needed.

We have recently developed a completely new DUV–FUV spectrometer based on ATR [23–25] that enables the measurement of the spectra of liquid and solid samples such as water [27], aqueous solutions [28, 29], and organic molecules [30–32] in the 140–300-nm region. During the ATR–DUV–FUV measurement, samples are typically placed on a sapphire internal reflection element (IRE), and ATR spectra are measured using the evanescent wave as a probe light [27]. This method allowed us for the first time to successfully observe the entire first electronic-transition absorption band of water and aqueous solutions without band saturation [27–29]. Moreover, a comparison of the observed spectra of organic molecules such as alkanes [32], alcohols [30], and ketones [31] with the corresponding quantum chemical calculations revealed the existence of Rydberg transitions in the liquid states. The more detailed description of the instrument is described in Chap. 2 *Instrumentation for FUV spectroscopy*.

6.2 Electronic States of Anatase TiO_2 Studied by DUV–FUV Spectroscopy [33]

Figure 6.1a shows a typical DUV–FUV spectrum in the 150–300-nm region of a commercial anatase TiO_2 particle (diameter = $\sim$5 μm, ST-41, Ishihara Sangyo Kaisha, Ltd.). As the refraction index at 250 nm of anatase TiO_2 ($\sim$2.5) is higher than that of sapphire ($\sim$1.8), ATR does not occur at their interface. However, the contact area between TiO_2 and the sapphire IRE is very small (point contact, ide-

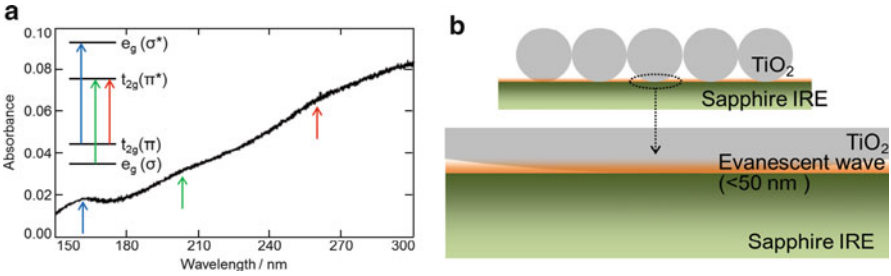

Fig. 6.1 (**a**) A typical DUV–FUV spectrum of TiO_2 and (**b**) the ATR-spectrometer measurement scheme

ally), because a spherical TiO_2 particle was used. Therefore, the absorption spectra of TiO_2 in the evanescent wave range were successfully measured (Fig. 6.1b). In this case, the penetration depth of the evanescent wave is less than 50 nm, with an incident angle of 70° and a measured wavelength region of 150–300 nm in air ($n = 1$).

In a previous study of Hosaka and coworkers [34], the reflection spectra of anatase TiO_2 single crystals were measured in the 40–620-nm wavelength range using synchrotron orbital radiation. According to these studies, the measured reflection spectra of anatase TiO_2 have three peaks in the 150–300-nm region (at ~155, 200, and 260 nm), in agreement with the absorption spectrum discussed here. The measured spectra were interpreted based on electronic-structure calculations performed by these authors [34, 35] and other research groups [36]. Hosaka and coworkers calculated the electric states of anatase TiO_2 using the linear combination of atomic orbital (LCAO) approximation with a discrete variational (DV)-Xα method based on the TiO_6 cluster model. By comparing the experimental and calculated spectra, they assigned the spectra in the 120–400-nm range to the transition from O(2p) to Ti(3d) states.

In addition, Sério and coworkers [37] measured the DUV–FUV absorption spectra of TiO_2 using a synchrotron-radiation facility; however, as they reported, only the data obtained in the DUV region (>200 nm) were considered to be reliable because of a strong influence of the adsorbed water. In line with their results, in our study we observed very weak and broad absorption bands at ~200 and 260 nm (Fig. 6.1a). Sério and coworkers assigned these two bands to the $e_g(\sigma) \rightarrow t_{2g}(\pi^*)$ and $t_{2g}(\pi) \rightarrow t_{2g}(\pi^*)$ transitions, respectively, based on a molecular orbital energy-level diagram [19] and band structures [19, 36] calculated by other groups. The comparison of the present DUV–FUV spectrum with these calculations suggests that the clear peak at 160 nm may be assigned to the $t_{2g}(\pi) \rightarrow e_g(\sigma^*)$ transition (inset in Fig. 6.1a). It should be noted that the upper $t_{2g}(\pi^*)$ and $e_g(\sigma^*)$ and lower $t_{2g}(\pi)$ and $e_g(\sigma)$ orbitals mainly consist of Ti(3d) and O(2p) orbitals, respectively.

The present spectral shape in the 150–180-nm region clearly differs from that of water, and thus the measurement of the absorption spectrum of TiO_2 in the 150–300-nm region, including the FUV region, was successfully achieved. The

assignments of the three bands to these electric states were confirmed by the reported theoretical calculations. Notably, this DUV–FUV spectrum was obtained using a 30-W deuterium lamp and commercial TiO_2 powder, instead of synchrotron orbital radiation and a TiO_2 single crystal.

6.3 Consistent Changes in the Electronic States and Photocatalytic Activities of TiO_2 upon Metal (Au, Pd, Pt)-Nanoparticle Deposition [33]

6.3.1 TiO_2 Spectral Changes upon Metal-Nanoparticle Deposition

TiO_2 and metal (Pt, Pd, Au) colloids were mixed in an agate mortar until the solvent completely evaporated. The DUV–FUV spectra of TiO_2 with Pt nanoparticles (diameter = 1–6 nm) were then measured. Figure 6.2 compares the DUV–FUV spectra of the TiO_2–Pt nanoparticles with that of TiO_2. When the amount of the mixed Pt nanoparticle is 0.04 wt% (green line in Fig. 6.2), the absorption intensity at longer wavelengths decreases, while that at shorter wavelengths increases upon Pt-nanoparticle deposition. The amount of the mixed Pt nanoparticle was changed from 0.02 to 0.12 wt%. The DUV–FUV spectrum of TiO_2 mixed with the 0.04 wt% Pt nanoparticle showed the largest increase in the shorter-wavelength region; when the amount of the Pt-nanoparticle was larger than 0.06 wt%, the absorption intensity was suppressed in the entire wavelength range. This indicates that the increase in the shorter-wavelength region is not due to the absorption of Pt nanoparticles.

If TiO_2 comes in contact with a metal with a higher work function, the electrons in TiO_2 flow into the metal until the Fermi levels become equal [1]. In this study, we

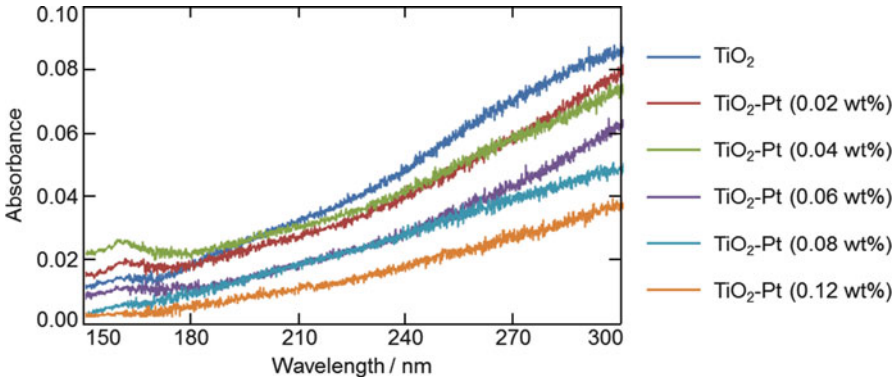

Fig. 6.2 DUV–FUV spectral changes of TiO_2 with various concentrations (0.00–0.12 wt%) of Pt nanoparticles

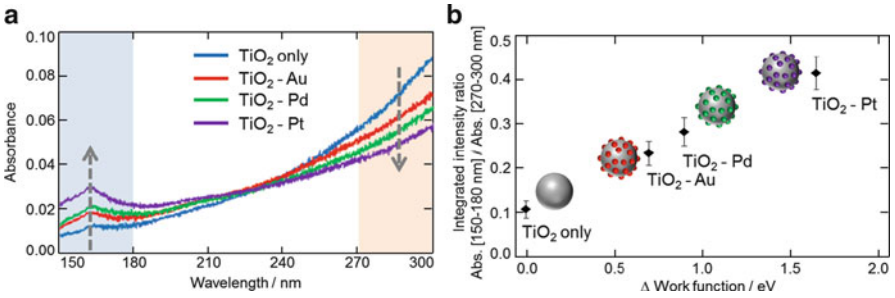

Fig. 6.3 (**a**) DUV–FUV spectra of TiO_2 (*blue*) and Au (*red*)-, Pd (*green*)-, and Pt (*purple*)-modified TiO_2. (**b**) Integrated intensity ratio between the absorption in the 150–180-nm region and that in the 270–300-nm region vs. the work-function difference between TiO_2 and each metal

determined the work functions of TiO_2 and Pt to be ~4.0 and 5.7 eV, respectively; thus, the electrons transfer from TiO_2 to Pt. As a result, the number of electrons in the relatively high-energy levels (i.e., electrons that can be excited at a relatively longer wavelength) is decreased, leading to a suppression of the absorption intensity at longer wavelengths. However, a Pt nanoparticle on TiO_2 can act as a sink for the photoexcited electrons [20, 21], which can enhance the charge-separation efficiency as described in Sect. 6.1.1. This results in an increase in the absorption intensity at shorter wavelengths. This enhancement may also occur at longer wavelengths; however, in this case, the total change of the absorption intensity is affected by both the enhancement and the decrease in the electrons upon contact of TiO_2 with Pt.

In addition, we also used Pd and Au instead of Pt nanoparticles on TiO_2 and measured the DUV–FUV spectra of the resulting systems (Fig. 6.3a). In all the studied cases, the absorption intensity at longer wavelengths decreases, while that at shorter wavelengths increases. The absorption intensity over the entire wavelength region changes by several percentage points depending on the sample, because the TiO_2 particle is not a perfect sphere; as a result, the amount of TiO_2 in the evanescent wave changes, but the spectral shapes of each sample are virtually the same. In order to provide an in-depth description of the degree of the spectral changes, we calculated an integrated intensity ratio between the absorption in the 150–180-nm region and that in the 270–300-nm region.

The integrated intensity ratios of TiO_2, TiO_2–Au, TiO_2–Pd, and TiO_2–Pt were determined to be 0.133 ± 0.018, 0.252 ± 0.025, 0.295 ± 0.030, and 0.423 ± 0.035 nm (average $\pm$ standard deviation, $n = 15$), respectively. Figure 6.3b displays the plots of the obtained ratios as a function of the difference in the work function between TiO_2 (~4.0 eV) and each metal (Au, Pd, Pt ~4.7, 4.9, 5.7 eV, respectively). Notably, a strong positive correlation between the intensity ratio and the work-function difference was found, indicating that a larger work-function difference results in a larger number of electrons that flow from TiO_2 into the metal as well as stronger enhancement of the charge separation.

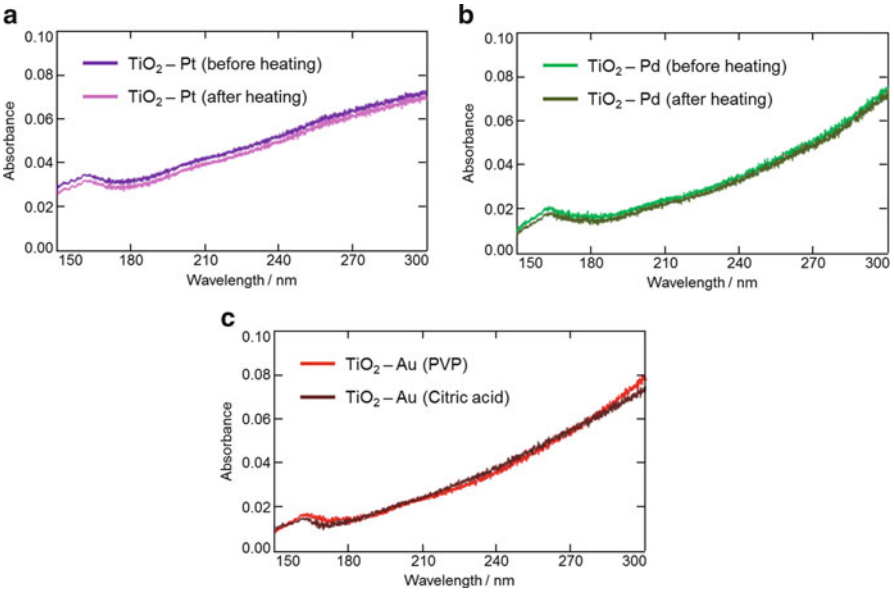

Fig. 6.4 (**a**) DUV–FUV spectra of TiO_2–Pt nanoparticles before (*purple*) and after (*pink*) heating (at 200 °C for 1 h, to remove the protecting agent PVP). (**b**) ATR–FUV spectra of TiO_2–Pd nanoparticles before (*green*) and after (*deep green*) heating (200 °C, 1 h). (**c**) ATR–FUV spectra of TiO_2–Au protected by PVP (*red*) and citric acid (*brown*) nanoparticles

To confirm the effect of the protecting agent (PVP) of the metal nanoparticles, it was removed by heating TiO_2–Pt (Fig. 6.4a) and TiO_2–Pd (Fig. 6.4b) at 200 °C for 1 h [38]. The DUV–FUV spectra did not change; in addition, a comparison of the DUV–FUV spectra of TiO_2–Au protected by PVP and citric acid (Fig. 6.4c) hardly differed. These results clearly suggest that the protecting agents have no substantial effects on the DUV–FUV spectra.

6.3.2 *Photocatalytic-Activity Enhancement of TiO_2 upon Metal-Nanoparticle Deposition*

The photocatalytic activities of TiO_2 and TiO_2 modified with Au, Pt, and Ad nanoparticles were estimated by the photodegradation reaction of methylene blue. Methylene blue was purchased from Wako Pure Chemical Industries, Ltd. A Hg–Xe lamp (Luminar Ace LA-300UV, Hayashi Watch Works) equipped with a UV-pass filter (wavelength = 300–350 nm, UTVAF-50S-34U, CVI Laser, LLC.) was used as the UV-light source. Methylene blue aqueous solution (10 μM, 10 mL) was mixed with TiO_2, TiO_2–Au, TiO_2–Pd, and TiO_2–Pt powder (5 mg) using a magnetic stirrer, followed by UV irradiation (~10 μW cm^{-2}) for 60 min. After the irradiation, TiO_2

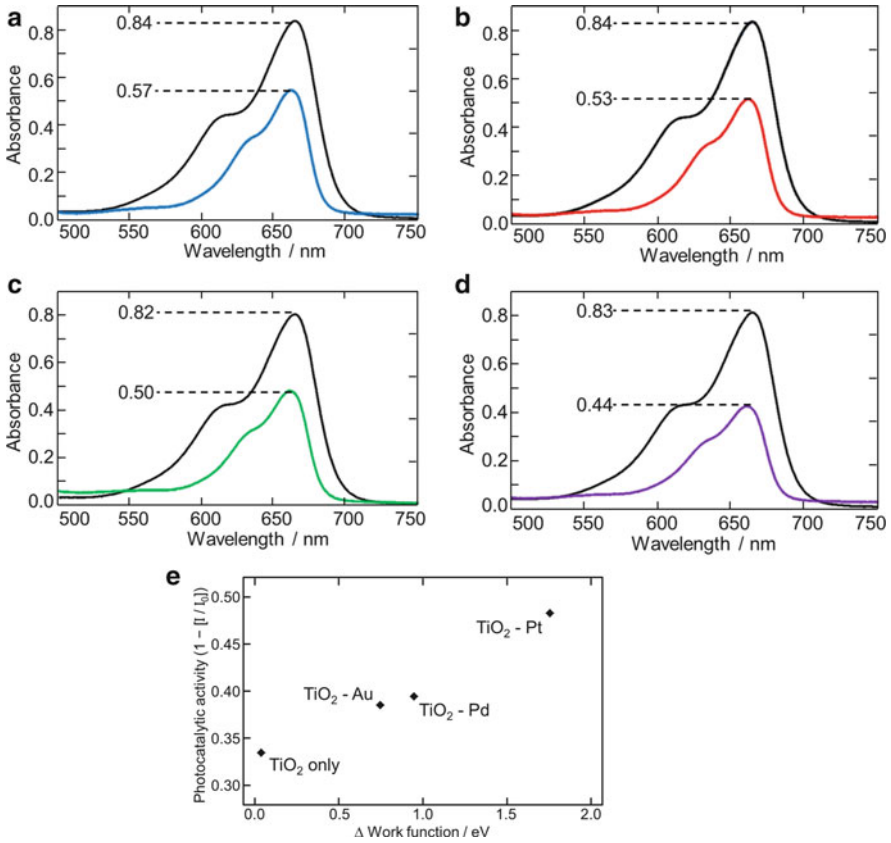

Fig. 6.5 (**a**–**d**) Absorption spectra of methylene blue aqueous solution before (*black*) and after (*color*) UV irradiation with (**a**) TiO_2 and (**b**) Au-, (**c**) Pd-, and (**d**) Pt-modified TiO_2. *Inset* values represent the absorption at 665 nm. (**e**) Photocatalytic activity ($1 - [I/I_0]$) plotted against the work-function difference between TiO_2 and each metal

was separated from the solution by centrifugation (15,000 rpm, 1 min). Before and after the UV irradiation, absorption spectra of the methylene blue aqueous solution were measured; the results are shown in Fig. 6.5a–d. The photocatalytic activity of each sample was estimated using Eq. (6.1), where I_0 and I represent the absorption intensities at 665 nm before and after the photodegradation reaction, respectively:

$$\text{Photocatalytic activity} = 1 - I/I_0 \tag{6.1}$$

Figure 6.5e shows the relationship between the photocatalytic activity and work-function difference between TiO_2 and each metal. Notably, a strong positive correlation, similar to that of the degree of spectral changes shown in Fig. 6.3b, was found.

This strong positive correlation indicates that the larger work-function difference results in an increased electron inflow from TiO_2 to the metal and, therefore, in a stronger enhancement of the charge separation, thereby increasing the TiO_2 photocatalytic activity (Fig. 6.5). This finding is in agreement with previous studies [18, 39] that reported a clear correlation between the work function of the metals and the photocatalytic activity assessed in other reactions such as the generation of NH_3 from N_3^- [18] and H_2 from the dehydration of 2-propanol [39]. These results indicate that the photocatalytic activity of modified TiO_2 can be systematically estimated by simple spectral measurements.

6.4 Significant Enhancement of the Photocatalytic Activity of Rutile TiO_2 Compared to That of Anatase TiO_2 upon Pt-Nanoparticle Deposition [40]

6.4.1 Two Types of Crystalline TiO_2: Anatase and Rutile

The two types of readily available varieties of crystalline TiO_2, anatase and rutile (Fig. 6.6), exhibit different chemical, physical, optical, and photocatalytic properties [19, 26, 41]. The bandgap energy of anatase TiO_2 (~3.2 eV) is higher than that of rutile TiO_2 (~3.0 eV) [19]; the reflectance spectra of anatase and rutile TiO_2 in the DUV region have also been reported [26]. However, until quite recently, several difficulties have limited the measurement of the optical properties of TiO_2 in the FUV region; thus, it has not been possible to clarify the differences in the optical properties of anatase and rutile TiO_2 in the FUV region, despite the fact that this

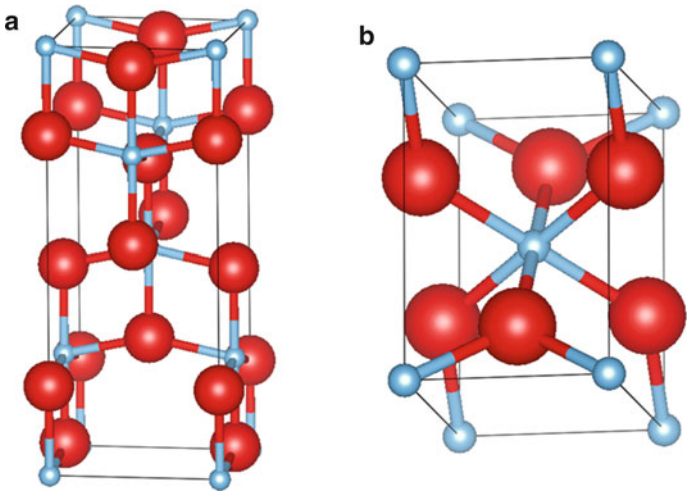

Fig. 6.6 Schematic representation of (**a**) anatase and (**b**) rutile structures

region potentially provides substantial information about the electronic states of these materials. TiO_2 is activated upon UV irradiation (<390 nm and <410 nm for the anatase and rutile phases, respectively); therefore, the investigation of the optical properties in both the DUV and FUV regions is important.

In addition, the differences in the electronic state and photocatalytic activity between anatase and rutile TiO_2 upon surface modifications such as metal-nanoparticle deposition are not well understood. A simple and systematic method to measure these differences for material design is thus needed. Herein, we measured the DUV–FUV spectra of anatase and rutile TiO_2 particles with a 5-μm secondary particle diameter and 200- and 40-nm diameters, respectively. Subsequently, the DUV–FUV spectra of TiO_2 with Pt nanoparticles were also obtained, and the spectral changes and photocatalytic activities of all TiO_2 species were investigated.

6.4.2 DUV–FUV Spectra of Various Sizes Anatase and Rutile TiO_2

The DUV–FUV spectra in the 150–300-nm wavelength region of commercial anatase and rutile TiO_2 particles with a 5-μm secondary particle diameter and 200- and 40-nm diameter, respectively, were measured. The spectra of the anatase TiO_2 particles showed a broad band at ∼160 nm, regardless of the particle size, which, as mentioned in Sect. 6.2, is assigned to the $t_{2g}(\pi) \rightarrow e_g(\sigma^*)$ transition (Fig. 6.7a). In addition, the spectral intensities of rutile TiO_2 particles were found to be lower than those of anatase TiO_2 (Fig. 6.7b), and the spectra showed no clear peak in the FUV region. Figure 6.8a–h displays the SEM images of the TiO_2 particles. Commercial TiO_2 nanoparticles have definite diameters for both the anatase and rutile phases (200 and 40 nm, respectively); however, for TiO_2 particles with 5-μm secondary particle diameters, the original particle diameters of the anatase and rutile phases vary by several dozen and several hundred nanometers, respectively. Absorbance of the DUV–FUV spectrum of anatase TiO_2 with a 5-μm secondary particle diameter is similar to that of anatase TiO_2 with a 40-nm particle diameter (Fig. 6.7a). Likewise, the intensity of rutile TiO_2 with a 5-μm secondary particle diameter is similar to that of rutile TiO_2 with a 200-nm particle diameter (Fig. 6.7b). These results suggest that the intensity of the TiO_2 spectra is largely dependent on the particle size. This is because the amount of TiO_2 with 40-nm-diameter particles in the evanescent wave range (Fig. 6.8i) is larger than that of TiO_2 with 200-nm-diameter particles (Fig. 6.8j).

6.4.3 DUV–FUV Spectral Changes of Anatase and Rutile TiO_2 upon Pt-Nanoparticle Deposition

The DUV–FUV spectra of TiO_2 modified with Pt nanoparticles were also measured. The Pt nanoparticles (1–6 nm in diameter) were deposited by mixing TiO_2 particles

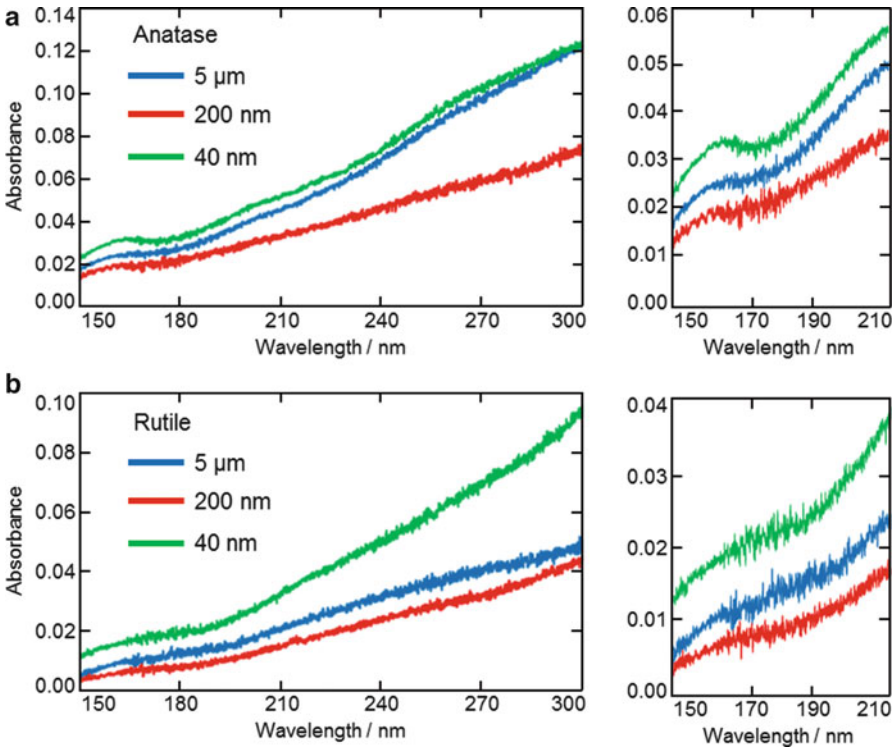

Fig. 6.7 DUV–FUV spectra of (**a**) anatase and (**b**) rutile TiO_2 particles with diameters of (*blue*) 5 μm, (*red*) 200 nm, and (*green*) 40 nm

(1 g) with commercially available Pt nanoparticle colloids (200 μL, 10 mM in water/ethanol solution, protected by PVP, Wako Pure Chemical Industrial, Ltd.) in an agate mortar until the solvent completely evaporated. Figure 6.9a–f compares the ATR–FUV spectra of TiO_2–Pt nanoparticles (red lines) with those of TiO_2 (black lines). The ATR–FUV spectra of rutile TiO_2 particles modified with Pt nanoparticles and those of anatase TiO_2 particles show bands at ∼170 nm and ∼160 nm, respectively. This behavior results from the differences in the electronic structures of the anatase and rutile phases, as shown by previous calculations [42]. The spectral differences between the anatase and rutile phases in the DUV (>200 nm) region have been previously reported [26]; according to this study, the band wavelengths of rutile-phase TiO_2 are longer than those of anatase-phase TiO_2. By employing an ATR–FUV spectrometer, we can compare for the first time the optical spectra of anatase and rutile TiO_2 in the FUV region.

Upon Pt-nanoparticle deposition, the spectral intensity of the anatase-TiO_2 particles (Fig. 6.3a–c) at longer wavelengths decreases, while that at shorter wavelengths increases. As described in Sect. 6.3, the decrease in the intensity in the longer-wavelength region is due to a charge transfer at the TiO_2–Pt interface,

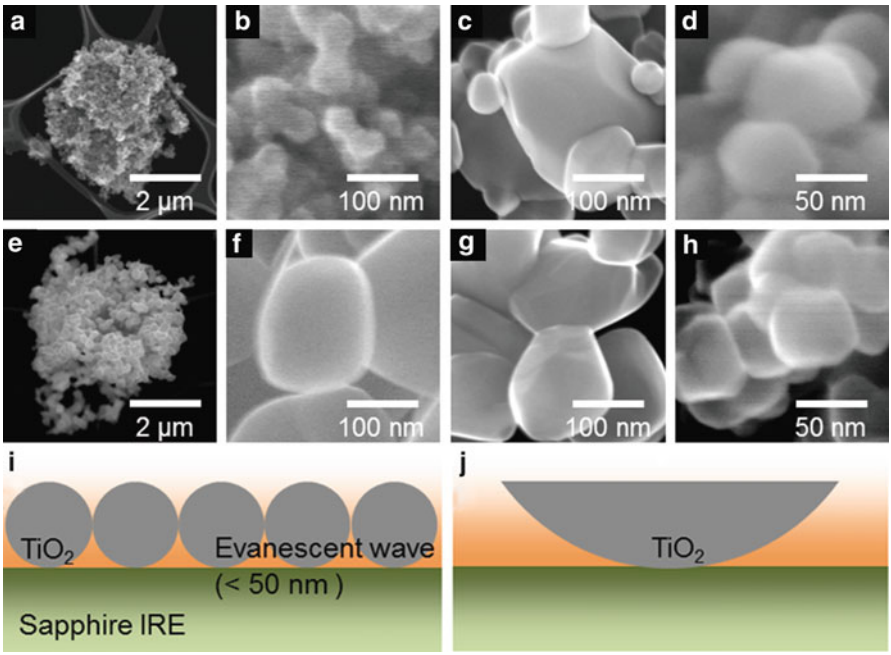

Fig. 6.8 SEM images of (**a**–**d**) anatase and (**e**–**h**) rutile TiO_2 particles with diameters of (**a**, **b**, **e**, and **f**) 5 μm, (**c** and **g**) 200 nm, and (**d** and **h**) 40 nm. (**i** and **j**) Scheme of ATR–FUV spectrometer measurement of TiO_2 particles with diameters of (**i**) 40 nm and (**j**) 5 μm

and the increase in the shorter-wavelength region is due to the enhancement of the charge-separation efficiency upon the deposition of the Pt nanoparticles. The work function of TiO_2 (∼4.0 eV for anatase-phase TiO_2) is smaller than that of Pt (∼5.7 eV). Therefore, when TiO_2 contacts the Pt nanoparticles, the electrons in TiO_2 flow into the Pt nanoparticles until the Fermi levels are equalized. As a result, the number of electrons in the relatively high-energy levels (i.e., electrons that can be excited at a relatively longer wavelength) is decreased, resulting in the suppression of the spectral intensity in the longer-wavelength region. In contrast, Pt nanoparticles on TiO_2 can act as a sink for the photoexcited electrons, resulting in an enhancement of the charge-separation efficiency and an increase in the spectral intensity in the shorter-wavelength region. This process may also occur in the longer-wavelength region; however, the total change in the spectral intensity depends on this enhancement and the decrease in the number of electrons upon contact between TiO_2 and Pt nanoparticles.

In contrast, the spectral intensity of the rutile-TiO_2 nanoparticles (Fig. 6.9d–f) increases over the entire region upon deposition of Pt nanoparticles. When anatase TiO_2 is modified with Au nanoparticles, the intensity in the longer-wavelength region decreases, as it does for the anatase TiO_2–Pt nanoparticles based on

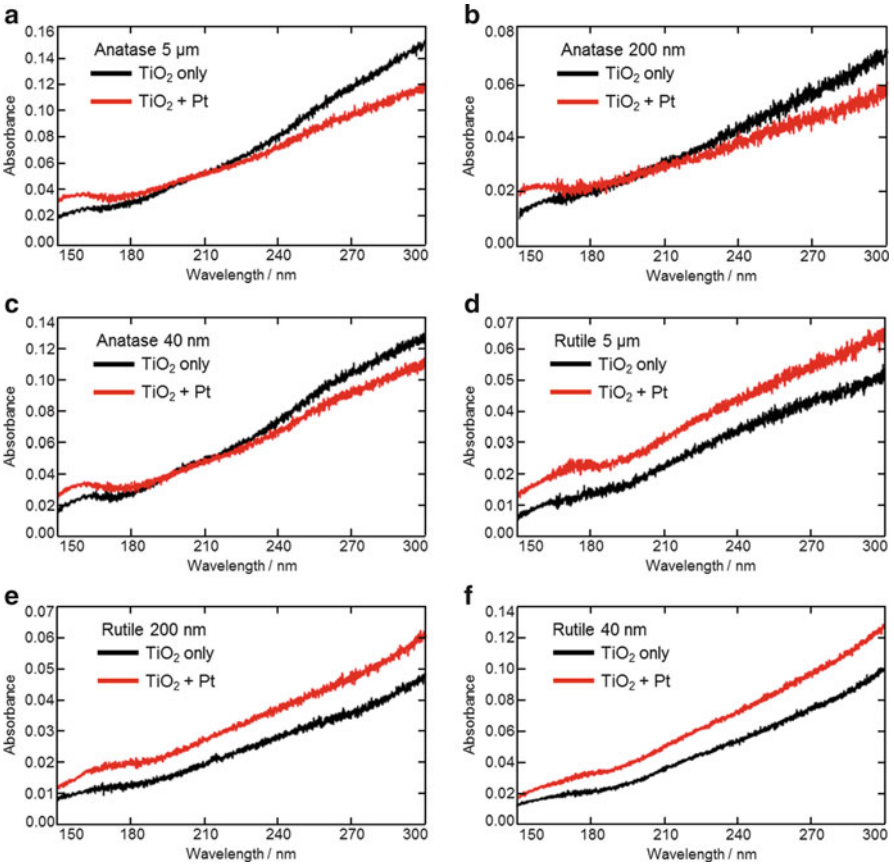

Fig. 6.9 DUV–FUV spectra of (**a**–**c**) anatase and (**d**–**f**) rutile TiO_2 particles with diameters of (**a** and **d**) 5 μm, (**b** and **e**) 200 nm, and (**c** and **f**) 40 nm, before (*black*) and after (*red*) the deposition of Pt nanoparticles

the electron transfer described above. The work function of Au (∼4.7 eV) is approximately 1.0 eV lower than that of Pt, while that of rutile TiO_2 is 0.2 eV lower than that of anatase TiO_2 (at most) [19, 41]. Therefore, if the magnitude of the effect of the charge-separation enhancement for rutile TiO_2 is the same as that for anatase TiO_2, the intensity in the longer-wavelength region should decrease. However, in practice, the spectral intensity of rutile TiO_2 increases even in the longer-wavelength region. In this regard, the increase in the spectral intensity implies an enhancement of charge separation, as ascribed in Sect. 6.3.1. Therefore, these results indicate that the magnitude of the effect of charge-separation enhancement for rutile TiO_2 is higher than that for anatase TiO_2. In order to estimate this enhancement, we investigated their photocatalytic activities.

6.4.4 Photocatalytic-Activity Enhancement in Anatase and Rutile TiO_2 upon Pt-Nanoparticle Deposition

The photocatalytic activities of TiO_2 particles with and without Pt nanoparticles were estimated based on the photodegradation reaction of methylene blue. A methylene blue aqueous solution (20 μM, 20 mL), including TiO_2 particles with/without Pt nanoparticles (5 mg), was irradiated with UV light (300–350 nm, ~10 μW cm^{-2}) for 30 min, and the absorption spectra before and after UV irradiation were measured (Fig. 6.10). The photocatalytic activity of each sample was also estimated using Eq. (6.1).

Figure 6.11(a) (anatase TiO_2) and (b) (rutile TiO_2) show the plots of the photocatalytic activities of TiO_2 (black) and TiO_2 with Pt nanoparticles (red) as a function of the particle diameter. For a 5-μm secondary particle diameter and 200-nm-diameter TiO_2 particles, the photocatalytic activity of anatase TiO_2 is higher than that of rutile TiO_2 of the same size, in agreement with previous studies [3]. For rutile TiO_2, a smaller TiO_2 particle shows a larger photocatalytic activity, and TiO_2 with a 5-μm secondary diameter shows the smallest photocatalytic activity. These trends are a result of the smaller particle size and the consequent larger surface area [43].

The anatase TiO_2 particles with 40-nm diameters show an exceptionally low photocatalytic activity, probably because of the synthesis of small anatase TiO_2 nanoparticles, which requires a lower temperature than that of large anatase particles and rutile particles [44]. In addition, anatase TiO_2 particles with 40-nm diameters are characterized by a larger number of lattice defects, which may decrease the photocatalytic activity [45]. The photocatalytic activities of all TiO_2 nanoparticles are enhanced upon deposition of Pt nanoparticles. The photocatalytic activities of anatase TiO_2 were determined to be 0.47, 0.53, and 0.33 (5-μm-, 200-nm-, and 40-nm-diameter particles, respectively) and increased to 0.52, 0.62, and 0.36, respectively, upon the deposition of Pt nanoparticles. The photocatalytic activities of rutile TiO_2 were found to be 0.13, 0.23, and 0.44 (5-μm-, 200-nm-, and 40-nm-diameter particles, respectively) and increased to 0.18, 0.28, and 0.55, respectively. The "enhancement factor" was calculated for each TiO_2 particle as the ratio between the photocatalytic activity of TiO_2 modified with the Pt nanoparticles and that of TiO_2 alone [46, 47]. As shown in Fig. 6.11c, the rutile TiO_2 particles (open circles) show a higher photocatalytic-activity enhancement than the anatase TiO_2 particles (filled circles). Several research groups have reported that the photocatalytic activity of TiO_2 is improved upon the deposition of metal nanoparticles [1, 16–21, 48]. However, most of these groups have focused on either anatase TiO_2 or a mixture of anatase and rutile TiO_2 [16–21], because both these systems show a higher photocatalytic activity in many reactions than bare rutile TiO_2. Rutile TiO_2 has been primarily used for the investigations of reaction mechanisms. For example, Li and coworkers showed that the (110) surface of rutile TiO_2 can be more selectively deposited with Pt nanoparticles than the (001) surface and that the photocatalytic activity is improved by Pt deposition [48]. However, no studies are available about a

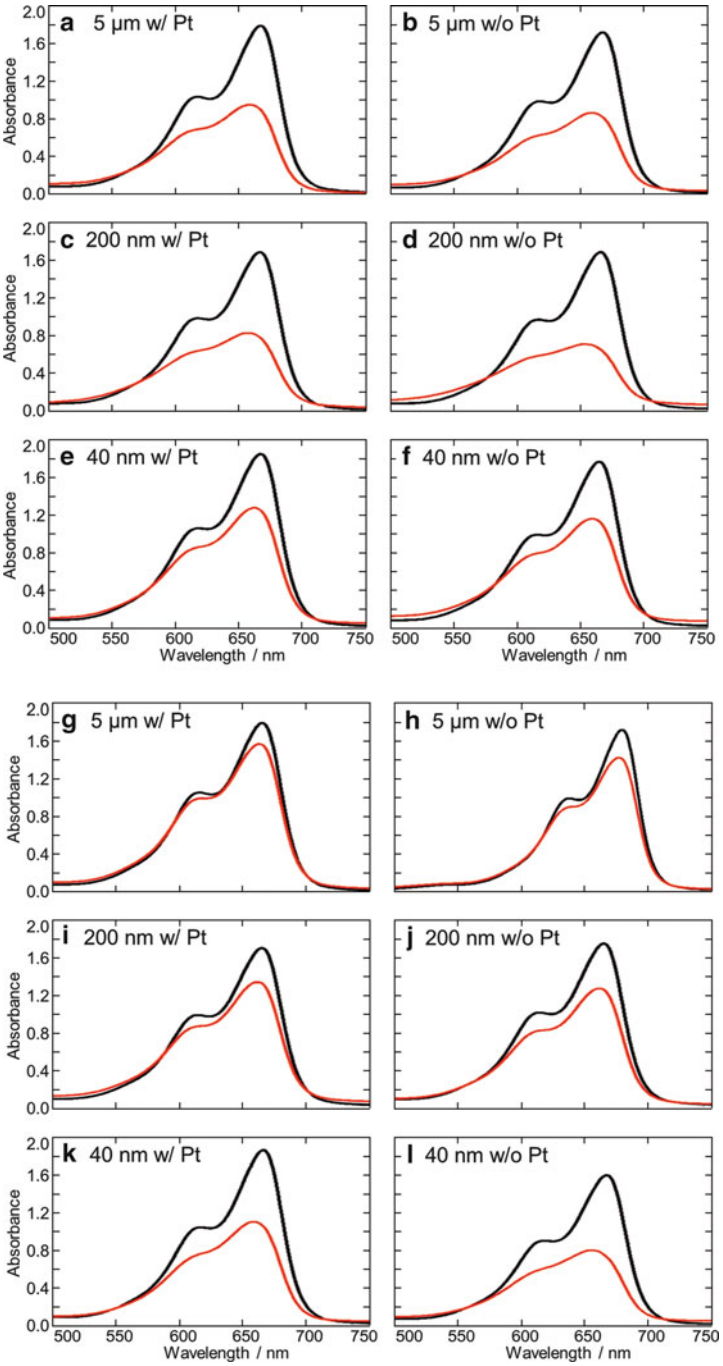

Fig. 6.10 Absorption spectra of aqueous methylene blue before (*black*) and after (*color*) UV irradiation with (**a**–**f**) anatase or (**g**–**l**) rutile TiO_2. TiO_2 particle size and state (i.e., with/without Pt nanoparticles) are displayed in each graph

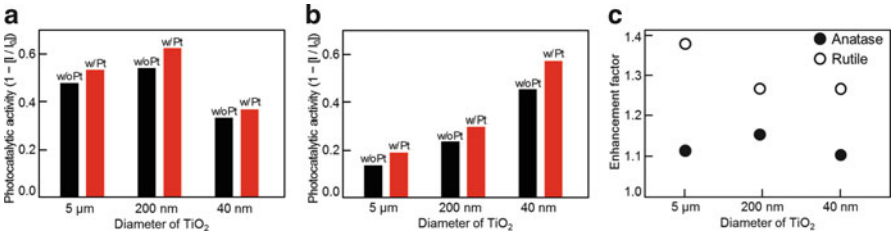

Fig. 6.11 Photocatalytic activities ($1 - [I/I_0]$) of (**a**) anatase and (**b**) rutile TiO_2 particles (*black*) before and (*red*) after the deposition of Pt nanoparticles. (**c**) Enhancement factors of (*filled circle*) anatase and (*open circle*) rutile TiO_2 particles. TiO_2 particle diameters are 5 μm, 200 nm, and 40 nm

systematic comparison of anatase and rutile TiO_2 in terms of their optical and/or photocatalytic property changes upon metal deposition. In our study, we have systematically compared the electronic-state changes and photocatalytic activity of anatase and rutile TiO_2; based on the DUV–FUV spectral measurements and estimations of the photodegradation reaction activity, we have shown that the enhancement of the charge-separation efficiency upon Pt-nanoparticle deposition is higher for rutile TiO_2 than for anatase TiO_2.

6.5 Size Effect of Modified Au Nanoparticles on TiO_2 Electronic States [49]

6.5.1 Size Effect of Modified Au Nanoparticles on the TiO_2 Photocatalytic Activity Under UV- and Visible-Light Irradiation

The effects of the Au-nanoparticle size on the photocatalytic activity of TiO_2–Au nanoparticles have been reported. For instance, Idriss and coworkers estimated the photocatalytic activity of TiO_2 modified with Au nanoparticles, whose size ranged between 3 and 30 nm, based on the photocatalytic hydrogen production from ethanol under UV-light irradiation [50]. When they adopted anatase TiO_2, the photocatalytic-reaction rate was not affected by the Au-nanoparticle size over the 3–12-nm range. When the size was increased to 16 nm, the reaction rate of the anatase TiO_2–Au nanoparticle was considerably reduced. In the case of rutile TiO_2 with Au nanoparticles with a diameter of 20–35 nm, the photocatalytic activity was found to be virtually independent of the Au-nanoparticle size.

Tatsuma's group has reported that the responsible wavelength range of TiO_2 can be expanded into the visible region by decorating TiO_2 with Au nanoparticles that absorb visible light via the localized surface plasmon resonance (LSPR) [51–53]. They used the deposited Au nanoparticles with different sizes (e.g., 15, 40,

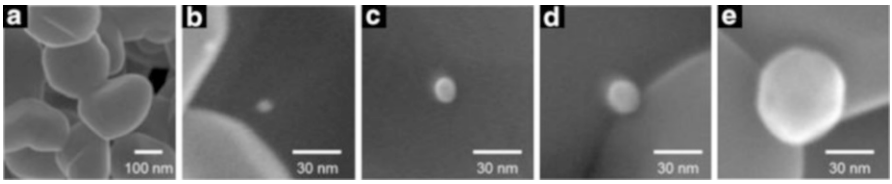

Fig. 6.12 SEM images of (**a**) TiO_2 and Au-modified TiO_2 with Au-nanoparticle diameters of (**b**) 5 nm, (**c**) 10 nm, (**d**) 20 nm, and (**e**) 60 nm

and 100 nm) and found that the quantum efficiency proportionally increased with the particle size, while the maximum photocurrent decreased under visible-light irradiation [53]. Ohtani et al. [54] measured the visible-light-induced photocatalytic-reaction rate of the oxidation reaction of 2-propanol. In their study, the Au-particle size on TiO_2 was varied in the 10–60-nm range, and a positive relationship was found between the particle size and the photocatalytic activity under visible-light irradiation.

Heretofore, only a few studies about the electronic-state changes of TiO_2–Au nanoparticle as a function of the Au-nanoparticle size have been reported. Kamat and coworkers measured the Fermi levels of TiO_2–Au nanoparticle samples (the diameters of the Au nanoparticles were 3, 5, and 8 nm on average) under UV-light irradiation [55]. However, the particle-size range was strictly limited to 3–8 nm, and no information about the shape of the Au nanoparticles was provided. The photocatalytic activity is strongly related to its electronic states, and, therefore, insight into the electronic states may help understand the mechanism of the photocatalytic enhancement and develop high-efficiency optical materials such as solar cells.

6.5.2 Size Effect of Modified Au Nanoparticles on TiO_2 Electronic States

Spherical Au colloids (diameters of 5, 10, 20, and 60 nm, aqueous solution, protected by hexadecyltrimethylammonium bromide, CTAB) were purchased from Tanaka Kikinzoku Kogyo. Anatase or rutile TiO_2 powder (5-μm secondary particle diameter) and Au colloids were mixed in an agate mortar until the solvent completely evaporated. In this study, the amount of colloids was regulated to obtain a similar number of Au nanoparticles ($\sim 3.8 \times 10^{10}$ per 1 g TiO_2). Figure 6.12 shows the typical SEM images of Au nanoparticles on rutile TiO_2 (5-μm secondary particle diameter; the original particle diameter is several hundred nanometers).

Then, the DUV–FUV spectra of the TiO_2–Au nanoparticles were measured. Upon the deposition of Au nanoparticles on anatase TiO_2, the spectral intensity at longer wavelengths (> about 210 nm) decreased, while that at shorter wavelengths (< about 210 nm) increased independently from the size of Au (Fig. 6.13a); these

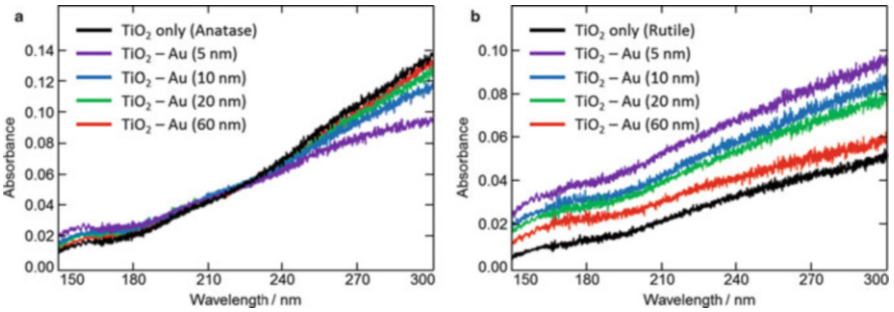

Fig. 6.13 DUV–FUV spectra of (**a**) anatase and (**b**) rutile TiO_2 with/without Au nanoparticles (5, 10, 20, and 60 nm)

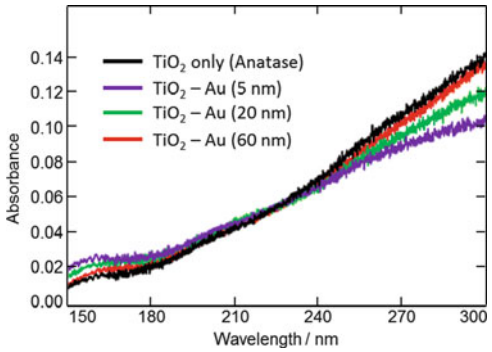

Fig. 6.14 DUV–FUV spectra of anatase TiO_2 with/without Au nanospheres (5, 20, and 60 nm). The weight of the Au nanospheres is regulated to be approximately the same

spectral changes are a result of the electron transfer from TiO_2 to the metal and the enhancement of the charge separation, respectively, as discussed in Sect. 6.3.1. In addition, the degree of the spectral changes at both longer and shorter wavelengths increased as the size of the deposited Au nanoparticles decreased. When rutile TiO_2 was used (Fig. 6.13b), the spectral intensity after the deposition of the Au nanoparticles increased over the entire wavelength region, similarly to the effect of the deposition of the Pt nanoparticles (Fig. 6.9d–f). The degree of the spectral changes also increased as the size of the deposited Au nanoparticles decreased.

Even with a similar weight of the deposited Au nanoparticles ($\sim 1.3 \times 10^{-4}$ g on 1 g TiO_2), the amount of spectral changes decreased as the size of the Au nanoparticles increased (Fig. 6.14).

These results suggest that smaller Au nanoparticles lead to larger electronic-state changes, which in turn may exert a strong effect on the photocatalytic activities. Therefore, these were measured based on the photodegradation reaction of methylene blue. The experimental details are described in the Sects. 6.3.2 and 6.4.4.

The photocatalytic activities of TiO_2 alone and TiO_2 with Au nanospheres of size 5, 10, 20, and 60 nm were determined to be 0.30 ± 0.030, 0.51 ± 0.031, 0.41 ± 0.024, 0.37 ± 0.043, and 0.33 ± 0.058, respectively (average $\pm$ standard

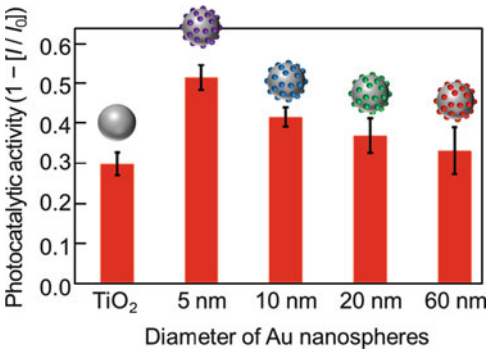

Fig. 6.15 Photocatalytic activities ($1 - [I/I_0]$) of anatase TiO_2 with/without Au nanospheres of various sizes

deviation, $n = 3$). As shown in Fig. 6.15, the photocatalytic activity strongly depends on the Au size, i.e., TiO_2 with smaller Au nanoparticles shows a higher photocatalytic activity. Our results are in agreement with those of Wei and coworkers, who reported that the photocatalytic activity of TiO_2 with ~5-nm Au is larger than that of TiO_2 with ~40-nm Au under UV-light irradiation [56]. From the results obtained from the DUV–FUV spectra (Figs. 6.13 and 6.14) and photocatalytic activities (Fig. 6.15), we concluded that the electronic state changed significantly and the photocatalytic activities increased as the Au size decreased, confirming that these strongly depend on the Au-nanoparticle size.

We then measured the DUV–FUV spectra of TiO_2–Au nanorod samples with various aspect ratios. All Au nanorods have the same diameter (25 nm), and their lengths are 34, 47, and 60 nm, with the corresponding aspect ratios being 1.36, 1.88, and 2.40, respectively. The SEM images of the Au nanorods are shown in Fig. 6.16. Au nanorods (purchased from Sigma-Aldrich Co. LLC.) were dissolved in the aqueous solution with CTAB used as a stabilizer. The number of Au nanorods was chosen to be $\sim 3.8 \times 10^{10}$ per 1 g TiO_2 (as for the Au nanospheres). As shown in Fig. 6.17, no significant changes in the DUV–FUV spectra of TiO_2 modified with these three types of Au nanorods were observed. This result suggests that the electronic state of TiO_2 may mainly depend on the diameter of the modified Au nanoparticles, with the length (i.e., aspect ratio) of the nanorods exerting only a small effect.

In addition, we synthesized Au nanocubes (Fig. 6.18, ~60 nm length) [57] and measured the DUV–FUV spectra of anatase TiO_2 with these Au nanocubes (Fig. 6.18). No significant differences between the spectrum of TiO_2 with Au nanocubes and that with the Au nanospheres of the corresponding size (60 nm diameter) were observed, indicating that the electronic-state changes are independent of the Au-nanoparticle shapes. We discuss reasons why the electronic states of TiO_2 with Au nanoparticles strongly depend on the Au size rather than on the Au shape.

As described in Sect. 6.3.1, upon the contact between TiO_2 and a metal, the electrons in TiO_2 are transferred to the metal. At the same time, a potential gradient is generated at the interface between TiO_2 and the metal, which prevents a recombination between the electrons in the metal and the holes in TiO_2, leading

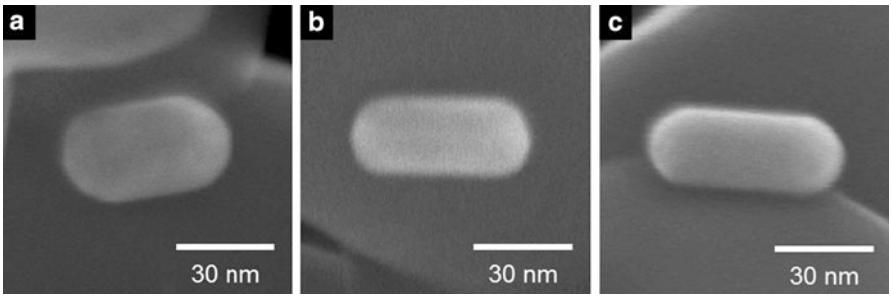

Fig. 6.16 SEM images of Au nanorods on TiO_2 with the following sizes: (**a**) 25 nm × 34 nm, (**b**) 25 nm × 47 nm, and (**c**) 25 nm × 60 nm

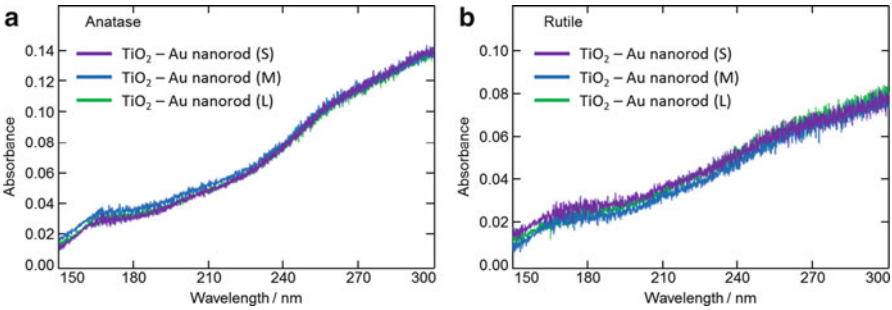

Fig. 6.17 DUV–FUV spectra of (**a**) anatase and (**b**) rutile TiO_2 modified with Au nanorods of various aspect ratios. The sizes of the Au nanorods are (S) 25 nm × 34 nm, (M) 25 nm × 47 nm, and (L) 25 nm × 60 nm

Fig. 6.18 DUV–FUV spectra of anatase TiO_2 modified with (*red*) Au nanospheres or (*yellow*) Au nanocubes. The SEM image of a deposited nanocube is also shown (*inset*)

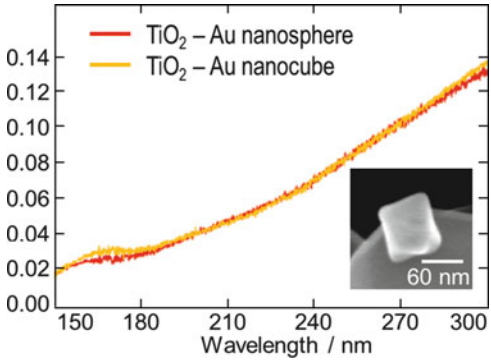

to an enhancement of the charge-separation efficiency. The depth and width of the potential gradient depend on the Fermi levels, size, electric conductivity, and other properties of TiO_2 and the metal. In the present case, only the Au-nanoparticle size and shape were systematically changed. However, the width of the Au nanoparticle was not changed, i.e., the diameter of all the Au nanorods was maintained constant

at 25 nm. Therefore, the ATR spectra suggest that the width of the deposited Au nanoparticles may have a strong effect on the electronic states of TiO_2. Thus, we have discussed not only the effect of the size of Au nanoparticles in the wide range of 5–60 nm but also that of their shape.

6.6 Conclusions and Perspectives

By using our DUV–FUV spectroscopy method, we systematically studied the electronic states of TiO_2 alone and those of TiO_2 with metal nanoparticles.

The obtained naked TiO_2 spectra were in line with the previously reported reflection spectra and theoretical calculations (Sect. 6.2). The deposition of metal (Au, Pd, and Pt) nanoparticles significantly affected their spectral shape, indicating changes in the electronic states of TiO_2. A strong positive relationship was found between the degree of the spectral changes and the work function of the modified metal. Larger spectral changes indicate a stronger enhancement of charge separation, which in turn leads to an improvement of the photocatalytic activity of TiO_2 (Sect. 6.3). Anatase TiO_2 and rutile TiO_2 showed different spectra and spectral changes upon Pt-nanoparticle deposition. In particular, the photocatalytic activity of rutile TiO_2 showed a stronger enhancement than that of anatase TiO_2 (Sect. 6.4). Although a low shape dependence was observed, smaller Au nanoparticles induced larger electronic-state changes, leading to a higher photocatalytic activity (Sect. 6.5).

The results illustrated in this contribution clearly demonstrate the potential of DUV–FUV spectroscopy as a novel investigation method for the electronic states of various materials. Now, we are applying this method not only to TiO_2 but also to other materials (other semiconductors such as ZnO, organic phosphates, ion liquids, and so on). It is also important to confirm the electronic changes by other methods such as X-ray photoelectron spectroscopy (XPS) and ultraviolet photoelectron spectroscopy (UPS), which is in progress. The application of this method provides critical information about the enhancement mechanism and supports the development of high-efficiency optical materials such as photocatalysts and solar cells.

References

1. A.L. Linsebigler, G. Lu, J.T. Yates Jr., Chem. Rev. **95**, 735–758 (1995)
2. X. Chen, S.S. Mao, Chem. Rev. **107**, 2891–2959 (2007)
3. M.R. Hoffmann, S.T. Martin, W. Choi, D.W. Bahnemann, Chem. Rev. **95**, 69–96 (1995)
4. B. O'Regan, M. Grätzel, Nature **353**, 737–740 (1991)
5. M.K. Nazeeruddin, P. Péchy, T. Renouard, S.M. Zakeeruddin, R. Humphry-Baker, P. Comte, P. Liska, L. Cevey, E. Costa, V. Shklover, L. Spiccia, G.B. Deacon, C.A. Bignozzi, M. Grätzel, J. Am. Chem. Soc. **123**, 1613–1624 (2001)
6. P.V. Kamat, J. Phys. Chem. C **112**, 18737 (2008)

7. H. Tang, K. Prasad, R. Sanjinbs, P.E. Schmid, F. Lévy, J. Appl. Phys. **75**, 2042 (1994)
8. M.A. Fox, M.T. Dulay, Chem. Rev. **93**, 341–357 (1993)
9. M. Fujihira, Y. Satoh, T. Osa, Nature **293**, 206–208 (1981)
10. F. Gruy, M. Pijolat, J. Am. Ceram. Soc. **75**, 657–661 (1992)
11. A. Fujishima, X. Zhang, D.A. Tryk, Surf. Sci. Rep. **63**, 515–582 (2008)
12. A.-W. Xu, Y. Gao, H.-Q. Liu, J. Catal. **207**, 151–157 (2002)
13. W. Choi, A. Termin, M.R. Hoffmann, J. Phys. Chem. **98**, 13669–13679 (1994)
14. A. Hattori, K. Shimoda, H. Tada, S. Ito, Langmuir **15**, 5422–5425 (1999)
15. Z.H. Yuan, J.H. Jia, L.D. Zhang, Mater. Chem. Phys. **73**, 323–326 (2002)
16. B. Kraeutler, A.J. Bard, J. Am. Chem. Soc. **100**, 2239–2240 (1978)
17. T. Kawai, T. Sakata, Nature **282**, 283–284 (1979)
18. Y. Nosaka, K. Norimatsu, H. Miyama, Chem. Phys. Lett. **106**, 128–131 (1984)
19. U. Diebold, Surf. Sci. Rep. **48**, 53–229 (2003)
20. M. Jakob, H. Levanon, P.V. Kamat, Nano Lett. **3**, 353–358 (2003)
21. P.V. Kamat, J. Phys. Chem. Lett. **3**, 663–672 (2012)
22. G.E. Jellison Jr., L.A. Boatner, J.D. Budai, B.-S. Jeong, D.P. Norton, J. Appl. Phys. **93**, 9537–9541 (2003)
23. Y. Ozaki, Y. Morisawa, A. Ikehata, N. Higashi, Appl. Spectrosc. **66**, 1 (2012)
24. Y. Morisawa, T. Goto, N. Higashi, K. Takaba, N. Kariyama, A. Ikehata, Y. Ozaki, Rev. Sci. Instrum. **83**, 073103 (2012)
25. Y. Morisawa, T. Goto, A. Ikehata, N. Higashi, Y. Ozaki, *Encyclopedia of Analytical Chemistry* (Wiley, 2013), pp. 1–21
26. J. Zhang, M. Li, A. Feng, J. Chen, C. Li, J. Phys. Chem. B **110**, 927–935 (2006)
27. N. Higashi, A. Ikehata, Y. Ozaki, Rev. Sci. Instrum. **78**, 103107 (2007)
28. A. Ikehata, M. Mitsuoka, Y. Morisawa, N. Kariyama, N. Higashi, Y. Ozaki, J. Phys. Chem. A **114**, 8319–8322 (2010)
29. T. Goto, A. Ikehata, Y. Morisawa, N. Higashi, Y. Ozaki, Phys. Chem. Chem. Phys. **14**, 8097–8104 (2012)
30. Y. Morisawa, A. Ikehata, N. Higashi, Y. Ozaki, Chem. Phys. Lett. **476**, 205–208 (2009)
31. Y. Morisawa, A. Ikehata, N. Higashi, Y. Ozaki, J. Phys. Chem. A **115**, 562–568 (2011)
32. S. Tachibana, Y. Morisawa, A. Ikehata, H. Sato, N. Higashi, Y. Ozaki, Appl. Spectrosc. **65**, 221–226 (2011)
33. I. Tanabe, Y. Ozaki, Chem. Commun. **50**, 2117 (2014)
34. N. Hosaka, T. Sekiya, M. Fujisawa, C. Satoko, S. Kurita, J. Electron Spectrosc. Relat. Phenom. **78**, 75–78 (1996)
35. N. Hosaka, T. Sekiya, C. Satoko, S. Kurita, J. Phys. Soc. Jpn. **66**, 877–880 (1997)
36. R. Asahi, Y. Taga, W. Mannstadt, A.J. Freeman, Phys. Rev. B **61**, 7459–7465 (2000)
37. S. Sério, M.E. Melo Jorge, M.L. Coutinho, S.V. Hoffman, P. Limão-Vieira, Y. Nunes, Chem. Phys. Lett. **508**, 71–75 (2011)
38. Y. Borodko, S.E. Habas, M. Koebel, P. Yang, H. Frei, G.A. Somoriai, J. Phys. Chem. B **110**, 23052 (2006)
39. S. Teratani, J. Nakamichi, K. Taya, T. Tanaka, Bull. Chem. Soc. Jpn. **55**, 1688–1690 (1982)
40. I. Tanabe, T. Ryoki, Y. Ozaki, Phys. Chem. Chem. Phys. **16**, 7749 (2014)
41. K. Tanaka, M.F.V. Capule, T. Hisanaga, Chem. Phys. Lett. **187**, 73 (1991)
42. M. Landmann, E. Rauls, W.G. Schmidt, J. Phys. Condens. Matter **24**, 195503 (2012)
43. N. Xu, Z. Shi, Y. Fan, J. Dong, J. Shi, M.Z.-C. Hu, Ind. Eng. Chem. Res. **38**, 373 (1999)
44. Q. Zhang, L. Gao, J. Guo, J. Eur. Ceram. Soc. **20**, 2153 (2000)
45. S. Ikeda, N. Sugiyama, S. Murakami, H. Kominami, Y. Kera, H. Noguchi, K. Uosaki, T. Torimoto, B. Ohtani, Phys. Chem. Chem. Phys. **5**, 778 (2003)
46. J.I.L. Chen, G. von Freymann, V. Kitaev, G.A. Ozin, J. Am. Chem. Soc. **129**, 1196 (2007)
47. Z. Zhang, Z. Wang, S.-W. Cao, C. Xue, J. Phys. Chem. C **117**, 25939 (2013)
48. J. Zhang, L. Li, T. Yan, G. Li, J. Phys. Chem. C **115**, 13820 (2011)

49. I. Tanabe, T. Ryoki, Y. Ozaki, The effects of Au nanoparticle size (5-60 nm) and shape (sphere, rod, cube) over electronic states and photocatalytic activities of TiO_2 studied by far- and deep-ultraviolet spectroscopy. RSC Adv. **5**, 13648–13652 (2015)
50. M. Murdoch, G.I.N. Waterhouse, M.A. Nadeem, J.B. Metson, M.A. Keane, R.F. Howe, J. Llorca, H. Idriss, Nat. Chem. **3**, 489 (2011)
51. Y. Tian, T. Tatsuma, Chem. Commun., 1810 (2004)
52. Y. Tian, T. Tatsuma, J. Am. Chem. Soc. **127**, 7632 (2005)
53. K. Yu, Y. Tian, T. Tatsuma, Phys. Chem. Chem. Phys. **8**, 5417 (2006)
54. E. Kowalska, R. Abe, B. Ohtani, Chem. Commun., 241 (2009)
55. V. Subramanian, E.E. Wolf, P.V. Kamat, J. Am. Chem. Soc. **126**, 4943 (2004)
56. K. Qian, B.C. Sweeny, A.C. Johnston-Peck, W. Niu, J.O. Graham, J.S. Duchene, J. Qiu, Y.-C. Wang, M.H. Engelhard, D. Su, E.A. Stach, W.D. Wei, J. Am. Chem. Soc. **136**, 9842 (2014)
57. J. Zhang, C. Xi, C. Feng, H. Xia, D. Wang, X. Tao, Langmuir **30**, 2480 (2014)

Chapter 7
Deep-Ultraviolet Microscopy and Microspectroscopy

Yasuaki Kumamoto

Abstract Microscopy and microspectroscopy are popular techniques for chemical analysis of a specimen having a micron to submicron distribution of material or material properties, such as living cells, drug agents, microelectronic devices, and nanocarbon materials. Deep-ultraviolet (DUV) light has several advantages compared to visible or infrared (IR) light for microscopy and microspectroscopy. DUV imaging techniques have largely advanced since the 1990s, while DUV microscopy appeared more than 100 years ago. This chapter first looks back at the early days of DUV microscopy and microspectroscopy to see how the research fields have grown and why they have advanced in the recent years. The chapter then describes in detail the recent advances, followed by future perspectives.

Keywords Deep ultraviolet • Ultraviolet microscopy • Ultraviolet microspectroscopy • Autofluorescence • Resonance Raman scattering

7.1 Introduction

Microspectroscopy is a popular research field for chemical analysis and imaging of a specimen having a micron to submicron distribution of material or material properties. Spectral imaging with such a high spatial resolution, often called microspectroscopic imaging, is particularly essential for the study of microscale or smaller specimens such as living cells, drug agents, microelectronic devices, and nanocarbon materials. A variety of microspectroscopic imaging techniques were developed in the 1990s and 2000s.

Use of deep-ultraviolet (DUV) light has advantages in microspectroscopy compared to visible or near-infrared(NIR) light. In biology, DUV microspectroscopic

Y. Kumamoto (✉)
Department of Applied Physics, Osaka University, 2-1 Yamadaoka, Suita, Osaka 565-0871, Japan
e-mail: kumamoto@ap.eng.osaka-u.ac.jp

Y. Ozaki, S. Kawata (eds.), *Far- and Deep-Ultraviolet Spectroscopy*,
DOI 10.1007/978-4-431-55549-0_7

imaging can provide high sensitivity and selectivity to detect nucleotide bases and aromatic amino acids in a cell [1]. These molecules have absorption bands in the DUV range but not in the visible and NIR ranges. Additionally, other molecules in a cell typically do not absorb DUV light. DUV light scattering is also useful for measuring these molecules. The scattering efficiency in the DUV range is enhanced due to the electronic resonance effect by a factor of up to 10^8 compared to that in the visible and NIR ranges [2]. The general advantage of using DUV light in microspectroscopic imaging is higher spatial resolution than visible or NIR light can provide, in accordance with the theoretical resolution limit of microscopes. Upon a scattering measurement of a luminescent material, one advantage of using DUV light is that the spectral overlap of luminescence and scattering, which overwhelms the scattering signal when using visible light, can be avoided [3]. Apart from the above, DUV excitation is advantageous for selective analysis of sp^3 bonding of carbon and hydrocarbon, while visible or NIR excitation highlights sp^2-bonding structures [4, 5]. The small penetration depth of DUV light into a material is useful for selective measurements on or near the surface of a specimen. In a fluorescence measurement, unlike visible-light excitation, DUV excitation can efficiently excite the intrinsic fluorescence of a material and enable label-free analysis [6, 7].

Capitalizing on these advantages, a variety of DUV microspectroscopic imaging techniques and applications have been developed. DUV Raman scattering microscopy was first developed for chemical analysis of chemical-vapor-deposition (CVD) diamonds without interference of sp^2-bonding Raman bands and luminescence [4]. The imaging technique was improved for non-destructive analysis of Martian meteorites without any labeling [8] and label-free, selective imaging of nucleotide bases in cells [1]. The Raman technique was advanced as a nanoanalysis technique with tip-enhanced Raman scattering in the DUV range [9]. DUV fluorescence microscopy has been utilized for label-free bioimaging. Nonlinear DUV excitation with visible or NIR light in fluorescence microscopy has been achieved with the use of multiphoton absorption [10]. This technique enabled deep-tissue imaging with minimal photodamage [11–13]. Single-photon excitation as a conventional technique has also been used in DUV fluorescence microscopy. The technique has been enhanced for fluorescence lifetime analysis [14, 15], label-free nanoimaging [16], and molecular environment analysis [17]. In absorption microscopy, an advanced imaging technique has been developed for quantitative mass mapping of nucleic acids and proteins in a living cell [17–19].

While DUV imaging was a popular technique, especially as a bioimaging technique, for half a century since the first development of a DUV microscope in 1904, interest waned until these recent advances sparked a renewed interest in the technique. For a deeper understanding of the recent advances in DUV imaging, it is worth describing why DUV imaging was invented, its rise and fall in popularity, and why it is attracting attention again. This chapter first reviews the early history of DUV imaging.

7.2 History in the Early Days

Basic study of DUV microspectroscopy was initiated more than 100 years ago. After Abbe's theory on the resolution limit of microscopes was published in 1873, scientists attempted to improve the spatial resolution in a practical microscope by increasing the numerical aperture (NA) of objective lenses or by using a shorter wavelength of light. Abbe and Zeiss improved the spatial resolution by implementing high NA objective lenses, while Koehler and his colleagues improved it by developing a microscope operating in the DUV range. In 1904, Koehler published the first paper describing a transmission microscope equipped with DUV light sources at wavelengths of 275 and 280 nm. The DUV microscope was developed using an objective lens made of quartz and calcium fluoride and DUV light emission from an electric spark of cadmium and magnesium [20]. In his paper, Koehler presented a series of the first images obtained using a DUV microscope. In 1906, American pathologists also developed a DUV microscope and presented microscopic pictures clearly showing microstructures inside bacteria [21]. Some of these pictures are shown in Fig. 7.1. Results from these studies revealed the potential

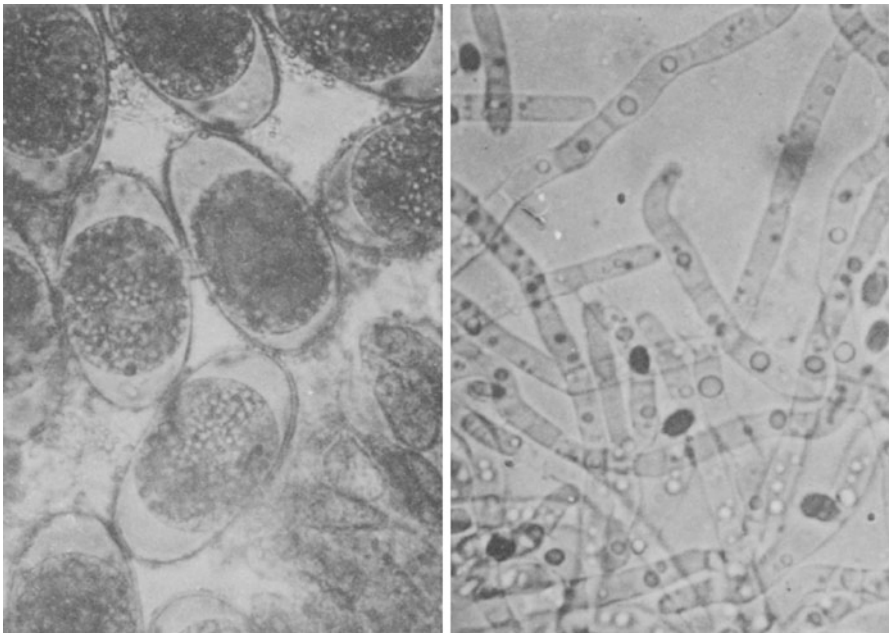

Fig. 7.1 Early DUV microscopy images of (*left*) *Coccidium oviforme*, a parasitic protist prepared from fresh liver showing nuclei-like structures at the center, and (*right*) *Bacillus megaterium* showing internal spores (Figures are reused with permission from the publisher of Ref. [21])

of DUV microscopy for distinguishing intracellular microstructures that could not be observed by visible light without any sample pretreatment, such as staining. They did not mention spectroscopy in the DUV range, but opened the door for DUV microspectroscopy.

After these pioneering studies, use of DUV microscopes continued to be popular until the 1950s, mostly for visualizing cellular structures transparent to visible light. Studies in the earlier days used a DUV microscope to observe microorganisms without any staining and revealed the bacterial morphology to discuss their growth [22, 23]. Later studies focused on visualizing detailed microstructures inside cells. Intranuclear microstructures such as chromosomes, chromomere vesicles, chromonema, and mitochondria in the cytoplasm of living sperm cells at different stages in mitosis were visualized due to the remarkable DUV absorbance of nucleic acids and proteins, and mitotic dynamics were discussed [24]. Intranuclear microstructures were also observed in dividing cells and nondividing cells to understand how the growth of intranuclear microstructures differs between the two [25, 26]. DUV microscopes were also used to visualize bacterial spores including proteins, which have large DUV absorbance. Bacteria cultured for a varied number of days were analyzed, and their growing phases were discussed through observation of spores [27]. Detecting viruses whose diameters are on the order of 0.1 μm was one of the applications of DUV microscopy in biology [28]. Thanks to its high spatial resolution, a DUV microscope can better distinguish such small viruses by size. Caspersson, who made significant contributions to genetics, employed a DUV microscope for his research. Different from previous researchers, he considered the DUV absorption spectra of intracellular components to quantitatively discuss their contents in microstructures. To confirm any evidence of a relation between nucleic acid metabolism and gene duplication, he and his colleague estimated the nucleic acid content in some of the chromosome bands through DUV microscopy [29]. They also conducted quantitative measurements of distributions of aromatic amino acids in the colloid, cytoplasm, and nucleus in thyroid gland tissues and studied mechanisms of secretion [30]. The abovementioned early studies, except for reference [28] in which the spatial resolution of microscopes operating with different wavelengths was discussed, used DUV light in a relatively longer wavelength range ($\lambda = 275$ nm or 280 nm). In the 1930s and later, many studies used light with shorter wavelength ranges of 250–270 nm. Nucleic acids absorb DUV light in this wavelength range efficiently and dominantly in living organisms; thus, DUV light in this wavelength range was employed to accurately measure distributions of nucleic acids with high sensitivity and selectivity [31–43]. These studies include examination of therapeutic X-rays and gamma irradiation on malignant tumors [32] and DUV radiation to living cells during DUV imaging [36, 37, 42] by inspecting the dynamics of the nucleic acid content and distribution.

There were a few applications of DUV microscopy in research fields other than biology [44–46]. The ability of a DUV microscope to see microstructures was mostly appreciated by biologists, since most of the biological microscopes in use today such as the phase contrast microscope, differential interference contrast microscope, and laser microscope were not invented or standardized at

that time. Only a few techniques including dark-field microscopy and fluorescence microscopy were available for observation of transparent microstructures inside cells. Fluorescence microscopy was, however, not at all versatile at that time since labeling technology was not very advanced and was sometimes seen as an unreliable imaging technique due to the labeling, which could possibly change cellular structures and conditions. Dark-field microscopy was preferred for visualizing fine structures in living organisms, but was not suitable for distinguishing microstructures. A DUV microscope was one of the most reliable, useful devices for observing the distribution and morphology of microstructures in living organisms as they live.

All the abovementioned studies utilized single wavelengths. To extend microscopy to microspectroscopy, where observation at multiple wavelengths is necessary, the apparatus needed to be improved. In pursuing a brighter light source with a sharp linewidth [46] and higher spatial resolution with shorter wavelengths of light [23], the wavelength range in which a DUV microscope could operate was extended. Additionally, to shorten the acquisition duration, a sensitive picture film was integrated in the DUV microscope [47]. The sensitive picture film reduced the photodamage of samples because of the small radiation dose required for photographing [26]. To avoid the extra exposure of samples to DUV light, a system for adjusting the DUV focal plane to the sample without using DUV light was developed [22, 48]. This adjustment system has enabled Z-sectioning [49] and time-course measurements [25] of living cells. These improvements and developments overcame the issue of photodamage accumulation in a specimen through repetitive observation and have enabled multiwavelength DUV microscope imaging of a single living specimen without fatal photodamage. Additionally, they shortened the time required for photographing and made DUV microscope imaging practical and easy.

These advances in the apparatus enabled DUV microspectroscopic imaging in the 1930s. Anticipating that several different materials could be observed at different wavelengths, two research teams individually performed DUV microspectroscopic imaging almost at the same time. Three cancer researchers measured transmission images of tissues and microorganisms using multiple lines of a mercury lamp ($\lambda = 234$–435 nm) and showed that nuclei were highlighted clearly at $\lambda = 250$–260 nm but not at other wavelengths [50]. Some of their results are shown in Fig. 7.2. The authors also studied the wavelength dependence of radiation effects on living organisms and discussed the influence of secondarily radiated DUV light in cancer treatment by X-ray or γ-ray radiation. The other group developed a DUV reflection microscope working at various wavelengths and demonstrated observations of opaque aluminum alloys with light at wavelengths of 275 and 231 nm [46].

The DUV microspectroscopic imaging technique soon became useful as a quantitative technique to measure local absorbance in cells at different wavelengths [51]. With development of a bright light source with narrow, spectrally isolated emission lines and a high-throughput monochromator, live-cell imaging at multiple wavelengths in the DUV range (220, 231, 248, 257, 265, 270, 275, 280, 289, and 297 nm) became possible, and more precise study of wavelength dependence

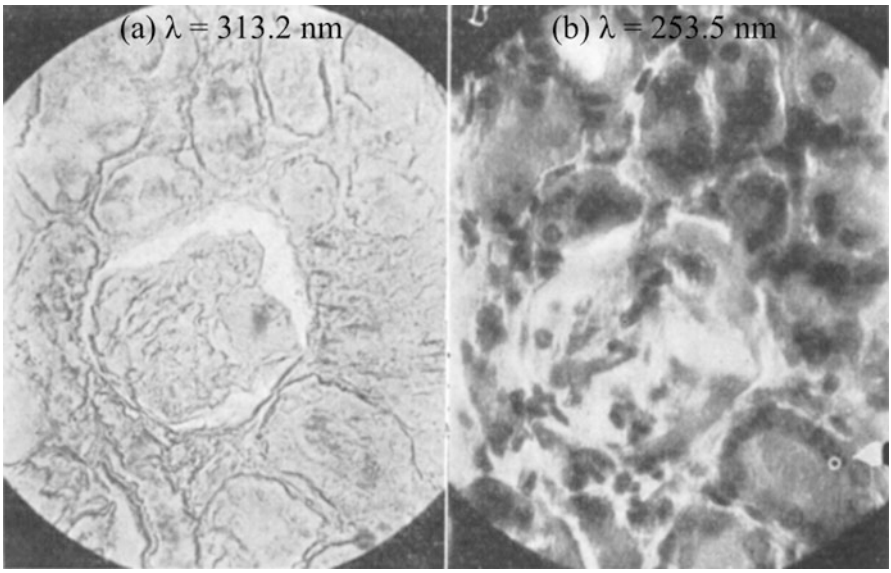

Fig. 7.2 The first microspectroscopy images of mouse kidney cells in the (**a**) UV ($\lambda = 313$ nm) and (**b**) DUV ($\lambda = 254$ nm) ranges. The cells are almost transparent in the UV light, while the nuclei of the cells, highlighted as *black circles*, are opaque in DUV light (Figures are reused with permission from the publisher of Ref. [50])

in DUV microspectroscopic imaging of cells was conducted [52]. The apparatus was later improved using a reflecting objective lens, which overcame chromatic aberration, leading to more accurate, quantitative measurements of local absorbance in the cytoplasm and nucleus in the DUV and longer ranges [39]. These studies indicated that DUV microspectroscopy could be a powerful technique for evaluating distributions of a variety of materials coexisting in a complex sample such as a biological cell.

All the work described above in this section involved absorption imaging, but scattering and fluorescence were also utilized in the early days of DUV microscopy. In fact, the first fluorescence microscope was invented using a DUV microscope, although current fluorescence microscopes mostly use visible light for fluorescence excitation. The idea of fluorescence microscopy occurred to Koehler during his development of the DUV microscope in 1904 [20, 53]. A DUV excitation fluorescence microscope was developed soon after the first paper on the DUV microscope was published [53]. DUV scattering microscopy was developed using dark-field condenser lenses [54]. The merit to using scattering and fluorescence in microscopy is good image contrast because of dark-field observation. These techniques in the early studies were, however, presented in only a few papers and used just as a compensation for transmission observation [28, 55, 56]. Scientists might not be able to overcome the disadvantages of scattering and fluorescence, such as low reaction cross sections and complicated image interpretation.

DUV microscopy and microspectroscopy are still popular in the 1940s and 1950s, but scientists started considering the influences of DUV irradiation on experimentally obtained images. One hot topic was cellular modification due to absorbance of DUV irradiation. Loofbourow and Joyce first claimed increases of DUV absorbance in bacterial cells during DUV imaging and attributed the increase to the production of nucleic acid-like hormones by cellular photodamage [57]. Brumberg and Larionow further supported the work of Loofbourow and Joyce by claiming that only injured cells and the nucleoli of uninjured cells absorbed DUV light; the other intracellular microstructures of the uninjured cells did not [58]. Contrary to these observations, Ludford and his colleagues observed intact living cells efficiently absorbing DUV light by an intrinsic nature of nucleotides [35]. To address this controversy, Bradfield and Errera measured the DUV absorption of various types of cells at different exposure durations and found that some types of cells showed decreases in DUV absorption and some types showed increases [36]. To explain the controversy more clearly, Walker and Davies examined the relationship among DUV absorbance and areas of a cell, and DUV irradiation doses, and found that the DUV absorbance was increased by shrinkage of the cell while total absorbance of the whole cell was decreased [37]. This result suggests that the controversy originated from diversities in cell shrinkage and decreases in total absorbance of irradiated cells.

During discussions of the influences of DUV irradiation on DUV imaging of living cells, the number of publications on DUV imaging decreased. This was possibly due in part to complications in interpreting the controversy. Another reason might be development and commercialization of new types of microscope such as the phase contrast microscope, differential interference contrast microscope, and electron microscope. Phase contrast and differential interference microscopes visualize transparent specimens with visible light. Because a specimen does not absorb light and the photon energy of visible light is half that of DUV photon energy or less in these microscopes, no significant photodamage occurs. Use of these new types of phase microscopes spread quickly in biology. Additionally, they were cheap compared with a DUV microscope. An electron microscope provides sub-100 nm spatial resolution, which is not possible with an optical microscope, including a DUV microscope. Moreover, fluorescence microscopes became versatile tools in biology because of improvements in labeling techniques. These new microscopes deprived DUV microscopes of their uniqueness, and use of DUV microscopy fell by the wayside in the 1970s and 1980s.

7.3 Recent Advances

7.3.1 Overview

After a few decades of little attention from scientists, there was a resurgence of interest in DUV microscopy and microspectroscopy. In the 1990s, two essential

techniques related to DUV microscopy and microspectroscopy were developed. One technique was DUV Raman microspectrometry [59–61], which was achieved using a nondestructive, continuous-wave (cw) DUV laser developed in the early 1990s [62]. Raman scattering, or inelastic light scattering, is highly sensitive to the chemical structure of a molecule and is therefore useful for characterization of molecular structure and material identification. The other technique was multiphoton excitation fluorescence microscopy, which became feasible using mode-locked pulsed lasers with tremendous peak power. Multiphoton excitation of a material having an absorption band at λ_1 is induced by light with a wavelength of $(n \times \lambda_1)$ where n is an integer larger than 1; that is, a material having a DUV absorption band ($\lambda = 200$–300 nm) can be excited with a light of $\lambda = 400$–600 nm and $\lambda = 600$–900 nm in a two- and three-photon excitation manner, respectively. The multiphoton excitation microscope was first developed to achieve 3D spatial resolution for observing a UV chromophore (having an absorption band at $\lambda = 315$ nm) with use of visible light ($\lambda = 630$ nm) [63]. The multiphoton fluorescence microscope was then extended for DUV excitation [10]. These two techniques launched new areas of study in DUV microscopy and microspectroscopy and stimulated improvements in and development of DUV optical components such as light sources, detectors, filters, and lenses.

In the beginning decade of the twenty-first century, DUV microspectroscopy and microscopy emerged as hot topics. This is due partially to development of the technologies of DUV optics as described and also to demands on DUV microspectroscopy and microscopy to study materials having absorption in the DUV range, such as wide-bandgap semiconductors for photocatalysis and light-emitting devices, metallic nanostructures for plasmonics, and nanocarbon materials for electronics. The newly developed techniques are based not only on Raman scattering microspectroscopy and multiphoton excitation fluorescence microscopy but also on old techniques including absorption microscopy and single-photon excitation fluorescence microscopy. Absorption microscopy was enhanced to be a more sensitive and quantitative technique for imaging nucleic acids and proteins in live cells [17]. Single-photon excitation fluorescence microscopy became more practical because of improvements in optical components and mature understanding of DUV chromophores [6]. Additionally, the single-photon technique was combined with advanced technologies such as near-field optical microscopy [16] and metal-enhanced fluorescence spectroscopy [64]. Advanced technologies were also integrated into DUV Raman scattering microscopy [4, 9].

In the following subsections, details of recent advances in DUV microscopy and microspectroscopy are described.

7.3.2 Absorption

As described in the previous section, DUV transmission absorption microscopy and microspectroscopy have been used to observe intracellular microstructures for many years. Absorption imaging has some advantages in DUV microscopy. Unlike

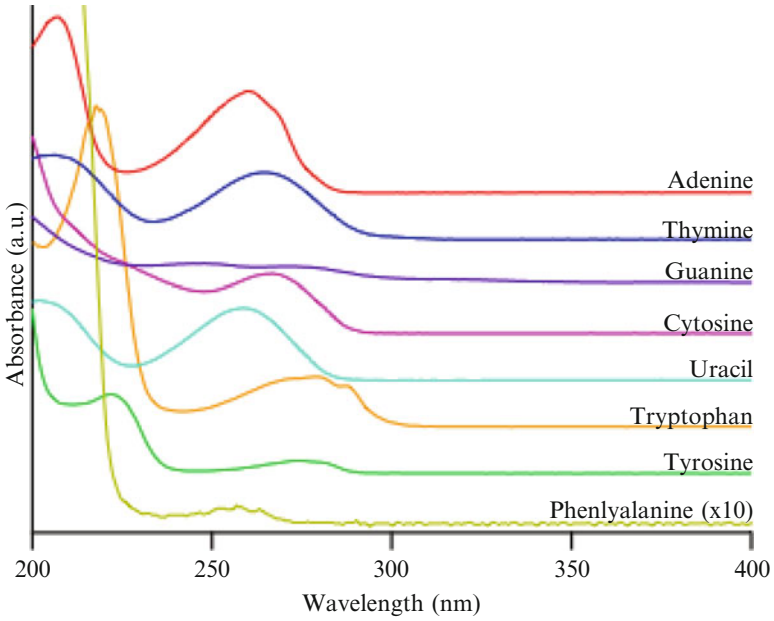

Fig. 7.3 UV absorption spectra of nucleotide bases and aromatic amino acids. All the components except for guanine were dissolved in water at a concentration of 100 μM. Guanine was dissolved in water at its saturation concentration. The curve of phenylalanine is displayed at 10 times magnification, while the other curves are not magnified but vertically shifted for visibility

fluorescence, absorption can be detected from any material that is not totally opaque. Furthermore, interpretation of a result is easier for absorption than scattering or fluorescence. Moreover, absorption is typically the most efficient optical response of a material.

For quantitative understanding of a result obtained with this technique, however, spectral overlap of absorption bands of different molecular species is an issue. Figure 7.3 shows UV absorption spectra of nucleotide bases and aromatic amino acids. These molecular species dominate DUV absorbance of living cells. Although absorption peaks of nucleotide bases and aromatic amino acids are located at different wavelengths, the broad spectra overlap each other. Because of this overlap, nucleic acids and proteins are hard to distinguish in DUV absorption microscopy.

Zeskind et al. recently developed a simple method to solve this issue [17]. They unmixed distributions of nucleic acids and proteins out of DUV absorption images of living cells to derive the quantitative mass distribution of nucleic acids and proteins in living cells. In this method, the authors assumed that the measured optical density in the longer half range of DUV ($\lambda = 250$–300 nm) should be only attributable to nucleobases in nucleic acids and aromatic amino acids in proteins. Based on this assumption, a measured optical density at an arbitrary wavelength in the DUV range at arbitrary spatial coordinates, $OD_\lambda(x, y)$, could be expressed as

$$\mathrm{OD}_{\lambda}(x, y) = \varepsilon_{\lambda}{}^{\mathrm{protein}} \times c^{\mathrm{protein}}(x, y) \times L(x, y) + \varepsilon_{\lambda}{}^{\mathrm{NA}} \times c^{\mathrm{NA}}(x, y) \times L(x, y),$$

where λ is the measurement wavelength, c is the sample concentration, L is the path length, and ε is the extinction coefficient. $c^{\mathrm{protein}}(x, y) \times L(x, y)$ and $c^{\mathrm{NA}}(x, y) \times L(x, y)$ represent the cellular mass distribution of proteins and nucleic acids, respectively. $\mathrm{OD}_{\lambda}(x, y)$ was measured, and ε was estimated. $\varepsilon^{\mathrm{NA}}$ was estimated by averaging extinction coefficients of DNA and RNA. $\varepsilon^{\mathrm{protein}}$ was estimated from the extinction coefficients of tryptophan, tyrosine, and phenylalanine, the dominant chromophores in proteins in the longer half range of DUV, and the average content of these residues in proteins. $(c \times L)^{\mathrm{NA}}$ and $(c \times L)^{\mathrm{protein}}$ are the only unknown quantities. To determine these quantities, $\mathrm{OD}_{260}(x, y)$ and $\mathrm{OD}_{280}(x, y)$ were acquired in DUV absorbance imaging of a cell at 260 nm and 280 nm. Additionally, $\varepsilon_{260}{}^{\mathrm{NA}}$, $\varepsilon_{280}{}^{\mathrm{NA}}$, $\varepsilon_{260}{}^{\mathrm{protein}}$, and $\varepsilon_{280}{}^{\mathrm{protein}}$ were estimated by the scheme described. Thus, simultaneous equations of OD_{260} and OD_{280} were set up and solved. Derived $(c \times L)$ at all the pixels in the image were used to yield a mass distribution of nucleic acids or proteins by calculating a product of $(c \times L)$ with a corresponding sample area of a pixel of a measured OD image. Figure 7.4 shows OD images of cells at 260 nm and 280 nm and yielded mass maps of nucleic acids and proteins at

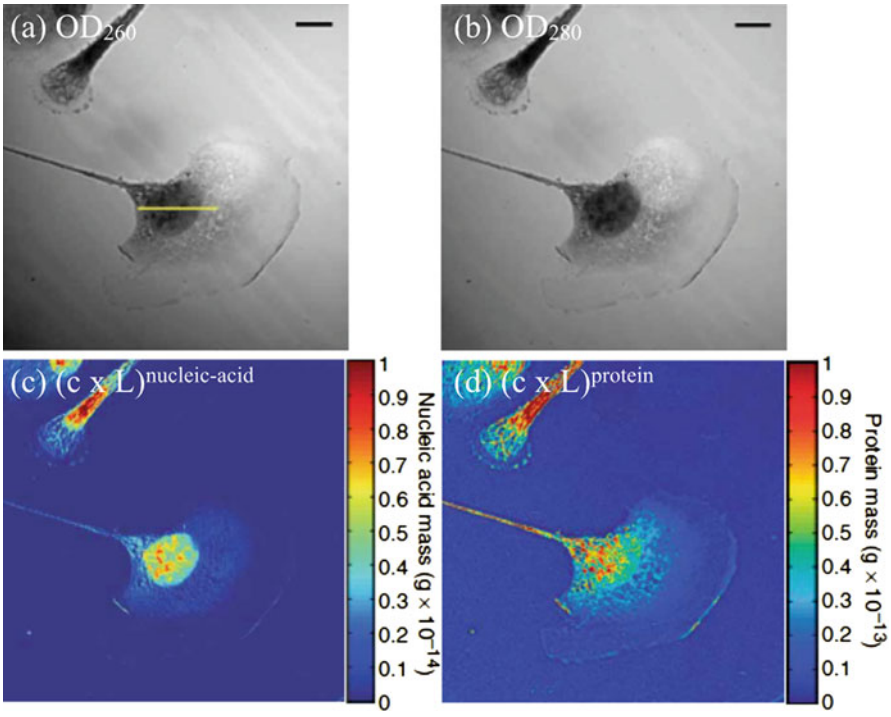

Fig. 7.4 (**a**, **b**) Transmission images of living cells at wavelengths of (**a**) 260 nm and (**b**) 280 nm. (**c**, **d**) Calculated mass distributions of (**c**) nucleic acids and (**d**) proteins. Scale bars are 10 μm (Figures are reused with permission from the publisher of Ref. [17])

femtogram concentrations. Two OD images look similar to each other, indicating that the images show a mixed distribution of nucleic acids and proteins, while two mass maps show different distributions, indicating distributions of nucleic acids and proteins are successfully unmixed by the scheme.

The technique was further improved for higher accuracy of unmixing and higher sensitivity to nucleic acids and proteins [18]. Cheung et al. modified the algorithm to estimate the extinction coefficients (ε) through extension of the wavelength range down to 200 nm using an intense and spectrally flat, broadband DUV light source [65]. The modified algorithm used ODs at 220 and 260 nm and improved the accuracy of unmixing proteins and nucleic acids. The study demonstrates the versatility of the technique for quantitative measurements of not only mass distribution but also total content of proteins and nucleic acids in cells. Furthermore, the technique has been applied to measure mass distribution and total content of proteins and nucleic acids in various types of cells [19].

The abovementioned development of and improvements in DUV absorption microscopy and microspectroscopy relied largely on improvements in DUV optics including bright, broadband light sources and highly sensitive detectors. A DUV absorption image was obtained with the exposure duration of only 100 ms or less at moderate illumination intensity. Such a moderate exposure has enabled time-lapse imaging of living cells for hours without any visual photodamage [17]. Live-cell time-lapse imaging has been demonstrated only at a single wavelength, but the results are impressive. In the future, time-lapse mass mapping of proteins and nucleic acids in a living cell will be possible with further development of a DUV microscope with higher signal collection efficiency.

7.3.3 Fluorescence

In biology, fluorescence microscopy is one of the most popular imaging techniques along with phase contrast and differential interference contrast microscopy. With visible-light illumination, a fluorescence microscope typically works with staining of target molecules with a fluorescence probe such as a dye, a fluorescence protein, or a quantum dot. Since current staining technology enables highly selective labeling of target molecules (even a single kind of molecule), fluorescence microscopy can distinguish target molecules in a living cell with high selectivity.

DUV excitation can play a different role from visible excitation in fluorescence microscopy. DUV excitation does not require molecular labeling since intrinsic chromophores in a specimen are targeted. In biology, the indole ring or its derivatives, such as tryptophan and serotonin, emit fluorescence with DUV excitation with efficiency similar to artificial dyes excited by visible or longer UV light. Fluorescence from these chemical structures appears in the longer UV range ($\lambda = 300$–400 nm) and is well distinguishable since it is far more efficient than UV fluorescence of other biological molecules in living organisms. Tryptophan is often used for label-free study of proteins containing tryptophan residues.

Fluorescence microscope imaging with DUV excitation has some advantages over other types of DUV imaging. Compared to scattering imaging, fluorescence imaging has two essential advantages. The fluorescence signal is easy to detect because the process occurs more efficiently by several orders of magnitude and the detection wavelength shifts to the incident wavelength. The other advantage is molecular selectivity due to the fact that efficient DUV excitation fluorescence occurs only from some absorbers while resonance scattering occurs from almost all absorbers. This advantage is adapted also for comparison with transmission absorption imaging. Another advantage compared with transmission absorption imaging is being able to obtain images with high contrast due to dark-field observation. Additionally, fluorescence imaging is applicable to totally opaque specimens. Furthermore, a fluorescence imaging setup can be easily combined with advanced microscope technologies such as near-field microscopes. Details of this combination are described later in this section.

One of the recent achievements in the field of DUV fluorescence microscopy is multiphoton excitation microscopy. Multiphoton absorption occurs with light at multiple orders of the wavelength of an absorption band, that is, visible or NIR light can excite a DUV absorption band. Since the intensity of multiphoton excitation fluorescence is proportional to the power of multiple orders of the excitation intensity, the excitation volume is confined to a tightly focused region. Thus, photodamage can be confined compared with single-photon excitation fluorescence microscopy. Furthermore, 3D imaging of deep inside a sample is possible, while 3D imaging in single-photon fluorescence microscopy is difficult due to large DUV absorbance and large scattering efficiency at optical paths in the sample.

Multiphoton excitation DUV microscopy was first reported in 1995 [10]. The article showed a line intensity profile of quartz luminescence across a quartz cover slip excited by a 532 nm picosecond laser; that is, the sample was excited at the energy corresponding to DUV light ($\lambda = 266$ nm). The authors mentioned the applicability of the technique to imaging of a variety of biological molecules such as non-stained DNA and labeling fluorescence probes that have strong absorption bands in the DUV range. They also mentioned another advantage of multiphoton excitation—it does not require DUV optics, which usually have poorer performances than visible or NIR optics. For example, high NA apochromats, which are impossible to design and produce with current DUV optical technologies, are used for multiphoton excitation microscopy.

Multiphoton excitation DUV microscopy has been used for several applications in biological research. Maiti and his colleagues first applied the technique to live-cell imaging [11]. They focused on the indole group, which has absorption bands in the DUV range and emits fluorescence in the UV range with high efficiencies. Serotonin, a neurotransmitter belonging to the indole group, was loaded into rat basophilic leukemia cells that were then incubated for 6 h. The serotonin distribution in cells was then observed in the 3D space. An intense, pulsed laser with $\lambda = 700$ nm was used for excitation of the DUV absorption band of serotonin via the three-photon absorption process. Serotonin imaging has been used to study the secretion process of cells [66]. The distribution of granule containing serotonins in mast

cells treated with antigen stimulation, which initiates the secretion process, was imaged with UV fluorescence of serotonin excited by a three-photon process with $\lambda = 740$ nm. Serotonin imaging has also been used to evaluate the potential of multiphoton DUV excitation fluorescence microscopy for high-resolution Z-sectioning in tissues [12] and to clarify differences between three-photon and two-photon excitations [67]. In a recent study, tryptophan fluorescence was used as a native protein marker in cells [13]. Measuring tryptophan fluorescence excited by the two-photon process with 532 nm pulsed laser, the authors showed Z-sectioning of mouse skin as deep as 70 μm from the surface. Such depth cannot be reached by single-photon DUV excitation. These results represented the potential of the multiphoton DUV excitation technique for deep-tissue imaging.

Single-photon DUV excitation imaging has also been used in recent studies of DUV fluorescence microscopy [6, 7]. Single-photon excitation has several advantages compared to multiphoton excitation. One advantage is high sensitivity. The absorption cross section of the single-photon process is higher than that of the multiphoton process. Additionally, unlike multiphoton excitation imaging, which requires tight focusing of the laser beam and scanning of the focused beam (or sample), single-photon excitation imaging can be used for wide-field imaging and thus is suitable for observing a wide field of view. The wide-field and highly sensitive DUV excitation fluorescence imaging has been employed for in situ label-free detection of a tiny amount of bacteria on the surface of environmental samples [7].

Single-photon excitation fluorescence microscopy has been combined with other advanced analytical techniques. A DUV fluorescence lifetime microscope was developed through a time-resolved imaging technique using a picosecond or femtosecond pulsed laser and time-gating detector [7, 15]. A nanoscale imaging technique was also developed using a near-field optical microscope technique [16]. The method used DUV ($\lambda = 266$ nm) near-field light generated at the apex of a fine optical fiber with a pure quartz core for excitation of fluorescence from polymers and achieved a spatial resolution of 50 nm. The research also demonstrated DUV excitation native-fluorescence nanoscale imaging of a cell surface. Near-field optics using surface plasmons was also combined with DUV fluorescence microscopy [64]. An aluminum-coated fused silica prism was irradiated by DUV light with the total internal reflection configuration, and near-field light generated with surface plasmon polaritons at the metal-air interface was utilized for efficient excitation of fluorescence of cells cultured on the aluminum film. Another fluorescence imaging technique utilized tryptophan fluorescence to discuss the microenvironments of proteins in a cell [17].

Although DUV excitation fluorescence microscopy typically does not require molecular labeling, the combination with labeling techniques can yield an advanced imaging scheme. Kikawada et al. demonstrated multicolor imaging of HeLa cells labeled with multiple fluorescence dyes with a DUV excitation fluorescence imaging technique [64]. The dyes used in the study, MitoTracker, ATTO488, and DAPI, are usually excited by visible light and require different excitation wavelengths. However, the authors used DUV light to simultaneously excite all three dyes at a single-frequency wavelength in the DUV range, at which all the dyes share

an absorption band. Since each of these dyes labeled a different cell organelle, they achieved simultaneous imaging of cell organelles with single-frequency DUV fluorescence microscopy.

As an analogue to fluorescence, cathodoluminescence has also been utilized for microscope imaging. To characterize materials emitting cathodoluminescence in the DUV range, a DUV microscope was used. Aluminum nanostructures have been observed with cathodoluminescence in the DUV range, and their plasmonic properties such as plasmon modes and resonance wavelengths in the DUV have been analyzed [68]. Semiconducting materials have also been studied with cathodoluminescence in the DUV range [69]. The chemical structures in tiny pieces of semiconductors were studied.

7.3.4 Raman Scattering

Light scattering is secondary radiation of light as a result of electron oscillations generated by the electromagnetic field of incident light. When the wavelength of light is close to or matches the wavelength of an absorption band of a material, light scattering is amplified by a factor of up to 10^8 due to the electronic resonance effect, compared to when the wavelength of light is far from the absorption band. Because of the resonance effect, light scattering in the DUV range is also useful for the study of a sample containing materials absorbing DUV light.

Among light scattering processes, a type of inelastic light scattering processes, Raman scattering, provides many advantages over fluorescence and absorption. Raman scattering is the result of an inelastic collision of a photon with a molecule or a phonon. As a result of the collision, a photon is scattered while losing or gaining vibration energy from a molecule or a phonon; thus, the wavelength of Raman scattering is shifted from the wavelength of incident light. Since the wavelength shift is based on the chemical structure of a molecule or crystal, Raman scattering provides chemical information on specimens without the need for sample labeling. At first glance, this advantage does not seem special for Raman spectroscopy but adaptable to fluorescence and absorption spectroscopy. However, Raman scattering is highly sensitive to chemical structures compared with these other techniques and thereby is capable of identifying materials and of probing structural or environmental changes in molecules or crystals with high sensitivity and accuracy. Such high sensitivity to chemical structure is sustained by the narrow bandwidth of Raman scattering when a single-frequency laser is used as incident light. The typical bandwidth of Raman scattering is in the range of 10–100 cm^{-1} while those of fluorescence and absorption are approximately 1,000 cm^{-1}. Thus, Raman scattering microscopy is a powerful technique for revealing the distribution of structures and environments of a sample. Moreover, unlike fluorescence, DUV Raman scattering can be electronically resonant in almost all the materials absorbing DUV light. Unlike absorption, a totally opaque sample can be measured because of scattering.

Despite these advantages, light scattering microscopy was hardly used in the twentieth century. The main drawback of light scattering techniques is the weak scattering intensity. Light scattering efficiency is lower, even in the resonance condition, than the absorption and fluorescence efficiencies. It was difficult to excite and collect scattering light efficiently from a sample without lethal photodamage since the detection throughputs of microscopes and spectrographs were low. A few reports presented DUV scattering imaging, but they seemed to suffer from weak signal [28, 54–56].

DUV Raman scattering microscope imaging was achieved at the beginning of the twenty-first century owing to development of DUV micro-spectrographs in the 1990s. A DUV Raman micro-spectrograph equipped with an intense, cw laser, a high-throughput micro-spectrograph, and a sensitive multichannel detector was used for micro-Raman spectral measurements of single or a small number of cells [59–61]. With the apparatus, DUV micro-Raman spectra were measured from nuclei in cells, and nucleotide bases and aromatic amino acids were selectively observed [59, 61].

After improvements in and development of DUV optics, the first DUV scattering microspectroscopic imaging was, to the best of our knowledge, presented in 2002 [4]. The report presented a sample-scanning confocal Raman microscope equipped with single-frequency cw laser emitting at the wavelength of 244 nm. To demonstrate the performance of the microscope, authors performed Raman imaging of CVD diamond films grown on a silicon substrate in two dimensions and compared the results with Raman images obtained with 515 and 633 nm excitations. Measurements were performed over a 40 μm $\times$ 40 μm square area of the sample with the scanning step of 2 μm. The laser power given to the sample was set to be as low as 1 mW to avoid sample burning. Obtained Raman images showed the first-order diamond and graphite band. Results indicated that DUV excitation could discriminate diamond and graphite in a sample more clearly compared with visible-light excitations. The reason for the better discrimination is the absence of luminescent background at DUV excitation. Additionally, Raman bands of disordered carbon are not observed because the bands are out of the resonance in the DUV range. Moreover, substrate does not provide any Raman scattering and luminescence because of the low penetration depth of DUV light into the silicon substrate. Thus, a quantitative analysis of CVD diamond using Raman microscopy is possible with DUV excitation.

Similarly, polycrystalline CVD diamond films were studied with DUV Raman microscopy [5, 70]. With DUV excitation, a defective domain running along a (111) homoepitaxial film was analyzed. The defective domain was probed through sp^3 C-H vibrations, to which DUV excitation is more sensitive than visible and NIR excitations. This is partly because the wavenumber range containing C-H vibration modes is free from photoluminescence and second-order disorder Raman band with DUV excitation. The authors also analyzed boron-doped films. Doping can modify chemical structures of diamond and consequently modify optical and electrical properties. DUV Raman microscopy is a powerful technique for probing slight structural changes in diamond doped with boron through broadening and shift

of the diamond band. As a function of the boron concentration, the peak shift of the diamond band was analyzed. The high sensitivity to the diamond band makes DUV Raman microscopy a unique and useful technique for probing slight structural changes in doped diamond materials.

DUV Raman microscopy has been applied for unique analysis of inorganic samples—Martian meteorites [8]. It is possible to classify meteorites by their alteration and evolutionary history through mineral analysis. Raman microscopy is powerful for in situ analysis of such minerals. The high chemical sensitivity is the advantage of Raman spectroscopy compared with other techniques such as X-ray spectroscopy and electron microscopy. Additionally, a Raman measurement can be performed without destroying a sample. Use of DUV excitation makes a Raman measurement more useful since overlap of luminescence with the Raman spectrum is avoided. Furthermore, the scattering efficiency is large because of the resonance Raman effect and fourth-power relationship of the scattering efficiency with the frequency of light. Because of these advantages, the number of detectable minerals in Martian meteorites with DUV excitation can be twice or more compared to visible and NIR excitations.

The application of DUV Raman microscopy is not limited to inorganic material. In biology, DUV excitation in general can selectively excite nucleotide bases and aromatic amino acids in a cell, thanks to the resonance effect, while it does not efficiently excite other molecules such as lipids and aliphatic amino acids because there is no resonance in these materials. Figure 7.5 shows typical Raman spectra of mammalian cells excited with DUV ($\lambda = 244$ nm) and visible ($\lambda = 532$ nm) light. The selectivity of DUV excitation to nucleotide bases and aromatic amino acids is clear, while these species are hardly observed with visible-light excitation. These species are also observed with NIR excitation, at which none of the biomolecules is in the resonance condition. However, DUV excitation is more selective than IR to detect those species.

Kumamoto et al. have realized applications of DUV resonance Raman spectroscopy to biological imaging [1]. To achieve DUV Raman imaging of a cell, we first analyzed spectral evolution of cells during DUV resonance Raman measurements and correlated measurement conditions with biomolecular photodegradation [71]. Based on the results, we estimated imaging conditions appropriate for cell imaging and performed DUV Raman imaging of a cell. In this method, we employed a DUV laser with $\lambda = 257$ nm to excite resonance Raman scattering of nucleotide bases and aromatic amino acids in a HeLa cell. Using a well-isolated, sharp band selectively assigned to adenine and guanine vibration modes of 1,490 cm^{-1} (see Fig. 7.5), we reconstructed a two-dimensional spatial distribution of nucleic acids present in a HeLa cell. Figure 7.6 shows one of the reconstructed Raman images and a visible light transmission image of the cell for comparison. The comparison clarifies that the Raman image highlights the nucleoli and the cytoplasm, where RNA is concentrated.

In DUV resonance Raman microscopy of a cell, the choice of an excitation wavelength is important. The best wavelength among available cw oscillation

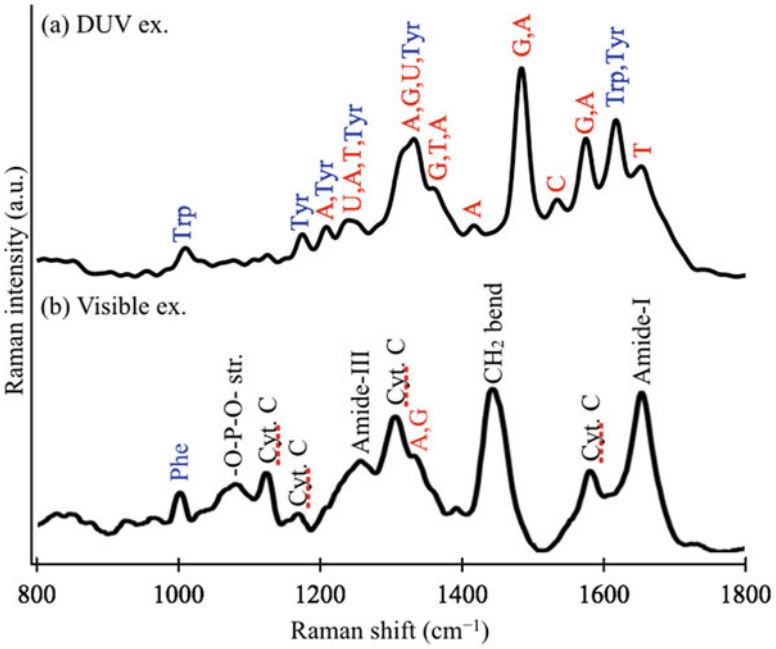

Fig. 7.5 Raman spectra of HeLa cells excited with (**a**) DUV light ($\lambda = 244$ nm) and (**b**) visible light ($\lambda = 532$ nm). A, G, T, C, U, Tyr, Trp, Phe, and Cyt represent adenine, guanine, thymine, cytosine, uracil, tyrosine, tryptophan, phenylalanine, and cytochrome, respectively

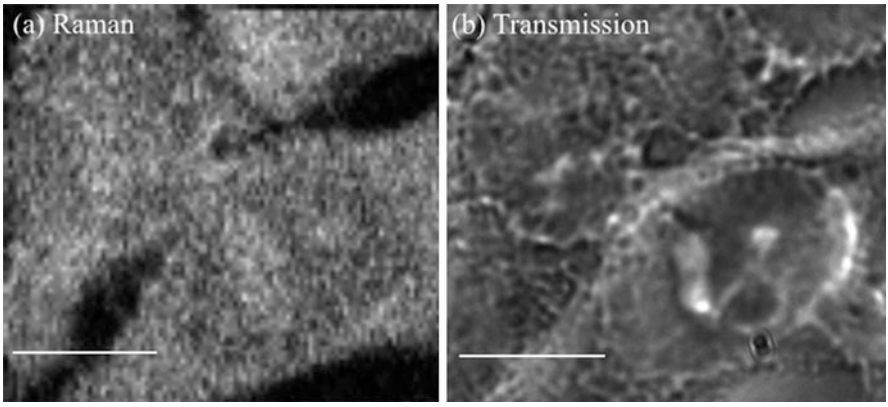

Fig. 7.6 (**a**) A DUV ($\lambda = 257$ nm) excitation resonance Raman image reconstructed from Raman intensity of the adenine and guanine band at 1,490 cm^{-1} in HeLa cell spectra. (**b**) A visible light transmission image of the corresponding cell. The scale bar is 10 μm

lines with sufficiently narrow bandwidth and high output power for performing a micro-Raman measurement is $\lambda = 257$ nm. At this wavelength, the excitation cross sections of nucleotide bases are high, and there is very little overlap of the

native fluorescence of tryptophan with a Raman scattering spectrum. Additionally, performances of optics such as a spectrometer, objective lens, and Rayleigh rejection filter are sufficient. Indeed, the author estimates that 252–253 nm is the best in considering the large excitation cross section of nucleotide bases and no overlap of the native fluorescence. Development of a high power and narrow bandwidth laser and other high-performance optics at these wavelengths are expected.

As another potential application of DUV Raman microscopy, Frosch et al. reported on its utility for astrobiology in which one of the research interests is to detect traces of living organisms on the surface of a meteorite and planet [8]. They also performed in situ DUV resonance micro-Raman analysis of plants for trace detection of localized aromatic chemicals [72, 73]. Imaging analysis can reveal more details about these kinds of samples.

Before concluding this section, one important, advanced technique of DUV Raman imaging must be described. In the first report of DUV Raman imaging, a DUV scanning near-field Raman microscope was also demonstrated [4]. The system employed a tapered optical fiber having a 200 nm aperture at the apex at which DUV near-field light was produced. The sample was situated close to the apex for near-field Raman excitation. The scattered photons were collected by an objective lens and guided into a spectrometer. To obtain a near-field DUV Raman image, the sample stage was scanned horizontally. The spatial resolution of 200 nm was achieved in observation of CVD diamond films. The spatial resolution is not beyond the theoretical diffraction limit of a conventional confocal DUV Raman microscope, but it exceeded the spatial resolution in an aberration-limited conventional DUV Raman microscope. Recently, Taguchi et al. reported on tip-enhanced Raman scattering with DUV excitation for high scattering efficiency in nanoimaging [9]. A DUV tip-enhanced Raman scattering microscope will enable DUV Raman imaging analysis of nanomaterials. Details are described in Chap. 8.

7.4 Conclusions and Future Perspectives

This chapter reviewed the history and recent advancements in DUV microscopy and microspectroscopy. DUV microscopic and microspectroscopic imaging were considered powerful analytical techniques particularly in biology to highlight transparent microstructures in the first half of the twentieth century. Interest subsequently waned but resurged at the end of the twentieth century due to development of a new type of DUV imaging technique, improvements in and development of DUV optics, and demands for techniques to analyze materials absorbing DUV light. In the most recent decade, DUV microscopy and microspectroscopy are becoming hot topics in microscopy, and a variety of imaging techniques using absorption, fluorescence, and resonance Raman scattering have been developed. In the future, further enhancement of DUV optics, especially light sources, detectors, and objective lenses, and establishment of methods to minimize sample photodegradation will drive the evolution of current imaging techniques and the development of new imaging techniques in DUV microscopy and microspectroscopy.

References

1. Y. Kumamoto, A. Taguchi, N.I. Smith, S. Kawata, Deep ultraviolet resonant Raman imaging of a cell. J. Biomed. Opt. **17**, 076001 (2012)
2. S.A. Asher, UV resonance Raman spectroscopy for analytical, physical, and biophysical chemistry. Part 1. Anal. Chem. **65**, 59A–66A (1993)
3. S.A. Asher, C.R. Johnson, J. Murtaugh, Development of a new cw UV resonance Raman spectrometer for the 217-400-nm spectral region. Rev. Sci. Instrum. **54**, 1657–1662 (1983)
4. H.S. Sands, F. Demangeot, E. Bonera, S. Webster, R. Bennett, I.P. Hayward, F. Marchi, D.A. Smith, D.N. Batchelder, Development of a combined confocal and scanning near-field Raman microscope for deep UV laser excitation. J. Raman Spectrosc. **33**, 730–739 (2002)
5. A. Crisci, M. Mermoux, B. Saubat-Marcus, Deep ultra-violet Raman imaging of CVD boron-doped and non-doped diamond films. Diam. Relat. Mater. **17**, 1207–1211 (2008)
6. F. Jamme, S. Kascakova, S. Villette, F. Allouche, S. Pallu, V. Rouam, M. Refregiers, Deep UV autofluorescence microscopy for cell biology and tissue histology. Biol. Cell. **105**, 277–288 (2013)
7. R. Bhartia, E.C. Salas, W.F. Hug, R.D. Reid, A.L. Lane, K.J. Edwards, K.H. Nealson, Label-free bacterial imaging with deep-UV-laser-induced native fluorescence. Appl. Environ. Microbiol. **76**, 7231–7237 (2010)
8. T. Frosch, N. Tarcea, M. Schmitt, H. Thiele, F. Langenhorst, J. Popp, UV Raman imaging – a promising tool for astrobiology: comparative Raman studies with different excitation wavelengths on SNC Martian meteorites. Anal. Chem. **79**, 1101–1108 (2007)
9. A. Taguchi, N. Hayazawa, K. Furusawa, H. Ishitobi, S. Kawata, Deep-UV tip-enhanced Raman scattering. J. Raman Spectrosc. **40**, 1324–1330 (2009)
10. O. Nakamura, T. Okada, A two-photon scanning fluorescence microscope with deep UV excitation and near UV detection. Optik **100**, 167–170 (1995)
11. S. Maiti, J.B. Shear, R.M. Williams, W.R. Zipfel, W.W. Webb, Measuring serotonin distribution in live cells with three-photon excitation. Science **275**, 530–532 (1997)
12. W.R. Zipfel, R.M. Williams, R. Christie, A.Y. Nikitin, B.T. Hyman, W.W. Webb, Live tissue intrinsic emission microscopy using multiphoton-excited native fluorescence and second harmonic generation. Proc. Natl. Acad. Sci. **100**, 7075–7080 (2003)
13. C. Li, R.K. Pastila, C. Pitsillides, J.M. Runnels, M. Puoris'haag, D. Cote, C.P. Lin, Imaging leukocyte trafficking *in vivo* with two-photon-excited endogenous tryptophan fluorescence. Opt. Express **18**, 988–999 (2010)
14. Q. Li, T. Ruckstuhl, S. Seeger, Deep-UV laser-based fluorescence imaging microscopy of single molecules. J. Phys. Chem. B **108**, 8324–8329 (2004)
15. T.A. Smith, L.M. Hirvonen, C.N. Lincoln, X. Hao, Deep-UV confocal fluorescence imaging and super-resolution optical microscopy of biological samples. J. Innov. Opt. Health Sci. **5**, 120025 (2012)
16. H. Aoki, T. Hamamatsu, S. Ito, Deep ultraviolet scanning near-field optical microscopy for the structural analysis of organic and biological materials. Appl. Phys. Lett. **84**, 356–358 (2004)
17. B.J. Zeskind, C.D. Jordan, W. Timp, L. Trapani, G. Waller, V. Horodincu, D.J. Ehrlich, P. Matsudaira, Nucleic acid and protein mass mapping by live-cell deep-ultraviolet microscopy. Nat. Methods **4**, 567–568 (2007)
18. M.C. Cheung, J.G. Evans, B.K. McKenna, D.J. Ehrlich, Deep ultraviolet mapping of intracellular protein and nucleic acid in femtograms per pixel. Cytometry A **79**, 920–932 (2011)
19. M.C. Cheung, R. LaCroix, B.K. McKenna, L. Liu, J. Winkelman, D.J. Ehrlich, Intracellular protein and nucleic acid measured in eight cell types using deep-ultraviolet mass mapping. Cytometry A **83**, 540–551 (2013)
20. A. Koehler, Mikrophotographische Untersuchungen mit ultraviolettem licht. Zeitschrift fuer wissenschaftliche Mikroskopie und mikroskopische Technik. **21**, 129–165 and 273–304 (1904)
21. H.C. Ernst, S.B. Wolbach, Ultra-violet photomicrography. J. Med. Res. **14**, 463–470 (1906)

22. S. Mudd, S. Warren, A readily cultivable vibrio, filterable through Berkefeld "V" candles, *Vibrio percolans* (New species). J. Bacteriol. **8**, 447–457 (1923)
23. J.E. Barnard, The microscopical examination of filterable viruses. Lancet **206**, 117–123 (1925)
24. F.F. Lukas, M.B. Stark, A study of living sperm cells of certain grasshoppers by means of the ultraviolet microscope. J. Morphol. **52**, 91–113 (1931)
25. R.W.G. Wyckoff, A.H. Ebeling, A.L. Ter Louw, A comparison between the ultraviolet microscopy and the Feulgen staining of certain cells. J. Morphol. **53**, 189–199 (1932)
26. R.W.G. Wyckoff, Ultraviolet microscopy as a means of studying cell structure. Cold Spring Harb. Symp. Quant. Biol. **2**, 39–46 (1934)
27. R.W.G. Wyckoff, A.L. Ter Louw, Some ultraviolet photomicrographs of *B. subtilis*. J. Exp. Med. **54**, 449–451 (1931)
28. J.E. Barnard, Microscopical evidence of the existence of saprophytic viruses. Brit. J. Exp. Pathol. **16**, 129–133 (1935)
29. T. Caspersson, J. Schultz, Nucleic acid metabolism of the chromosomes in relation to gene reproduction. Nature **142**, 294–295 (1938)
30. L. Gersh, T. Caspersson, Total protein and organic iodine in colloid and cells of single follicles of the thyroid gland. Anat. Rec. **78**, 303–319 (1940)
31. T. Caspersson, Ueber den chemischen Aufbau der Strukturen des Zellkernes. Protoplasma **27**, 463–467 (1937)
32. J.S. Mitchell, Increase in ultra-violet absorption of cytoplasm after therapeutic X- and gamma-irradiation. Nature **146**, 272–273 (1940)
33. E.B. Harvey, G.I. Lavin, The chromatin in the living *Arbacia punctulata* egg and the cytoplasm of the centrifuged egg as photographed by ultra-violet light. Biol. Bull. **86**, 163–168 (1944)
34. R.J. Ludford, J. Smiles, F.V. Welch, Ultra-violet microscopy of living malignant cells. Nature **162**, 650–651 (1948)
35. R.J. Ludford, J. Smiles, F.V. Welch, The study of living malignant cells by phase-contrast and ultra-violet microscopy. J. R. Microsc. Soc. **68**, 1–9 (1948)
36. J.R.G. Bradfield, M. Errera, Ultra-violet absorption of living cells. Nature **164**, 532–533 (1949)
37. P.M.B. Walker, H.G. Davies, Ultra-violet microspectro- graphy of living tissue culture cells. Part II. Microspectrographic studies of living cells and ultraviolet-irradiated chick fibroblasts. Discuss. Faraday Soc. **9**, 461–470 (1950)
38. R.J. Ludford, J. Smiles, The structure of living malignant cells demonstrable by ultra-violet microscopy. J. R. Microsc. Soc. **70**, 194–200 (1950)
39. R.C. Mellors, R.E. Berger, H.G. Streim, Ultraviolet microscopy and microspectroscopy of resting and dividing cells: studies with a reflecting microscope. Science **111**, 627–632 (1950)
40. B. Thorell, Some aspects of ultraviolet microscopy in haematology. Acta Haematol. **7**, 334–342 (1952)
41. R.J. Ludford, J. Smiles, Ultra-violet microscopy of living malignant cells: I. The interphase nucleus. J. R. Microsc. Soc. **73**, 173–178 (1953)
42. R.P. Perry, Changes in the ultraviolet absorption spectrum of parts of living cells following irradiation with an ultraviolet microbeam. Exp. Cell Res. **12**, 546–559 (1957)
43. A. Cosslett, Some applications of the ultra-violet and interference microscopes in electron microscopy. J. R. Microsc. Soc. **79**, 263–271 (1960)
44. B.K. Johnson, Sources of illumination for ultra-violet microscopy. Proc. Phys. Soc. **43**, 127–137 (1931)
45. B.K. Johnson, Notes on ultra-violet microscopy. J. R. Microsc. Soc. **51**, 268–271 (1931)
46. B.K. Johnson, An ultra-violet microscope for the examination of opaque objects. J. Sci. Instrum. **11**, 384–394 (1934)
47. R.W.G. Wyckoff, A.L. Ter Louw, On the ultra-violet photography of living cells. Science **74**, 664–665 (1931)
48. J.E. Barnard, Microscopy with ultra-violet light. Nature **106**, 378–381 (1920)

49. F.F. Lukas, The architecture of living cells – recent advances in methods of biological research – optical sectioning with the ultra-violet microscope. Proc. Natl. Acad. Sci. **16**, 599–607 (1930)
50. A.J. Allen, R. Franklin, E. McDonald, Photomicrography and radiation studies with various wave-lengths of monochromatic ultraviolet radiation. J. Franklin Inst. **218**, 701–716 (1934)
51. T. Caspersson, Methods for the determining of the absorption spectra of cell structures. J. R. Microsc. Soc. **60**, 8–25 (1939)
52. P.A. Cole, F.S. Brackett, Technical requirements in the determination of absorption spectra by the ultraviolet microscope. Rev. Sci. Instrum. **11**, 419–427 (1940)
53. F.W.D. Rost, The history of fluorescence microscopy, in *Fluorescence Microscopy*, vol. 2 (Cambridge University Press, Cambridge, 1995), pp. 183–195
54. J.E. Barnard, Presidential address. Some aspects of ultra-violet microscopy. J. R. Microsc. Soc. **49**, 91–101 (1929)
55. J.E. Barnard, F.V. Welch, Fluorescence microscopy with high powers. J. R. Microsc. Soc. **56**, 361–364 (1936)
56. J. Laennergren, Location of U.V.-absorbing substance in isolated skeletal muscle fibres. The effect of stimulation. J. Physiol. **270**, 785–800 (1977)
57. J.R. Loofbourow, L. Joyce, Increased ultra-violet absorption of cells following irradiation with ultra-violet light. Nature **148**, 166 (1941)
58. E.M. Brumberg, L. Th Larionow, Ultra-violet absorption in living and dead cells. Nature **158**, 663–664 (1946)
59. F. Sureau, L. Chinsky, C. Amirand, J.P. Ballini, M. Duquesne, A. Laigle, P.Y. Turpin, P. Vigny, An ultraviolet micro-Raman spectrometer: resonance Raman spectroscopy within single living cells. Appl. Spectrosc. **44**, 1047–1051 (1990)
60. S. Chadha, W.H. Nelson, J.F. Sperry, Ultraviolet micro-Raman spectrograph for the detection of small numbers of bacterial cells. Rev. Sci. Instrum. **64**, 3088–3093 (1993)
61. V. Pajcini, C.H. Munro, R.W. Bormett, R.E. Witkowski, S.A. Asher, UV Raman microspectroscopy: spectral and spatial selectivity with sensitivity and simplicity. Appl. Spectrosc. **51**, 81–86 (1997)
62. S.A. Asher, R.W. Bormett, X.G. Chen, D.H. Lemmon, N. Cho, P. Peterson, M. Arrigoni, L. Spinelli, J. Cannon, UV resonance Raman spectroscopy using a new cw laser source: convenience and experimental simplicity. Appl. Spectrosc. **47**, 628–633 (1993)
63. W. Denk, J.H. Strickler, W.W. Webb, Two-photon laser scanning fluorescence microscopy. Science **248**, 73–76 (1990)
64. M. Kikawada, A. Ono, W. Inami, Y. Kawata, Enhanced multicolor fluorescence in bioimaging using deep-ultraviolet surface plasmon resonance. Appl. Phys. Lett. **104**, 223703 (2014)
65. M. Islam, L. Ciaffoni, G. Hancock, G.A.D. Ritchie, Demonstration of a novel laser-driven light source for broadband spectroscopy between 170 nm and 2.1 μm. Analyst **138**, 4741–4745 (2013)
66. R.M. Williams, J.B. Shear, W.R. Zipfel, S. Maiti, W.W. Webb, Mucosal mast cell secretion processes imaged using three-photon microscopy of 5-hydroxytryptamine autofluorescence. Biophys. J. **76**, 1835–1846 (1999)
67. J. Bajaji, R. Desai, S. Maiti, Live cell ultraviolet microscopy: a comparison between two- and three-photon excitation. Microsc. Res. Tech. **63**, 67–71 (2004)
68. M.W. Knight, L. Liu, Y. Wang, L. Brown, S. Mukherjee, N.S. King, H.O. Everitt, P. Nordlander, N.J. Halas, Aluminum plasmonics nanoantennas. Nano Lett. **12**, 6000–6004 (2012)
69. H. Saijo, Y. Suzuki, M. Shiojiri, Deep UV imaging by spectrometric full-colour cathodoluminescence microscopy. J. Phys. Conf. Ser. **241**, 012079 (2010)
70. A. Crisci, B. Saubat-Marcus, M. Mermoux, Deep ultraviolet Raman imaging with micron resolution: application to chemical-vapor-deposited diamond films. Jpn. J. Appl. Phys. **47**, 8868–8870 (2008)

71. Y. Kumamoto, A. Taguchi, N.I. Smith, S. Kawata, Deep UV resonant Raman spectroscopy for photodamage characterization in cells. Biomed. Opt. Express **2**, 927–936 (2011)
72. T. Frosch, M. Schmitt, J. Popp, Ultrasensitive *in situ* tracing of the alkaloid dioncophylline A in the tropical liana *Triphyophyllum peltatum* by applying deep-UV resonance Raman microscopy. Anal. Chem. **79**, 986–993 (2007)
73. T. Frosch, M. Schmitt, T. Noll, G. Bringmann, K. Schenzel, J. Popp, *In situ* UV resonance Raman micro-spectroscopic localization of the antimalarial quinine in cinchona bark. J. Phys. Chem. B **111**, 4171–4177 (2007)

Chapter 8
Deep-Ultraviolet Surface-Enhanced Raman Scattering

Atsushi Taguchi

Abstract Surface-enhanced Raman scattering (SERS) is a technique for amplifying a Raman scattering signal, which is intrinsically weak and therefore hard to detect. The Raman enhancement factor can be as high as 10^2–10^6 and may even be as high as 10^{15}, which is sufficient to detect Raman scattering from single molecules. By combining this powerful SERS technique with deep-ultraviolet (DUV) resonance Raman spectroscopy, ultrasensitive detection and analysis of molecules by DUV resonance Raman spectroscopy become possible. In this chapter, recent progress in DUV-SERS is reviewed. Also, the available metals for selection as SERS substrates are discussed. As an application of DUV-SERS to molecular nanoimaging, the development of DUV tip-enhanced Raman scattering (TERS) is also described. Finally, some issues to be overcome and future perspectives are discussed.

Keywords Deep-UV • Surface-enhanced Raman scattering (SERS) • Resonance Raman scattering • Surface plasmon • Aluminum

8.1 Surface-Enhanced Raman Scattering

Raman spectroscopy is a powerful technique for optically analyzing molecules. Information about molecular species, chemical bonds, and crystalline structures can be obtained from the Raman scattering spectra of samples. However, the Raman scattering process is extremely weak: a typical Raman scattering cross section is on the order of $10^{-30}\,\mathrm{cm}^2/\mathrm{molecule}$ [1]. Because of the small cross section, typically at least $\sim 10^8$ molecules are required for detection of a Raman scattering signal [1]. Meanwhile, Raman analysis of trace amounts of molecules is becoming increasingly important, especially in the fields of nano- and microscale sciences, advanced materials, and life sciences.

A. Taguchi (✉)
Osaka University, Suita 565-0871, Osaka, Japan
e-mail: taguchi@ap.eng.osaka-u.ac.jp

Y. Ozaki, S. Kawata (eds.), *Far- and Deep-Ultraviolet Spectroscopy*,
DOI 10.1007/978-4-431-55549-0_8

In 1974, an unexpectedly strong Raman scattering was observed from pyridine molecules placed on a metallic electrode [2]. This phenomenon was named surface-enhanced Raman scattering (SERS). The observed Raman enhancement was shown to arise from the effect of surface plasmons on the metal [3–5]. A surface plasmon is a collective oscillation of free electrons in a metal and can be resonantly excited by an electromagnetic field [6]. The excitation of surface plasmons accompanies a strong electromagnetic field that is localized on the metal surface. Molecules placed on the metal surface are strongly excited by this plasmonically enhanced field. The Raman scattered light from the molecules couples again to the surface plasmons on the metal, strongly boosting the scattering efficiency. Through these enhancement processes, the detected signal intensity of Raman scattering is increased. In the initial SERS study, van Duyne reported the Raman enhancement factor of pyridine molecules on a rough silver electrode to be 10^5–10^6 [4]. Various metallic nanostructures, including roughened metal surfaces, metallic nanoparticles, and their aggregations and assemblies, have been investigated to achieve stronger SERS enhancement. Detection of Raman scattering from a single molecule has been reported using a technique in which resonance Raman scattering is utilized to achieve higher Raman scattering cross sections in combination with SERS enhancement [7, 8].

8.2 Metals for DUV Plasmon

Since the discovery of SERS, noble metals such as silver and gold have been the predominant choice of metals for obtaining SERS enhancement. This is because, among practically available metals, these metals support strong plasmon resonances in the visible and near-infrared spectral regions with minimal absorption loss. However, at deep-ultraviolet (DUV) wavelengths, silver and gold lose their metallic character and behave as dielectrics, which means that no plasmonic enhancement is obtained in the DUV region. Thus, SERS has been studied only in the visible region, and not much attention has been paid to the DUV spectral region.

The first demonstration of DUV-SERS was reported in 2007 [9]. Aluminum was used as the metal for SERS in place of gold or silver. The dielectric function of aluminum is shown in Fig. 8.1 [10]. It has been shown that localized surface plasmon resonance of metal nanoparticles occurs at the wavelength at which the real part of the dielectric function of the metal becomes less than −2 [12]. In aluminum, this region lies at wavelengths longer than 140 nm. At the same time, the strength of plasmon resonance is governed by the value of the imaginary part of the dielectric function describing absorption loss: a smaller value provides stronger electromagnetic field enhancement. The imaginary part of the dielectric function in aluminum becomes smaller at shorter wavelengths. Thus, it is anticipated that aluminum nanoparticles will provide strong plasmon resonance at wavelengths

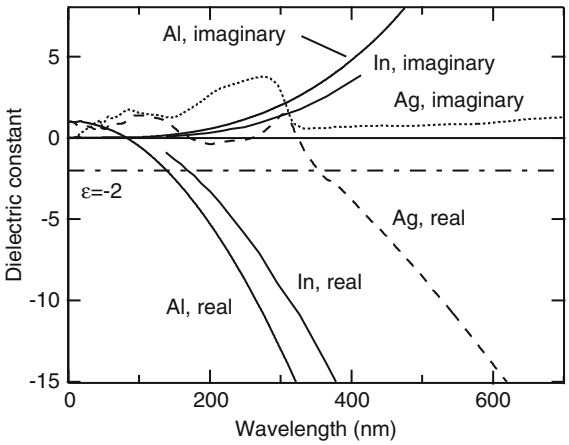

Fig. 8.1 Dielectric functions of aluminum [10], indium [11], and silver [10]. *Dashed-dotted line* represents $\epsilon = -2$

between 140 and 300 nm [13–16]. For reference, the dielectric function of silver is also shown in Fig. 8.1 [10]. Unlike aluminum, the plasmonics region of silver lies at wavelengths longer than 350 nm. In the DUV, silver does not meet the criteria (real part of dielectric function ≤ -2) to support localized surface plasmon resonance.

In addition to that of aluminum, the dielectric function of indium is also shown in Fig. 8.1 [10, 11]. Indium behaves as a plasmonic metal at wavelengths down to 170 nm. The imaginary part of the dielectric function is reasonably small, similar to that of aluminum. DUV-SERS using indium has been also demonstrated [17].

In order to examine surface plasmons in aluminum nanoparticles, near-field enhancement given by aluminum nanorods is calculated and shown in Fig. 8.2a. The lengths of the nanorods are 10, 20, and 30 nm, and the width is 10 nm. The nanorods are excited by a plane wave that is polarized parallel to the rod axis. The spectra are evaluated at the ends of the nanorods (indicated by the stars in the figure inset). For comparison, field enhancement obtained by silver nanorods having the same dimensions is also shown. The calculation results clearly demonstrate that nanorods made of aluminum have plasmon resonance in the DUV, whereas nanorods made of silver have plasmon resonance in the visible. The difference in resonance wavelength arises from the difference in dielectric functions between aluminum and silver, as shown in Fig. 8.1. It is also seen in the calculation results that the resonance wavelength shifts toward longer wavelength as the nanorod length increases. This means that the resonance wavelength of localized surface plasmons can be controlled by selecting the size of the aluminum nanoparticles. Figure 8.2b–d shows calculated field distributions near the nanoparticles at the peak wavelength of the plasmon resonance. Electromagnetic fields are localized at the ends of the nanorods. The calculations were performed using a finite-difference time-domain method [18], using the dielectric function shown in Fig. 8.1.

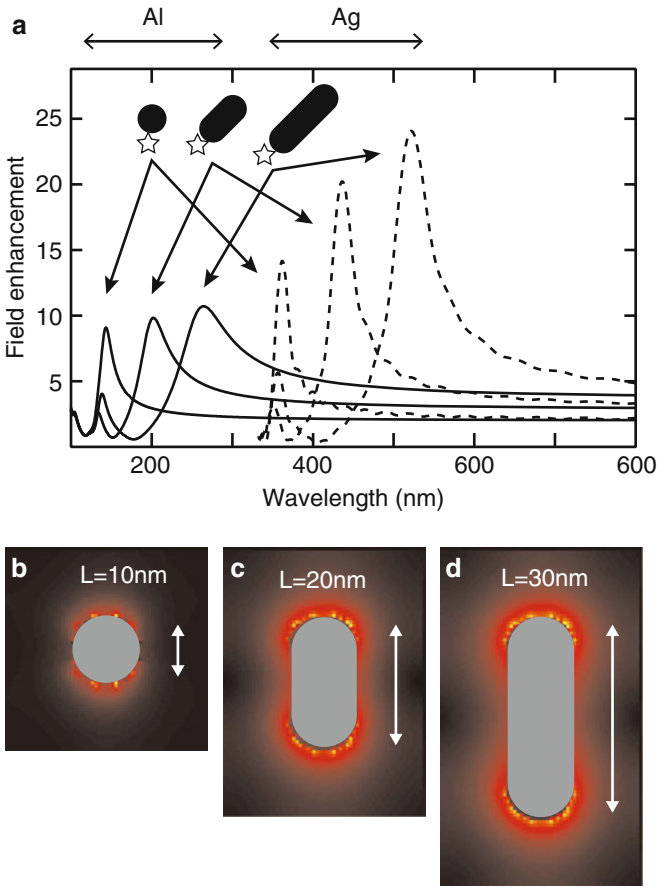

Fig. 8.2 (**a**) Calculated localized plasmon resonance at the ends (indicated by *stars*) of a nanosphere (10 nm diameter) and nanorods (20 and 30 nm long by 10 nm wide) made of aluminum and silver. The *solid* and *dashed lines* represent the spectra for aluminum and silver, respectively. (**b**)–(**d**) Calculated field distributions near the aluminum nanoparticles in the plasmon resonance of the 10-nm-diameter nanosphere, 20-nm-long nanorod, and the 30-nm-long nanorod, respectively

8.3 Progress in DUV-SERS and TERS

In the experimental demonstrations of single-molecule detection by SERS in the visible region, dye molecules having absorption in the visible were used as samples to take advantage of the resonance Raman effect [7, 8]. In the DUV spectral region, many molecules have intrinsic absorption; that is to say, molecules are naturally colored. For example, biologically important molecules such as proteins and deoxyribonucleic acids (DNAs) show characteristic absorption at DUV wavelengths from 220 to 280 nm. Excited by DUV light, such molecules exhibit the resonance Raman scattering effect, which can increase the Raman scattering cross section to

as high as $\sim 10^8$ [19]. Because the resonance Raman effect is rather ubiquitous in the DUV, ultrasensitive molecular detection is anticipated for a variety of molecules using DUV-SERS. The use of DUV excitation is also useful for selectively sensing a specific molecule of interest out of a mixture of heterogeneous substances, such as biological cells [20].

The following sections are devoted to reviewing recent progress in DUV-SERS and TERS. At present, the number of reports in the literature on DUV-SERS is not large. Most published papers have been dedicated to proof-of-principle experiments.

8.3.1 DUV-SERS

SERS in the DUV region was first reported by a group led by Popp [9]. Using a wavelength of 244 nm for Raman excitation, they measured the Raman scattering of a crystal violet aqueous solution placed on an aluminum thin film. They could detect two-orders-of-magnitude lower concentration of crystal violet solution on aluminum compared to one placed on a quartz substrate. Before this report, the shortest wavelength reported for SERS experiments was 325 nm [21, 22].

The crystal violet used as a sample has an absorption band around 250 nm, originating from benzene rings in the molecular structure. The wavelength of 244 nm used for Raman excitation nearly matches the DUV absorption of crystal violet, allowing the resonance Raman spectrum to be measured. They observed a change in the resonance Raman spectral shape when the molecules were placed on aluminum, which they attributed to a manifestation of the surface enhancement effect of aluminum.

Proteins and DNAs have characteristic absorption bands between 200 and 300 nm in the DUV, depending on the molecules. The use of DUV light as Raman excitation is useful for detecting these biologically important molecules, thanks to the resonance Raman effect. Detection of adenine molecules using DUV-SERS has been reported by Taguchi et al. using an aluminum thin film [16].

Aluminum nanoparticles also work as a substrate for DUV-SERS [23]. The resonance modes of plasmons in isolated nanoparticles are localized modes and can be excited by an electromagnetic field propagating in free space [6, 12]. The resonance mode is determined by the size and shape of the nanoparticles. Uniformly fabricated nanoparticles provide well-defined plasmon resonances. This is the main difference from the plasmons in continuous films used in the previous experiments: because the plasmons are excited through surface roughness or grains that are randomly distributed on the film, the resonance mode of the plasmon broadens through the inhomogeneous size distribution of the grains. A scanning-electron-microscopy (SEM) image of an aluminum nanoparticle array fabricated by Ekinci's group using extreme-UV interference lithography ($\lambda = 13.5$ nm) is shown in Fig. 8.3a [23, 24]. Such a short wavelength is required to achieve high spatial resolution in lithography to precisely control the diameter of nanoparticles. A convenient technique to control

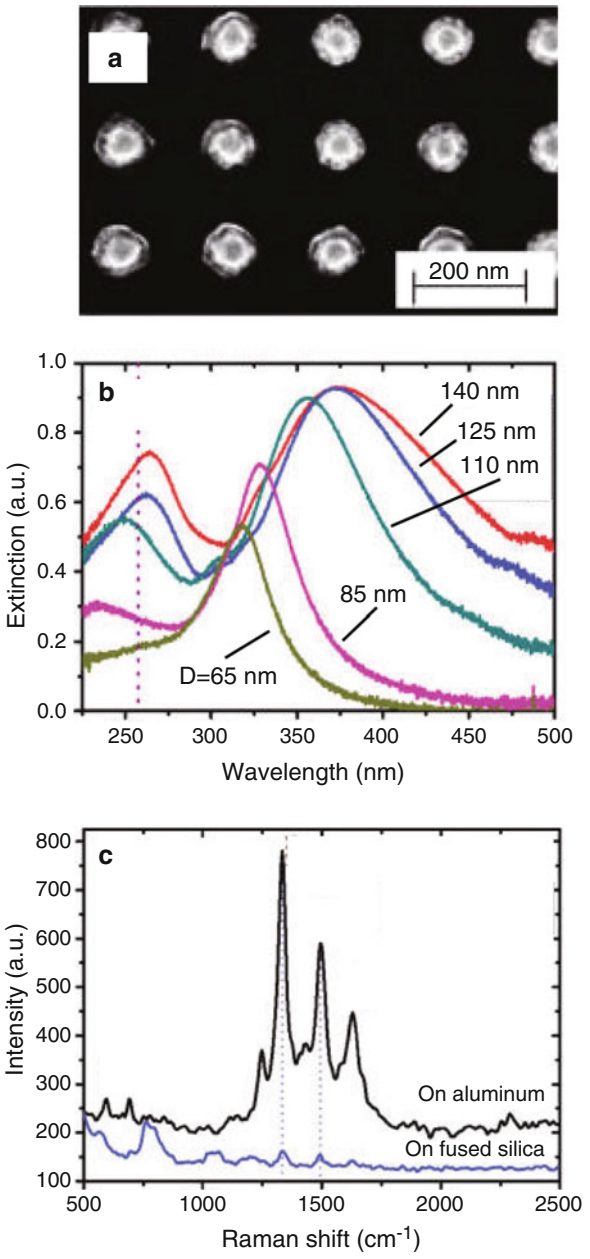

Fig. 8.3 (**a**) Scanning electron micrograph of aluminum nanoparticle array fabricated by extreme-UV interference lithography. (**b**) Optical extinction spectra of nanodisc arrays having a height of 70 nm, a periodicity of 200 nm, and various particle diameters. The *vertical dashed line* indicates the laser wavelength for Raman excitation (257.2 nm). (**c**) Raman spectra of a 1-nm-thick adenine film deposited on fused silica (FS) and on an Al nanoparticle array having a diameter of 140 nm (Adapted with permission from [23]. Copyright 2012 American Chemical Society)

the diameter of aluminum nanoparticles has been proposed for controlling localized plasmon resonance in the DUV [25].

Figure 8.3b shows extinction spectra of aluminum nanoparticles having different diameters. A nanoparticle having a diameter of 65 nm shows plasmon resonance at a

wavelength of 320 nm, which is assigned to the dipolar resonance mode. The peak of the resonance mode shifts to longer wavelengths as the diameter of the nanoparticle increases. A 110-nm-diameter particle has multiple peaks at 350 and 250 nm. The former is the dipole resonance, whereas the latter is assigned to the quadrupolar resonance mode. Strong quadrupolar resonance is observed in a 140-nm-diameter particle.

Figure 8.3c shows Raman spectra of a 1-nm-thick adenine film deposited on a 140-nm-wide aluminum nanoparticle array and on fused silica [23]. The Raman scattering intensity of adenine on aluminum nanoparticles was significantly increased compared with that on fused silica. The excitation laser wavelength was 257 nm, which matches the observed quadrupolar plasmon resonance in a 140-nm-diameter aluminum nanoparticle. The adenine sample has absorption at 270 nm (see also the inset in Fig. 8.6b). The excitation laser wavelength was in the absorption band of adenine.

As shown in Fig. 8.3b, resonance modes of metal nanoparticles are determined by the particle size. From the analogy of a microwave antenna, the term "optical antenna" has been used to describe the resonance properties of nanoparticles [26, 27]. The most fundamental antenna is a dipole antenna. In the microwave range, the length of a dipole antenna is half the working wavelength. In contrast, at optical wavelengths, the length of a dipole antenna is determined by the wavelength of the surface plasmon on metal. The plasmon wavelength on metal is always shorter than the wavelength of the light propagating in free space [28]. This is the primary reason why optical antennas have dimensions on the order of nanometers. A nano-sized particle can confine light in a nanoscale region. The nano-confinement of light enables the application of SERS to nano-resolution optical microscopy (Sect. 8.3.2).

A nanovoid—a complementary structure of nanoparticles—also works as an optical antenna. DUV-SERS using an aluminum nanovoid structure has been reported [29]. The resonance wavelength of a nanovoid is determined by the diameter of the rim of the nanovoid.

Each aluminum nanoparticle shown in Fig. 8.3a is isolated from neighboring particles. If the separation between particles is small, the localized plasmons in two adjacent particles hybridize through near-field coupling [30–32]. A nanoparticle dimer—a pair of nanoparticles that are nearly touching—is a prime example of such a system [33, 34]. A strong electromagnetic field is produced in the nanogap between the two particles. The highly enhanced electromagnetic field provided by such gap-mode plasmons has been applied to ultrasensitive detection of Raman scattering and fluorescence from molecules [35–40].

A bow-tie antenna is a pair of triangles whose tips are facing each other across a nanogap [36, 37, 41, 42]. Similar to the particle dimer, a strong field is localized in the gap between the two tips. DUV-SERS using an aluminum bow-tie antenna structure has been reported [43]. A Raman enhancement factor of $\sim 10^4$ has been reported. The field enhancement in a bow-tie antenna is strongly polarized parallel to the dimer axis. Thus, strong enhancement is observed only for the excitation polarized along the dimer axis.

As shown in Fig. 8.1, indium is another promising material for plasmonic enhancement in the DUV. Judging from the value of the dielectric function, indium has smaller absorption loss compared with aluminum between 200 and 300 nm. This makes indium an attractive metal for DUV-SERS. It has been also found that indium deposited on a fused silica substrate tends to form discrete nanoparticles separated by several nanometers [44]. The ease of fabricating discrete nanoparticles is another attraction of indium. In the case of vacuum-deposited aluminum, a continuous film is usually formed [9, 16]. To obtain discrete aluminum particles, lithography [13, 14, 23–25, 29, 43] and substrate surface modification either by chemical [45] or physical [46] treatment have been developed. An SEM image of indium deposited on fused silica is shown in Fig. 8.4a. Polycrystalline indium particles having an average size of 95 nm were attached with a separation of several nanometers. Strong field enhancement is anticipated in the nanogaps. The size of the indium can be changed by adjusting the deposition mass thickness, and the resonance peak wavelength can be controlled by the size of nanoparticles. The Raman scattering spectrum of adenine (thickness 1 nm) coated on indium nanoparticles excited by 266-nm wavelength laser light is shown in Fig. 8.4b. The Raman intensity of the adenine on the indium nanoparticles was strongly enhanced compared with that on the fused silica. The Raman enhancement factor was estimated to be ∼100.

8.3.2 DUV-TERS

As described so far, the origin of SERS enhancement is the localized surface plasmons generated on a metal surface. It is possible to obtain plasmon resonance at the tip of a sharpened metallic probe. SERS using a metallic nanotip is called tip-enhanced Raman scattering (TERS) [47–51]. Figure 8.5 shows the principle

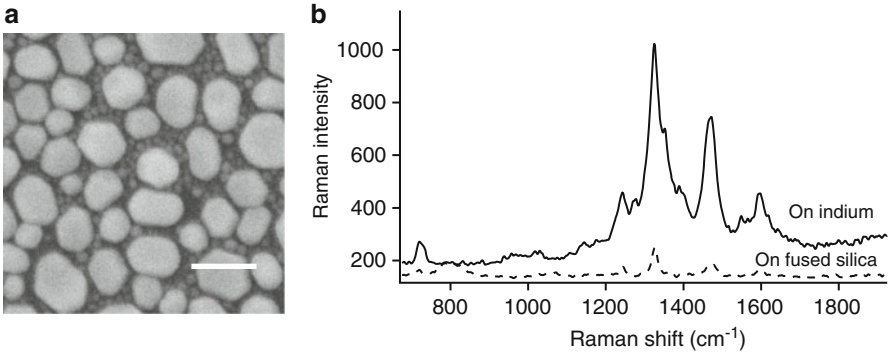

Fig. 8.4 (**a**) SEM image of indium-coated quartz substrate prepared by vacuum thermal vapor deposition with mass thickness of 25 nm. The scale bar is 200 nm. (**b**) Raman spectra of 1-nm-thick adenine films deposited on the indium-coated substrate and on a bare fused silica substrate

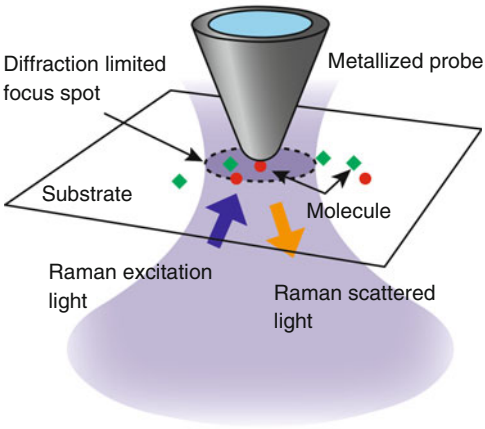

Fig. 8.5 The principle of tip-enhanced Raman scattering (TERS)

of TERS. Unlike SERS, in TERS only the Raman scattering from the molecules located under the metallic tip is sensed with plasmonic Raman enhancement. By scanning the probe on the sample surface, the molecular distribution in the sample can be visualized based on the Raman vibrational signature [52–54].

For optical microscopy, the most significant advantage of TERS is its high spatial resolution beyond the diffraction limit of light: An optical field is spatially confined into a region several tens of nanometers in size at the tip of the metallic probe [55, 56]. On the other hand, according to Abbe's theory, the minimum size Δ that can be resolved by a conventional optical microscope is given by [57]

$$\Delta = \frac{0.61\lambda}{n \times \sin\theta}, \tag{8.1}$$

where λ is the wavelength of light, n is the refractive index of the surrounding medium, and θ is the half-angle of the lens aperture. The spatial resolution of optical microscopy is in principle no better than half the wavelength of light. The use of a plasmonic nanotip provides a way to break through this spatial resolution limit in optical microscopy [58, 59]. Since the invention of TERS in 2000 [47–51], it has become an important analytical tool in the field of rapidly developing nanoscience and technology. The great potential of TERS has been demonstrated through the successful application of TERS to the analysis and imaging of organic dye molecules [54], carbon nanotubes [51–53, 60, 61], DNA bases [62, 63], single molecules [64–69], and advanced semiconductor materials, such as strained silicon [70, 71].

TERS in the DUV was first demonstrated by Taguchi et al. using an aluminum probe with an excitation wavelength of 266 nm [16]. The aluminum probe was prepared by thermally depositing aluminum onto a silicon cantilever under high-vacuum conditions. A SEM image of the prepared aluminum tip is shown in Fig. 8.6a.The size of the aluminum grains at the tip apex was around 10–20 nm.

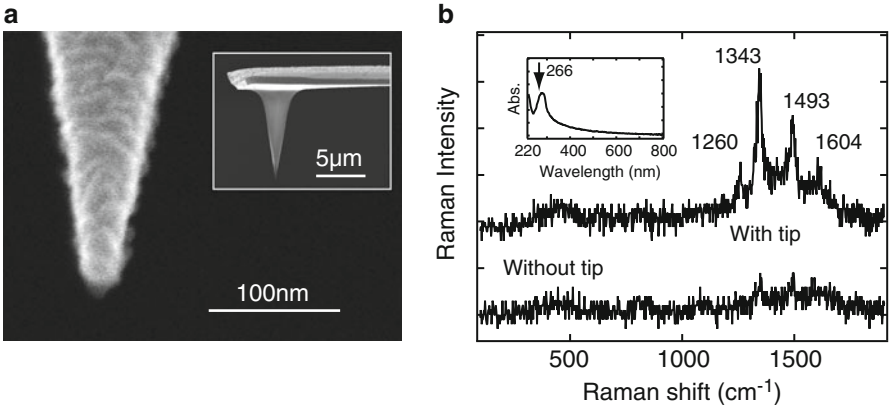

Fig. 8.6 (**a**) SEM image of aluminum-coated probe, showing a nanoparticle attached at the probe apex. The deposition thickness was 25 nm. The *inset* shows a low-magnification image. (**b**) DUV-TERS spectra of adenine nanocrystals excited with 266-nm laser wavelength measured with and without tip. The *inset* shows the absorption spectrum of adenine nanocrystals

DUV light was focused on the sample surface with an objective lens made of quartz. The Raman scattered light was collected with the same objective in a backscattering geometry and delivered to a spectrometer. The apex of the aluminum-coated tip was set in contact with the sample surface using an atomic force microscope apparatus.

The measured Raman spectra of adenine nanocrystals with and without the tip are shown in Fig. 8.6b. Strong enhancement of the Raman peaks was observed when the tip was in contact with the sample. The inset of Fig. 8.6b shows the absorption spectrum of the adenine nanocrystals. The Raman excitation wavelength (266 nm) used in the experiment was closely matched to the maximum absorption peak of adenine nanocrystals. The observed spectra of the adenine nanocrystals were consistent with the reported resonance Raman spectrum of the deoxyribonucleotides of adenine (dAMP) for 266-nm excitation [72–74]. This experiment is the first demonstration of plasmonically enhanced DUV resonance Raman scattering from biologically relevant molecules. The quartz peaks observed around 500 cm^{-1} remained unchanged with and without the tip, indicating the localized character of the tip-enhancement effect. The estimated enhancement factor was 1.3×10^3.

8.4 Summary and Future Perspectives

By using aluminum and indium, it has become possible to obtain SERS enhancement in the DUV spectral region. Several types of aluminum nanostructures have been used, including rough films, nanoparticles, and bow-tie antennas. At present, however, only a few different molecules—mostly adenine—have been tested as samples for DUV-SERS. To push the development of DUV-SERS to the next

stage, it is desired to perform DUV-SERS experiments using various samples, including organic materials and inorganic materials such as wide-gap materials. Photodegradation of the sample induced by DUV light is a major stumbling block in finding practical applications of DUV-SERS [75]. Achieving higher SERS enhancement will be beneficial for reducing DUV photodamage because this will make it possible to reduce the Raman excitation laser power required for detecting the Raman signal. Issues that remain to be addressed in order to achieve strong plasmon resonance in aluminum include the effect of the purity of the deposited aluminum [76], the effect of a native oxidation layer [13, 14], and the design of efficient nanostructures.

References

1. K. Kneipp, H. Kneipp, I. Itzkan, R.R. Dasari, M.S. Feld, Ultrasensitive chemical analysis by Raman spectroscopy. Chem. Rev. **99**, 2957–2975 (1999)
2. M. Fleischmann, P.J. Hendra, A.J. McQuillan, Raman spectra of pyridine adsorbed at a silver electrode. Chem. Phys. Lett. **26**, 163–166 (1973)
3. M.G. Albrecht, J.A. Creighton, Anomalously intense Raman-spectra of pyridine at a silver electrode. J. Am. Chem. Soc. **99**, 5215–5217 (1977)
4. D.L. Jeanmaire, R. Van Duyne, Surface Raman spectroelectrochemistry. Part 1. Heterocyclic, aromatic, and aliphatic-amines adsorbed on anodized silver electrode. Electroanal. Chem. **84**, 1–20 (1977)
5. M. Moskovits, Surface-enhanced spectroscopy. Rev. Mod. Phys. **57**, 783–826 (1985)
6. S. Kawata (ed.), *Near-Field Optics and Surface Plasmon Polaritons* (Springer, Berlin, 2001)
7. S. Nie, S. Emery, Probing single molecules and single nanoparticles by surface-enhanced Raman scattering. Science **275**, 1102–1106 (1997)
8. K. Kneipp, Y. Wang, H. Kneipp, L. Perelman, I. Itzkan, R. Dasari, M. Feld, Single molecule detection using surface-enhanced Raman scattering (SERS). Phys. Rev. Lett. **78**, 1667–1670 (1997)
9. T. Dörfer, M. Schmitt, J. Popp, Deep-UV surface-enhanced Raman scattering. J. Raman Spectrosc. **38**, 1379–1382 (2007)
10. E.D. Palik, *Handbook of Optical Constants of Solids* (Academic, Boston, 1991)
11. J.C. Lemonnier, G. Jezequel, J. Thomas, Optical properties in the far UV and electronic structure of indium films. J. Phys. C Solid State Phys. **8**, 2812–2818 (1975)
12. C.F. Bohren, D.R. Huffman, *Absorption and Scattering of Light by Small Particles* (Wiley, New York, 1983)
13. G.H. Chan, J. Zhao, G.C. Schatz, R. Van Duyne, Localized surface plasmon resonance spectroscopy of triangular aluminum nanoparticles. J. Phys. Chem. C **112**, 13958–13963 (2008)
14. C. Langhammer, M. Schwind, B. Kasemo, I. Zoric, Localized surface plasmon resonances in aluminum nanodisks. Nano Lett. **8**, 1461–1471 (2008)
15. A. Schilling, J. Schilling, C. Reinhardt, B. Chichkov, A superlens for the deep ultraviolet. Appl. Phys. Lett. **95**, 121909 (2009)
16. A. Taguchi, N. Hayazawa, K. Furusawa, H. Ishitobi, S. Kawata, Deep-UV tip-enhanced Raman scattering. J. Raman Spectrosc. **40**, 1324–1330 (2009)
17. Y. Kumamoto, A. Taguchi, M. Honda, K. Watanabe, Y. Saito, S. Kawata, Indium for deep-ultraviolet surface-enhanced resonance Raman scattering. ACS Photon. **1**, 598–603 (2014)
18. A. Taflove, *Computational Electrodynamics: The Finite Difference Time Domain Method* (Artech House, London, 1995)

19. S. Asher, in *Handbook of Vibrational Spectroscopy*, ed. by J.M. Chalmers, P.R. Griffiths (Wiley, Chichester, 2002)
20. Y. Kumamoto, A. Taguchi, N.I. Smith, S. Kawata, Deep ultraviolet resonant Raman imaging of a cell. J. Biomed. Opt. **17**, 076001 (2012)
21. B. Ren, X. Lin, Z. Yang, G. Liu, R. Aroca, B. Mao, Z. Tian, Surface-enhanced Raman scattering in the ultraviolet spectral region: UV-SERS on rhodium and ruthenium electrodes. J. Am. Chem. Soc. **125**, 9598–9599 (2003)
22. X.F. Lin, B. Ren, Z.L. Yang, G.K. Liu, Z.Q. Tian, Surface-enhanced Raman spectroscopy with ultraviolet excitation. J. Raman Spectrosc. **36**, 606–612 (2005)
23. S.K. Jha, Z. Ahmed, M. Agio, Y. Ekinci, J.F. Löffler, Deep-UV surface-enhanced resonance Raman scattering of adenine on aluminum nanoparticle arrays. J. Am. Chem. Soc. **134**, 1966–1969 (2012)
24. Y. Ekinci, H.H. Solak, J.F. Löffler, Plasmon resonances of aluminum nanoparticles and nanorods. J. Appl. Phys. **104**, 083107 (2008)
25. A. Taguchi, Y. Saito, K. Watanabe, S. Yijian, S. Kawata, Tailoring plasmon resonances in the deep-ultraviolet by size-tunable fabrication of aluminum nanostructures. Appl. Phys. Lett. **101**, 081110 (2012)
26. D.W. Pohl, Near-field optics: light for the world of nano-scale science. Thin Solid Films **264**, 250–254 (1995)
27. L. Novotny, N.F. van Hulst, Antennas for light. Nat. Photon. **5**, 83–90 (2011)
28. I.I. Smolyaninov, C.C. Davis, J. Elliott, A.V. Zayats, Resolution enhancement of a surface immersion microscope near the plasmon resonance. Opt. Lett. **30**, 382–384 (2005)
29. D.O. Sigle, E. Perkins, J.J. Baumberg, S. Mahajan, Reproducible deep-UV SERRS on aluminum nanovoids. J. Phys. Chem. Lett. **4**, 1449–1452 (2013)
30. K.H. Su, Q.H. Wei, X. Zhang, J.J. Mock, D.R. Smith, S. Schultz, Interparticle coupling effects on plasmon resonances of nanogold particles. Nano Lett. **3**, 1087–1090 (2003)
31. E. Prodan, C. Radloff, N.J. Halas, P. Nordlander, A hybridization model for the plasmon response of complex nanostructures. Science **302**, 419–422 (2003)
32. P. Nordlander, C. Oubre, E. Prodan, K. Li, Plasmon hybridization in nanoparticle dimers. Nano Lett. **4**, 899–903 (2004)
33. I. Romero, J. Aizpurua, G.W. Bryant, F.J. García de Abajo, Plasmons in nearly touching metallic nanoparticles: singular response in the limit of touching dimers. Opt. Exp. **14**, 9988–9999 (2006)
34. J. Aizpurua, G.W. Bryant, L.J. Richter, F.J. García de Abajo, Optical properties of coupled metallic nanorods for field-enhanced spectroscopy. Phys. Rev. B **71**, 235420 (2005)
35. C.E. Talley, J.B. Jackson, C. Oubre, N.K. Grady, C.W. Hollars, S.M. Lane, T.R. Huser, P. Nordlander, N.J. Halas, Surface-enhanced Raman scattering from individual au nanoparticles and nanoparticle dimer substrates. Nano Lett. **5**, 1569–1574 (2005)
36. P.J. Schuck, D.P. Fromm, A. Sundaramurthy, G.S. Kino, W.E.W. Moerner, Improving the mismatch between light and nanoscale objects with gold bowtie nanoantennas. Phys. Rev. Lett. **94** (2005)
37. F. Jäckel, A.A. Kinkhabwala, W.E.W. Moerner, Gold bowtie nanoantennas for surface-enhanced Raman scattering under controlled electrochemical potential. Chem. Phys. Lett. **446**, 339–343 (2007)
38. J.N. Farahani, H.J. Eisler, D.W. Pohl, M. Pavius, P. Flückiger, P. Gasser, B. Hecht, Bow-tie optical antenna probes for single-emitter scanning near-field optical microscopy. Nanotechnology **18**, 125506 (2007)
39. A. Kinkhabwala, Z. Yu, S. Fan, Y. Avlasevich, K. Muellen, W.E.W. Moerner, Large single-molecule fluorescence enhancements produced by a bowtie nanoantenna. Nat. Photon. **3**, 654–657 (2009)
40. M. Mivelle, T.S. van Zanten, L. Neumann, N.F. van Hulst, M.F. Garcia-Parajo, Ultrabright bowtie nanoaperture antenna probes studied by single molecule fluorescence. Nano Lett. **12**, 5972–5978 (2012)

41. R.D. Grober, R.J. Schoelkopf, D.E. Prober, Optical antenna: towards a unity efficiency near-field optical probe. Appl. Phys. Lett. **70**, 1354 (1997)
42. L. Zhou, Q. Gan, F.J. Bartoli, V. Dierolf, Direct near-field optical imaging of UV bowtie nanoantennas. Opt. Exp. **17**, 20301–20306 (2009)
43. L. Li, S. Fang Lim, A.A. Puretzky, R. Riehn, H.D. Hallen, Near-field enhanced ultraviolet resonance Raman spectroscopy using aluminum bow-tie nano-antenna. Appl. Phys. Lett. **101**, 113116 (2012)
44. A.I. Dragan, C.D. Geddes, Indium nanodeposits: a substrate for metal-enhanced fluorescence in the ultraviolet spectral region. J. Appl. Phys. **108**, 094701 (2010)
45. J. Martin, J. Proust, D. Gérard, J. Plain, Localized surface plasmon resonances in the ultraviolet from large scale nanostructured aluminum films. Opt. Mater. Exp. **3**, 954 (2013)
46. G. Maidecchi, G. Gonella, R. Proietti Zaccaria, R. Moroni, L. Anghinolfi, A. Giglia, S. Nannarone, L. Mattera, H.L. Dai, M. Canepa, F. Bisio, Deep ultraviolet plasmon resonance in aluminum nanoparticle arrays. ACS Nano **7**, 5834–5841 (2013)
47. N. Hayazawa, Y. Inouye, Z. Sekkat, S. Kawata, Metallized tip amplification of near-field Raman scattering. Opt. Commun. **183**, 333–336 (2000)
48. R.M. Stöckle, Y.D. Suh, V. Deckert, R. Zenobi, Nanoscale chemical analysis by tip-enhanced Raman spectroscopy. Chem. Phys. Lett. **318**, 131–136 (2000)
49. B. Pettinger, G. Picardi, R. Schuster, G. Ertl, Surface enhanced Raman spectroscopy: towards single molecular spectroscopy. Electrochemistry **68**, 942–949 (2000)
50. B. Pettinger, G. Picardi, R. Schuster, G. Ertl, Surface-enhanced and STM-tip-enhanced Raman spectroscopy at metal surfaces. Single Mol. **5**, 285–294 (2002)
51. N. Hayazawa, T. Yano, H. Watanabe, Y. Inouye, S. Kawata, Detection of an individual single-wall carbon nanotube by tip-enhanced near-field Raman spectroscopy. Chem. Phys. Lett. **376**, 174–180 (2003)
52. T. Yano, P. Verma, S. Kawata, Y. Inouye, Diameter-selective near-field Raman analysis and imaging of isolated carbon nanotube bundles. Appl. Phys. Lett. **88**, 093125 (2006)
53. A. Hartschuh, E.J. Sánchez, X.S. Xie, L. Novotny, High-resolution near-field Raman microscopy of single-walled carbon nanotubes. Phys. Rev. Lett. **90**, 095503 (2003)
54. N. Hayazawa, Y. Inouye, Z. Sekkat, S. Kawata, Near-field Raman imaging of organic molecules by an apertureless metallic probe scanning optical microscope. J. Chem. Phys. **117**, 1296–1301 (2002)
55. H. Furukawa, S. Kawata, Local field enhancement with an apertureless near-field-microscope probe. Opt. Commun. **148**, 221–224 (1998)
56. E.J. Sánchez, L. Novotny, X.S. Xie, Near-field fluorescence microscopy based on two-photon excitation with metal tips. Phys. Rev. Lett. **82**, 4014–4017 (1999)
57. M. Born, E. Wolf, *Principles of Optics* (Pergamon, London, 1959)
58. Y. Inouye, S. Kawata, Near-field scanning optical microscope with a metallic probe tip. Opt. Lett. **19**, 159 (1994)
59. S. Kawata, Y. Inouye, P. Verma, Plasmonics for near-field nano-imaging and superlensing. Nat. Photon. **3**, 388–394 (2009)
60. N. Anderson, A. Hartschuh, S. Cronin, L. Novotny, Nanoscale vibrational analysis of single-walled carbon nanotubes. J. Am. Chem. Soc. **127**, 2533–2537 (2005)
61. T. Yano, T. Ichimura, S. Kuwahara, F. H'Dhili, K. Uetsuki, Y. Okuno, P. Verma, S. Kawata, Tip-enhanced nano-Raman analytical imaging of locally induced strain distribution in carbon nanotubes. Nat. Commun. **4**, 2592 (2013)
62. T. Ichimura, N. Hayazawa, M. Hashimoto, Y. Inouye, S. Kawata, Tip-enhanced coherent anti-Stokes Raman scattering for vibrational nanoimaging. Phys. Rev. Lett. **92**, 220801 (2004)
63. A. Rasmussen, V. Deckert, Surface- and tip-enhanced Raman scattering of DNA components. J. Raman Spectrosc. **37**, 311–317 (2006)
64. C.C. Neacsu, J. Dreyer, N. Behr, M.B. Raschke, Scanning-probe Raman spectroscopy with single-molecule sensitivity. Phys. Rev. B **73**, 193406 (2006)
65. K.F. Domke, D. Zhang, B. Pettinger, Toward Raman fingerprints of single dye molecules at atomically smooth Au(111). J. Am. Chem. Soc. **128**, 14721–14727 (2006)

66. N. Hayazawa, H. Watanabe, Y. Saito, S. Kawata, Towards atomic site-selective sensitivity in tip-enhanced Raman spectroscopy. J. Chem. Phys. **125**, 244706–244706 (2006)
67. W. Zhang, B.S. Yeo, T. Schmid, R. Zenobi, Single molecule tip-enhanced Raman spectroscopy with silver tips. J. Phys. Chem. C **111**, 1733–1738 (2007)
68. T. Ichimura, H. Watanabe, Y. Morita, P. Verma, S. Kawata, Y. Inouye, Temporal fluctuation of tip-enhanced Raman spectra of adenine molecules. J. Phys. Chem. C **111**, 9460–9464 (2007)
69. J. Steidtner, B. Pettinger, Tip-enhanced Raman spectroscopy and microscopy on single dye molecules with 15 nm resolution. Phys. Rev. Lett. **100**, 236101 (2008)
70. D. Mehtani, N. Lee, R.D. Hartschuh, A. Kisliuk, M.D. Foster, A.P. Sokolov, J.F. Maguire, Nano-Raman spectroscopy with side-illumination optics. J. Raman Spectrosc. **36**, 1068–1075 (2005)
71. N. Hayazawa, M. Motohashi, Y. Saito, H. Ishitobi, A. Ono, T. Ichimura, P. Verma, S. Kawata, Visualization of localized strain of a crystalline thin layer at the nanoscale by tip-enhanced Raman spectroscopy and microscopy. J. Raman Spectrosc. **38**, 684–696 (2007)
72. S. Fodor, R.P. Rava, T.R. Hays, T.G. Spiro, Ultraviolet resonance Raman-spectroscopy of the nucleotides with 266-, 240-, 218-, and 200-nm pulsed laser excitation. J. Am. Chem. Soc. **107**, 1520–1529 (1985)
73. D.C. Blazej, W.L. Peticolas, Ultraviolet resonant Raman spectroscopy of nucleic acid components. Proc. Natl. Acad. Sci. U.S.A. **74**, 2639–2643 (1977)
74. L.D. Ziegler, B. Hudson, D.P. Strommen, W.L. Peticolas, Resonance Raman spectra of mononucleotides obtained with 266 and 213 nm ultraviolet radiation. Biopolymers **23**, 2067–2081 (1984)
75. Y. Kumamoto, A. Taguchi, N.I. Smith, S. Kawata, Deep UV resonant Raman spectroscopy for photodamage characterization in cells. Biomed Opt. Exp. **2**, 927–936 (2011)
76. M.W. Knight, N.S. King, L. Liu, H.O. Everitt, P. Nordlander, N.J. Halas, Aluminum for plasmonics. ACS Nano **8**, 834–840 (2014)

Chapter 9
Coupling of Deep-Ultraviolet Photons and Electrons

Yuika Saito

Abstract Recent advances in deep-ultraviolet (DUV) spectroscopy and related technologies have targeted the observation of photon–electron coupling in wide-bandgap materials. The energy of a single photon of DUV light is high enough to excite an electron to the first or higher electronic levels of a material. This is the main drawback of DUV spectroscopy for soft materials since higher-order excitations are often followed by photodamage. At the same time, high photon energy can be an advantage from the viewpoint of energy conversion between photons and electrons in a wide-bandgap material. DUV spans a marginal range of wavelengths that can occur under atmospheric pressure in sunlight on Earth. Its high photon energy and availability are expected to lead to great applications in DUV photonics. As mentioned in the previous chapter, photons couple with free electrons in metals at the nanometer scale, exhibiting a localization and enhancement effect known as localized surface plasmon resonance (LSPR). LSPR has been exploited in many scientific and industrial fields, such as sensors, optical waveguides, high-sensitivity optical detection, and high-resolution microscopy (Willets and Van Duyne, Rev Phys Chem 58:267–97, 2007). In this chapter, I review some important aspects of DUV photons, mainly focusing on DUV-LSPR applications in, for example, photocatalysis, photovoltaic devices, and light-emitting diodes (LEDs), including enhancement mechanisms such as carrier generation, photoexcited lifetime modifications, emission pattern controls, and coulombic forces.

Keywords Localized surface plasmon resonance • Plasmonic nanostructure • Photocatalysis • DUV-LED

9.1 DUV Plasmonic Nanostructures

For efficient coupling between a photon wave vector and free electrons in a material, the specific shape and size of nanostructures, the so-called plasmonic nanostructures, should be prepared to host LSPR. In order to achieve LSPR in

Y. Saito (✉)
Department of Applied Physics, Osaka University, Suita, Japan
e-mail: yuika@ap.eng.osaka-u.ac.jp

Y. Ozaki, S. Kawata (eds.), *Far- and Deep-Ultraviolet Spectroscopy*,
DOI 10.1007/978-4-431-55549-0_9

the DUV range, we need a metal that has a negative dielectric constant at UV wavelengths with minimal absorption loss. Poor metals such as aluminum, gallium, indium, tin, thallium, lead, and bismuth have been found to exhibit plasmonic properties in the UV range [2, 3]. Among these candidates, aluminum (Al) is the most frequently used, since it exhibits metallic properties in the full UV range and is stable, nontoxic, and readily available [4, 5]. Second to Al, indium and gallium are also used in DUV plasmonics [6–8]. The use of these metals in fabricating plasmonic nanostructures requires a specific method since the uniformity of the size and shape of the nanoparticles and having a good isolation between particles are important for better coupling of electrons with DUV photons [9]. Moreover, achieving DUV-LSPR requires a particle size as small as a few nanometers [10]. There are only a handful of methods that can be employed to fabricate UV-sensitive metal nanoparticles capable of meeting these criteria. The best method might be lithography [11–17]. Ekinci et al. reported the first clear LSPR at DUV wavelengths, with a peak at 270 nm, from 40-nm-wide Al nanodiscs fabricated by extreme-ultraviolet (EUV) interference lithography using a wavelength of 13.4 nm from a synchrotron radiation source [11]. Small particles close to this record have been achieved by nanosphere lithography (NSL), which is low cost and readily available [12]. In NSL, colloidal spherical particles of polystyrene (PS) beads were self-assembled to form a hexagonal close-packed (hcp) monolayer on a quartz substrate, which was then used as a mask for metal deposition onto the substrate to produce triangular Al nanostructured arrays. Mask heating was used to modify the nanosphere morphology, whereby ultrasmall nanostructures (down to 50 nm) with good size tunability were obtained [15]. Before metal deposition, the aligned nanoparticles were thermally expanded in a microwave while maintaining their alignment in the hcp monolayer. By adjusting the heating duration, the size of the aperture was continuously reduced until it became infinitesimally small, which enabled seamless size reduction of the fabricated Al nanostructure. An example of template-tunable NSL for DUV plasmonics was demonstrated by Taguchi et al. [16]. The size-controlled PS templates are shown in Fig. 9.1 for heating times of 0, 90, 100, and 110 s. Clearly, the size of the gaps between PS beads decreased with increasing microwave heating time. Control of Al nanoparticle size was achieved through Al deposition followed by removal of the PS templates as indicated in Fig. 9.2a–d. Al nanoparticles made from PS beads heated for longer times clearly produced structures with smaller lateral sizes. These results demonstrated that metal nanostructures as small as several tens of nanometers can easily be fabricated by a combination of NSL and the mask heating technique. Figure 9.3 shows the extinction spectra of the nanostructures fabricated, as measured by a UV–visible spectrophotometer. The results clearly reveal LSPR peaks for all of the fabricated samples. The extinction spectra showed LSPR peaks at 342, 314, 295, and 270 nm for Al structures obtained with masks heated for different durations, indicative of resonant coupling between the DUV photons and electron oscillations. The shortest wavelength obtained was 270 nm. A further reduction in the LSPR wavelength to 240 nm was achieved through optimization of the aspect ratio by changing the Al deposition thickness [17].

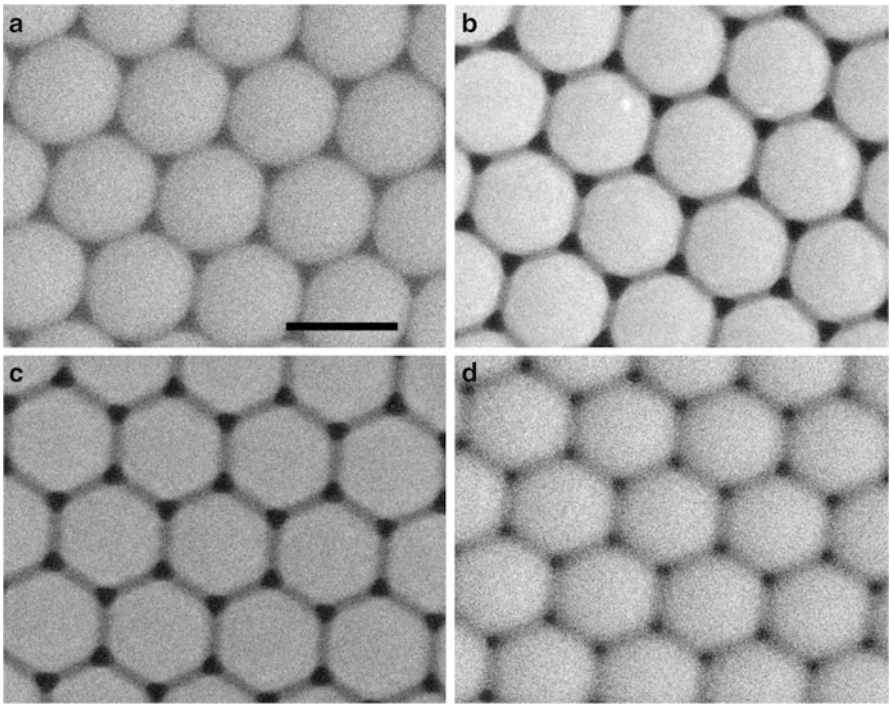

Fig. 9.1 Self-assembled pattern for NSL. SEM images, demonstrating the shrinkage of the gaps between aligned PS beads upon microwave heating [16]. The size control of nanostructures was thus obtained. The heating durations were (**a**) 0, (**b**) 90, (**c**) 100, and (**d**) 110 s. The scale bar is 300 nm (From Ref. [16])

Void nanostructure arrays, e.g., nanoholes and nanocups, are among other types of system, suitable for LSPR. Extraordinarily optical transmissions have been reported using Al [18, 19] in the earliest study of DUV plasmonics. In this effect nanohole array fabricated on a film hosts LSPR to enhance the photons passing through. Nanoholes or hemispherical nanovoids are able to support surface plasmons with well-defined cavities [20]. Sigel et al. fabricated aluminum nanovoids using a modified template stripping technique with a soluble backing layer to fabricate Al nanovoids [21]. They studied surface-enhanced resonance Raman spectroscopy (SERRS) on nanovoids and achieved a high enhancement of adenine molecules an order of $\sim 10^6$.

The advantages of lithographic methods are good size controllability and structural uniformity. However, since these methods rely on 2D self-assembling array structures, the enhancements are limited only on surfaces. It is therefore impossible to observe a sample in a bulk matrix or in a solution. Though the number of studies remains limited, wet chemical synthesis of Al and indium nanocrystals has been reported [22–26]. Al nanocrystals 50–100 nm in size have been successfully fabricated using alane derivatives as precursors and molecules with one or a pair of

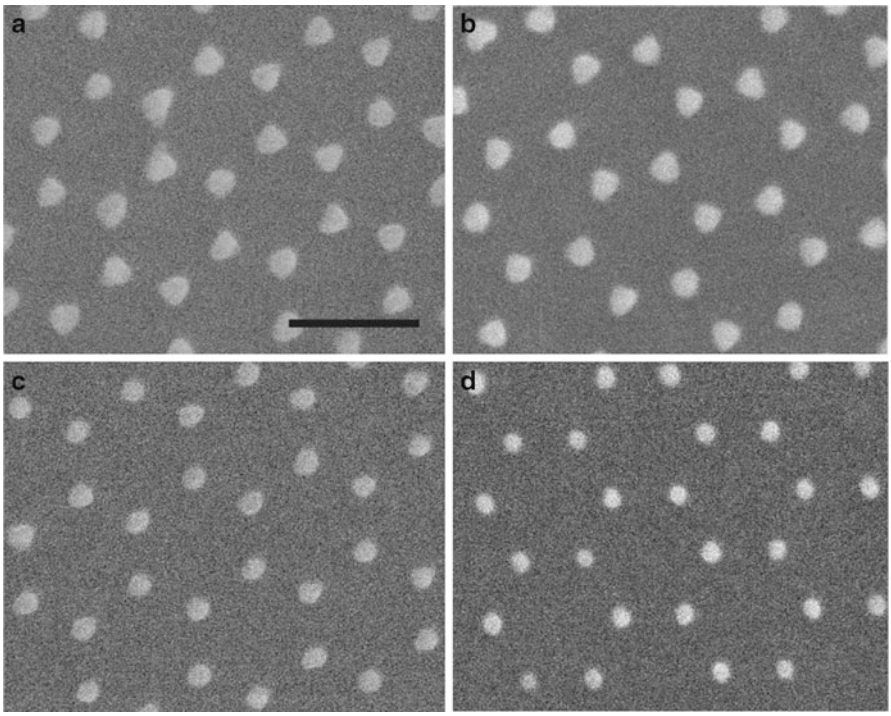

Fig. 9.2 SEM images of Al nanostructures fabricated using the nanosphere masks shown in Fig. 9.1 [16]. Heating durations: (**a**) 0, (**b**) 90, (**c**) 100, and (**d**) 110 s. The deposited metal layer thickness was 30 nm. The average lateral sizes of the nanostructures were (**a**) 80, (**b**) 71, (**c**) 59, and (**d**) 50 nm. The scale bar is 300 nm

carboxylic acid groups as surface passivation agents [25]. Size-controlled indium nanocrystals, i.e., nanowires, octahedra, and truncated octahedra, have also been synthesized by borohydride reduction of In^{3+} [26].

The simplest way to prepare a plasmonic nanostructure is thermal and electron beam deposition in vacuum on a flat substrate that is either hydrophilic or hydrophobic. Even though the roughness of the structure depends on the contact angle between the metal and substrate, which is less controllable, the method can be well applied to some metals. DUV plasmonic nanostructures were readily formed by thermal deposition of indium onto a glass substrate. The size of indium nanostructures can be controlled from 15 to 50 nm by the evaporation speed, pressure, and the deposited thickness. The resulting extinction peaks due to the dipole resonance were tuned to between 260 and 600 nm, which were used for surface enhancement of Raman spectroscopy by DUV excitation [7]. Self-assembled arrays of hemispherical gallium nanoparticles were deposited by molecular beam epitaxy on a sapphire support as a substrate for UV plasmonics. The mean NanoParticle radii of 23, 26, and 70 nm were fabricated at LSPR frequencies

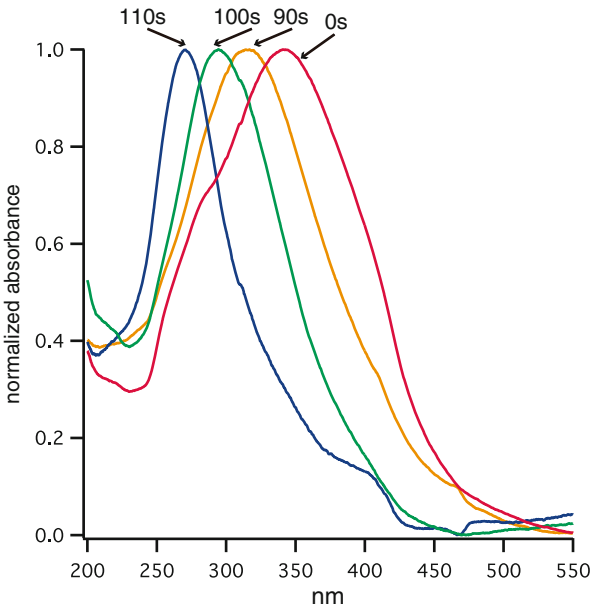

Fig. 9.3 Extinction spectra of Al nanostructures fabricated through PS masks using different heating durations [16]. The intensities of the spectra are normalized. The spectra show peaks at 342, 314, 295, and 270 nm for Al structures obtained with masks heated for different durations, exhibiting resonant coupling between DUV photon and electron oscillations

of 4.5, 3.81, and 1.95 eV, respectively. A measured local Raman enhancement factor of 10^7 was achieved under excitation at 325 nm [8]. Oblique-angled deposition (OAD) also extends the capability of vacuum deposition and is used in cases where parallel deposition does not work owing to the affinity between the substrate and the deposited materials [27]. Besides the abovementioned approaches, Al nanoparticles have also been prepared by laser ablation [28, 29] and in gas or plasma phases [30, 31].

9.2 Photon-to-Electron Conversion

9.2.1 DUV Plasmon-Enhanced Photocatalysis

Under the condition of LSPR, where the incident light field is intensified, a numerous number of applications exist including surface-enhanced spectroscopy, which we have mentioned in the previous chapter. One of the most promising applications of DUV plasmonics in the viewpoint of a conversion from photon to electron without an optical emission is in the field of photocatalysis [32–35]. A photocatalyst traps photons to generate electron–hole (e–h) pairs and thus induces redox reactions [35]. Plasmonics is particularly applicable to photocatalytic systems since the metal nanostructure serves to accumulate photons at the interface between the metal and catalyst where the reactions occur. A common photocatalyst that has been receiving considerable attention is titanium dioxide (TiO_2) because of its

strong redox power as well as its physical and chemical stability [36, 37]. TiO_2 has been used in a variety of environmental or green applications such as self-cleaning surfaces, water splitting, disinfection, and air purification [38–42]. Despite these applications, the photocatalytic activity of TiO_2 needs to be improved in order to make it a practical, green solution for many energy-related problems. The possible reaction that can occur on a photocatalyst is determined by its bandgap. Since the bandgap of TiO_2 is in the UV range (3.2 eV) [36], it is expected that the photocatalytic performance of TiO_2 would be further enhanced if the plasmonic metal used has a resonance wavelength in the UV range as well.

Honda et al. reported an increase in the photocatalytic activity of TiO_2 through DUV plasmonics employing Al nanoparticles [43]. Figure 9.4 illustrates the concept of plasmon-enhanced photocatalysis. A TiO_2 thin film was deposited on a quartz substrate. Hexagonal patterns of Al nanoparticles were then formed on the surface of the TiO_2 film using NSL. The Al nanoparticle diameter can be tuned within the range that can be used for LSPR in the DUV region. To determine the photocatalytic activity, a test sample of methylene blue dye was applied to the substrate. By irradiating the substrate with UV light from above, an enhanced field is generated in the vicinity of the Al nanoparticles, exciting the *e–h* pair in TiO_2 with an accelerated reaction rate. Figure 9.5 shows the observed photocatalytic reaction on TiO_2 with and without Al nanoparticles under UV irradiation in the range of 260–340 nm. The decay curves plot the residual methylene blue as a function of integrated irradiation time. The black line represents the results without Al nanoparticles, while the colored lines represent the results with Al nanoparticles. The red, blue, and green curves correspond to the rates obtained with Al nanoparticles having lateral sizes of 28, 34, and 80 nm, respectively. The height of the structure was fixed at 30 nm. A comparison between the decay curves of samples with and without Al nanoparticles reveals that the photocatalytic reaction rates of TiO_2 with Al nanoparticles were remarkably enhanced. To quantify the enhancement, curve fitting was performed using exponential functions. The enhancements of the photocatalytic reaction rate of Al nanoparticles were 9.8, 14.3, and 12.9 times for 28, 34, and 80 nm nanoparticles, respectively. The results show the dependence of the photocatalytic enhancement on nanoparticle size. The enhancement of the photocatalytic reaction rate was also found to depend on the plasmon resonance in the UV region, as supported by discrete dipole approximation simulation results. These results demonstrate that the plasmonic enhancement of photocatalysis on TiO_2 arises from the Al nanoparticles. We note that in the case of photocatalysts other than TiO_2, the size of the plasmonic structure needs to be retuned.

The performance of photovoltaic devices was also improved with the aid of plasmonics such as solar cells or photodetectors [44–48]. Xu et al. used Al nanoparticles to enhance the optical absorption of dye-sensitized solar cells [44]. They succeeded in incorporating a high concentration of Al nanoparticles into the TiO_2 anodes, thus improving the power conversion efficiency of the solar cell by nearly 13 %. In their system, the Al nanoparticles not only enhance the light in solar cells with the LSPR effect but also suppress the quenching process and reduce the loss of carriers. Butun et al. examined the effects of plasmonic scattering

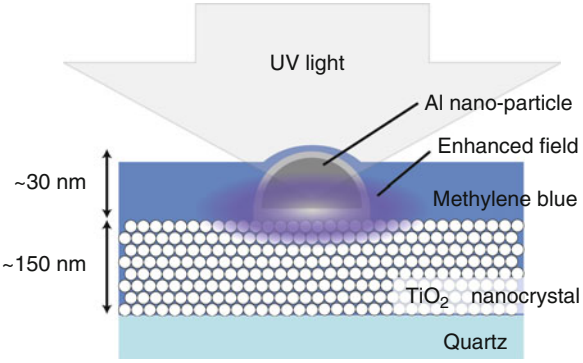

Fig. 9.4 Schematic of a plasmon-enhanced photocatalyst. Al nanoparticles are placed on a TiO_2 film consisting of 6 nm nanocrystals. Methylene blue was applied to monitor the photocatalytic performance [43]. A UV lamp illuminates the sample from the *top* of a methylene blue layer. An enhanced field is generated in the vicinity of the Al nanoparticles, causing the methylene blue layer to decompose at an accelerated reaction rate

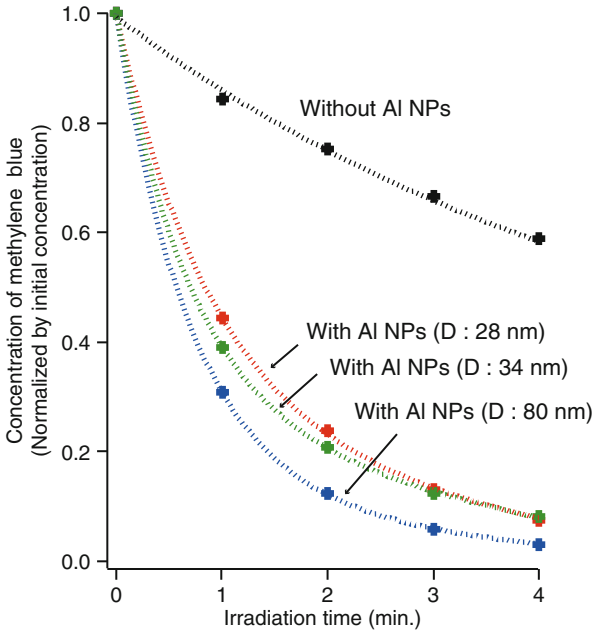

Fig. 9.5 Photocatalytic reaction with and without Al nanoparticles under irradiation of UV light in the wavelength range of 260–340 nm [43]. The results obtained with Al nanoparticles having lateral sizes, *D*, of 28, 34, and 80 nm, respectively. The photocatalytic reaction rate was enhanced by a factor of 9.8, 14.3, and 12.9, respectively

on absorption and photocurrent collection in a GaN photodetector with size-optimized Al nanoparticles. At wavelengths of LSPR, incident light scattered by the nanoparticles enhances absorption in the active layer of the photodetector [48].

In a metal–semiconductor system, when the metal and semiconductor come into contact, a Schottky junction forms. This band deformation enhances the separation

of *e–h* pairs, reduces the chance of recombination, and significantly increases the lifetime of the photoexcited charge carriers [35]. This effect is not necessarily classified under plasmonics, but is considered as an important contributor to enhanced photocatalytic efficiency. Prolonged carrier lifetimes result in an enhanced photoconductive gain. Thus, in most plasmon-assisted photovoltaic devices, this effect should be taken into account.

9.2.2 Enhancement of Charge Carrier Generation

The LSPR energy contributes to the catalytic cycle not only by the intensified local field through the coupling of collective free electron oscillations but also by the excitation of few high-energy electrons. It has been reported that "hot electrons" (so called because they are not in thermal equilibrium) generated by plasmonic nanostructures help to mediate DUV photocatalysis and photovoltaic devices [49–54]. In the case of metal–semiconductor systems, when a metal is illuminated with highly energetic photons, electrons from occupied energy levels are excited above the Fermi energy. Hot electrons with energies high enough to overcome the Schottky barrier are injected into the conduction band of the neighboring semiconductor [51]. Plasmon effects on hot electrons generating nonradiative relaxation in electronically quantized systems have started to attract attention since the work done by Neretina et al. [49]. They report the enhancement of nonradiative electronic relaxation rates in CdTe nanowires upon the addition of a thin gold nanoshell, especially at excitation energies overlapping with those of surface plasmon oscillations. They suggested that localized surface plasmon fields can possibly enhance nonradiative relaxation processes of electronic excitations.

Transient hot electrons on metal surfaces are usually formed by direct excitation using short pulse laser illumination. But the excitation in such cases is usually an inefficient process requiring high incident light intensities to produce any detectable effect. In contrast, hot electron production through plasmon decay in nanoparticles is much more efficient. The following work experimentally verified the effects of hot electrons and the relationship between the product made by photochemical reaction and the plasmonic effect. Halas and her group reported that surface plasmons excited in Au nanoparticles decay into hot electrons with energies between the vacuum level and the work function of the metal [52]. They examined this process by detecting the formation of HD molecules through the dissociation of H_2 and D_2 and investigated the effects of Au nanoparticle size and wavelength of incident light on the rate of HD formation. In the transient state, hot electrons can transfer into a Feshbach resonance of an H_2 molecule adsorbed on the Au nanoparticle surface, triggering its dissociation [52]. The more interesting feature of hot electrons is that even though plasmonic nanostructures are designed for visible or longer wavelengths, they can be utilized for a reaction involving a wider potential gap. Mubeen et al. reported significant photosensitization of TiO_2 due to direct injection by quantum tunneling of hot electrons produced during the decay of localized surface plasmon

polaritons excited in Au nanoparticles embedded in TiO_2. This decay of surface plasmon produces *e–h* pairs in gold. They proposed that a large fraction of these electrons tunnel into the semiconductor's conduction band, resulting in an increased electron current in TiO_2, even when the device is illuminated with light having photon energies well below the semiconductor's bandgap [55].

9.3 Electron-to-Photon Conversion

9.3.1 DUV-LEDs

The direct electron-to-photon conversion in DUV wavelength should be discussed based on the possibility of realizing semiconductor light-emitting diodes (LEDs). Semiconductor DUV-LEDs have been investigated extensively as substitutes for conventional vapor lamps because of their reduced energy consumption, nontoxicity, convenient mass production, and ease of assemblage in other devices [56, 57]. Recently, DUV-LEDs emitting at 261 nm exhibited an output power of 10.8 mW at 150 mA, and a lifetime of over 10,000 h was achieved [58]. Although UV-LEDs are about to go on the market, wavelengths shorter than 250 nm are still suffering from low efficiency.

With the aid of photon localization and enhancement by DUV-LSPR [59–61] LSPR, the output power of LEDs is expected to improve [62–65]. Huang et al. demonstrated for the first time that the enhanced emission of DUV-LEDs coupled to LSPRs generated by Al nanoparticles prepared on quantum wells (QWs) [66, 67]. Size- and density-controlled Al nanoparticles were fabricated by OAD (see Sect. 9.1) on the surface of $Al_xGa_{1-x}N$ ($x = 0.25$), used as an active layer (see Fig. 9.6). Figure 9.7 shows the emitted electroluminescence (EL) spectra of samples with and without Al nanoparticles and the enhancement ratio that represents their relative intensities under a 15-mA injection current. Figure 9.7a, b shows the top emission (epitaxial layer side) and bottom emission(sapphire substrate side), respectively. A maximum tenfold top-emission enhancement and a maximum 2.8-fold bottom-emission enhancement were

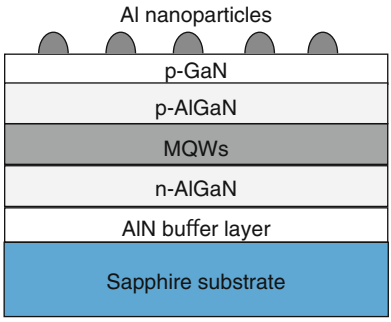

Fig. 9.6 Schematic of a plasmon-enhanced DUV-LED. The active layer is $Al_xGa_{1-x}N$ ($x = 0.25$), and Al nanoparticles are fabricated on the top surface by OAD (Referred from [66])

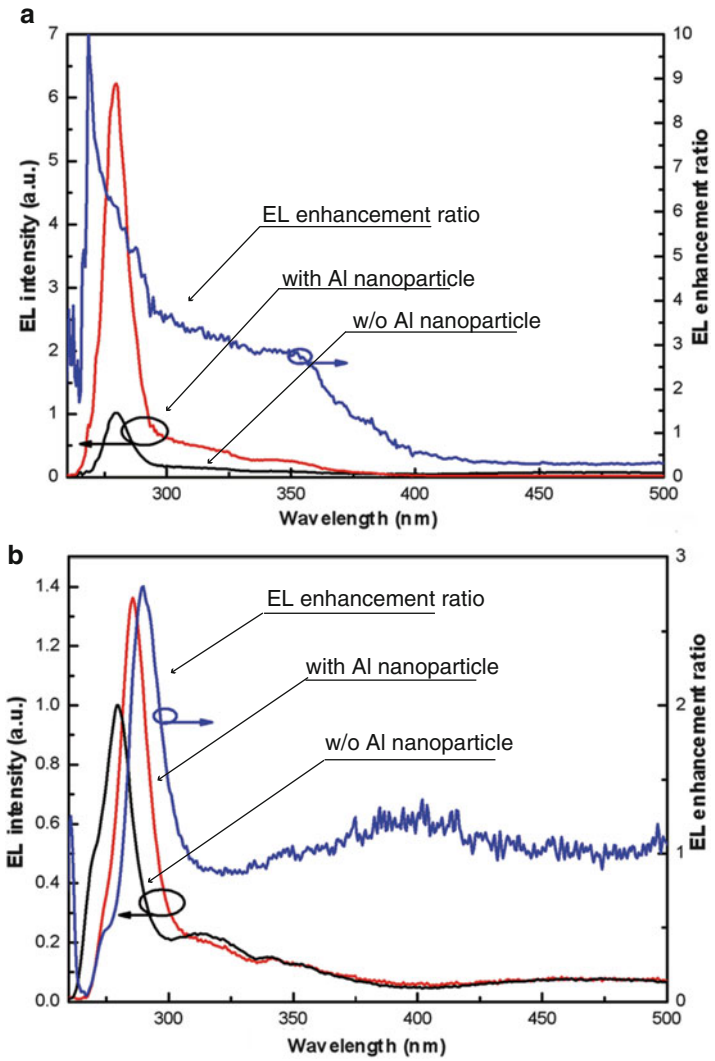

Fig. 9.7 Electroluminescence measurements on a plasmon-enhanced DUV-LED. (**a**) Top-emission EL spectra from the LED sample without Al nanoparticles and with Al nanoparticles deposited on the top surface, as well as the enhancement ratio between them. (**b**) Bottom-emission EL spectra of the LED samples without Al nanoparticles and with Al nanoparticles deposited on the top surface, as well as the enhancement ratio between them (Huang et al. Scientific Reports 4, 4380, doi:10.1038/srep04380)

observed at a wavelength of 269 and 291 nm, respectively. They attributed the increased emission mostly to the light extraction efficiency (LEE) of the Al nanoparticles, rather than an increase in internal quantum efficiencies (IQEs) [66].

9.3.2 The Mechanism of Enhanced Photoemission Efficiency

Besides incident field enhancements, there have been additional contributions to the enhancement of light-emitting devices coupled with LSPR, such as emission pattern and radiative decay control, enhancement of spontaneous emission rate, and an image charge effect. This section will discuss the origin of the LSPR-induced photoemission enhancement to elucidate electron–photon interactions in DUV plasmonics, where, unlike plasmonics in visible, the absorption and scattering losses of the supporting media are not negligible.

The emission pattern from an active LED media can be changed by the presence of plasmonic structures acting as a nano-antenna [68, 69]. In the $Al_xGa_{1-x}N$ system, which we have introduced in the last section, the most dominant emission is photons with a polarization parallel to the crystal axis. As a result, DUV photons propagate parallel to the active layers of LEDs [66]. The LSPR on a roughened metal structure has a broad momentum spectrum, possibly matching the momentum of all photons generated in the active layer of LEDs. Thus, the light generated by the recombination of LSPRs can be extracted more easily from the top or bottom side of the LEDs. The emission directivity can better be controlled by periodic grating structures. Feng et al. reported a highly directional EL from top-emitting organic light-emitting devices (OLEDs) by using a two-dimensional periodically corrugated silver film as a cathode and a europium complex dye as an emissive layer [70]. The resonant excitation of surface plasmons on the interfaces of silver film contributes to the light transmission through the silver cathode and to the directional emission. The device shows a beam divergence of less than 4°; at the same time, the beam direction was controlled by periodicity of the grating structures. The additional requirement for such a sharp directivity is a narrow spectral emission from the active media, because the nanodesign for LSPR usually targets a specific wavelength.

The IQEs of LEDs arise from the recombination of *e–h* pairs at a P–N junction. LSPR helps to accelerate the recombination by an order of magnitude, owing to the Purcell effect resulting in a faster photoemission cycle [71–74]. The spontaneous emission for a radiation dipole is given by Fermi's golden rule, which is determined by the photon density of state (DOS) and the dipole emission matrix element of a material. Thus, it is possible to control spontaneous emission by altering the photon DOS. A LED quantum well (QW) can experience strong quantum electrodynamic coupling to a surface plasmon mode if it is placed within the near field of metal nanostructures. An *e–h* pair in a QW recombines and emits a photon into a plasmon mode, rather than into free space. The degree of spontaneous emission rate modification for a given wavelength depends on the surface plasmon DOS at the wavelength. A strong enhancement occurs near LSPR, where the DOS is very high [74]. The enhancement factor can be measured by comparing the luminescence decay rates from the photoexcited QW on metal-coated and uncoated samples.

We note that plasmonic enhancement accompanied by a strong decrease in excited lifetime has also been observed in a molecular fluorescence system in the vicinity of metal nanoparticles [75]. The phenomenon is called metal-enhanced

fluorescence (MEF) and has been intensively studied by Lakowicz et al. [76–78]. DUV-MEF is often applied to biological studies for molecular-specific imaging [79]. Since radiative and nonradiative processes exhibit different distance dependences, the separation between a fluorophore and metal explains the enhancement and quenching of photoluminescence in MEF [80]. This mechanism is experimentally verified using scanning probe technology, positioning the Au nanoparticle in front of the molecule with nanometer precision [81].

Surface plasmons also provide coulombic forces to attract the *e–h* pairs at the surface of the metal nanoparticles, increasing the local concentration of charge carriers and thus resulting in the enhancement of recombination rates. The latter effect can be obtained for a wider frequency range and can therefore be used to improve the efficiency of broadband light emitters, not limited at the LSPR wavelength. Llopis et al. propose an electrostatic mechanism for carrier–metallic nanoparticle interactions, comparable in effect to plasmonic interactions [82]. Arising from the coulomb attraction of electrons and holes to their image charges in a metal produces large carrier concentrations near metallic nanoparticles. These charge drifts are often influenced by the temperature and incident photon density. An increased concentration enhances the rate of *e–h* recombination and manifests itself as an emission enhancement in the QW.

9.4 Summary and Future Applications in DUV Spectroscopy

In this chapter, the efficient coupling between photons and electrons in wide-bandgap materials was discussed on the basis of DUV plasmonics. In order to realize LSPR in the DUV range, fabrication methods of metal nanostructures specifically designed for the target wavelength were reviewed. With the aid of DUV plasmonics, the efficiency of photocatalysts as well as photovoltaic devices such as solar cells and UV photodetectors has been remarkably improved. This growing research field holds promise for the next-generation green and environmental technology. The usefulness of DUV plasmonics has also been demonstrated by the enhanced emission rate of DUV-LEDs, which have been intensively studied in order to replace conventional UV light sources and ultimately realize a DUV solid laser. The development of semiconductor-based DUV lasers and photodetectors would be a tremendous advantage for DUV spectroscopy. Moreover, fundamental research on photon–electron coupling in DUV plasmonics, e.g., emission pattern controls, excitation lifetime modulations, photon localizations, and enhancement, is expected to lead to significant advances in spectroscopic analysis, such as MEF, nonlinear spectroscopy, surface-enhanced Raman spectroscopy, and tip-enhanced Raman imaging. We would like to conclude by emphasizing that photon–electron coupling at DUV wavelengths has the potential to shape the future of spectroscopy.

References

1. K.A. Willets, R.P. Van Duyne, Localized surface plasmon resonance spectroscopy and sensing. Ann. Rev. Phys. Chem. **58**, 267–297 (2007)
2. J.M. McMahon, G.C. Schatza, S.K. Gray, Plasmonics in the ultraviolet with the poor metals Al, Ga, In, Sn, Tl, Pb, and Bi. Phys. Chem. Chem. Phys. **15**, 5415 (2013)
3. M. Sanz, D. Ortiz, R. Alcaraz de la Osa, J.M. Saiz, F. González, A.S. Brown, M. Losurdo, H.O. Everitt, F. Moreno, UV plasmonic behavior of various metal nanoparticles in the near and Far-field regimes: geometry and substrate effects. J. Phys. Chem. C **117**, 19606–19615 (2013)
4. E.D. Palik, *Handbook of Optical Constants of Solids* (Academic press, London, 1998)
5. W. Knight, N.S. King, L. Liu, H.O. Everitt, P. Nordlander, N.J. Halas, Aluminum for plasmonics. ACS Nano **8**, 834–840 (2014)
6. M.B. Ross, G.C. Schatz, Aluminum and indium plasmonic nanoantennas in the ultraviolet. J. Phys. Chem. C **118**, 12506–12514 (2014)
7. Y. Kumamoto, A. Taguchi, M. Honda, K. Watanabe, Y. Saito, S. Kawata, Indium for deep-ultraviolet surface-enhanced resonance raman scattering. ACS Photonics **1**, 598–603 (2014)
8. Y. Yang, J.M. Callahan, T.-H. Kim, S. Brown, H.O. Everitt, Ultraviolet nanoplasmonics: a demonstration of surface-enhanced raman spectroscopy, fluorescence, and photodegradation using gallium nanoparticles. Nano Lett. **13**, 2837–2841 (2013)
9. T. Okamoto, in *Near-Field Spectral Analysis of Metallic Beads*, ed. by S. Kawata. Topics in Applied Physics 81 (Springer, Heidelberg, 2001), pp. 97–121
10. C.F. Bohren, D.R. Huffman, Chapter 4: *Absorption and scattering by a sphere, in Absorption and Scattering of Light by Small Particles* (Wiley, New York, 2007), pp. 82–129
11. Y. Ekinci, H.H. Solak, J.F. Löffler, Plasmon resonances of aluminum nanoparticles and nanorods. J. Appl. Phys. **104**, 083107 (2008)
12. T.R. Jensen, M.D. Malinsky, C.L. Haynes, R.P. Van Duyne, Nanosphere lithography: tunable localized surface plasmon resonance spectra of silver nanoparticles. J. Phys. Chem. B **104**, 10549–10556 (2000)
13. C. Langhammer, M. Schwind, B. Kasemo, I. Zoric, Localized surface plasmon resonances in aluminum nanodisks. Nano Lett. **8**, 1461–1471 (2008)
14. G.H. Chan, J. Zhao, G.C. Schatz, R.P. Van Duyne, Localized surface plasmon resonance spectroscopy of triangular aluminum nanoparticles. J. Phys. Chem. C **112**, 13958–13963 (2008)
15. A. Kosiorek, W. Kandulski, H. Glaczynska, M. Giersig, Fabrication of nanoscale rings, dots, and rods by combining shadow nanosphere lithography and annealed polystyrene nanosphere masks. Small **1**, 439–444 (2005)
16. A. Taguchi, Y. Saito, K. Watanabe, Y. Song, S. Kawata, Tailoring plasmon resonances in the deep-ultraviolet by size-tunable fabrication of aluminum nanostructures. Appl. Phys. Lett. **101**, 081110 (2012)
17. Y. Saito, M. Honda, K. Watanabe, A. Taguchi, Y. Song, S. Kawata, Design of aluminum nanostructures for DUV plasmonics: blue shifts in plasmon resonance wavelength by height control. J. Jpn. Inst. Metals **77**, 27–31 (2013)
18. Y. Ekinci, H. Solak, C. David, Extraordinary optical transmission in the ultraviolet region through aluminum hole arrays. Opt. Lett. **32**, 172–174 (2007)
19. G. Ctistis, P. Patoka, X. Wang, K. Kempa, M. Giersig, Optical transmission through hexagonal arrays of subwavelength holes in thin metal films. Nano Lett. **7**, 2926–2930 (2007)
20. M. Schwind, B. Kasemo, I. Zoric, Localized and propagating plasmons in metal films with nanoholes. Nano Lett. **13**, 1743–1750 (2013)
21. D.O. Sigle, E. Perkins, J.J. Baumberg, S. Mahajan, Reproducible deep-UV SERRS on aluminum nanovoids. J. Phys. Chem. Lett. **4**, 1449–1452 (2013)
22. S.R. Ghanta, K. Muralidharan, Chemical synthesis of aluminum nanoparticles. J. Nanopart. Res. **15**, 1715 (2013)

23. F. Magnan, J. Gagnon, F.G. Fontaine, D. Boudreau, Indium@silica core–shell nanoparticles as plasmonic enhancers of molecular luminescence in the UV region. Chem. Commun. **49**, 9299–9301 (2013)
24. E. Cottancin, C. Langlois, J. Lerme, M. Broyer, M.A. Lebeaulta, M. Pellarin, Plasmon spectroscopy of small indium–silver clusters: monitoring the indium shell oxidation. Phys. Chem. Chem. Phys. **16**, 5763–5773 (2014)
25. M.J. Meziani, C.E. Bunker, F. Lu, H. Li, W. Wang, E.A. Guliants, R.A. Quinn, Y.-P. Sun, Formation and properties of stabilized aluminum nanoparticles. Appl. Mater. Interfaces **1**, 703–709 (2009)
26. N.H. Chou, X. Ke, P. Schiffer, R.E. Schaak, Room-temperature chemical synthesis of shape-controlled indium nanoparticles. J. Am. Chem. Soc. **130**, 8140–8141 (2008)
27. Y. He, F. Junxue, Y. Zhao, Oblique angle deposition and its applications in plasmonics. Front. Phys. **9**, 47–59 (2014)
28. C.A. Crouse, E. Shin, P.T. Murray, J.E. Spowart, Solution assisted laser ablation synthesis of discrete aluminum nanoparticles. Mater. Lett. **64**, 271–274 (2010)
29. R. Singh, R.K. Soni, Laser synthesis of aluminium nanoparticles in biocompatible polymer solutions. Appl. Phys. **A116**, 689–701 (2014)
30. C. Mandilasa, E. Daskalosa, G. Karagiannakisa, A. Konstandopoulosa, Synthesis of aluminium nanoparticles by arc plasma spray under atmospheric pressure. Mater. Sci. Eng. B **178**, 22–30 (2013)
31. L. Liu, Q. Zhang, J. Zhao, W. Yan, L. Zhang, Z. Wang, W. Tie, Study on characteristics of nanopowders synthesized by nanosecond electrical explosion of thin aluminum wire in the argon gas. IEEE Trans. Plasma Sci. **41**, 2221–2226 (2013)
32. J. Liqianga, Q. Yichuna, W. Baiqia, L. Shudana, J. Baojianga, Y. Libina, F. Weia, F. Honggang, S. Jiazhong, Review of photoluminescence performance of nano-sized semiconductor materials and its relationships with photocatalytic activity. Sol. Energy Mater. Sol. Cells **90**, 1773–1787 (2006)
33. W. Kubo, T. Tatsuma, Photocatalytic remote oxidation with various photocatalysts and enhancement of its activity. J. Mater. Chem. **15**, 3104–3108 (2005)
34. K. Awazu, M. Fujimaki, C. Rockstuhl, J. Tominaga, H. Murakami, Y. Ohki, N. Yoshida, T. Watanabe, A plasmonic photocatalyst consisting of silver nanoparticles embedded in titanium dioxide. J. Am. Chem. Soc. **130**, 1676–1680 (2008)
35. X. Zhang, Y.L. Chen, R.-S. Liu, D.P. Tsai, Plasmonic photocatalysis. Rep. Prog. Phys. **76**, 046401–046441 (2013)
36. K. Hashimoto, H. Irie, A. Fujishima, TiO_2 photocatalysis: a historical overview and future prospects. Jpn. J. Appl. Phys. **44**, 8269–8285 (2005)
37. R. Thiruvenkatachari, S. Vigneswaran, I.S. Moon, A review on UV/TiO2 photocatalytic oxidation process. Korean J. Chem. Eng. **25**, 64–72 (2008)
38. L.S. Kilvington, S.C. Kehoe, F.A. Touati, K.G. McGuigan, Solar and photocatalytic disinfection of protozoan, fungal and bacterial microbes in drinking water. Water Res. **39**, 877–883 (2005)
39. J.-M. Herrmann, Heterogeneous photocatalysis: fundamentals and applications to the removal of various types of aqueous pollutants. Catal. Today **53**, 115–129 (1999)
40. S. Hager, R. Bauer, Heterogeneous photocatalytic oxidation of organics for air purification by near UV irradiated Titanium dioxide. Chemosphere **38**, 1549 (1999)
41. M. Kang, The superhydrophilicity of Al–TiO2 nanometer sized material synthesized using a solvothermal method. Mater. Lett. **59**, 3122–3127 (2005)
42. S. Liu, G. Liu, Q. Feng, Al-doped TiO_2 mesoporous materials: synthesis and photodegradation properties. J. Porous. Mater. **17**, 197–206 (2010)
43. M. Honda, Y. Kumamoto, A. Taguchi, Y. Saito, S. Kawata, Plasmon-enhanced UV photocatalysis. Appl. Phys. Lett. **104**, 061108 (2014)
44. Q. Xu, F. Liu, Y. Liu, W. Meng, K. Cui, X. Feng, W. Zhang, Y. Huang, Aluminum plasmonic nanoparticles enhanced dye sensitized solar cells. Opt. Express **22**, A301–A310 (2014)

45. N.P. Hylton, X.F. Li, V. Giannini, K.-H. Lee, N.J. Ekins-Daukes, J. Loo, D. Vercruysse, P. Van Dorpe, H. Sodabanlu, M. Sugiyama, S.A. Maier, Loss mitigation in plasmonic solar cells: aluminium nanoparticles for broadband photocurrent enhancements in GaAs photodiodes. Sci. Rep. **3**, 2874 (2013)
46. G. Li, J. Song, J. Zhang, X. Hou, ZnO based UV detectors with Surface Plasmon Polariton enhancement on responsivity. Solid State Electron. **92**, 47–51 (2014)
47. Z. Jin, L. Gao, Q. Zhou, J. Wang, High-performance flexible ultraviolet photoconductors based on solution-processed ultrathin ZnO/Au nanoparticle composite films. Sci. Rep. **4**, 4268 (2014)
48. S. Butun, N.A. Cinel, E. Ozbay, LSPR enhanced MSM UV photodetectors. Nanotechnology **23**, 444010–444014 (2012)
49. S. Neretina, W. Qian, E. Dreaden, M.A. El-Sayed, R.A. Hughes, J.S. Preston, P. Mascher, Plasmon field effects on the nonradiative relaxation of hot electrons in an electronically quantized system. Nano Lett. **8**, 2410–2418 (2008)
50. A. Sobhani, M.W. Knight, Y. Wang, B. Zheng, N.S. King, L.V. Brown, Z. Fang, P. Nordlander, N.J. Halas, Narrowband photodetection in the near-infrared with a plasmon-induced hot electron device. Nat. Commun. **4**, 1643 (2013)
51. C. Clavero, Plasmon-induced hot-electron generation at nanoparticle/metal-oxide interfaces for photovoltaic and photocatalytic devices on Au. Nat. Photonics **8**, 95–103 (2014)
52. S. Mukherjee, F. Libisch, N. Large, O. Neumann, L.V. Brown, J. Cheng, J.B. Lassiter, E.A. Carter, P. Nordlander, N.J. Halas, Hot electrons do the impossible: plasmon-induced dissociation of H2. Nano Lett. **13**, 240–247 (2013)
53. Y. Keun Lee, C.H. Jung, J. Park, H. Seo, G.A. Somorjai, J.Y. Park, Surface plasmon-driven hot electron flow probed with metal-semiconductor nanodiodes. Nano Lett. **11**, 4251–4255 (2011)
54. E.A. Moulin, U.W. Paetzold, B.E. Pieters, W. Reetz, R. Carius, Plasmon-induced photoexcitation of "hot" electrons and "hot" holes in amorphous silicon photosensitive devices containing silver nanoparticles. J. Appl. Phys. **113**, 144501 (2013)
55. S. Mubeen, G.H. Sosa, D. Moses, J. Lee, M. Moskovits, Plasmonic photosensitization of a wide band gap semiconductor: converting plasmons to charge carriers. Nano Lett. **11**, 5548–5552 (2011)
56. T. Matsumoto, Handheld DUV LED source is 4 % efficient. Laser Focus World **48**, 10 (2012)
57. H. Hirayama, S. Fujikawa, N. Noguchi, J. Norimatsu, T. Takano, K. Tsubaki, N. Kamata, 222–282 nm AlGaN /and InAlGaN-based deep-UV LEDs fabricated on high-quality AlN on sapphire. Phys. Status Solidi A **206**, 1176–1182 (2009)
58. T. Kinoshita, T. Obata, T. Nagashima, H. Yanagi, B. Moody, S. Mita, S. Inoue, Y. Kumagai, A. Koukitu, Z. Sitar, Performance and reliability of deep-ultraviolet light-emitting diodes fabricated on AlN substrates prepared by hydride vapor phase epitaxy. Appl. Phys. Express **6**, 092103 (2013)
59. N. Akbay, J.R. Lakowicz, K. Ray, Distance-dependent metal-enhanced intrinsic fluorescence of proteins using polyelectrolyte layer-by-layer assembly and aluminum nanoparticles. J. Phys. Chem. C **116**, 10766–10773 (2012)
60. C. Forestiere, A. Handin, L.D. Negro, Enhancement of molecular fluorescence in the UV spectral range using aluminum nanoantennas. Plasmonics **9**, 715–725 (2014)
61. X. Jiao, S. Blair, Optical antenna design for fluorescence enhancement in the ultraviolet. Opt Express **20**, 29909 (2012)
62. K. Okamoto, I. Niki, A. Shvartser, Y. Narukawa, T. Mukai, A. Scherer, Surface-plasmon-enhanced light emitters based on InGaN quantum wells. Nat. Mater. **3**, 601–605 (2004)
63. A.I. Zhmakin, Enhancement of light extraction from light emitting diodes. Phys. Rep. **498**, 189–241 (2011)
64. C.Y. Cho, Y. Zhang, E. Cicek, B. Rahnema, Y. Bai, R. McClintock, M. Razeghi, Surface plasmon enhanced light emission from AlGaN-based ultraviolet light-emitting diodes grown on Si (111). Appl. Phys. Lett. **102**, 211110 (2013)

65. W.Z. Liu, H.Y. Xu, C.L. Wang, L.X. Zhang, C. Zhang, S.Y. Sun, J.G. Ma, X.T. Zhang, J.N. Wang, Y.C. Liu, Enhanced ultraviolet emission and improved spatial distribution uniformity of ZnO nanorod array light emitting diodes via Ag nanoparticles decoration. Nanoscale **5**, 8634–8639 (2013)
66. K. Huang, N. Gao, C. Wang, X. Chen, J. Li, L. Shuping, X. Yang, J. Kang, Top- and bottom-emission-enhanced electroluminescence of deep-UV light-emitting diodes induced by localised surface plasmons. Sci. Rep. **4**, 4380 (2014)
67. N. Gao, K. Huang, J. Li, S. Li, X. Yang, J. Kang, Surface-plasmon-enhanced deep-UV light emitting diodes based on AlGaN multi-quantum wells. Sci. Rep. **2**, 816 (2012)
68. I. Gryczynski, J. Malicka, Z. Gryczynski, J.R. Lakowicz, Radiative decay engineering 4. Experimental studies of surface plasmon-coupled directional emission. Anal. Biochem. **324**, 170–182 (2004)
69. J.M. Sanz, D. Ortiz, R. Alcaraz de la Osa, J.M. Saiz, F. González, A.S. Brown, M. Losurdo, H.O. Everitt, F. Moreno, M.W. Knight, L. Liu, Y. Wang, L. Brown, S. Mukherjee, N.S. King, H.O. Everitt, P. Nordlander, N.J. Halas, Aluminum plasmonic nanoantennas. Nano Lett. **12**, 6000–6004 (2012)
70. J. Feng, T. Okamoto, S. Kawata, Highly directional emission via coupled surface-plasmon tunneling from electroluminescence in organic light-emitting devices. Appl. Phys. Lett. **87**, 241109 (2005)
71. N.E. Hecker, R.A. Höpfel, N. Sawaki, Enhanced light emission from a single quantum well located near a metal coated surface. Phys. E. **2**, 98 (1998)
72. N.E. Hecker, R.A. Höpfel, N. Sawaki, T. Maier, G. Strasser, Surface plasmon-enhanced photoluminescence from a single quantum well. Appl. Phys. Lett. **75**, 1577 (1999)
73. I. Gontijo, M. Boroditsky, E. Yablonovitch, S. Keller, U.K. Mishra, S.P. DenBaars, Coupling of InGaN quantum-well photoluminescence to silver surface plasmons. Phys. Rev. B **60**, 11564 (1999)
74. A. Neogi, C.W. Lee, H.O. Everitt, T. Kuroda, A. Tackeuchi, E. Yablonovitch, Enhancement of spontaneous recombination rate in a quantum well by resonant surface plasmon coupling. Phys. Rev. B **66**, 153305 (2002)
75. J.O. Karolin, C.D. Geddes, Reduced lifetimes are directly correlated with excitation irradiance in metal-enhanced fluorescence (MEF). J. Fluoresc. **22**, 1659–1662 (2012)
76. I. Gryczynski, J. Malicka, Z. Gryczynski, K. Nowaczyk, J.R. Lakowicz, Ultraviolet surface plasmon-coupled emission using thin aluminum films. Anal. Chem. **76**, 4076–4081 (2004)
77. E. Fort, S. Grésillon, Surface enhanced fluorescence, topical review. J. Phys. D. Appl. Phys. **41**, 013001–013031 (2008)
78. C. Forestiere, A. Handin, L.D. Negro, Enhancement of molecular fluorescence in the UV spectral range using aluminum nanoantennas. Plasmonics **9**, 715–725 (2014)
79. M. Kikawada, A. Ono, W. Inami, Y. Kawata, Enhanced multicolor fluorescence in bioimaging using deep-ultraviolet surface plasmon resonance. Appl. Phys. Lett. **104**, 223703 (2014)
80. R. Carminati, J.-J. Greffet, C. Henkel, J.M. Vigoureux, Radiative and non-radiative decay of a single molecule close to a metallic nanoparticle. Opt. Commun. **261**, 368–375 (2006)
81. S. Kühn, U. Håkanson, L. Rogobete, V. Sandoghdar, Enhancement of single-molecule fluorescence using a gold nanoparticle as an optical nanoantenna. Phys. Rev. Lett. **97**, 017402 (2006)
82. A. Llopis, J. Lin, S.M.S. Pereira, T. Trindade, M.A. Martins, I.M. Watson, A.A. Krokhin, A. Neogi, Electrostatic mechanism of strong enhancement of light emitted by semiconductor quantum wells. Phys. Rev. B **87**, 201304 (2013)